

DISSERTATION

# Track Quality Evaluation Using a Dynamic Black-Box Model of a Railway Vehicle: A Feasibility Study

ausgeführt zum Zwecke der Erlangung des akademischen Grades  
eines Doktors der technischen Wissenschaften

eingereicht an der Technischen Universität Wien,  
Fakultät für Maschinenbau

von

Dipl.-Ing. Martin Kozek  
Pfadenhauergasse 22/28  
1140 Wien

Geboren am 13.02.1967  
Matr.Nr.: 85 25 427

Wien, im Oktober 1998

## Kurzfassung

Das Ziel der vorliegenden Arbeit war es eine Beurteilung der Gleisqualität mittels der Prädiktion der dynamischen Fahrzeugreaktionen durch ein dynamisches black-box Modell durchzuführen. Das Modell soll dabei imstande sein, die dynamischen Fahrzeugreaktionen für eine gegebene Strecke zu präzisieren. Um eine zeitaufwendige physikalische Modellierung zu vermeiden werden Systemidentifikations-Algorithmen verwendet.

Ein wichtiger Teil der Aufgabe besteht daher in der Untersuchung und Beurteilung der vorhandenen Meßdaten für Gleisgeometrie und Fahrzeugreaktion, um über die Eigenschaften der Meßsignale (wie Filterung, Eckfrequenzen und Übertragungsfunktionen) sowie systematische und zufällige Fehler Aufschluss zu erhalten. Außerdem kann durch die Verwendung mehrfacher Messfahrten auf derselben Strecke und durch redundante Messungen in jedem Datensatz die Genauigkeit und Konsistenz der Messvorgänge überprüft werden. Dateneigenschaften, die eine starke Einschränkung für eine Identifikation darstellen werden isoliert und aufgelistet.

Da Gleis- und Fahrzeugdaten völlig unabhängig voneinander gemessen werden, müssen die beiden Datensätze vor einer Identifikation synchronisiert werden. Methoden für eine geeignete Synchronisierung von Gleis- und Fahrzeugdaten werden entwickelt und die Performance der einzelnen Algorithmen wird sowohl an simulierten als auch an gemessenen Daten festgestellt. Die mit diesen Methoden erzielbare Genauigkeit ist wesentlich höher als es mit der Verwendung von Synchronisationspunkten oder Krümmungssignalen möglich ist. Außerdem verwenden die Synchronisationsalgorithmen jeden Abtastpunkt im Datensatz während einfache Methoden nur spezielle Punkte in den Datensätzen berücksichtigen, die oftmals weit auseinander liegen.

Wegen der Einschränkungen, die durch die systematischen Fehler der Datensätze gegeben sind, werden nur ein paar beispielhafte Identifikationen durchgeführt. Dennoch zeige die Ergebnisse klar, daß eine Vorhersage der Fahrzeugreaktionen möglich sein müßte, obwohl die Effekte von nichtlinearen Stabilitätsproblemen mit vertretbarem Aufwand nicht zuverlässig vorhergesagt werden können.

## Abstract

The aim of the present work was to study the feasibility of track quality assessment by prediction of the vehicle dynamics with a dynamic black-box model. The model should be able to predict the dynamic vehicle response for given track data. In order to avoid a time consuming physical modeling of the vehicle, system identification algorithms will be applied.

An important part of the task therefore was to evaluate existing measurement data of both track geometry and vehicle response to learn about inherent characteristics (like filtering, cut-off frequencies, and transfer functions), systematic and stochastic errors. Furthermore, by utilizing multiple measurements from the same track section and redundant information within each data record the accuracy and consistency of the measuring procedures could be assessed. Data properties which pose a strong limitation for an identification are isolated and listed.

Since track and vehicle data sets are recorded independently they have to be synchronized prior to an identification. Methods for proper synchronization of track and vehicle data are developed and the performance of the individual algorithms are tested with both simulated and measured data. The achievable synchronization accuracy of these algorithms is much higher than by a use of synchronization marks or curvature readings. Furthermore, the synchronization algorithms make use of each sample in the data records as opposed to simple approaches which just take into account distinct features which are often far apart from each other.

Due to the limitations posed by systematic errors in the data sets, only a few exemplary identification procedures are carried out. Nevertheless, the results clearly indicate that a prediction of a generic vehicle response could be possible although the effects of nonlinear stability phenomena can not be reliably predicted with acceptable costs.

## Preface

Although only one author is named in the title of this work it stands for the contributions of many more. I am especially grateful to Prof. Dr. H.P. Jörgl who gave me all the support and freedom I could wish for. Without the perfect working conditions he set up at the Institute for Machine- and Process-Automation (IMPA) this work would not have been possible. Prof. Dr. K. Rießberger has to be thanked also in the first place for he is the one who initiated the whole project in the spring of 1996. From this first meeting on he personally took care of all the necessary conditions for the successful progress of this work. It is the consequence of his manifold contacts to other people in the railway industry and in the ÖBB that the necessary data for this investigation were recorded.

The ÖBB as an organization was always friendly and helpful and did not spare any expenses to make the necessary data available. Dipl.-Ing. W. Hanreich, Dipl.-Ing. J. Stephanides, and Ing. H. Hutterer were the competent persons who assisted me with answers to any question and they provided many invaluable suggestions.

Dr. P. Mittermayr (head of the Büro für angewandte Mechanik und Mathematik, Wien) was of great help in clearing the sight for the main obstacles. He pointed out the difficulties of the task and he also went to great lengths to support this work with the results of his own work.

Another person who expanded my insight in the secrets of track geometry recording is Dr. W. Oberlechner from Plasser American Corp. He made it possible for me to visit the place where the measuring devices and recording systems for the superstructure measuring coach of the ÖBB were developed and manufactured. Most important, his knowledge helped to identify many sources of formerly unexplained data characteristics.

The Austrian Department for Science and Transportation supported this work with a Kurt-Gödel scholarship which I consumed at the University of Utah, Salt Lake City. I have to be very thankful to the people at the University of Utah, but especially to Prof. Dr. S. Devasia from the Nonlinear Controls group and to Dr. M. Skliar from the Chemical Engineering Department for their warm and friendly support during my stay in the United States. They provided an environment where it was not only fun to work but where scientific and social components were very luckily balanced.

Of course I am indebted to my friends and colleagues at the IMPA who indirectly formed a vast part of this work. Their influence extends much farther than to the host of discussions, innumerable technical supports, and many informal conversations. Acting for all of my colleagues stand the names of Dr. R. Korb, who patiently shared his knowledge on Radial Basis Function Networks whenever I needed advice and Dipl.-Ing. S. Jakubek, who guided me in clearing all the obstacles of  $\LaTeX$ .

Finally, I have to thank the one person who gave me the motivation to take all the less pleasant things upon me to finish this work. My wife Sybille not only was an example to follow but she provided everything nobody else could give.

M.K.

# Contents

<b>1</b>	<b>Introduction</b>	<b>1</b>
1.1	Motivation . . . . .	2
1.2	Problems . . . . .	3
1.3	Overview . . . . .	4
<b>2</b>	<b>Investigation of Track Data</b>	<b>5</b>
2.1	Track Geometry . . . . .	5
2.2	Measuring Method . . . . .	7
2.3	Data Channels Considered . . . . .	8
2.4	Data Sets . . . . .	8
2.5	Distance . . . . .	9
2.6	Speed . . . . .	12
2.7	Level . . . . .	14
2.8	Alignment . . . . .	17
2.9	Curvature . . . . .	20
2.10	Gauge . . . . .	25
2.11	Cant . . . . .	28
2.12	Redundancy of Measurements . . . . .	31
2.12.1	Level and Cant . . . . .	31
2.12.2	Alignment and Gauge . . . . .	34
2.13	Evaluation of Track Data . . . . .	38
2.13.1	Distance . . . . .	38
2.13.2	Speed . . . . .	39
2.13.3	Level . . . . .	39
2.13.4	Alignment . . . . .	39
2.13.5	Curvature . . . . .	40
2.13.6	Gauge . . . . .	40
2.13.7	Cant . . . . .	40
<b>3</b>	<b>Vehicle Response</b>	<b>41</b>
3.1	Measuring Method . . . . .	41
3.2	Data Channels Considered . . . . .	42
3.3	Data Sets . . . . .	42
3.4	Distance . . . . .	43
3.5	Speed . . . . .	44
3.6	Wheel Forces . . . . .	45
3.6.1	Lateral Forces ( $Y$ ) . . . . .	45
3.6.2	Vertical Forces ( $Q$ ) . . . . .	47
3.7	Twist Between Bogie and Car Body . . . . .	49
3.8	Car Body Accelerations . . . . .	51

3.9	Accelerations of Mounting Frame (Measuring Coach)	56
3.10	Evaluation of Vehicle Data	57
3.10.1	Distance	57
3.10.2	Speed	57
3.10.3	Lateral Forces ( $Y$ )	58
3.10.4	Vertical Forces ( $Q$ )	59
3.10.5	Twist	59
3.10.6	Car Body Accelerations	59
3.10.7	Accelerations of Mounting Frame	60
<b>4</b>	<b>Data Synchronization</b>	<b>61</b>
4.1	Sampling Rate Conversion	62
4.1.1	Constant Speed	62
4.1.2	Varying Speed	65
4.2	Data Correlations	66
4.2.1	Linear Correlations	66
4.2.2	Nonlinear Correlations	67
4.3	Calculation of Shift Function Estimate	68
4.3.1	Basic Principle	68
4.3.2	Calculation of Shift	69
4.4	Absolute Reference	71
4.5	Properties of Relative Shift Estimate	73
4.6	Model Based Synchronization	78
4.7	Simulation Results	80
4.7.1	Relative Shift	80
4.7.2	Absolute Shift	82
4.8	Effect of Absolute Shift on the Relative Shift Estimate	86
<b>5</b>	<b>Synchronization of Measured Data Sets</b>	<b>92</b>
5.1	Coarse Adjustment	92
5.2	Comparison of Signal Pairs	93
5.2.1	Cross Correlation Estimates	93
5.2.2	Shift Function Estimates	95
5.3	Synchronization of Data Sets	97
5.3.1	Straight Track	97
5.3.2	Curved Track	104
5.4	Comparison of Synchronization Methods	112
5.5	Absolute Shift in Measured Data	115
<b>6</b>	<b>Identification of Vehicle Dynamics</b>	<b>118</b>
6.1	Model Order Tests	118
6.1.1	Model Order Estimation Using Lipschitz Coefficients	118
6.1.2	Model Order Estimation Using Higher Order Correlations	119
6.2	Identification of Wheel Forces	121
6.2.1	Identification of Low-Frequency Dynamics	121
6.2.2	Lateral Wheel Forces	125

<b>7</b>	<b>Conclusion</b>	<b>130</b>
7.1	Data Acquisition . . . . .	130
7.2	Signal Synchronization . . . . .	132
7.3	Identification . . . . .	133
7.4	Outlook . . . . .	133
<b>A</b>	<b>Transfer Functions in Geometry Measurement</b>	<b>134</b>
A.1	Versine Measurement . . . . .	134
A.2	Moving Average . . . . .	135
<b>B</b>	<b>Nonlinear Model Validation</b>	<b>138</b>
B.1	Higher Order Correlations . . . . .	138
B.1.1	Basic Principle and Algorithm . . . . .	138
B.1.2	Simulated Examples . . . . .	140
B.2	Continuity Property of Function Mapping . . . . .	142
B.2.1	Basic Principle and Algorithm . . . . .	143
B.2.2	Simulated Examples . . . . .	144
<b>C</b>	<b>Calculation of Spectra</b>	<b>150</b>
C.1	Nonparametric Spectral Estimation . . . . .	150
C.1.1	Periodogram . . . . .	150
C.1.2	Bartlett Method . . . . .	151
C.1.3	Blackman-Tukey Method . . . . .	151
C.1.4	Welch Method . . . . .	151
C.2	Errors in Spectral Analysis Due to Sampling Jitter . . . . .	152
<b>D</b>	<b>Spline Interpolation</b>	<b>153</b>
D.1	Interpolation Polynomials . . . . .	153
D.2	Cubic Spline Interpolation . . . . .	153
D.2.1	Simulation: Comparison of Resampling by Cubic Splines versus Low-Pass Filtering . . . . .	155

# Kapitel 1

## Introduction

Modern railway track has to suffice many demands: The costs for building and maintenance should be reasonably low while the service life should be as high as possible. Therefore, the choice of the superstructure of a railway track already determines the overall costs at a very early stage. It is a difficult task to find the economic optimum between too short service intervals and no maintenance at all. This is true not only because of the service costs themselves but also because of costs associated with closed tracks, speed limitations, and other impediments. The technological constraints for such an economic strategy have to be laid down in advance and therefore must be known as precisely as possible. But above all, the track must guarantee a safe travel for all vehicles running along it. Although this seems to be a trivial criterion it is far more complex because of the multitude of vehicle types operating on the same track. Basically three categories of railway cars are in use:

1. Freight cars with high loads at moderate speeds
2. Passenger cars with small loads at high speeds
3. Engines pulling the respective trains

Especially the demands of the first two types are quite different. This is most obvious in curved track where a certain superelevation of the outer rail is added by design. Since the car body is tilted to the inside the lateral forces acting upon the wheels are ideally compensated to zero at a certain speed. If the speed is higher or lower than that particular speed a positive or negative lateral force will result. Because of the differing train speeds this is an unavoidable fact and some compromise has to be accepted. Again, some safety criterion is necessary to limit the possible range of the aforementioned parameters. Another criterion for track quality is riding comfort. The need for such a criterion is easily understandable for passenger cars, however, it becomes increasingly important for the safe transport of sensitive goods. Although railway vehicle manufacturers have gone great lengths to assure a safe and comfortable ride at high speeds and have already achieved a very high level the quality of the railway track is still most influential.

From the short enumeration given above it becomes apparent that track quality affects many areas in railway transportation and is crucial for safe travel. Although most demands originate in a dynamical reaction of the vehicle (safety against derailment, passenger comfort) track quality assessment is still mostly based on geometric measurement data of the track. In order to link the information contained in track data to knowledge about the dynamic vehicle reactions three basic possibilities exist. First, an expert can look at the track data plots and rate the track based on his knowledge. Apparently, the performance of this method is subjected to personal expertise, a possible subjective bias, and, typically, humans tend to pay more attention to large amplitudes whereas they can not easily evaluate the frequency content. Second, data can be



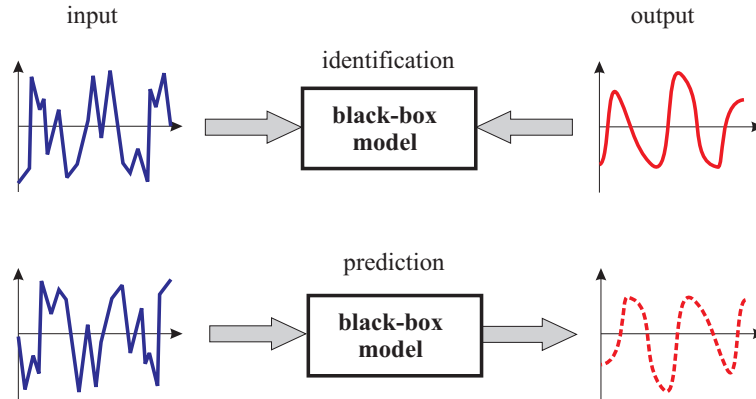


Abbildung 1.1: *Black-box model. Top: Identification of model parameters with known input- and output-data. Bottom: Prediction of unknown output with known input.*

evaluated by statistical methods. The most important parameter is usually the standard deviation which is computed for track sections of different lengths to compare average and localized deviations. Additionally, maximum amplitudes are detected and evaluated [14, 44, 40]. Although this procedure can be applied to band-pass filtered components of track signals it is again in principal an evaluation in the spatial domain which can not directly detect possibly harmful frequency components with relatively small amplitude. The third and most expensive approach is a simulation of the dynamic vehicle reactions with a high-order rigid body model which may even be combined with finite element methods [12, 26, 51]. Although these models can be fine tuned to give a very accurate prediction of the reactions of every vehicle part they are very complex and because of the large number of components it takes a lot of time and effort to find the correct parameters. A prerequisite for this goal is the availability of vehicle data for a given track to evaluate the accuracy of the model. However, as opposed to the first two possibilities, the last approach gives a description of the vehicle reactions which are of immediate importance when it comes to evaluate ride comfort and safety.

## 1.1 Motivation

It would be tempting to compute the vehicle reactions from track data without having to build and evaluate a large and complex model. By using a black-box model the need for evaluation data can not be circumvented but the model building process can be strongly shortened. A black-box model is a structure which is capable of producing a unique output to a certain input signal without knowledge of the inner structure of the model. This can be achieved by identification methods where the parameters of a linear black-box model are adjusted by an algorithm so that the error between the predicted and the actual output is minimized [34, 46]. In the case of nonlinear models either models with nonlinear differential equations (e.g. Volterra-Wiener series [45]) or Neural Networks may be applied. The process of identification (training) is symbolized by the top sketch in figure 1.1. Once the model parameters are determined properly the model may be used to predict unknown outputs for a given input (bottom of figure 1.1). If such a method is applied to the problem of track quality assessment, it can be solved by evaluating the dynamic vehicle response, i.e. well established criteria for safety against derailment and passenger comfort can be utilized [14, 15].

The reason why a black-box approach has not been implemented in railway systems in a large scale is twofold: For the identification purpose two data sets (input/output) are necessary, moreover, these data sets have to be synchronized so that every sample in one set has a distinct counterpart in the other set. Additionally, the dynamic response of railway vehicles is known to exhibit a strong nonlinear relationship with geometric track irregularities. This fact is very important since

it renders the well established and extensive linear system theory less useful. A nonlinear grey-box model identification (partial knowledge on physical structure is incorporated) is investigated in [20]. The resulting model parameters are in poor agreement with the actual ones because of a sensitive parameter mapping. In contrast, the black- and grey-box models with ANNs in [39] and [28] produce very promising results. This is the reason why Artificial Neural Networks (ANNs) are used as model structure. ANNs are capable of learning any static or dynamic nonlinear function mapping with an accuracy only depending on the complexity of the network [35, 27]. They are therefore well suited for this nonlinear identification task and their performance is expected to be superior to linear methods in this application. Additionally, Neural Networks can be easily implemented for on-line learning which offers the possibility to adjust them to a changing system behavior.

Nevertheless, ANNs have already been applied to some problems in railway systems. In a recent paper [33] the combination of fuzzy logic together with neural networks was employed to improve the maintenance of ticket vending machines in a mass transit system. A vehicle model for steering dynamics using ANNs is presented in [19]. The problem of identifying the vertical wheel-rail interaction for a simple linear model with ANNs is investigated in [22]. Although the problem treated there is very similar to the core task of the current work the model is far too simple to be considered as useful (compare [51]).

Part of the aim of the present work is to evaluate existing measurement data of both track geometry and vehicle response to learn about inherent characteristics (filtering, cut-off frequencies, and transfer functions), systematic and stochastic errors. Furthermore, by utilizing multiple measurements from the same track section and redundant information within each data record the accuracy and consistency of the measuring procedures should be assessed.

## 1.2 Problems

The trade-off for the additional knowledge of the vehicle reactions is the need for an additional data set (vehicle responses) and the identification process. The most important signals of the vehicle response are the wheel-rail contact forces and the accelerations of the car body. It would be absolutely possible to measure these reactions directly on the superstructure measuring car. Indeed, the superstructure measuring car of the Austrian Federal Railways is already equipped with measuring wheelsets [40, 47]. Nevertheless, until now the vehicle responses are only recorded during special test runs for prototypes. These data sets are recorded completely independently from the track geometry with a dedicated dynamics measuring car. Therefore, both data sets have to be synchronized to assure proper assignment of corresponding signals.

Usually, track records are sampled in the spatial domain with a fixed nominal sampling interval of 0.25m or 0.5m. Distance is measured by a decoder which resolves the rotation of a wheelset into a number of pulses [40]. Each pulse is assigned a certain fraction of the wheel's circumference. Unfortunately, the circumference is not known exactly since the wheel tread is approximately conical and even changes in temperature affect the distance measurement. To relate the measurement records to the real track synchronization marks are also recorded. These marks provide only a very coarse means and are not suitable for a synchronization task. Both data sets will be affected by this problem.

On the other hand, any identification algorithm critically relies on the assumption that input and output signals are perfectly synchronized. If this assumption does not hold poor convergence (duration of identification), bad generalization (ability to correctly map an output to a given input), or even unstable models (no convergence) may result [6, 46]. Regardless of the identification method it is of utmost importance to have well synchronized data sets.

Therefore, synchronization methods should be developed and the performance of the individual algorithms should be evaluated with simulated and measured data.

## 1.3 Overview

Data for this investigation were recorded during consecutive test runs on two different types of track. The first series of test runs was carried out on the same section of straight track with differing speeds. The second series was executed in the same fashion although the track section was chosen to include many curves. Both track geometry and vehicle response data were recorded.

The remainder of this thesis is structured in the following chapters: Chapter 1 is dedicated to the investigation of track geometry data. The definitions of the geometric measurements are given and the measuring and recording process is described. For each data channel the investigation is structured in the parts Mean and Variance, Spectra, and Shift. In the first part the basic statistic quantities are computed to give a quick grasp of the differences between test runs. More room is dedicated to the spectral estimation of the signals. This method is important since inherent filter characteristics of the measurement setup and systematic errors may be detected by comparison of the spectral estimates from test runs at different speed. In the last part all signals of each quantity are compared by cross correlation methods in order to find relative shifts between different test runs. Since the measuring system records a redundant set of signals this redundancy is employed to check for consistent measurements. An evaluation with respect to the suitability for an identification concludes the chapter.

In chapter 2 the vehicle response data is analyzed and tested for systematic errors. Throughout the chapter the same structure as in chapter 1 was maintained including the front section with details on the measuring and recording process and the final evaluation.

A large part of the work is taken up by the problem of synchronization. Chapter 3 contains the theoretical aspects of the synchronization problem. Starting with basic remarks on the resampling problem it continues with definitions for correlations and relative and absolute shift functions. The basic idea for a localized shift estimate is developed and its properties are documented. A recursive model based algorithm is also developed to improve the purely correlation based approach and numerical simulations are carried out. The influence of absolute shift is discussed theoretically and numerical simulations are performed to establish quantitative effects.

The algorithms for synchronization are applied to actual measurement data in chapter 4. First, approximate synchronization procedures are mentioned. Then, optimal signal pairs for the synchronization algorithm are established by experiment. The resulting procedure is applied to signals from real measurement data. This investigation is divided into two parts: One for straight track and the other one for curved track. This division was adopted because the additional problems of curve negotiation were expected to aggravate the problems of the synchronization process.

Chapter 5 contains a short outline of the first steps of an identification procedure. Because of the systematic measurement errors especially in the wheel-rail contact forces this section is very limited in space. Nevertheless, the nonlinear nature of the rail-wheel interaction is clearly demonstrated and basic model structures are evaluated. The superior performance of nonlinear models is shown by comparison of performance data.

In the last chapter a discussion recapitulates and summarizes the main findings. Suggestions for future research and necessary improvements in the measuring systems are made.

An appendix consisting of several parts helps to keep the main chapters more readable and to give the necessary theoretical background. The bibliography lists either standard text books if the theory of an area is already well established or it contains citations of publications which are applicable to a special problem treated in the current work.



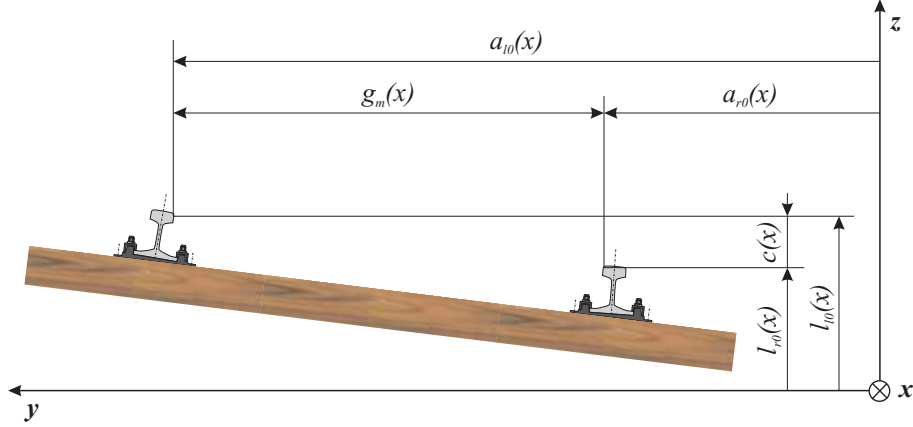


Abbildung 2.2: Cross section of railway track with wooden sleeper. Geometry in absolute coordinates.

of:

- Level (or vertical profile): mean of the z-coordinates of rails

$$\bar{l}(x) = \frac{l_{l0}(x) + l_{r0}(x)}{2} \quad (2.1)$$

- Alignment: mean of the y-coordinates of rails

$$\bar{a}(x) = \frac{a_{l0}(x) + a_{r0}(x)}{2} \quad (2.2)$$

- Gauge: difference of y-coordinates of rails

$$g_m(x) = a_{l0}(x) - a_{r0}(x) \quad (2.3)$$

- Cant (or cross level): difference of z-coordinates of rails

$$c(x) = \Delta l(x) = l_{l0}(x) - l_{r0}(x) \quad (2.4)$$

These values are defined with the absolute geometry of the track (subscript 0). Exceptions are the cant and the curvature signals, since in curves a certain cant (superelevation) is designed to compensate for centrifugal forces. The signal for curvature has to be regarded as a purely nominal (absolute) value due to its low-pass characteristic. Therefore, the track geometry can be split up into two parts: the nominal value and the measured deviations. The deviations from an ideal value are typically recorded in a medium to high frequency range while the nominal track exhibits only long wavelengths. However, when defects with increasingly greater wavelengths are investigated this division becomes difficult to maintain.

For the purpose of measuring track geometry the irregularities are defined in a slightly different manner. Nevertheless, all measurements are either relative or they consist of differences. Figure 2.3 shows the nominal rail position in dotted lines while the positions of the actual rails are measured relative to them. No absolute reference exists in the track data sets. By the following enumeration it becomes apparent that the measured signals are redundant. However, since different measurement setups might be used to directly acquire these signals, additional information can in fact be gathered. The main geometry signals recorded by the OEBB superstructure testing car are:

- Deviation from nominal level, left rail  $l_l(x)$  and right rail  $l_r(x)$  separately

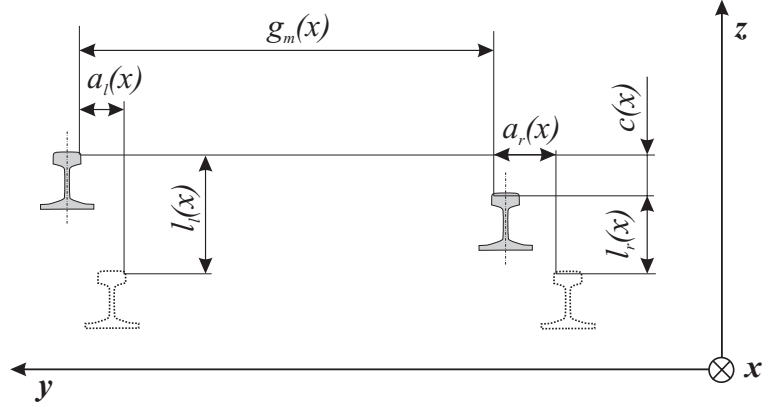


Abbildung 2.3: Cross section of nominal (dotted lines) and actual (continuous lines) railway track with position of rails. Geometry measurements without absolute reference.

- Deviation from nominal alignment, left rail  $a_l(x)$  and right rail  $a_r(x)$  separately
- Curvature, low-pass filtered to give nominal value  $\rho(x)$
- Deviation from nominal gauge, single signal  $g(x) = g_m(x) - g_0$
- Cant, difference of z-coordinates of rails  $c(x) = l_l(x) - l_r(x)$

Additionally, speed and relative distance are recorded for each sampling instance.

## 2.2 Measuring Method

It is an attractive idea to use modern survey techniques to get a very accurate track geometry. Unfortunately, the railway track is not absolutely rigid structure but it deforms under load and even exhibits pronounced dynamical effects varying with speed. State of the art in track recording systems therefore is a measurement coach which can be attached to normally scheduled trains. In such a setup the track geometry is recorded under real-world conditions other rail vehicles will also encounter.

The data investigated in this work were recorded by the superstructure testing car and the dynamics measuring car of the OEBC. It was developed and built in cooperation between the OEBC, Plasser American Corp. Plasser&Theurer, Jenbacher Transportsysteme, and various other contractors. The testing car is based on a 4-axle RIC coach with adapted bogies MD 524 suitable for speeds up to 250 km/h. One bogie is equipped with an electro-magnetic rail shoe brake the other with a mounting frame carrying part of the measuring equipment.

A laser gauge is connected to this mounting frame measuring directly the distance between two reference points on the inside of the rails. Additional laser arrays for both rails provide data for the shape of each rail head and the relative position of the two rails.

Two acceleration sensors attached to the floor of the testing car together with sensors recording the relative distance of the axle to the car floor form the basis for level and alignment signals. By double-integrating the vertical acceleration readings and adding the relative distance recordings, the level signals for both rails are computed. To avoid drifts and offsets because of the integration data are high-pass filtered.

Lateral acceleration sensors and an inertial system utilizing gyros produce the raw data for a spatial curve split up into three separately recorded signals. First the curvature, which is computed as the average curvature over 20m, and second the alignment for the right respectively left rail. The alignment signals are computed as deviations from a 60m mean value therefore exhibiting an

implicit high-pass characteristic. The inertial system also provides the basis for the computation of the cant signal.

Two acceleration sensors attached to the bearings of the axle allow for the registration of corrugation and other isolated faults on the rail surface. On two axles force measuring bearings are installed for the acquisition of wheel-rail contact forces.

On one axle an encoder is attached with a resolution of 8000 pulses per revolution. Data are sampled every 0.25m corresponding to a certain number of pulses regardless of speed. The train speed is calculated according to the time passing between two sampling instants.

## 2.3 Data Channels Considered

Data channels considered were limited to the geometric characteristics which are expected to contribute most strongly to vehicle responses:

- Distance  $x$
- Speed  $v(x)$
- Level, left  $l_l(x)$  and right  $l_r(x)$  rail
- Alignment, left  $a_l(x)$  and right  $a_r(x)$  rail
- Curvature  $\varrho(x)$
- Gauge, deviation from nominal value  $g(x)$
- Cant  $c(x)$

Some of these geometry signals have to be redundant, since only 4 degrees of freedom exist for the geometric deviations (see section 2.1). However, this redundancy can be utilized to perform an additional check on the reliability of data, as can be seen in section 2.12.

A major tool for investigation of measurement signals are spectra. A theoretical outline The frequency axis of the spectra has a unit of 1/m since all channels are sampled in the spatial domain. The reciprocal frequency  $\frac{1}{f_x}$  therefore becomes a wavelength  $\lambda_x$  which can be considered as an actual harmonic displacement of the rail. This simple connection is stated in equation 2.5:

$$\lambda_x = \frac{1}{f_x} \quad (2.5)$$

If this relation should be transferred into the time domain, the knowledge of momentary speed  $v(x)$  is of crucial importance. For constant speed a simple relation can be established

$$f_t = f_x \cdot v = \frac{v}{\lambda_x}, \quad v = \text{const.} \quad (2.6)$$

which allows an interpretation of spectra in the time domain. If a spectrum was obtained from a track portion not measured with constant speed, an oscillation with fixed frequency in the time domain would be spread over a range in the spectrum according to equation 2.6.

## 2.4 Data Sets

Data consists of two major groups, one for straight track and the other for curved track. Table 2.1 shows some characteristics of the two groups. Data were evaluated by shorter subsections over ranges with both large and minor deviations. The chosen range for the test runs at Angern -

Data Group	Location	Date	km	Speed Range
Straight	Angern - Drösing	10.06.97	39.9 - 58.3	60 - 140 km/h
Curved	Klagenfurt - Villach	25.06.97	127.0 - 123.1	100 - 140 km/h

Tabelle 2.1: *Main characteristics of data sets*

Test Runs	Color
ad7, da7	blue, 'b'
ad8, da8	red, 'r'
ad9, da9	green, 'g'
ad10, da10	magenta, 'm'
ad11, da11	cyan, 'c'

Tabelle 2.2: *Color key for figures*

Drösing, track 1, begins at km 49.40 and ends at km 52.40, for track 2 the range was km 45.80 to km 42.68. The test runs with direction Angern to Drösing were all performed with the engine pushing the train at defined forces except for the first test run (ad7). All other tests were performed in conventional configuration with the engine pulling. The color coding in spatial diagrams as well as in spectra is maintained as can be seen in table 2.2.

## 2.5 Distance

To assure that no gaps or double readings are included in distance data the numerical difference between all consecutive samples is computed. The resulting constant equaling the sampling interval is only interrupted by distinct peaks where a larger increment occurs. All test runs along the tracks of Angern-Drösing have consistent distance signals although the absolute distance shows shifts because of slightly differing starting points of the train. Data sets for straight track were recorded by starting from a standstill at a well defined milestone. Since the nominal value of the starting point is always the same there is a difference of at most 5 samples, corresponding to 1.25m. Data recording for curved track was started when the train was passing a milestone at full speed. Therefore, the shift between these measurements amounts up to 472 samples, corresponding to 118m. An uncertainty of this magnitude is certainly undesirable, allowing only for a very coarse allocation of track errors. Furthermore, distance data recorded on curved track were manually corrected during the test runs, each correction resulting in a large increment with either positive or negative sign. However, these discontinuities in distance records do not have any influence on other measured signals.

If the speed is calculated by simply dividing the sampling distance by the time passed between two sampling instances, a missed sample would produce a speed reading half as high as actually present since the time span has doubled in this case. No such evidence is found in the data.

To test whether the sampling intervals are uniform in length, the following procedure was carried out: Cross-correlation functions for the test runs 506-da7 and 507-da8, as well as for 506-da7 and 510-da11, were calculated for different sections of the track using the left alignment signals. The results for the shift at which the maximum of the cross-correlation function occurs are given in table 2.3. Obviously the shift between the two signals varies between -11 and -16 samples, leading to an average shift of -13 samples, and -9 and -21 samples leading to an average shift of -15 samples. Assuming constant sampling intervals, the difference in the sampling interval  $\Delta x_s$  can be calculated



Test Runs	Shift in Section						
	Global	1 to 1000	17E3 to 18E3	35E3 to 36E3	44E3 to 45E3	53E3 to 54E3	69E3 to 70E3
da7 / da8	-13	-11	-12	-13	-14	-15	-16
da7 / da9	-7	-5	-7	-7	-7	-8	-9
da7 / da10	3	6	5	3	3	2	-1
da7 / da11	-15	-9	-11	-13	-15	-17	-21

Tabelle 2.3: *Shift between test runs 506-da7, 507-da8, and 510-da11 respectively.*

according to

$$\Delta x_{s78} = \Delta k_{78} \cdot \frac{x_{N_{78}} - x_{0_{78}}}{N_{78}^2} = 5 \cdot \frac{18124.75}{72500^2} = 1.72 \cdot 10^{-5} m = 0.0172 mm, \quad (2.7)$$

$$\Delta x_{s711} = \Delta k_{711} \cdot \frac{x_{N_{711}} - x_{0_{711}}}{N_{711}^2} = 12 \cdot \frac{18124.75}{72500^2} = 4.14 \cdot 10^{-5} m = 0.0414 mm \quad (2.8)$$

where  $\Delta k$  is the difference in shifts between beginning and end of the signals,  $x_N - x_0$  is the length of the signals in m, and  $N$  is the number of samples for this distance. From table 2.3 it can be deducted that in the course of the measurement campaign during a sunny summer day the wheel temperature was rising, resulting in an increase in circumference and therefore sampling interval length. This conclusion is supported by the fact that the increase in sampling interval length is in accordance with the sequence of test runs.

The difference  $\Delta x_s$  may seem negligible but for system identification a shift of 12 samples almost certainly renders an identification algorithm worthless. Therefore, it is of great importance to verify that the track signals used for identification are resampled according to the sampling of the vehicle dynamics.

In order to get a quasi-continuous description of the shifts, the method outlined above is improved in two ways: First, the window for calculation of the cross-correlation functions is reduced in size from 1000 to 250 samples. The steps between calculations are also chosen much smaller, so that by overlapping windows smoothing is achieved. Second, the maximum of the correlation function is estimated by a 3-point interpolation, leading to a real number as opposed to an integer. The resulting shift function is also low-pass filtered in order to achieve a meaningful numerical derivative. This derivative of the shift function indicates how much each sampling interval is expanded or jolted respectively. The high-frequency remainder of the shift function has to be regarded as jitter, equal to additional noise in the signals. Thus, the choice of the cut-off frequency in the low-pass filter determines the content of noise in the signals. It would be tempting to choose a very high cut-off frequency to preserve as much information as possible, but in order to compensate for the distortion resampling has to be employed. If high-frequency distortions are present in the signal, a proportional high oversampling rate has to be chosen. Since the length of data records is rather big, the oversampling rate is limited by the memory available. Because of this trade-off, the cut-off frequency of the low-pass filter has to be chosen in accordance with the resampling algorithm and the system resources.

Figure 2.4 shows an example calculated from left level signals. Data were taken from test run Villach-Klagenfurt, km 145.5335 to km 143.0338, test run vk01 was chosen as reference. There was no low-pass filtering employed to illustrate the characteristics of the original signals. It becomes quite apparent that the increase in sampling interval size (lower plot) is not constant. The sampling intervals mostly change their size between  $\pm 5$ mm ( $\pm 20$ mm/m). However, there are erratic changes up to  $-65$ mm ( $-260$ mm/m). These values rather indicate a difference between the respective functions than an actual shift. By choosing a longer window for the calculation of the local shift some of these exceedances will disappear, although the shift function will also be smoothed.

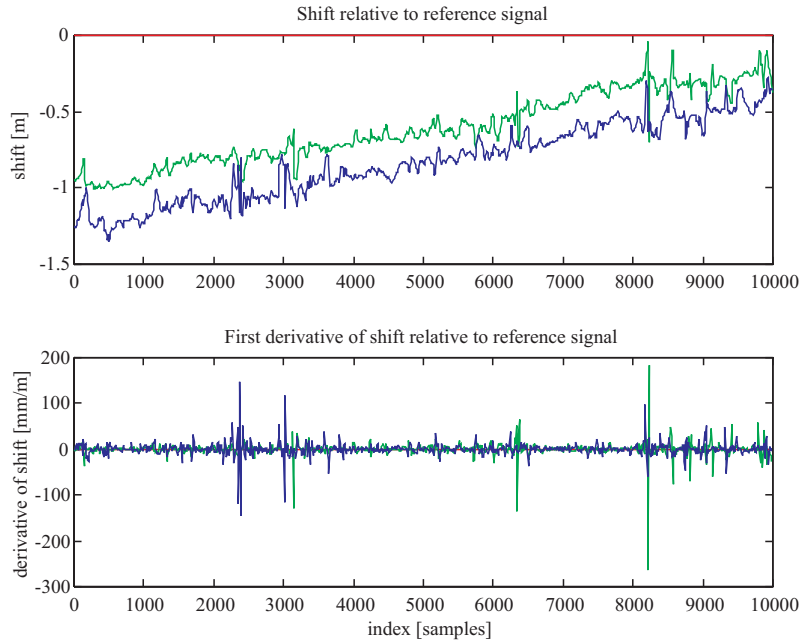


Abbildung 2.4: *Shift function for left level signals. Test run Villach-Klagenfurt, km 145.5 to km 143.0.*

Since optional low-pass filtering is provided by the algorithm, smoothing will be done separately, therefore allowing for a smaller window size and a more localized shift estimate.

For signals other than level signals the changes in sampling interval size are even bigger. Figure 2.5 shows the results for the same section and reference signal, but calculated from right alignment signals. Again, the same phenomena as in figure 2.4 can be seen, but they are more pronounced. Although the scales are different, the shift signals clearly show a more irregular shape. Around a sample number of 3250 (km 144.72) there is a most strong deviation. For approximately 80 samples the shift jumps from -1m to +4m within only 10 samples (the step size for this example) and then back again. Since all other signals do not show such an irregularity at the same section it has to be regarded as a measurement error. This is supported by the fact that shift signals calculated from left alignment signals as well as from the gauge signal show similar erratic behavior. There is no correlation between the respective irregularities. Inspection of the original signals around km 144.72 indeed shows a most strong deviation of the measured signal from the shape of the reference signal. The shift function has to be interpreted with caution: Sudden changes and jumps might not be caused by actual shift between signals but by differing signal shapes due to errors only present in one of the signals. Low-pass filtering and calculation of regression lines should therefore be applied to correct shift functions only, otherwise the results could be useless.

The overall shift between signals can be seen as the mean value of the derivatives over the whole distance. From the fact that the shift signals of test runs vk02 and vk04 in average show a constant slope with respect to vk01 it follows immediately that their sample size has to be different from that of test run vk01. Since the average slopes of vk02 and vk04 are approximately equal, they have the same sampling size. The difference in shift is approximately +0.75m (3 samples) for 10000 samples (2500m). Therefore, each sample contributes  $\Delta x_{s12} = \frac{0.75}{10000} \text{m} = 0.075 \text{mm}$  to this difference. This is in the same order of magnitude as the shift found in 2.7.

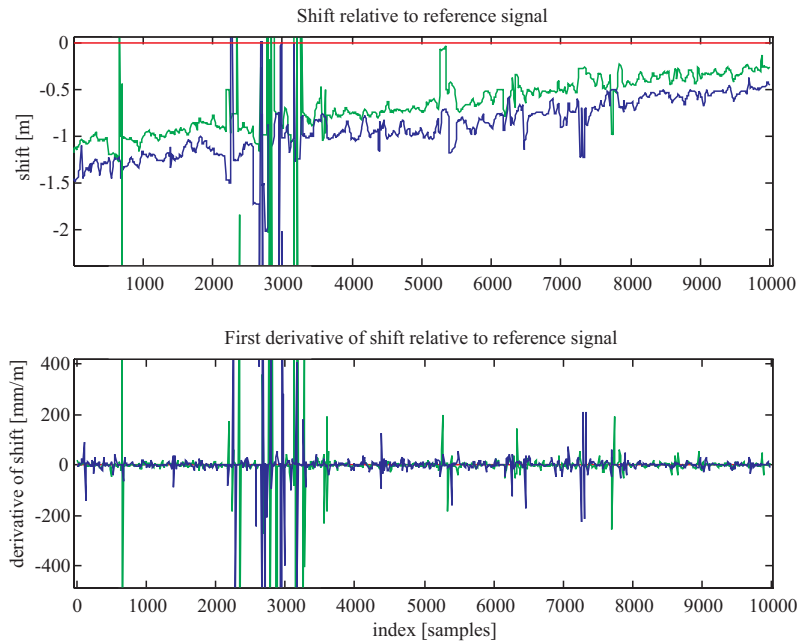


Abbildung 2.5: *Shift function for right alignment signals. Test run Villach-Klagenfurt, km 145.5 to km 143.0.*

Test Run	Mean [km/h]	Mean [m/s]	Variance [m <sup>2</sup> /s <sup>2</sup> ]
0006-ad7	59.99	16.66	0.0057
0007-ad8	80.64	22.40	0.0074
0008-ad9	88.96	24.71	0.0118
0009-ad10	100.76	27.99	0.0144
0010-ad11	110.88	30.80	0.0185

Tabelle 2.4: *Test runs on track 1. Statistics for speed.*

## 2.6 Speed

### Mean and Variance

Table 2.4 provides the basic statistical values. Although the variance is small the influence of measurement speed shows up very clearly. From 60 km/h to 110 km/h there is an increase of approximately 150% in variance.

### Spectra

All speed signals are more or less constant over the distance under investigation. However, a distinct oscillation is present in all of them. The average cycle is 11.6 samples long, corresponding to 2.89m.

The spectra of the different test runs in figure 2.6 clearly show this oscillation and higher harmonics at approximately 1.45m, 0.96m, 0.72m, 0.58m and 0.52m, respectively. The first five peaks almost certainly belong to an oscillation with the wheel circumference as basic harmonic and its higher harmonics derived by division by integer numbers.

This phenomenon could be caused by missing pulses at certain angles of the encoder. Assumed that a sampling instance is defined as the moment a fixed number of pulses have been registered, the following could happen: Since the angles for the same number of pulses vary, a simple algorithm

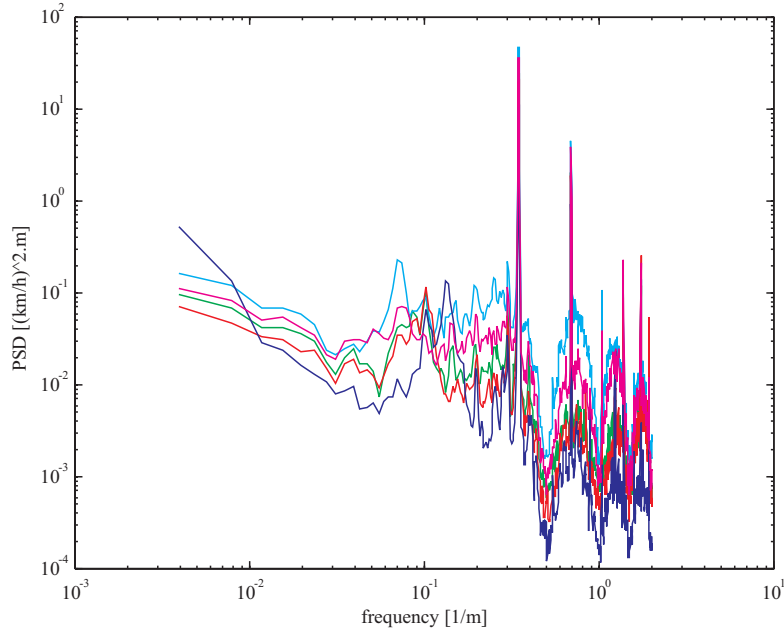


Abbildung 2.6: Spectra of speed signals. Test run Angern-Drösing (track 1), km 39.9 to km 38.4.

dividing the nominal sampling distance by the time span passed will lead to varying velocity readings at constant speed. However, since the missing pulses should be expected to be equally distributed, a periodic but non-harmonic signal should result. The actual speed signal is of a distinct harmonic nature, therefore asking for other explanations: The decoder is not mounted directly on the axle of the wheelset; rather, a small belt drive provides the transmission of wheel revolution to decoder movement. In both the wheelset, the pinion, and the belt itself misalignments may be present. If the effects of these imperfections accumulate they will certainly be found in the data.

It should also be noted that the first test run (blue) without pushing engine shows a different spectrum at low to medium frequencies. At higher frequencies the spectra are only differing in amplitude, exactly reflecting the different measurement speeds.

For the purpose of speed readings these faults can be easily overcome with a low pass filter since the train is only capable of certain maximum accelerations. However, the problem of converting spatial sampling into the time domain critically relies on the exact measurement of speed since this is the only signal which contains information about time.

If the harmonic oscillation superposed on the speed signal is caused by eccentric and misaligned wheels it should be possible to detect differences depending on which flange of the wheelset is closer to the rail shoulder. Indeed, in the data from curved track a strong correlation between curvature and the amplitude of the sinusoidal disturbance can be found. To find this correlation the low-frequency component of the speed signal is removed and the absolute value of the high-frequency part is correlated with the curvature signal. Data were taken from the test run Villach-Klagenfurt with curved track. For positive values of curvature a significantly smaller amplitude  $A^+$  of the harmonic disturbance results as compared to the amplitude  $A^-$  at negative values of curvature. In equations 2.9 and 2.10 the average value of the respective amplitude is given. Amplitudes were calculated from the RMS value of the high frequency part of speed signals in the sections given (average speed in these sections was 124.6 km/h).

$$A^+ = 0.57 \text{ km/h}, \quad 160.15 \text{ km} < x < 160.60 \text{ km} \quad (2.9)$$

$$A^- = 1.03 \text{ km/h}, \quad 160.85 \text{ km} < x < 161.08 \text{ km} \quad (2.10)$$

This amplitude of  $A^-$  relates to a difference in the radius of the wheels of 3.7mm. If a relative conicity of 1:10 is assumed (at a nominal radius of 0.46m) this would require a lateral deviation of 37mm. If an additional deviation of 1mm for the wheel-radius is assumed, this would still leave 27mm of lateral deviation. Because of these unrealistic large numbers it seems reasonable to assume that the belt drive of the decoder introduces much of the harmonic error found in speed data.

The cross-correlation indicates an average shift of 34m (136 samples) between the modulations in the speed signal and the curvature. The modulation in the speed signals lags behind the curvature signal, indicating that the wheelset (bogie) needs some distance to adapt to the rail geometry.

An additional offset to the speed signal is introduced by the dependence of the speed measurement on the local gauge. On a wide gauge the wheels will roll on a smaller radius because of the wheel conicity. In test run ad7-006 the average gauge from sample 10.418 to 20419 is  $-1.69mm$ , whereas between sample 20.420 and 30.246 it is  $7.35mm$ . This amounts to a difference in gauge of  $\Delta g = 9.04mm$ . We assume that the influence of the sine movement can be neglected because the sections under investigation are long enough to give an average of zero for that effect. Average measured speed on the first section is  $59.3299km/h$  ( $v_1 = 16.4805m/s$ ) and  $59.3784km/h$  ( $v_2 = 16.4940m/s$ ) on the second section. The proportion of speed increase amounts to  $\alpha = \frac{v_2}{v_1} = 1.000818$ . If we further assume that the car was travelling at the same constant speed  $v_{abs}$  over both sections and the measured speed  $v_i$  is calculated proportional to the angular velocity, the following will hold:

$$\alpha = \frac{v_2}{v_1} = \frac{k\omega_2}{k\omega_1} = \frac{k\frac{v_{abs}}{r_2}}{k\frac{v_{abs}}{r_1}} = \frac{r_1}{r_2}. \quad (2.11)$$

Therefore, the increase in speed is caused by a decrease in the rolling radius due to the wider gauge and the tire conicity. For a nominal value of the rolling radius  $r_1 = 0.46m$  the rolling radius on the wider gauge becomes  $r_2 = \frac{r_1}{\alpha} = 0.459624m$ . The absolute difference between rolling radii is hence  $\Delta r = r_1 - r_2 = 0.375776mm$ . Now we can calculate the relative conicity  $\gamma$  of the wheels for these two contact points:

$$\gamma = \frac{\Delta r}{\frac{\Delta g}{2}} = \frac{0.375776}{4.52} = 0.08313 \cong 1 : 12 \quad (2.12)$$

This value is in good agreement with worn wheel profiles on wide tracks [14].

## 2.7 Level

### Mean and Variance

The basic statistical values for the left and right level signals are shown in table 2.5. They were calculated from the values of track 1 between km 50.4995 to km 52.3995. Although the mean values are quite the same there are significant differences in the variances for left and right side. The bigger variances for the right side also show up in the spectra where bigger amplitudes occur at nearly unaltered shapes.

Error signals of curved track (Villach-Klagenfurt, km 145.53 to km 143.51) were calculated by subtracting the data of test runs vk02 and vk04 from the signals of vk01. They clearly show the eigenmode of the measuring coach (see table 2.6). The amplitude of this oscillation is approximately 0.5mm, the standard deviation is 0.29mm for the left rail and 0.28mm for the right rail respectively. Maximum difference on this section is +1.45mm, the minimum difference is -1.20mm.

### Spectra

The most significant property of the spectra for level is a band-pass characteristic. Low frequencies are cut off since they are regarded as deterministic parameters of the track (i.e. curves) and also because the double integration of car body accelerations could easily lead to a drift in level signals.

Test Run	Speed	Mean Left	Mean Right	Variance Left	Variance Right
0006-ad7	59.99	0.517	0.517	4.38	5.03
0007-ad8	80.64	0.518	0.517	4.11	4.81
0008-ad9	88.97	0.517	0.517	4.11	4.82
0009-ad10	100.78	0.517	0.516	4.27	5.04
0010-ad11	110.88	0.518	0.517	4.34	5.09

Tabelle 2.5: *Test runs on track 1. Statistics for level.*

Error Signal	Speed of Latter Run	Frequency Spatial Domain	Frequency Time Domain
(0006-ad7) - (0007-ad8)	22.40 m/s	0.052 1/m	1.16 Hz
(0006-ad7) - (0008-ad9)	24.71 m/s	0.047 1/m	1.16 Hz
(0006-ad7) - (0009-ad10)	27.99 m/s	0.043 1/m	1.20 Hz
(0006-ad7) - (0010-ad11)	30.80 m/s	0.041 1/m	1.23 Hz

Tabelle 2.6: *Frequencies of maxima in error signals.*

The spectra of the left level of the various test runs are depicted in figure 2.7. As mentioned above, spectra for the right level signals are very similar except for a slightly higher amplitude. On both sides the spectra differ only in a frequency range between approximately 0.025 1/m and 0.1 1/m. There is a very good agreement above the latter value. The spectra of the error signals reveal a more complex pattern. As can be seen in figure 2.8, there is a broad band where the error signals contain most of their power. A very important bandwidth is the range from 0.04 1/m to 0.055 1/m. This range corresponds to the possible natural frequency of the car body. A closer look at this frequency range depicted in figure 2.9 reveals two very distinct peaks for the test runs at higher speed and two less defined maxima for the test runs at medium velocities. Most important is the fact that the frequencies of these maxima in the time domain are within an accuracy of 5% of a frequency of 1.2Hz. Table 2.6 shows the frequencies and the results according to equation 2.6. Note that the frequencies are taken from various spectra at different numbers of points for FFT; therefore the vertical lines in figure 2.9 are not always at the current maximum. Since this frequency can be regarded as constant in the time domain and it fits the typical natural frequency of the car body, it has to be assumed that some dynamics of the measurement coach are falsely recorded as track characteristics. Moreover, the amplitudes increase with speed, leading to the conclusion that track recordings at high speeds are likely to have distorted spectra in the above mentioned range.

There is also a distinct peak at 0.35 1/m (0.3459 1/m). All signals regardless of speed show the peak at the same frequency. Since this peak occurs at the same frequency as the first peak of the speed signal (which in turn belongs to the wheel circumference) it has to be concluded that a fault at one wheel of the measuring coach is responsible for the peak. Although not visible in the spectra of figure 2.9, in other spectra of the error signals of level additional peaks at the wavelength of 1.45m, 0.96m, and 0.72m occur.

Another peak at the far right of the spectrum is nearly hidden in the noise. It can be confirmed, though, that this peak at 0.653m exists in the spectra of various test runs at different speeds. Its origin is not clear since the sleeper spacing on the track under investigation is 0.6m. At a frequency of approximately 0.086 1/m there is a peak where all error signals have the same amplitude. The corresponding wave length would be 11.6m. This phenomenon seems to be correlated with the longitudinal loads from the pushing engine only since all test runs with such loads differ in the same way from the reference signal measured without longitudinal load. Above this frequency the discrepancy between the error signals rises again to diminish at the frequency of the wheel circumference. In this range the peaks for a distinct natural frequency of the bogie should show up.

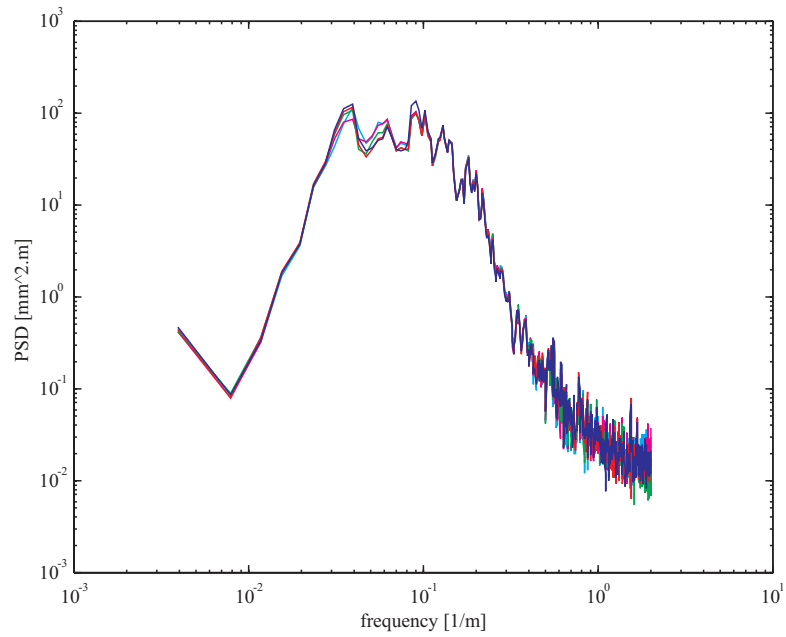


Abbildung 2.7: Spectra for left level. Test run Angern-Drösing (track1), km 50.5 to km 52.4.

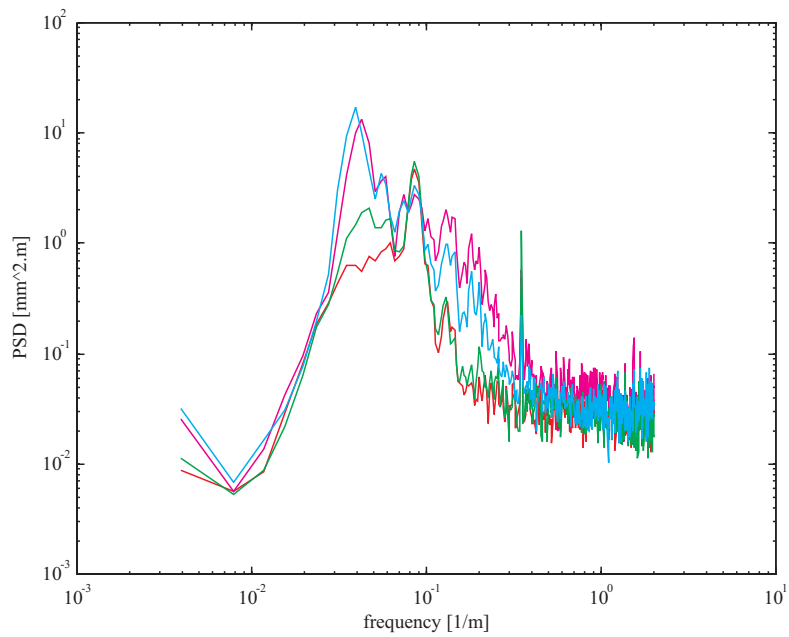


Abbildung 2.8: Spectra for error signals of level. Test run Villach-Klagenfurt, km 145.5 to km 143.5.

However, despite a considerable difference in amplitude the spectra show no peaks corresponding to a frequency of about 5-10 Hz.

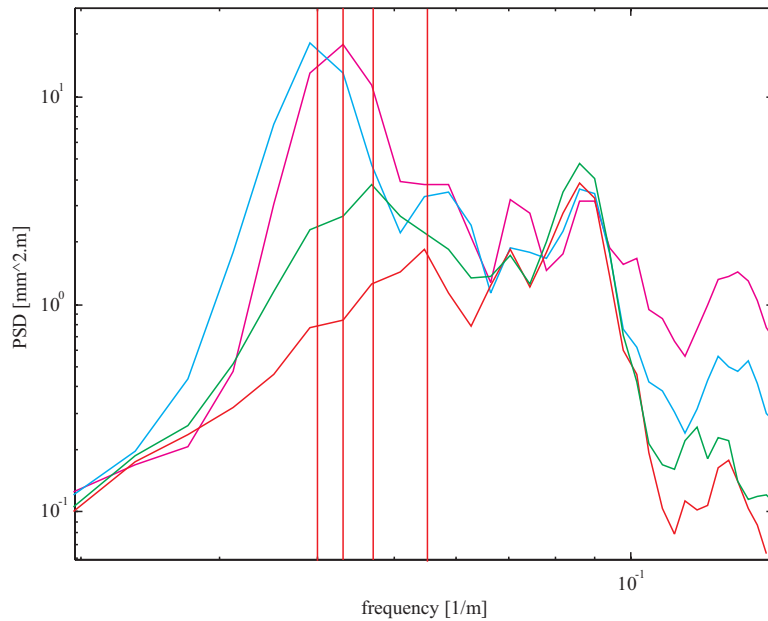


Abbildung 2.9: Spectra for error signals of right level. Test run Villach-Klagenfurt, km 163 to km 127.

### Shift

There is only one test run (009-ad10) which shows a shift of one sample. However, this test run is well correlated with the others within the sampling accuracy. Since the maximum of the cross-correlation function is somewhere between 0 and 1, the correction which more often produces zero shift was chosen. This is the best solution as well as from a statistical as from a practical point of view although in some signals there will show up a shift of 1 sampling instance.

## 2.8 Alignment

### Mean and Variance

The statistical values of alignment for km 50.4995 to km 52.3995 show similar properties as the values for level. In spite of very coherent values for the mean the variances are quite differing (table 2.7). There is no obvious correlation between the values for variances and the speed or the loads, respectively. When compared to table 2.5 there is also a lack of similarity. It looks as if the variances are in general increasing with speed (see also section 2.9), but there still have to be some other influential factors.

Error signals of curved track show a standard deviation of 0.58mm for the left rail and 0.64mm for the right rail respectively. Maximum difference on this section is +7.12mm, the minimum difference is -8.08mm. There obviously is a good coherence between all test runs except for some erratic and large differences. There are about 10 such large deviations in each kilometer of the section km 145.53 to km 143.51. These deviations are no simple outliers since some of them last for more than 7 samples (1.75m) but they come in the form of distinctive spikes. There are several deviations which take place in both error signals at the same sampling instances, indicating that a deterministic reason is existing. However, other deviations occur apparently accidentally in only one of the error signals. Large differences are not correlated to large deviations in the alignment signals but they rather seem to happen by chance.



Test Run	Speed	Mean Left	Mean Right	Variance Left	Variance Right
0006-ad7	59.99	0.479	0.479	1.57	1.60
0007-ad8	80.64	0.481	0.480	1.58	1.56
0008-ad9	88.97	0.479	0.480	1.81	1.57
0009-ad10	100.78	0.480	0.480	1.97	1.60
0010-ad11	110.88	0.480	0.480	1.84	1.85

Tabelle 2.7: *Test runs on track 1. Statistics for alignment.*

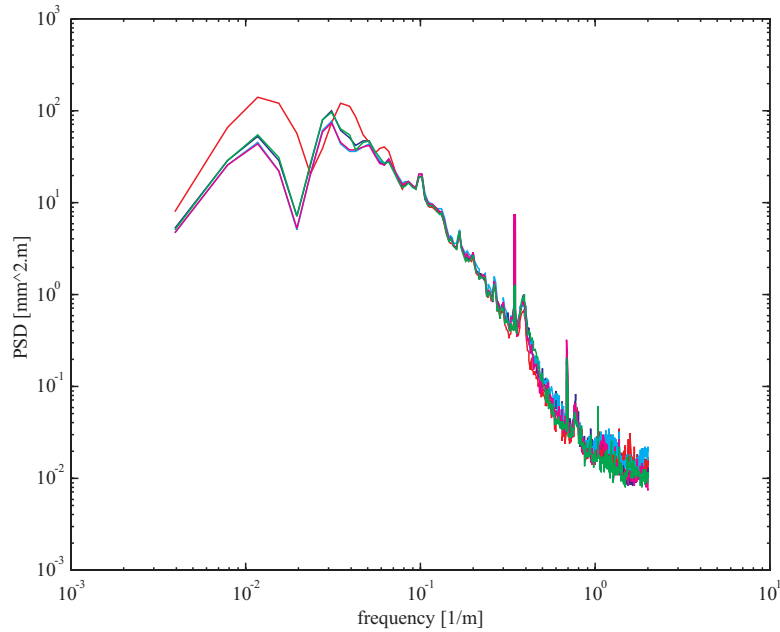


Abbildung 2.10: *Spectra for left alignment (track 2). Test run Drösing-Angern, km 58.4 to 39.9.*

## Spectra

The spectra shown in figure 2.10 are computed for the left rail since there is no significant difference to the spectra for the right rail. Most important is the fact that in spite of a noisy high frequency part distinct peaks at 0.35 1/m (0.3459 1/m) and 0.7 1/m can already be seen. The error spectra of figure 2.11 also show the peaks at 0.35 1/m, 0.69 1/m, 1.04 1/m, and 1.38 1/m respectively. These values are exactly the same as for the dominant oscillations found in the speed signals. Since the speed measurement is not likely to become affected by errors in the alignment it can in turn be concluded that the alignment measurements are corrupted by some sort of a wheel or bearing defect.

A possible cause for an oscillatory change in velocity could be a periodic misalignment at a distinct frequency. Assuming that the wheelset runs in a straight motion (or that the wavelength of the sine-run is much bigger than the wavelength of the disturbance) the effective radius of the wheels will change due to the conicity of the tires. The peak at 0.35 1/m in figure 2.10 would belong to a harmonic oscillation with an average amplitude of 0.198 mm (standard deviation of the band-filtered signal). Even under the assumption of a tire conicity of 1:5 at a nominal wheel radius of 0.45m, an amplitude in speed oscillation of only 0.0035 m/s will result at a speed of 38.89 m/s. However, the actual oscillation of this speed signal shows an amplitude of 0.244 m/s which is two orders of magnitude bigger.

A look at the coherence function between left and right alignment signals (figure 2.12) confirms

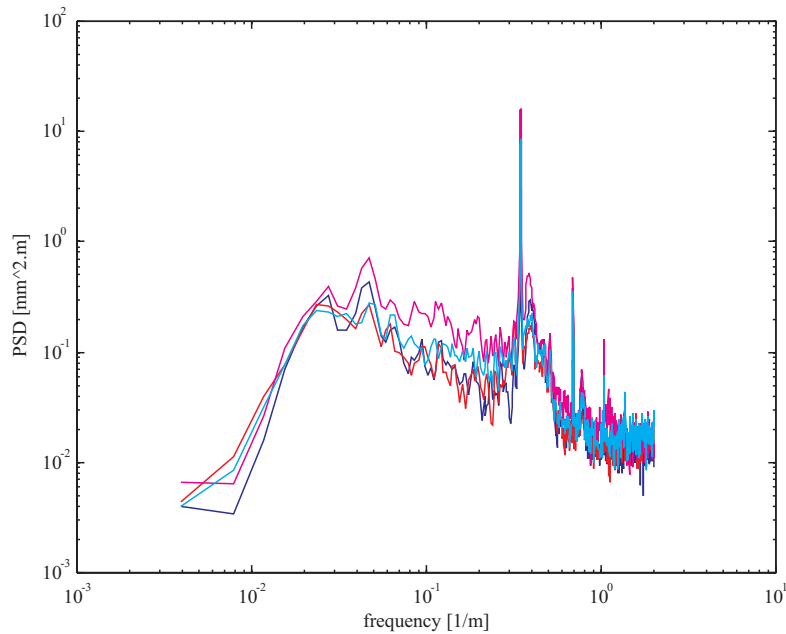


Abbildung 2.11: *Error spectra for left alignment (track 2). Test run Drösing-Angern, km 58.4 to 39.9.*

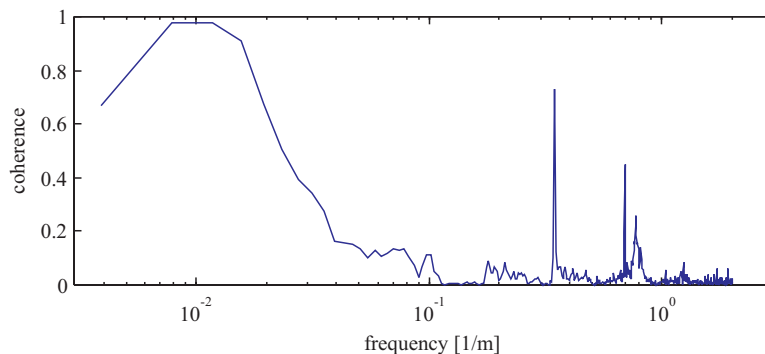


Abbildung 2.12: *Coherence function between left and right alignment signals. Test run Villach-Klagenfurt, km 163 to km 127.*

that a systematic error in alignment signals at wheel frequency is very likely. The coherence is very strong for wavelengths above 60m, because this frequency band already describes the curves of the nominal track. For shorter wavelengths a much weaker coherence is predominant. However, there are two very distinct peaks at 2.90m and 1.45m respectively. The accelerations due to the wheel fault affecting both sides are falsely interpreted as track characteristics and therefore lead to these strong peaks. A third peak at 1.30m seems to be associated with a real structural property of the track.

An additional problem arises from the procedure of separating the curvature and alignment signals by using a 30m moving average of the original spatial curve. This low-pass signal is consequently subtracted from the spatial curve yielding the mean alignment. Unfortunately, this type of filtering produces distinct ripples in the pass-band which can also be found in the spectra of the mean alignment signal. In figure 2.13 the PSD of the mean alignment  $((a_l(x) + a_r(x))/2)$  for test run ad7\_506 (blue) is plotted versus the magnitude of the transfer function of the moving average

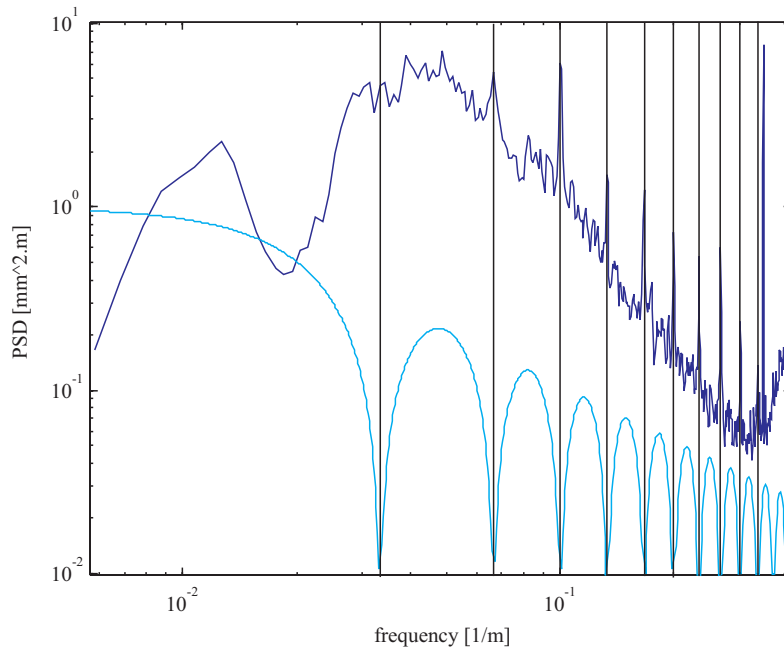


Abbildung 2.13: *PSD of mean alignment signal (blue) versus magnitude of transfer function of moving average (cyan): computed over 30m corresponding to 120 samples. Test run Angern-Drösing, km 39.9 to km 58.4, decimated to 1m sampling interval.*

over 30m or 120 samples. The zeros of the transfer function at whole numbered fractions of 30m coincide exactly with the distinct peaks in the spectrum of the mean alignment. The large peak at the high-frequency end of the spectrum is caused by the wheel fault and therefore comes to lie at 2.90m wavelength.

### Shift

Since the alignment signals served as reference for the correlation of the test runs, no shift could be detected between the signals of either side for all speeds by definition.

## 2.9 Curvature

### Mean and Variance

Error signals of curved track show a standard deviation of 0.81mm for error signal vk01-vk02 and 0.93mm for vk01-vk04 respectively. Maximum difference on this section is +4.48mm, the minimum difference is -2.85mm. The large maximum only occurs once at the beginning of a transition arc. Obviously, there is a good coherence between all test runs since the above values have to be seen in relation to the large absolute values of curvature ( $\pm 40\text{mm}$  in this section). Besides some quantization noise there is a small error correlated to the curvature signal. Signals from faster test runs show approximately 1% bigger amplitudes than the reference run. This can be regarded as a good accuracy.

To get meaningful values for a comparison of variances a straight portion of track 1 was chosen (km 50.4995 to km 52.3995). All values in the following section were calculated by using the data of only this section. Since there are no deterministic deviations from a zero mean-value, this portion

Test Run	Speed	Longitudinal Load	Variance	Mean
0006-ad7	59.96 km/h	0 kN	0.69	0.118
0007-ad8	80.61 km/h	100 kN	0.89	0.099
0008-ad9	89.02 km/h	130 kN	0.93	0.042
0009-ad10	100.73 km/h	50 kN	0.86	0.102
0010-ad11	110.83 km/h	75 kN	0.91	0.088

Table 2.8: *Test runs on track 1. Statistics for curvature.*

should be appropriate for variance measures. The calculation of the covariance-matrix  $\mathbf{C}$  yields

$$\mathbf{C} = \begin{bmatrix} 0.69 & 0.53 & 0.49 & 0.49 & 0.49 \\ 0.53 & 0.89 & 0.81 & 0.72 & 0.70 \\ 0.49 & 0.81 & 0.93 & 0.75 & 0.72 \\ 0.49 & 0.72 & 0.75 & 0.86 & 0.80 \\ 0.49 & 0.70 & 0.72 & 0.80 & 0.91 \end{bmatrix}. \quad (2.13)$$

The covariance-matrix 2.13 is symmetric by definition and shows an increase in the diagonal values which are just the variances of the respective measurements. It is of crucial importance that the longitudinal load applied to the test train by the pushing engine is taken into account when interpreting this data. Table 2.8 clearly shows the two main influences on the data: There is an increase in variance proportional to speed, and there also is an increase proportional to the load in longitudinal direction.

Since the first measurement was taken with pulling engine at the front of the train, there is the possibility to calculate an approximate variance without the influence of longitudinal load. If we assume by some physical insight that the relation

$$\sigma = \sigma_0 + \vartheta_1 v^2 + \vartheta_2 f \quad (2.14)$$

holds, where  $\sigma_0$  and the  $\vartheta_i$  are the unknown parameters, and  $v$  and  $f$  are the speed and the load, respectively. Equation. 2.14 can be transformed into matrix notation, covering all test runs:

$$\mathbf{\Sigma} = \mathbf{X}\mathbf{\Theta} \quad (2.15)$$

In this notation  $\mathbf{\Theta} = [\sigma_0 \ \vartheta_1 \ \vartheta_2]^T$  is the vector of unknown parameters (linear factors in equation 2.15),  $\mathbf{\Sigma} = [\sigma_7 \ \sigma_8 \ \sigma_9 \ \sigma_{10} \ \sigma_{11}]^T$  is the vector of variances, equaling the diagonal of the covariance matrix  $C$ , and the data matrix  $\mathbf{X} = \begin{bmatrix} 1 & 1 & 1 & 1 & 1 \\ v_7^2 & v_8^2 & v_9^2 & v_{10}^2 & v_{11}^2 \\ f_7 & f_8 & f_9 & f_{10} & f_{11} \end{bmatrix}^T$ . Then, a least squares fit is possible to determine the unknown parameters:

$$\mathbf{\Theta} = (\mathbf{X}^T \mathbf{X})^{-1} \mathbf{X}^T \mathbf{\Sigma} \quad (2.16)$$

The parameter vector  $\mathbf{\Theta}$  therefore is computed as  $\mathbf{\Theta} = [6.49 \cdot 10^{-1} \ 1.28 \cdot 10^{-5} \ 1.45 \cdot 10^{-3}]^T$  leading to estimated values for  $\hat{\mathbf{\Sigma}} = [0.70 \ 0.88 \ 0.94 \ 0.85 \ 0.92]^T$ . The error between estimated and measured values stays well under 1.5%. If we now estimate the variance without the presence of loads, the estimate yields

$$\tilde{\mathbf{\Sigma}} = [0.70 \ 0.73 \ 0.75 \ 0.78 \ 0.81]^T.$$

This clearly shows that an increase in variance of more than 10% can be expected, if the speed is increased from 60 to 110 km/h. Interestingly, the estimate of variance for zero measuring speed

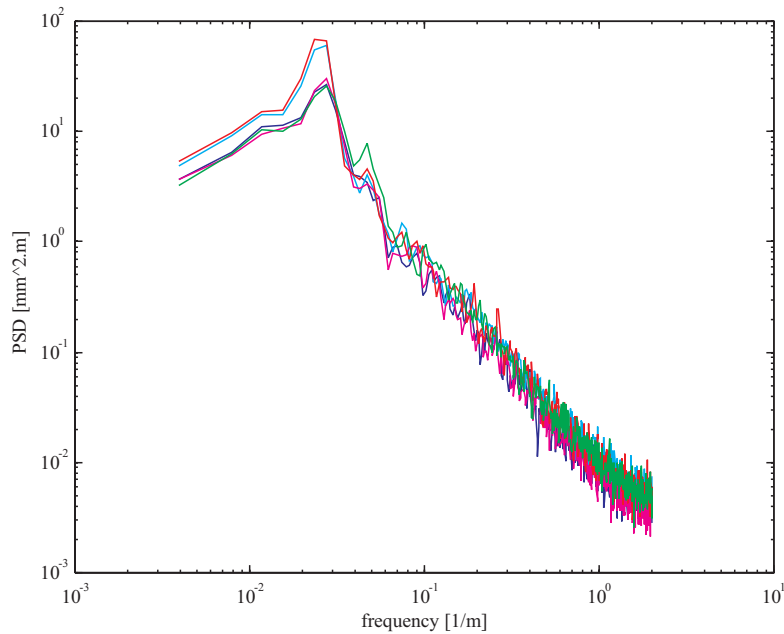


Abbildung 2.14: *Spectra of curvature (track 2). Test run Drösing-Angern, km 58.4 to km 39.9.*

yields a value of  $\sigma_0 = 0.65$ . If this value is regarded as the actual variance of curvature then the error in variance at 110 km/h is approximately 25%. This procedure could provide a means of getting more accurate results for variance with the cost of repeated test runs. However, it should be emphasized that the value for  $\sigma_0$  was extrapolated from existing data, therefore not being so reliable as the above data resulting from approximation.

## Spectra

The spectra of figure 2.14 already show that there is a frequency shift in the measurements of curvature between the slower three test runs and the two performed at 140 km/h, therefore leading to the peak in the spectra of the error signals (fig. 2.15). Over the range of short to medium length waves a good agreement is observed, however, above the wavelength of 20m there is a significant difference. There is a massive resonance peak for the test runs at 140 km/h and a less distinct peak for the test runs at 100 km/h and 110 km/h respectively. Additional spectra and analyses with auto-correlation functions reveal that the frequencies corresponding to these peaks are 1.06 Hz and 0.98 Hz respectively (0.0345 1/m at 30.7 m/s and 0.0262 1/m at 37.2 m/s). These deviations are also approximately proportional to the measuring speeds, therefore indicating that at higher speeds this eigenmode of the measurement coach is more strongly excited.

In the wavelengths above 50m a big gap remains between the test runs at different speeds. One possible conclusion would be that at higher speeds longer wavebands with big amplitudes are detected more accurately, while at lower speeds these big wavelengths are only detected with too small amplitudes. The spectra of curved track do not differ that much throughout the whole frequency range. Especially in the low frequencies the differences are negligible.

In the test runs on track 1 at Angern-Drösing a different situation arises. There are differences mainly between the first test run with pulling engine and all other test runs. They differ as well in amplitude as in the frequencies where peaks occur. It could be possible that a longitudinal pressure load alters the dynamical characteristics of the whole unit, therefore leading to a shift in natural frequencies. The fact that only the first test run differs from the group of tests with loads applied

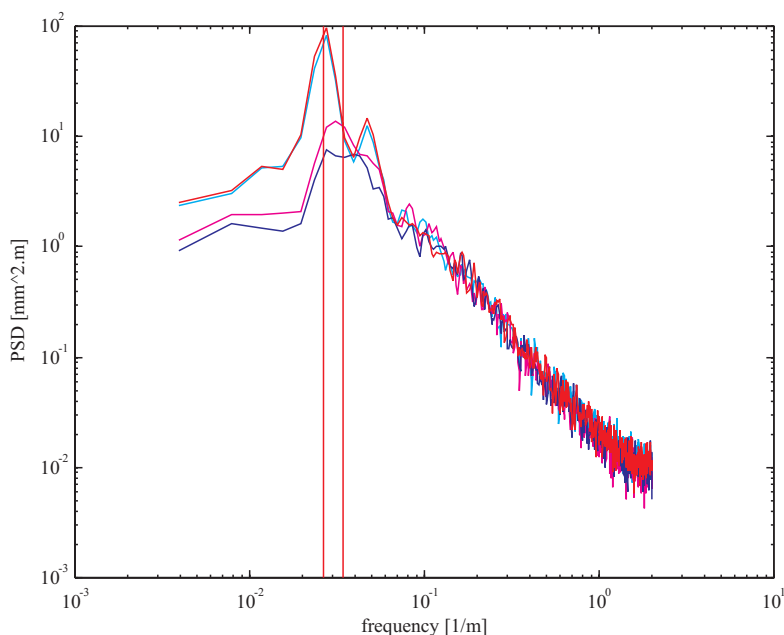


Abbildung 2.15: Spectra of error signals for curvature (track 2). Test run Drösing-Angern, km 58.4 to km 39.9.

is a strong support for this hypothesis.

The problem of properly splitting up the original horizontal spatial curve into two signals also affects the curvature signal. The small slope of the high-frequency asymptote is one disadvantage of using a moving average for low-pass filtering. The comparison of a spectral estimate of the transfer function between curvature and mean alignment to the theoretical transfer function gives the results depicted in figure 2.16. If the transfer function of the moving average is denoted by  $F_{ma}(s)$  the operation of subtracting the moving average from a signal is equal to applying a transfer function of  $F_{hp}(s) = 1 - F_{ma}(s)$ . Since the moving average is calculated off-line (or rather with a time delay to real-time signal acquisition) it can be implemented as a non-causal filter. The resulting functions from this model are plotted black whereas the estimated functions from measurement data are red. In the first plot of figure 2.16 the magnitudes versus spatial frequency of  $F_{hp}(s)$  are shown. Except for a constant bias in gain there is a good agreement between both functions. The second plot shows the phase portrait. Up to the first zero of the transfer function at 30m both estimate and theoretical value line up perfectly. Above this value the estimate becomes very inaccurate since the coherence between the two signals depicted in the third plot (red) becomes very poor. The function plotted in black in the third plot is the magnitude of the transfer function  $F_{ma}(s)$ . It is used here since a coherence function is not defined a priori for the transfer function  $F_{hp}(s)$ . Nevertheless, it clearly shows that the shape of the transfer function is not optimally suited for the task.

## Shift

The shift between signals was calculated by evaluating the shift at which the global maximum of the cross-correlation function of two measurements occurs. When using the whole section for analysis, the shifts with reference to test run 0006-ad7 were found to be as presented in table 2.9, column 'Global'. To find out if this shift is uniform over the whole range, the original signals were broken down into smaller adjacent sections, and the analysis was carried out on each of the sections. From table 2.9 it follows that the shift is not at all uniform, ranging from 0 to -13 samples (corresponding

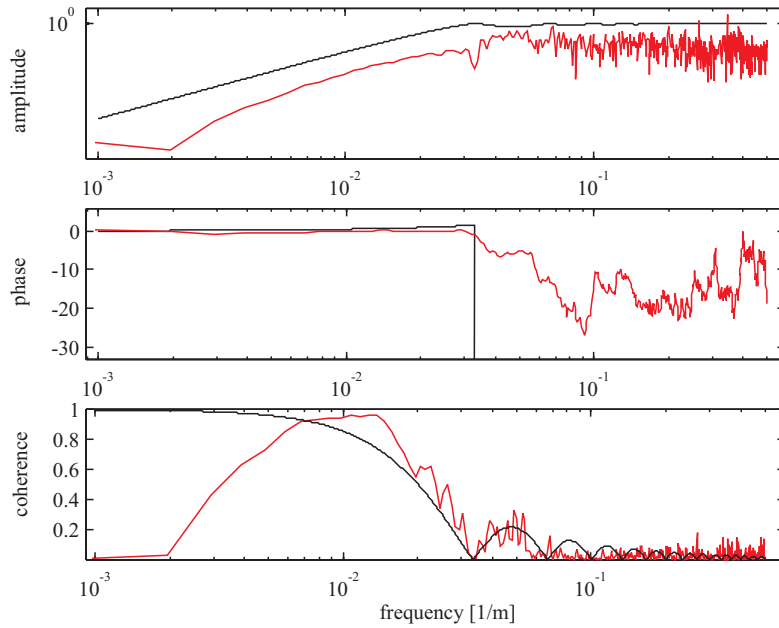


Abbildung 2.16: *Transfer and coherence functions between mean alignment (output) and curvature (input): Estimated functions (red), theoretical functions (black). Test run Angern-Drösing, km 39.9 to km 58.4, decimated to 1m sampling interval.*

Test Run	Global	km 49.99975 to 50.5995	km 50.59975 to 51.1995	km 51.19975 to 51.7995
0007-ad8	-4	0	-5	-9
0008-ad9	-6	0	-7	-12
0009-ad10	-4	0	-10	-10
0010-ad11	-6	0	-13	-11

Tabelle 2.9: *Shift between curvature signals. Reference signal: 0006-ad7*

to -3m) in the case of signal 0010-ad11.

In spite of these alarmingly high values no obvious shift can be seen in plots of the data. Moreover, in the section with four curves (km 49.99975 to 50.5995), where big deviations from zero-mean occur, no shift is indicated by cross-correlations. Since data for curvature are coarsely quantized, an accurate tracking of small deviations is not possible. It seems to be admissible to neglect shifts in curvature signals as long as they occur in sections with small absolute values.

Test Run	Speed	Longitudinal Load	Variance	Mean
0006-ad7	59.98 km/h	0 kN	3.62	-0.333
0007-ad8	80.63 km/h	100 kN	3.55	-0.327
0008-ad9	89.00 km/h	130 kN	3.69	-0.266
0009-ad10	100.75 km/h	50 kN	3.50	-0.321
0010-ad11	110.85 km/h	75 kN	3.63	-0.400

Tabelle 2.10: *Test runs on track 1. Statistics for gauge.*

## 2.10 Gauge

### Mean and Variance

To compute these values the portion of track 1 from km 49,9000 to km 52.39975 was chosen, including straight as well as curved track. The covariance-matrix  $\mathbf{C}$  is

$$\mathbf{C} = \begin{bmatrix} 3.62 & 3.39 & 2.35 & 3.19 & 2.95 \\ 3.39 & 3.55 & 2.38 & 3.22 & 2.85 \\ 2.35 & 2.38 & 3.69 & 2.32 & 2.46 \\ 3.19 & 3.22 & 2.32 & 3.50 & 2.81 \\ 2.95 & 2.85 & 2.46 & 2.81 & 3.63 \end{bmatrix}, \quad (2.17)$$

which does not show an increase of variance values with speed. Table 2.10 also shows that there is not the same correlation to speed as it was found in the other signals. The nominal zero mean value results from the fact that the deviation from the nominal value (1435 mm) is recorded rather than the gauge itself. Table 2.10 shows that the actual mean value of gauge measurements is just as constant as the values for variance. However, it does not equal zero but shows a value of approximately -0.3mm. This is a plausible value since small systematic errors may have been made during the last maintenance or reconstruction.

### Spectra

The spectra of the signals (fig. 2.17) do not seem to reveal anything unusual about the measurements. They show some minor deviations over the whole frequency range but in general are in good agreement with each other. However, due to the strange and erratically ordered error spectra in figure 2.18 some kind of fault has to be expected. From the recordings in the spatial domain it becomes clear that there is good agreement in portions with small deviations (besides a shift) but at larger deviations the different measurements become very erratic and only roughly follow the same course (fig. 2.19). Deviations in these sections exceed 15 mm. In each measurement there are repeatedly flat sections like saturation effects, but these phenomena occur at virtually every possible signal value. Therefore, it could also be possible that the sensor readings get frozen for different durations, producing constant values for these durations. However, there are some parts of the measurements where such constant values appear in different test runs with the same duration (km 51.3270 to km 51.3345).

A possible explanation could be the presence of lipped rail heads at these sections. The laser beam which measures a half gauge hits the rail head at a steep angle of  $18^\circ$  from the vertical. If the rail head is strongly flattened or even lipped, the camera will not be able to find the beam reflected from the rail surface. The same is true for rail surfaces with poor reflection characteristics (corrosion, dirt). Once the camera has lost the laser beam for a certain number of samples, the system delivers a constant reading and tries to find the correct reference point at the rail head again. Only after it has gathered a number of meaningful values it delivers a new output. This explains why a minimum number of constant readings can be found in the measurement data. In



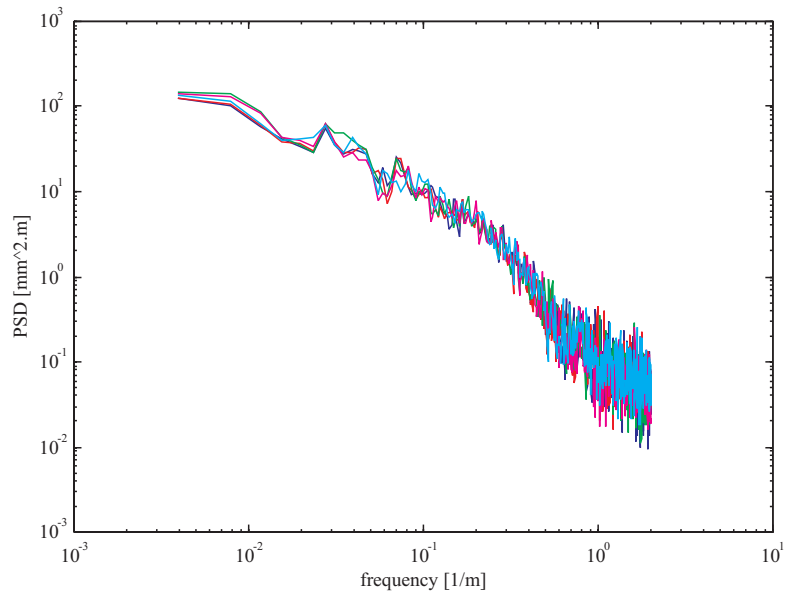


Abbildung 2.17: *Spectra of gauge measurements (track 1). Test run Angern-Drösing, km 39.9 to km 58.4.*

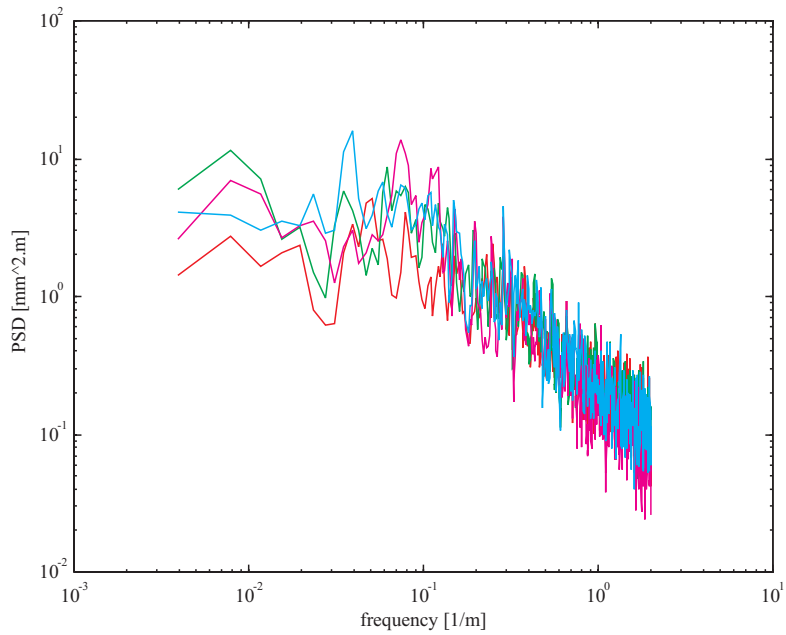


Abbildung 2.18: *Spectra of error signals for gauge (track 1). Test run Angern-Drösing, km 39.9 to km 58.4.*

the case of switches and crossings the same will happen, although the gauge measurements at these sections are of minor importance.

In the gauge signals of track 2 there is a much better coherence between the test runs and no obvious misreadings of the gauge are present. Therefore, the spectra of the error signals are one order of magnitude smaller and also exhibit a different shape. As can be seen from figure 2.20 they represent nearly white noise with an additional peak at a frequency of 0.35 1/m. This frequency is

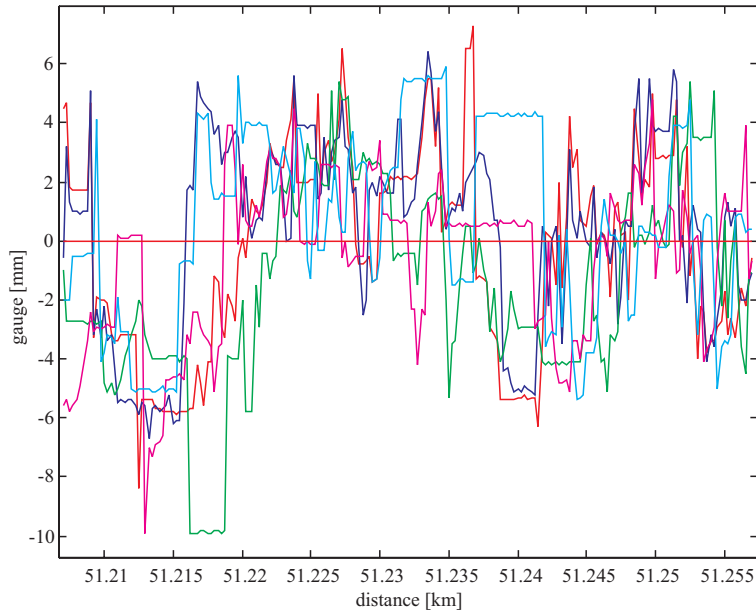


Abbildung 2.19: Gauge signals at a track section with large deviations (track 1). Test run Angern-Drösing, km 51.20 to km 51.26.

Test Run	Shift
0007-ad8	0
0008-ad9	-11
0009-ad10	0
0010-ad11	-4

Tabelle 2.11: Shift between gauge signals. Reference signal: 0006-ad7

the same as it was found in the signals of speed, alignment, and level. There is also a less distinct peak at a wavelength of 2.64m as it was seen in the spectra of alignment. Although hidden in the high-frequency noise, there also are the peaks at 0.69 1/m and with 1.3m wavelength respectively.

### Shift

As already mentioned above, there is a very constant shift between some of the signals. The shift shown in table 2.11 is the same throughout the test runs, as well globally as locally. Obviously there is a group of test runs without any shift, although the speed of these test runs is quite different. On the other hand there are two test runs with considerable shift, not showing any correlation to other data. This overall shift is due to communication problems between the gauge measuring system and the main recording unit. This is a pure software problem and was removed in later releases. In curved track the shift in three test runs was found to be -2 samples. This is certainly a small value and can be removed easily.

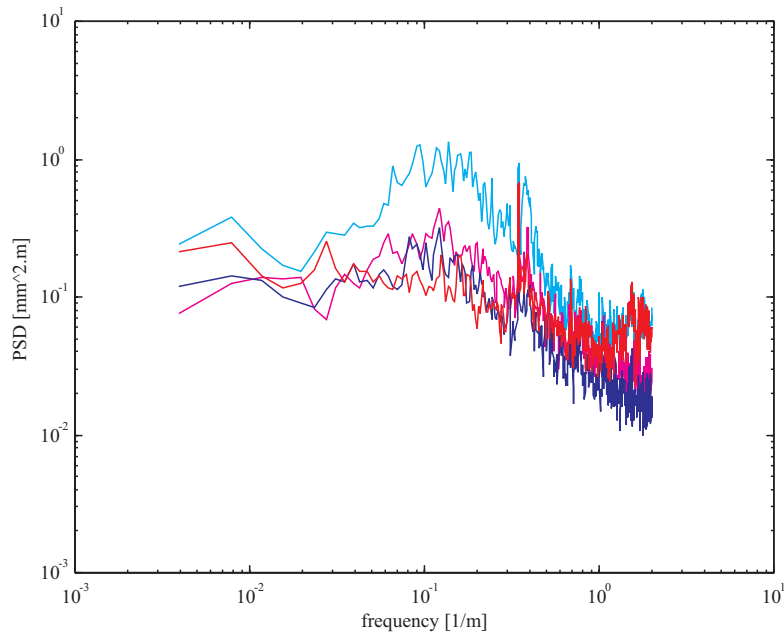


Abbildung 2.20: Spectra for error signals of gauge (track 2). Test run Drösing-Angern, km 58.4 to km 39.9.

## 2.11 Cant

### Mean and Variance

To get meaningful values for a comparison of variances a straight portion of track 1 was chosen (km 50.4995 to km 52.3995). All values in the following section were calculated by using the data of only this section. Since there are no deterministic deviations from a zero mean-value, this portion should be appropriate for variance measures. The calculation of the covariance-matrix  $\mathbf{C}$  yields

$$\mathbf{C} = \begin{bmatrix} 7.00 & 6.99 & 6.94 & 6.89 & 7.00 \\ 6.99 & 7.37 & 7.30 & 7.27 & 7.38 \\ 6.94 & 7.30 & 7.36 & 7.29 & 7.40 \\ 6.89 & 7.27 & 7.29 & 7.51 & 7.48 \\ 7.00 & 7.38 & 7.40 & 7.48 & 7.71 \end{bmatrix}. \quad (2.18)$$

This covariance-matrix is symmetric by definition and shows an increase in the diagonal values which are just the variances of the respective measurements. It is of crucial importance that the internal load applied to the test train is taken into account when interpreting this data. Table 2.12 clearly shows the two main influences on the data: There is an increase in variance proportional to speed, and there also is an increase proportional to the pressure load in longitudinal direction due the pushing engine at the rear of the train.

Although a straight portion was under investigation the mean value does not equal zero. However, the offset is small and reproduced by all test runs therefore confirming its being a track characteristic. A more disturbing fault can be seen in the data of track 2, km 45.79775 to km 42.6770. There are big deviations in the statistic data and furthermore a most strong deviation between km 43.77 and km 42.95 occurs, as can be seen in figure 2.21. The deviation shows up only for the test runs 507-da8 and 510-da11 which were conducted at the highest speed (134 km/h). It looks as if the cant measurement would drift away from the actual value until it reaches a maximum offset of 4 mm and then diminishes again.

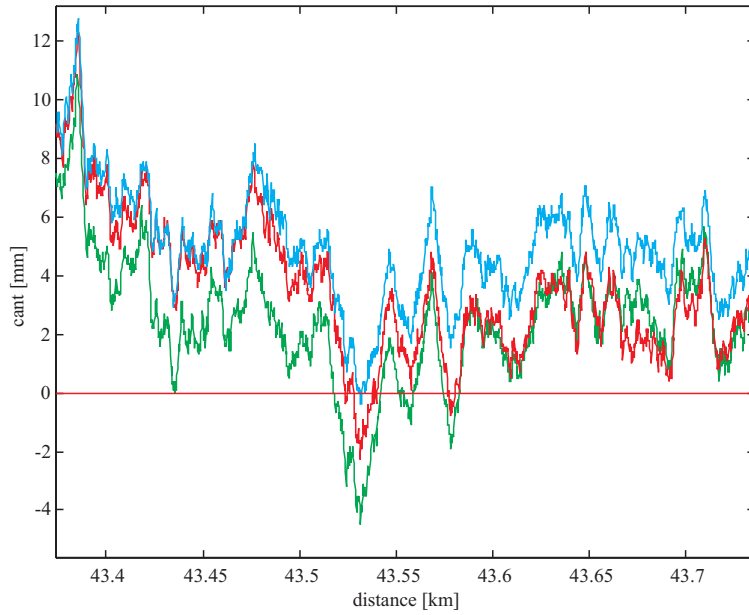


Abbildung 2.21: *Cant signals for track 2. Test run Drösing-Angern, km 43.4 to km 43.7.*

Test Run	Track	Speed	Longitudinal Load	Variance	Mean
0006-ad7	1	59.96 km/h	0 kN	7.00	2.56
0007-ad8	1	80.61 km/h	100 kN	7.37	2.51
0008-ad9	1	89.02 km/h	130 kN	7.36	2.49
0009-ad10	1	100.73 km/h	50 kN	7.51	2.59
0010-ad11	1	110.83 km/h	75 kN	7.71	2.46
0506-da7	2	100.41 km/h	0 kN	2.82	3.12
0507-da8	2	134.04 km/h	0 kN	2.72	3.37
0508-da9	2	80.59 km/h	0 kN	3.14	3.58
0509-da10	2	110.47 km/h	0 kN	2.84	3.32
0510-da11	2	132.97 km/h	0 kN	2.56	4.12

Tabelle 2.12: *Test runs on track 1 and 2. Statistics for cant.*

## Spectra

Spectra were calculated for a straight section of track 2 only (km 45.79775 to km 42.6770). The spectra clearly arrange into groups according to the speed of test runs (fig. 2.22), whereas the test runs conducted at the same speeds (red and cyan, 140 km/h) show the smallest deviations with respect to each other in the mid- to low-frequency range. In the high-frequency part there is a good coherence between the spectra except for two distinct peaks at 0.35 1/m and 1.38 1/m, where the amplitudes are roughly proportional to the measuring speeds. There are also two less well defined peaks at 1.3m and 2.64m wavelength where all spectra show the same amplitudes.

This is confirmed by the error spectra shown in figure 2.23. The two peaks at 0.35 1/m and 1.38 1/m are clearly visible while the other two peaks do not produce any additional error. A possible explanation would be that the distinct peaks mark faults on the wheel circumference since their magnitude depends upon measuring speed. The less pronounced peaks seem to arise from real rail defects since their magnitude is constant for all test runs. This observation is also true for the

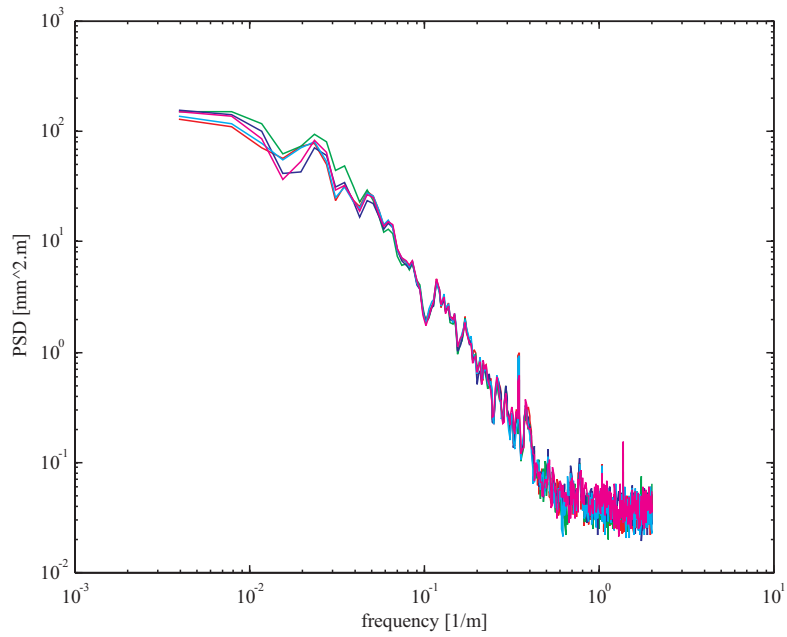


Abbildung 2.22: Spectra for cant (track 2). Test run Drösing-Angern, km 45.8 to 42.7.

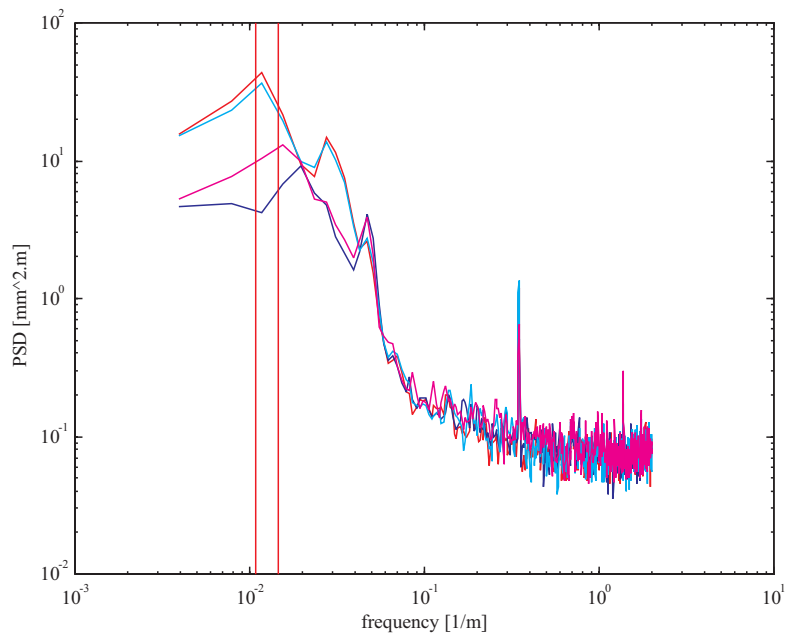


Abbildung 2.23: Spectra of error signals for cant (track 2). Test run Drösing-Angern, km 45.8 to 42.7.

spectra of alignment signals. Therefore, it would be possible that this phenomenon is produced by rolling defects of the rail introduced during the manufacturing process.

It is obvious that an influence from speed exists since the increase in power follows the difference in speed at which the test runs were conducted. The high content in low frequencies in the error signals can also be confirmed by analyzing the auto-correlation functions. The most important

characteristic of these low-frequency errors is a frequency shift in the maxima as already observed in sections 2.7 and 2.9. In the cant signals these frequencies - as confirmed by several FFT's with differing number of points - emerge as 0.0109 1/m for test runs conducted at 140 km/h and 0.0146 1/m for the test run at 110 km/h. The test run at 100 km/h did not produce a significant peak in the region in question. Transforming these frequencies into time domain according to equation 2.6 yields 0.41 Hz and 0.45 Hz respectively. However, the eigenmode of the car body for rolling motion should be in the vicinity of 1.8 Hz. It could still be possible that this low frequency is connected with the dynamics of the whole train, or that the gyro platform exhibits such an eigenmode.

## Shift

No significant shift could be found in the data for cant, neither globally nor in any of the shorter sections under investigation.

## 2.12 Redundancy of Measurements

An important tool for evaluation of track data is the comparison of redundant signals. In order to get the most meaningful signals for comparison only elementary transformations are performed. However, due to the band-pass character of both level and alignment signals an additional high-pass filtering of cant and gauge signals becomes also necessary.

### 2.12.1 Level and Cant

Since the cant of the track is measured as a difference in the individual heights of the left and the right rail head respectively, and only the deviations from the ideal track of these signals are available, the following relation should hold:

$$c(x) = (z_l(x) + l_l(x)) - (z_r(x) + l_r(x)) = c_{low}(x) + (l_l(x) - l_r(x)). \quad (2.19)$$

In expression 2.19  $c(x)$  is the actual cant,  $c_{low}(x)$  is the low frequency component,  $l_l(x)$  is the left level and  $l_r(x)$  is the right level signal respectively. Both signals for the absolute height of rails,  $z_l(x)$  and  $z_r(x)$ , are not available. It should be emphasized that the actual cant is composed of two distinct signal components: The first one being a low frequency signal representing the ideal cant due to curves (deterministic) and long wave stochastic signals, and the second one being a band-filtered stochastic signal due to irregularities in track. This division is meaningful since the level signals contain no low frequency information due to high-pass filtering. It is therefore important to remember that the signal component  $c_{low}(x)$  does not only represent an ideal track. However, if the cant signal is high-pass filtered in an appropriate way, the difference signal

$$\Delta l(x) = l_l(x) - l_r(x) \quad (2.20)$$

and the error signal for level

$$e_l(x) = c_{high}(x) - \Delta l(x) \stackrel{!}{=} 0 \quad (2.21)$$

are defined in a straightforward way. Because of the bandwidth of the level signals mentioned above the relation 2.21 will only make sense for frequencies higher than a certain threshold value.

From equation 2.19 it follows that the low frequency component  $c_{low}(x)$  can be explicitly calculated:

$$c_{low}(x) = c(x) - \Delta l(x) \quad (2.22)$$

This signal component can be split up

$$c_{low}(x) = l_{low}^l(x) - l_{low}^r(x) \quad (2.23)$$

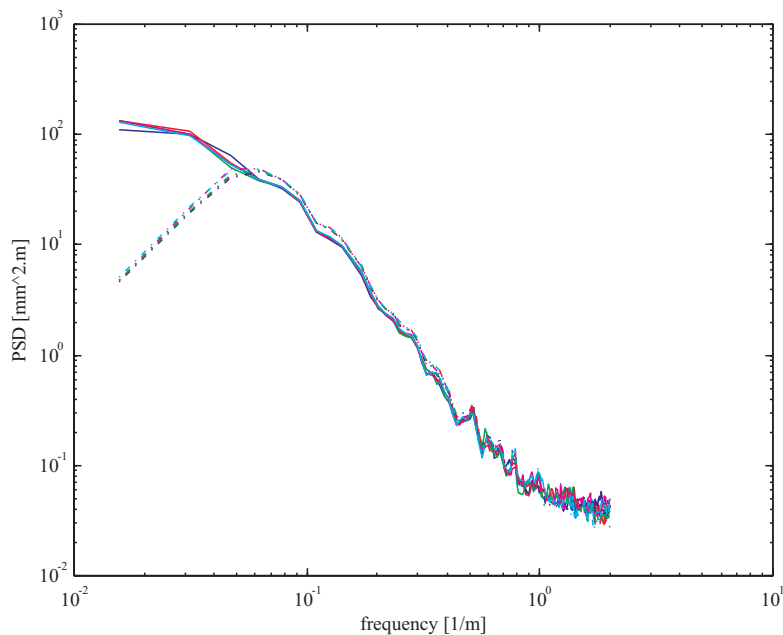


Abbildung 2.24: *Spectra of cant versus difference of level (track 1). Test run Angern- Drösing, km 39.9 to km 58.4.*

and added to the individual level signals in order to reconstruct the whole frequency content of level measurements. However, this reconstruction is not unique. There is no way to tell from cant and level signals alone how the difference in equation 2.23 should be formed. A possible way to decide this would be to look at the vertical accelerations of a vehicle going over the same track. The applicability of this procedure will then depend on the frequency range and reliability of these acceleration measurements.

In figure 2.24 the spectra of the cant signals  $c(x)$  and the spectra of the difference signals  $\Delta l(x)$  are depicted. The decrease for low frequencies in the spectra for difference signals  $\Delta l(x)$  is clearly visible. Above a frequency of approximately 0.05 1/m the spectra of the two groups of signals run parallel although there is a little offset. To evaluate the signals they have to be highpass-filtered and then the error signals according to equation 2.21 can be calculated for each test run.

A correlation analysis reveals a constant shift between the cant and the level signals of four sampling instants. This means that in the time domain the time delay is varying with speed, but in a digital implementation the time for every computation has to be measured in sampling instants. It is therefore possible that the shift of four instants comes from some sort of additional filtering.

After this shift is removed from the signals and the cant is high-pass filtered through a Butterworth-filter of second-order with a cut-off frequency of 0.034 1/m, the error signals for each test run can be calculated according to equation 2.21. The spectra for these error signals are depicted in figure 2.25. It is interesting to notice that in the middle-frequency range the amplitudes of the spectra decrease monotonically with an increase in speed. However, this is true only for low to medium frequencies; the peak at 0.35 1/m increases with speed. This observation proves that in spite of the presence of a distinct peak at 0.35 1/m in both kind of signals there is still a difference in the sensitivity of the two measurements. In a direct comparison the cant signal proves to have the greater amplitude at this peak.

There is also a less distinct peak at a frequency of 0.12 1/m, corresponding to a wavelength of 8.25m. This peak was also present in the spectra of cant signals (fig. 2.22), but it did not pose a prominent raising there.

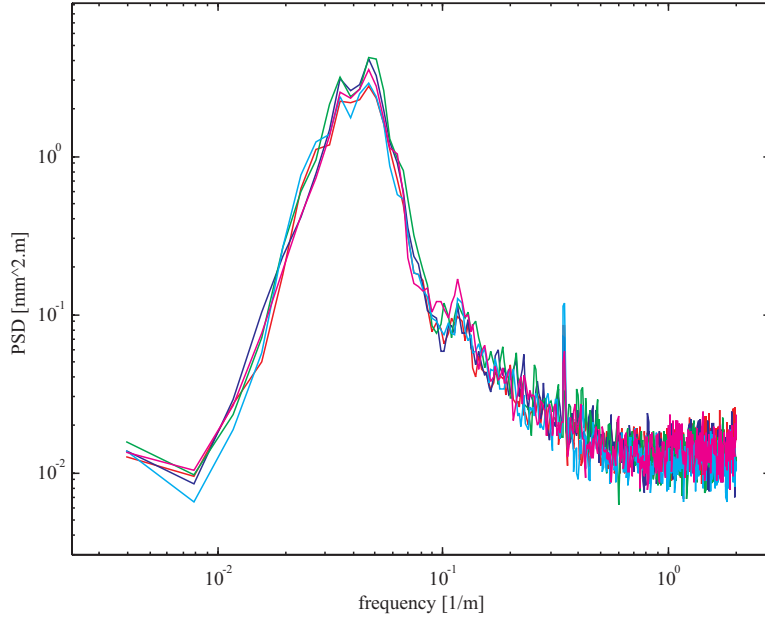


Abbildung 2.25: *Spectra of error signals between cant and difference of level (track 2). Test run Drösing-Angern, km 58.4 to km 39.9.*

The decreasing error signals for increasing speeds at low frequencies seem to be quite understandable. The little offset between the spectra of the two signals in figure 2.24 shows that the measurements of cant are smaller in amplitude than the difference of the level measurements. As the speed increases the longer waves in the track become shorter waves in the time domain. As the system is more consistent at higher frequencies, the error decreases at higher speeds. Since the cut-off frequency of the high-pass filters is relatively close to the strong increase of the spectra at 0.06 1/m a peak is formed at approximately 0.045 1/m. However, this peak might only be formed because of the filters, any kind of low-frequency noise could be present. It is therefore not possible to decide whether resonance effects occur in this range.

Another very useful tool in comparing the relation between signals is the coherence function (see appendix C for details). In figure 2.26 the coherence between cant  $c(x)$  and difference of level signals  $\Delta l(x)$  is plotted in red. The coherence between the mean value of both level signals

$$\bar{l}(x) = \frac{l_l(x) + l_r(x)}{2}, \quad (2.24)$$

often referred to as profile, and cant is plotted in blue. Obviously, the similarities between cant  $c(x)$  and difference of level signals  $\Delta l(x)$  already evident from figure 2.24 are confirmed by the coherence function. Furthermore, the problems introduced by a wheel fault are detected quite clearly. There is a small but distinct notch at the wavelength of 2.90m, which corresponds to a peak in the coherence of cant and profile (blue). The fault at wheel frequency effects both level and cant measurements. Since the general coherence between cant and profile is very weak, this artificially introduced oscillation produces a distinct peak. In contrast, this systematic error attenuates the already very strong coherence between cant and difference of level (red). It pushes the coherence below a value of 0.9 at that specific frequency while otherwise it is well above 0.95 at that range. The strong and distinct peak at 0.726m (which corresponds exactly to  $\frac{1}{4}$  of the wheel circumference) supports this assumption.

Other distinct peaks in the coherence function between cant and profile come to lie at 0.96m ( $\frac{1}{3}$  of wheel circumference), 0.65m, 0.578m ( $\frac{1}{5}$  of wheel circumference), and 0.52m.



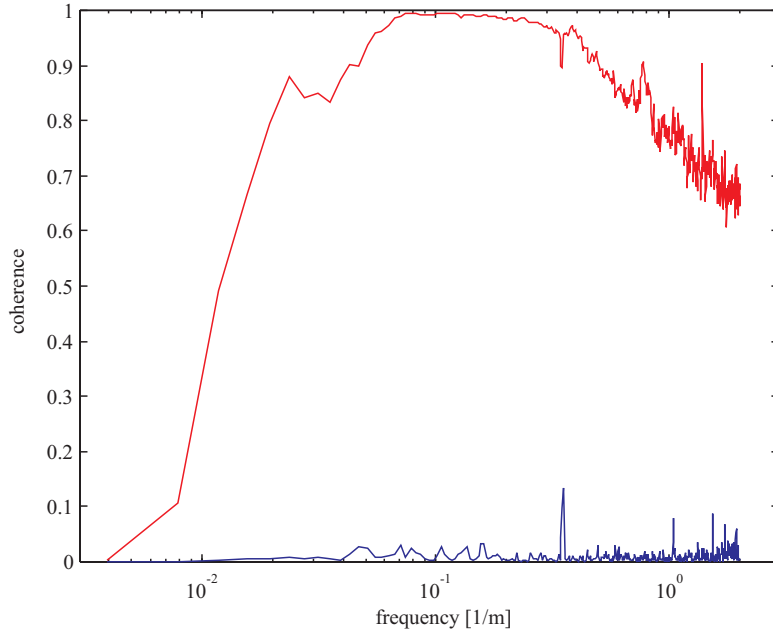


Abbildung 2.26: *Coherence function between cant and mean of level (blue) and between cant and difference in level (red). Test run Villach-Klagenfurt, km 163 to km 127.*

### 2.12.2 Alignment and Gauge

The connection between alignment and gauge signals is even simpler than in the preceding section. Both signals are measured in a relative coordinate system moving tangential along the ideal track. The nominal value for gauge of  $g_0 = 1435\text{mm}$  stays the same throughout the whole track. However, the measurements for alignment are also high-pass filtered for the aforementioned reasons. To take this into account, there has to be a differentiation between low-frequency contents and the remaining signal components. The measured signal for gauge

$$g(x) = y_l(x) - y_r(x) - g_0 = g_{low}(x) + (a_l(x) - a_r(x)) \quad (2.25)$$

therefore consists of a stochastic low frequency component  $g_{low}(x)$  and the difference between the left respectively right alignment signals  $a_l(x)$  and  $a_r(x)$ . The absolute coordinates  $y_l(x)$  and  $y_r(x)$  are of no importance for track description. By defining

$$\Delta a(x) = a_l(x) - a_r(x), \quad (2.26)$$

the difference signal of alignment measurements, the component of gauge above a certain threshold frequency  $g_{high}(x)$  should satisfy the relation

$$e_a(x) = g_{high}(x) - \Delta a(x) \stackrel{!}{=} 0, \quad (2.27)$$

where  $e_a(x)$  denotes the error signal between gauge and difference of alignment signals.

Actually, the spectra of gauge signals are in good agreement with those of the difference of alignment signals over the medium range of frequencies (fig. 2.27). Due to the high-pass filter the alignment spectra drop off at longer wavelengths, and because of a broad spread of gauge spectra at higher frequencies there is also a considerable difference.

As already mentioned in section 2.10 there are peaks at 1.3m and 2.6m wavelength respectively. All spectra regardless of recording speed show these peaks while the peak at 0.35 1/m (0.3459 1/m) is comparatively small and exhibits a strong dependence on measurement speed.

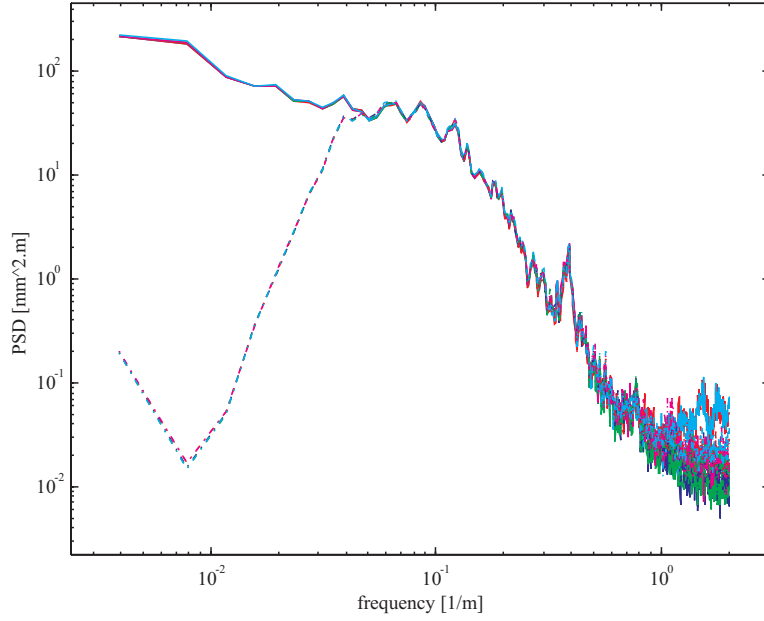


Abbildung 2.27: Spectra of gauge versus difference of alignment (track 2). Test run Drösing-Angern, km 58.4 to km 39.9.

The correlation analysis leads to some very interesting results. There are shifts between the gauge and alignment signals which differ in a wide range. Table 2.13 shows the results obtained by cross-correlation functions. This shift between different signals of the same test run must not be mixed up with the shift of the same signals between different test runs. However, there is a close connection between the two sets of shifts. Since all test runs have been synchronized by the same signal (alignment) a shift of some other signal between different test runs will certainly show up in a direct comparison of this very signal with the reference signal. So table 2.13 shows the absolute shift between signals while the tables in the preceding sections showed a relative shift between test runs. In a mathematical notation the shift between the  $i$ -th signal of test run  $j$ ,  $f_i^j$  and its reference function  $f_{ref}^j$  can be written as:

$$\arg \left[ \max_{\tau} \left( R_{xy} \left\{ f_{ref}^j(x) f_i^j(x - \tau) \right\} \right) \right] = s_i^j \quad (2.28)$$

The same is true for the corresponding signal in another test run  $k$ :

$$\arg \left[ \max_{\tau} \left( R_{xy} \left\{ f_{ref}^k(x) f_i^k(x - \tau) \right\} \right) \right] = s_i^k \quad (2.29)$$

If the two test runs are synchronized by the reference signals, this means that

$$\arg \left[ \max_{\tau} \left( R_{xy} \left\{ f_{ref}^j(x) f_{ref}^k(x - \tau) \right\} \right) \right] = 0. \quad (2.30)$$

Then, in conclusion

$$\arg \left[ \max_{\tau} \left( R_{xy} \left\{ f_i^j(x) f_i^k(x - \tau) \right\} \right) \right] = s_i^j - s_i^k \quad (2.31)$$

will hold. This can also be seen by inserting the value of the shift for test run 0006-ad7 for  $s_i^k$  and replacing  $s_i^j$  by the values for the other shifts in table 2.13. The resulting table will be identical to table 2.11.

Test Run	Speed	Shift
0006-ad7	59.96 km/h	-11
0007-ad8	80.61 km/h	-11
0008-ad9	89.02 km/h	-22
0009-ad10	100.73 km/h	-11
0010-ad11	110.83 km/h	-15

Tabelle 2.13: *Test runs on track 1. Shift between gauge and alignment signals.*

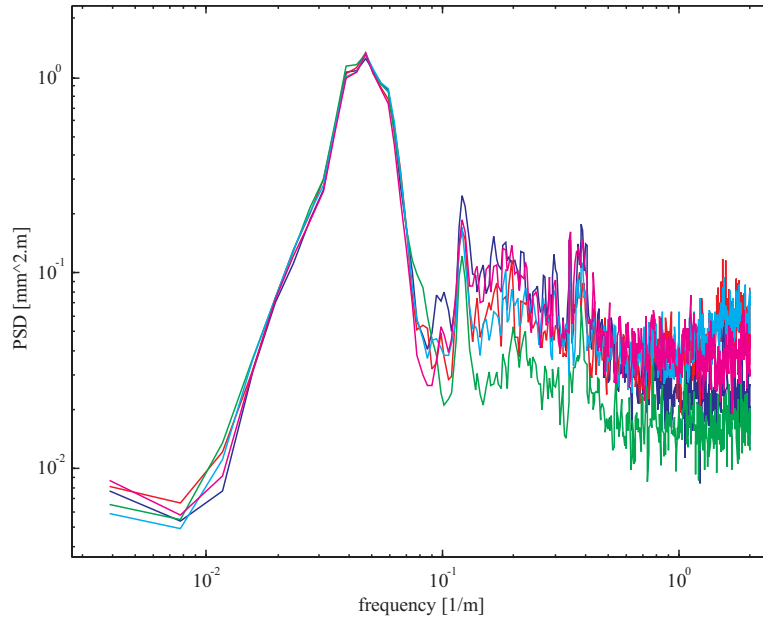


Abbildung 2.28: *Spectra of error signals between difference of alignment and gauge (track 2). Test run Drösing-Angern, km 58.4 to km 39.9.*

After these shifts between the gauge and the alignment signals have been removed, the gauge signals are high-pass filtered with a second-order Butterworth filter (cut-off frequency at 0.032 1/m) and error signals according to equation 2.27 can be computed. The spectra of these signals for straight track are depicted in figure 2.28. Because of the filter the spectra can only be interpreted above a frequency of 0.05. 1/m. There are two most obvious peaks in the spectra of the error signals. One is located at a frequency of 0.12 1/m (corresponding to 8.25m) and the other at a wavelength of 2.6m. The peak at 0.35 1/m (0.347 1/m) is also present although it exists only for the test runs at higher speeds. The peak at 0.12m is most interesting since it did neither show in the spectra of gauge nor in those of alignment. Instead, it could be found in the spectra of cant (fig. 2.22) and hence in the spectra of error signals between cant and the difference of level (fig. 2.25). The conclusion therefore has to be that this peak marks a distinct systematic difference between the two measurement methods. A closer investigation of the spectra in figure 2.27 reveals that at the frequencies in question the gauge signals have the greater amplitude. If the gauge measurement is regarded as the more accurate method, then the alignment measurements are insensitive to a wavelength of 8.25m.

Throughout the whole meaningful part of the spectra there is a great variance in amplitudes, especially at high frequencies. It should be noted that the spectra of error signals for curved track basically share the same characteristics except for generally higher amplitudes and a much broader

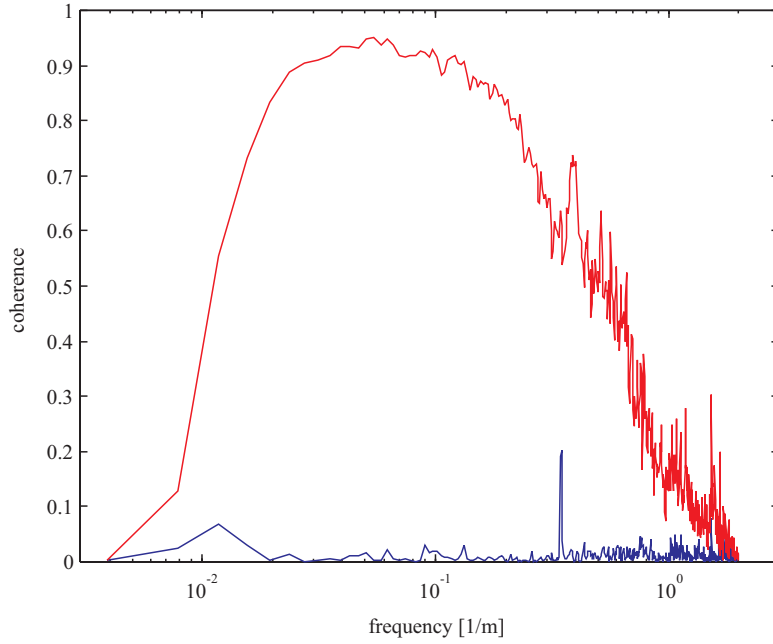


Abbildung 2.29: *Coherence function between gauge and mean alignment (blue) and between gauge and difference of alignment (red). Test run Villach-Klagenfurt, km 163 to km 127.*

maximum.

The coherence function between gauge  $g(x)$  and difference of alignment signals  $\Delta a(x)$  is plotted in blue in figure 2.29. The red plot represents the coherence between gauge and the mean value of alignment signals

$$\bar{a}(x) = \frac{a_l(x) + a_r(x)}{2}, \quad (2.32)$$

which is simply referred to as alignment. Again, this coherence is generally very poor except for a distinct peak at 2.90m, the wheel circumference. There is a broader peak in the coherence between gauge and difference of alignments at approximately 2.56m and a distinct peak at 0.65m. In general, the coherence between gauge  $g(x)$  and difference of alignment signals  $\Delta a(x)$  is not as good as the coherence found between cant  $c(x)$  and difference of level  $\Delta l(x)$ . A reason for this difference could be the completely independent measurement setup for gauge measurement, while all other measurement signals are somehow interconnected by the inertia platform on-board the measurement coach. From figure 2.29 it is apparent that this is especially true for higher frequencies.

The test runs on curved track (Villach-Klagenfurt) produce contradictory results. Gauge and alignment data of each test run are consistent within themselves but differ most strongly at some sections from the other data sets. In figure 2.30 the signals for gauge (highpass-filtered) respectively difference of alignment (left - right) are depicted. The color code can be seen in table 2.14. For each test run these two signals are very well correlated. However, between km 145.37 and km 145.39 there are deviations of more than 6mm between the respective test runs. These deviations occur approximately 10 times in one kilometer as already mentioned in section 2.8.

It is not very likely that the track alignment (gauge) will change that much between consecutive test runs on one day. On the other hand, the measurements of alignment and gauge are independent of each other and give consistent results for each test run. The only indicators for a wrong reading in these sections are the erratic behavior of the signals and the fact that constant readings in the gauge signals sometimes occur. A hint could lie in the fact that these differences take place right

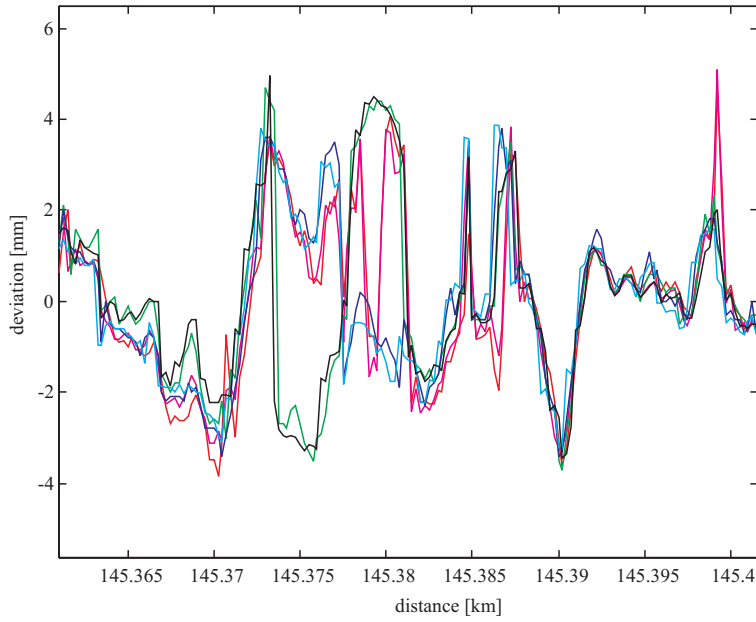


Abbildung 2.30: Gauge and difference of alignment signals for curved track. Villach-Klagenfurt, test runs 1, 2, and 4, km 145.36 to km 145.4.

Test Run	Signal	Color
vk01	Gauge	magenta
	Diff. of Alignments	red
vk02	Gauge	black
	Diff. of Alignments	green
vk04	Gauge	cyan
	Diff. of Alignments	blue

Tabelle 2.14: Color coding for figure 2.30

at the beginning of a transition curve. Still, the real reason for such a systematic error remains unclear.

## 2.13 Evaluation of Track Data

Due to repeated test runs over the same section at different speeds and the redundancy in measurements, several flaws in the track data have been detected. Their influence on the identification of the rail-vehicle interaction is discussed in the following subsections.

### 2.13.1 Distance

A reliable assignment of samples of the output to samples of the input forms the basis of every identification algorithm. Since both input and output data are sampled in the spatial domain, the distance signals are of particular importance. Due to the lack of absolute reference points along the track<sup>1</sup> only a relative position based on the number of samples can be utilized. In section 2.5

<sup>1</sup>The recording of the moment the train passes a certain landmark can not be considered a suitable reference in this context. The speed of the train together with the reaction time of the acting person generally leads to an

it was shown that the divergence over a distance of 18 km is much too big to be tolerated by any identification algorithm. This difference was presumably originating from changing temperatures of the wheels, a circumstance which is nearly impossible to track in existing data sets. In spite of varying sampling lengths between test runs, the sampling lengths for a short time frame can be considered constant on straight track. Data for curved track show much more problems in this respect.

As a remedy only short sections with an allowable amount of possible divergence could be used, or data are corrected by resampling if reliable end points exist. In curved track a much more sophisticated algorithm has to be used since the change in sampling interval length is not purely linear.

### 2.13.2 Speed

As already mentioned in section 2.6 the speed signals exhibit a distinct harmonic oscillation at the frequency of the wheel circumference. This is especially disturbing since the speed signal provides the only possibility to convert the spatial sampling into the time domain. Additionally, the variance of the speed signal exhibits a strong correlation with curvature signals, indicating that one wheel of the measuring axle has a more pronounced fault than its counterpart. To identify a dynamic system with marked natural frequencies, data sets in the time domain are most suitable. If a faulty speed is used to form the time axis, data will most certainly become distorted.

### 2.13.3 Level

There are two main faults in the level signals: First of all, and most adversely for identification, the natural frequency of the car body for vertical motion seems to be hidden in the data (see section 2.7). If track signals are used as input signals which falsely show disturbances in the critical wavelength for resonance of the car body, the identification algorithm will identify a much too damped vehicle characteristic leading to a wrong model.

On the other hand, a harmonic disturbance with the frequency of the wheel circumference is recorded, with its amplitude growing with increasing measurement speed. This is probably caused by a defect on a wheelset, which produces dynamics falsely recorded as track properties. Here the above mentioned problem also arises: If some distinct disturbance is present in the input and not matched by the output, an identification will produce a model which does scarcely respond to such inputs.

An implicit problem of level signals is the high-pass filtering. The cut-off frequency is in the 30-40m range, which is of greatest importance for medium to high speed trains because of the excitation of the eigenmodes of the car body. A cut-off frequency in input signals always poses a rigid limit to the range of output predictions. In a strongly nonlinear system, due to the phenomenon of dispersion, this could render the whole identification useless.

### 2.13.4 Alignment

For alignment signals the problems of high-pass filtering and oscillations with wheel frequencies arise as in the previous section. No eigenmodes of the measuring coach could be found in the data, instead the amplitudes of alignment signals differ most strongly at the wheel frequencies. If the amplitudes of band-pass filtered alignment signals are compared, differences of more than  $\pm 0.6$  mm are found between test runs on the same section. This value is at least one order of magnitude bigger than the admissible inaccuracy stated in [14]. However, it must be pointed out that the spectral content of the current signals is on the upper limit of the range stated there.

---

uncertainty of at least several sampling intervals.

The use of a moving average filter produces peaks at wavelengths where the zeros of the filter transfer function come to lie (whole numbered fractions of the moving window length). This distortion will most likely affect an identification since it artificially alters the alignment signals at those frequencies.

### 2.13.5 Curvature

In section 2.9 it could be shown that the variance of curvature signals is not only subjected to the influence of measuring speed but also to the effect of longitudinal loads. Furthermore, the results of this section indicate that the measured variance at 110 km/h is 25% above the real value. If this increase in variance is not a systematic error, an identification would still be feasible although the convergence speed could severely suffer.

Unfortunately, there is a similar problem with eigenmodes of the measurement coach as for level signals. Although the curvature signals exhibit no high-pass characteristic they show poor agreement in the low-frequency range. Above a wavelength of 33m amplitudes differ up to  $\pm 3.5$  mm. This is due to sections with constant differences which last up to 25 samples.

These deviations seem big but compared to maximum amplitudes of  $\pm 90$  mm for tight curves they should be qualified as admissible. The curvature signal should therefore be regarded rather as indicator of the actual track curvature than as an absolutely accurate measurement.

### 2.13.6 Gauge

The gauge signals show differing shifts with respect to the alignment signals, varying between 11 and 22 samples. These shifts can be easily detected and removed from the data sets.

A considerably more adverse defect was found in the gauge signals for track 1, Angern-Drösing. The erratic differences between signals at sections with great deviations exceed values of 15 mm. No comparable effect was found in the signals for track 2, but without additional measurements the reliability of gauge signals at great deviations has to be doubted.

Other than that, gauge signals also exhibit distinct peaks at wheel frequencies, although they are smaller in amplitude than for alignment. Additional deviations between gauge and difference of alignment signals (section 2.12.2) raise the question which of the two measurements is more accurate. In order to reduce the number of input signals it would be of great importance to remove redundant signals. The rejected signal should not contain any additional information, which means that the least accurate signal should be omitted (e.g. by a weighted least squares method).

### 2.13.7 Cant

Cant signals are the third group of measurements which exhibit oscillations with fixed frequency in the time domain. However, in the case of cant the frequency does not match the eigenmode of a car body as it happened to be for level and curvature. Without knowing the real cause for this phenomenon, the effect on an identification algorithm is still the same.

The temporary offset which arose for some test runs (section 2.11) leads to the problem of reliability of data in dependence on measurement speed. From the available data it has to be concluded that measuring speeds exceeding 110 km/h might lead to biased data.

Distinct peaks at the wheel frequency are also present in the spectra for cant.

# Kapitel 3

## Vehicle Response

In this chapter an investigation of vehicle data will be presented. It is structured just like the previous chapter for track data: First, a short overview of the notions and terms is given. Then the measuring methods and devices are described. The remainder consists of the results for each channel, organized into parts for mean and variance, spectra, and shift respectively.

The chapter is concluded by an evaluation of vehicle response data considering the demands of identification algorithms.

### 3.1 Measuring Method

Data were collected using a standard PC platform with the software Lab View 4.0 from National Instruments. Most signals were available in analog form, being prefiltered and corrected for offsets prior to sampling and recording. Whenever additional offsets occurred they were compensated for off-line in the binary data. Therefore, data provided in ASCII-files cannot be regarded as raw data, they rather are approximate representations of the physical quantities under investigation. This is even more true since the analog filtering of the signals cuts off considerable information, although the filters are implemented to the relevant regulations [36].

Distance and consequently speed were measured by an optical pulse counter mounted to one axle of the measuring coach. A frequency-voltage converter transforms the pulse train into an analog voltage being proportional to the speed of the train. The OEBB measurement group specifies the accuracy of the speed signal to be better than  $\pm 2\%$  and that of the distance measurements to be better than  $0.2\%$ . Nominal sampling interval is  $0.1m$ .

The railway car whose dynamics were to be investigated was equipped with measuring wheelsets on axles 1 and 2 (leading bogie for directions Angern-Drösing and Klagenfurt-Villach respectively).

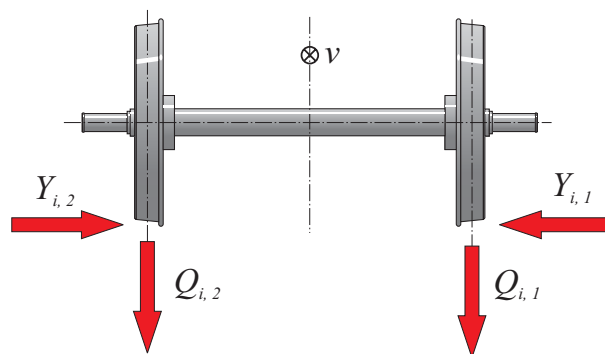


Abbildung 3.1: Rail forces for a single wheelset  $i$ , direction of travel into the paper plane.



These wheelsets provided signals of the vertical forces  $Q_{i,j}$  and lateral forces  $Y_{i,j}$  acting upon the rails and caused by the respective wheels. Figure 3.1 shows the positive directions of the individual forces. The first subscript  $i$  denotes the wheelset (1 or 2, beginning at the front of the car) and the second subscript  $j$  denotes the side (1 corresponding to the right side looking in direction of travel, 2 to the left side). Forces are measured by means of 24 strain gauges applied to each wheel disc. While this setup ensures a high bandwidth due to low unsprung mass, the main shortcomings are thermic drifts affecting the measurement of lateral forces and the immanent averaging of vertical forces over each half revolution. The actual output signal of the strain gauge array is of trapezoidal shape with one wheel revolution as cycle. A dedicated computer calculates the mean value of this signal for each half revolution. All signals of wheel forces were filtered with 6th-order low-pass Butterworth filters, at a cut-off frequency of 20Hz (-3dB). Drifts in the lateral forces  $Y_{i,j}$  were compensated on-line while running on straight track: If the mean value over a certain distance on straight track differs significantly from zero, the actual mean value is calculated for this distance and finally subtracted from the incoming signal. These on-line calibrations reset the mean value to zero in a stepwise manner, therefore partitioning the lateral force signals into sections with the mean value drifting from zero to some negative end-value.

Accelerations in vertical  $\ddot{z}$  and lateral directions  $\ddot{y}$  were measured on the car floor right above the center of the measuring bogie (subscript  $I$ ) and in the middle of the car (subscript  $M$ ). Additional acceleration sensors were fixed on the mounting frame of the superstructure testing car where the equipment for gauge measurement is mounted (superscript  $+$ ). The relative angle (twist) between the measuring bogie and the car body  $\Psi_I$  was recorded using distance sensors. An additional lateral acceleration signal  $a_q$  is measured at the cover of the wheelset bearing. All acceleration signals were filtered with bandpass filters 0.4-10Hz according to [36].

## 3.2 Data Channels Considered

Data channels under consideration included 17 signals listed in table 3.1. Channel 1 contains the lateral acceleration measured on the cover of the wheelset bearing. It should be noticed that this acceleration is not identical to the lateral acceleration of the bogies' frame.

Channels 3 to 10 contain the wheel forces of the bogie equipped with measuring axles.  $Y$ -forces act laterally upon the rails (positive direction from outside the track to the inside),  $Q$ -forces act vertically upon the rails (positive direction downwards).

The relative twist between the measuring bogie and the car body is recorded on channel 11. This signal usually provides a means to roughly correlate track and vehicle data (except for records with purely straight track).

Accelerations of the car body are measured in  $y$ - and  $z$ -direction. There were two locations for the respective accelerometers: The middle of the car body (subscript  $M$ ) and right above the  $z$ -axis of the measuring bogie (subscript  $I$ ). Additional accelerations were recorded at the mounting frame of the track measuring coach (channels 16 and 17).

## 3.3 Data Sets

Data sets under investigation were recorded on the same test runs as those for the recording of track data. Color coding depends on which signals are depicted: If signals from different test runs are shown in the same figure the color coding of table 3.2 is valid. Spectra of force signals, however, are always dedicated to one specific test run only. In this case table 3.3 shows the correct color coding.

Test runs m0008r and m0010r were conducted with the engine pushing the train, therefore applying a longitudinal pressure load to the train. All test runs with a leading 0 in the code

Channel #	quantity	unit
1	$a_q$	$[m/s^2]$
2	$v$	$[km/h]$
3	$Y_{1.1}$	$[kN]$
4	$Y_{1.2}$	$[kN]$
5	$Y_{2.1}$	$[kN]$
6	$Y_{2.2}$	$[kN]$
7	$Q_{1.1}$	$[kN]$
8	$Q_{1.2}$	$[kN]$
9	$Q_{2.1}$	$[kN]$
10	$Q_{2.2}$	$[kN]$
11	$\Psi_I$	$[mrad]$
12	$\ddot{y}_I^*$	$[m/s^2]$
13	$\ddot{y}_M^*$	$[m/s^2]$
14	$\ddot{z}_I^*$	$[m/s^2]$
15	$\ddot{z}_M^*$	$[m/s^2]$
16	$\ddot{y}^+$	$[m/s^2]$
17	$\ddot{z}^+$	$[m/s^2]$

Tabelle 3.1: *Data channels for dynamic vehicle data*

Test Runs	Color
m0507r, m0006r, m6612r	red, 'r'
m0508r, m0008r, m6616r	blue, 'b'
m0509r, m0010r, m6618r	green, 'g'

Tabelle 3.2: *Color key for figures*

number (m0\*\*\*r) had the tested car unloaded, while test runs with a leading 6 (m6\*\*\*r) were performed with a loaded test car.

### 3.4 Distance

Although there is no explicit distance signal contained in the vehicle data, the nominal sampling length of  $0.1m$  provides a means of comparing track distances. To test whether the individual sampling lengths are constant, the shifts between consecutive test runs on the same track are evaluated. Data from test runs 0507, 0508, and 0509, Drösing-Angern, km 58.3 - km 39.9, were used for comparison. The indices of the maxima of the cross-correlation functions between horizontal wheel forces were used as estimates for the relative shift between data sets. Each computation was performed for the right wheel ( $Y_{1.1}$ ) as well as for the left one ( $Y_{1.2}$ ) to avoid the influence of singular phenomena.

Force	Color
$Y_{1.1}, Q_{1.1}$	red, 'r'
$Y_{1.2}, Q_{1.2}$	blue, 'b'
$Y_{2.1}, Q_{2.1}$	green, 'g'
$Y_{2.2}, Q_{2.2}$	cyan, 'c'

Tabelle 3.3: *Color key for figures*

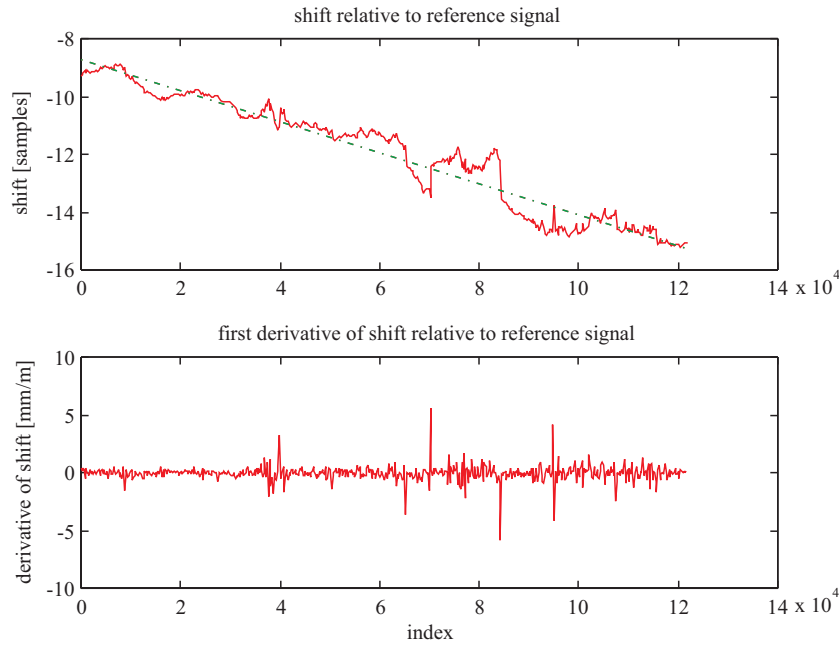


Abbildung 3.2: *Shift functions for  $Y_1$  forces. Test run Drösing-Angern, km 56.3 to km 44.2.*

The evaluation of a continuous shift function with data from test run 0507 as reference brought the following results: Linear changes in the shift between signals are present just as they were in track data. However, there are also strong nonlinear deviations present in the vehicle data. These nonlinear changes in shift seem to be continuous. Figure 3.2 illustrates these phenomena for test run 0509 (shift of  $Y_{1,2}$  red). From the beginning to the end of the signal there are strong nonlinear changes. The dash-dotted line indicating the linear interpolation obviously does not approximate this shift function sufficiently well. From the shift function itself but even more from its derivative it becomes clear that the shift becomes more irregular towards the second half of the record. Because the linear approximation was calculated for the whole record, it fits well for some parts but strongly deviates at some points in the middle. For curved track the deviations are similar to the ones present in data from straight track. Nonlinear deviations amount up to 10 samples locally.

It should be noted that the shift functions computed here are relative to a signal from another test run (0507), therefore no absolute changes in the sampling lengths are known. It would be possible to synchronize the various test runs with vehicle data at least by approximate nonlinear resampling, but the problem of synchronizing these data sets with the track data still remains.

### 3.5 Speed

Speed measurements are based on distance readings from indicators on one wheel of the measuring coach. Each revolution of the wheel corresponds to the nominal wheel circumference, which is divided by the time span since the last full revolution. The speed readings are unaffected by noise or harmonic disturbances which is confirmed by a constant low energy content in the PSD of the speed signal. However, when compared to the speed record of the track measuring coach, there is a small difference in the mean speed reading. Test runs da8\_507 (samples 8.001 to 59.000) and m0507r (samples 20.002 to 147.500) were chosen for comparison of straight tracks. The average

Test Run	Mean [km/h]	Mean [m/s]	Variance [m <sup>2</sup> /s <sup>2</sup> ]
m0006	60.48	16.80	0.0040
m0008	88.97	24.71	0.0033
m0010	110.43	30.68	0.0009
m0507	139.77	38.83	0.0301
m0508	80.78	22.44	0.0122
m0509	109.96	30.54	0.0062
m6115	133.80	37.17	1.1047
m6117	80.41	22.33	0.0151
m6612	118.95	33.04	0.1615
m6616	134.52	37.37	0.9289
m6618	100.06	27.80	0.1348

Tabelle 3.4: *Vehicle data. Statistics for speed.*

values of the speed signals from track data  $\bar{v}_t$  and vehicle data  $\bar{v}_v$  within these ranges are

$$\bar{v}_t = 140.87 \text{ km/h} \quad (3.1)$$

$$\bar{v}_v = 139.67 \text{ km/h}. \quad (3.2)$$

This difference obviously is due to different assumptions for the actual rolling radius of the wheel used for measurements. Although the relative error between the two speed signals is only 0.86%, this uncertainty is also transferred into the time domain since the speed signals have to be used for reconstruction of a time axis.

Table 3.4 shows the mean values for test runs Angern-Drösing on track 2, samples 95.000-115.000, Drösing -Angern track 1, samples 20002-146000, Klagenfurt-Villach track 2, samples 120000-240000, and Villach-Klagenfurt track 1, samples 120500-240500. The variance of speed for test runs m6115 and m6616 is rather large, since their speed signal shows some slow variations in the section under investigation. Therefore, the time domain frequencies for these test runs cannot be more accurate than to 3%, all other errors in time domain frequencies should stay well beyond a 1% error (although there may be additional errors due to the limited resolution of the spectral estimates). A meaningful value for variance could not be computed for m0006 since the quantization level of the speed signal from test run m0006 is twice as high as the level for the two other ones.

## 3.6 Wheel Forces

### 3.6.1 Lateral Forces ( $Y$ )

The tested coach was equipped with measuring axles on the leading bogie for direction Angern-Drösing. The mean values and variances for all 4 wheels are listed in table 3.5. For test runs m0006, m0008, and m0010 samples 95000:115000 were used for computation, for the other test runs samples 70000:90000 were used. The strong changes in the mean values are caused by offsets between the individual test runs and additional linear trends present in the data. Both effects can be seen in the upper graphic of figure 3.3. The signals plotted are the sums over all lateral forces of bogie I after a low-pass filter has been applied. The lower graphic shows the relative twist  $\Psi_I$  between bogie I and car body. From the data it is quite apparent that the sums of the lateral forces exhibit offsets between test runs and change their mean value even along straight track portions. Obviously, finding the correct gain for the  $Y$ -forces is a difficult problem since it does not only require a single calibration but rather an adaptive correction. Data measured on curved track contains stepwise corrections at nonuniform intervals as explained in section 3.1.

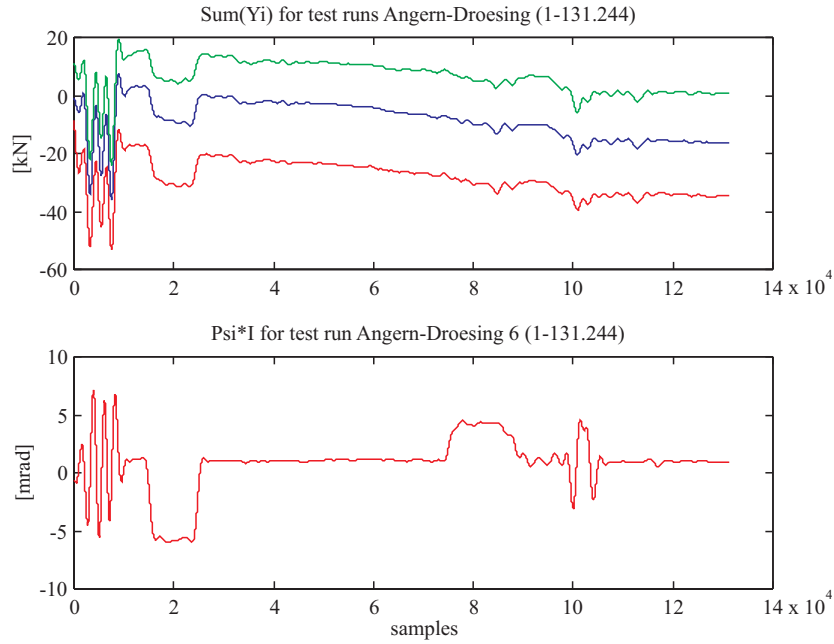


Abbildung 3.3: *Sum of lateral wheel forces for test runs Angern-Drösing (track 1), km 41 to km 54.1.*

Test Run	Quantity	Y1.1	Y1.2	Y2.1	Y2.2	Unit
m0006	mean	-8.59	-9.22	-9.26	-7.58	kN
	variance	3.93	4.39	3.44	3.09	kN <sup>2</sup>
m0008	mean	-3.75	-4.69	-4.07	-3.20	kN
	variance	4.39	4.80	3.54	3.59	kN <sup>2</sup>
m0010	mean	-0.0261	-0.0783	-0.547	1.19	kN
	variance	4.27	5.82	6.05	5.81	kN <sup>2</sup>
m0507	mean	-3.03	-2.44	-1.91	-1.60	kN
	variance	4.30	4.79	3.64	3.74	kN <sup>2</sup>
m0508	mean	-2.33	-2.69	-2.55	-2.82	kN
	variance	1.87	2.39	2.79	1.89	kN <sup>2</sup>
m0509	mean	-1.94	-1.49	-1.36	-1.79	kN
	variance	2.67	3.26	2.70	2.57	kN <sup>2</sup>

Tabelle 3.5: *Statistical values for lateral wheel forces*

Spectra of these signals clearly show that the low-pass filter in the time domain cuts off important information at higher speeds.

The spectra of lateral wheel forces for test run m0006r can be seen in figure 3.4. The main peaks in the low frequency range are located at 31m (0.0323 1/m) or 0.54 Hz. Many smaller but sharp peaks exist in the high-frequency range of the spectra. At 1.42m (0.703 1/m) and 2.84m (0.351 1/m) very distinct peaks show up in all spectra. As supported by evidence given in the following sections, these frequencies correspond to the wheel circumference and half its value. Other distinct peaks are: 0.95m (1.0518 1/m) for  $Y_{1,2}$ , 0.65m (1.5349 1/m) for  $Y_{1,2}$  and  $Y_{2,1}$ , 0.54m (1.8465 1/m) or 31.0 Hz for  $Y_{1,1}$ , and 0.46m (2.1843 1/m) or 36.7 Hz for  $Y_{2,1}$ .

It should be noticed that on straight track the lateral wheel forces depend on the direction of travel. As the train changes direction a different load distribution and spectrum will result [37].

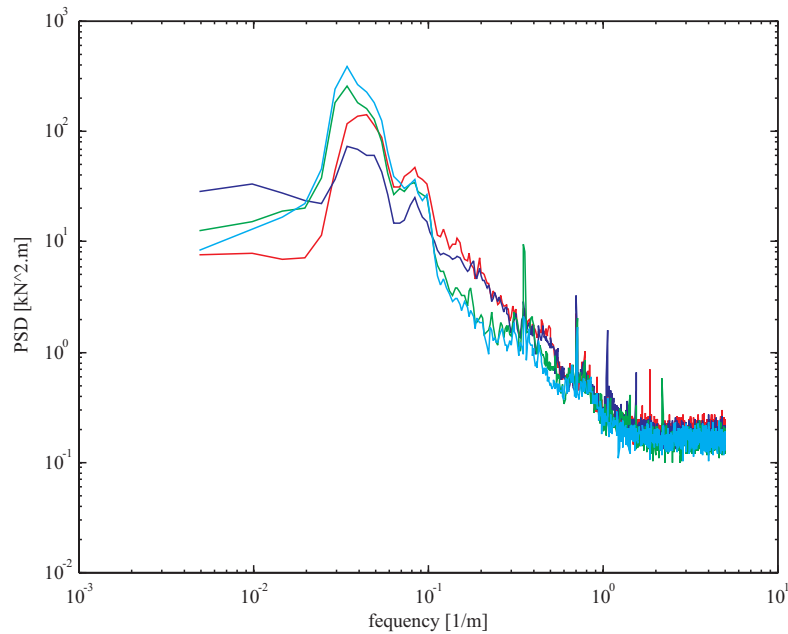


Abbildung 3.4: Spectra of lateral wheel forces for test run m0006r, Angern-Drösing, km 43.5 to km 48.5.

In the test run which is depicted in figure 3.4 the instrumented bogie was the leading one with axle 1 running before axle 2. For the spectra of figure 3.5 the instrumented bogie was trailing and therefore axle 2 was running before axle 1. By comparing these two figures it follows that the main resonance peak is most pronounced for the trailing wheelset, whereas the magnitude of the spectra above a frequency of approximately 0.12 1/m (8.3m) is bigger for the leading wheelset.

The spectra of lateral wheel forces for test run m0008r can be seen in figure 3.6. The main peaks in the low frequency range are located at 30.1m (0.0332 1/m) or 0.82 Hz. The high frequency peaks are arranged at 2.84m and 1.42m (wheel circumference), 0.95m (1.0529 1/m) for  $Y_{1,2}$ , 0.82m (1.2229 1/m) or 30.2 Hz for  $Y_{1,1}$ , and 0.69m (1.4446 1/m) or 35.7 Hz for  $Y_{2,1}$ . Spectra computed from the  $Y$ -forces of test run m0010r can be seen in figure 3.7. With increasing speed the low frequency peaks become broader and more jagged. Still, the first (lowest frequency) peak is located at 31.1m (0.0322 1/m). The wheel frequencies are also present for the spectra of this test run. Additional peaks are located at 10m (0.0995 1/m) for  $Y_{1,2}$ , 0.95m (1.0542 1/m) for  $Y_{1,2}$ , 1m (0.9998 1/m) or 30.7 Hz for  $Y_{1,1}$ , and 0.85m (1.1826 1/m) or 36.3 Hz for  $Y_{2,1}$ . It also should be noticed that the mean value of the lateral forces differs most strongly while negotiating curved track. As already reported in [Olson60], all lateral wheel forces are negative (therefore providing the necessary centripetal acceleration) along constant curvature except for the inner wheel on the second axle in the direction of travel. There is also a significant difference in the mean values for front and rear axle as indicated by the low-frequency content in the PSD estimates.

### 3.6.2 Vertical Forces ( $Q$ )

The mean values and variances of vertical wheel forces for all 4 wheels are listed in table 3.6 (computed from samples 95000:115000).

Spectra of  $Q$ -forces for test run m0006r are depicted in figure 3.8. There is a distinct low-frequency peak in each of the spectra at 31.1m (0.0321 1/m). At a frequency of 10m (0.0995 1/m) only the PSDs of the signals of axle 1 exhibit a peak. There are no obvious high-frequency peaks

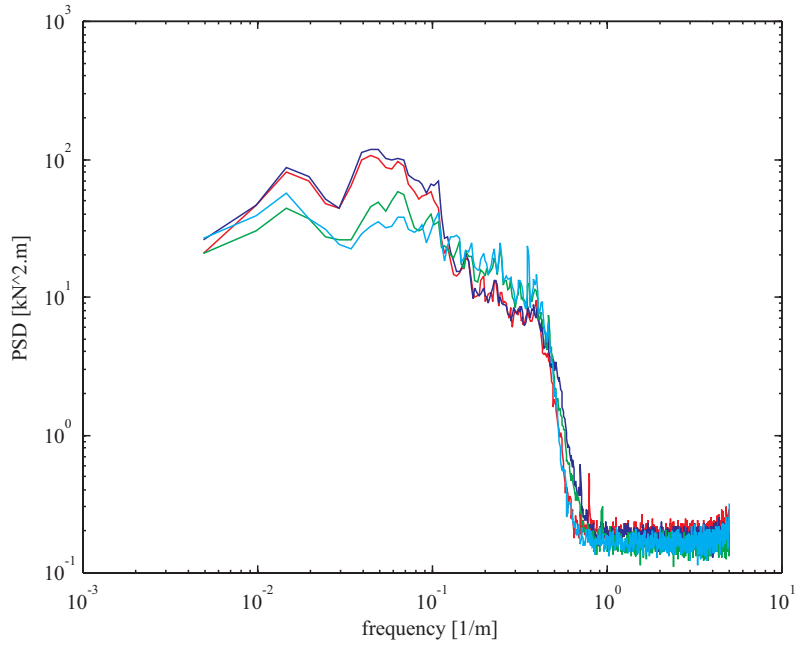


Abbildung 3.5: Spectra of lateral wheel forces for test run m0507r, Drösing-Angern, km 52.2 to km 42.7.

Test Run	Quantity	Q1.1	Q1.2	Q2.1	Q2.2	Unit
m0006	mean	58.45	63.18	63.45	58.94	kN
	variance	6.49	9.71	7.94	7.88	kN <sup>2</sup>
m0008	mean	58.64	64.17	64.26	60.08	kN
	variance	7.30	10.1	11.2	10.37	kN <sup>2</sup>
m0010	mean	58.64	63.03	64.72	59.15	kN
	variance	17.7	24.1	26.5	24.39	kN <sup>2</sup>

Tabelle 3.6: Statistical values for vertical wheel forces

in the signals. The fact that the level of high-frequency noise in the signal of  $Q_{2.1}$  is clearly raised above the levels of all other signals indicates that this signal was corrected for a bias after recording. An overall amplification of the signal will also result in a higher noise level.

More important, the special shape of the signals together with lowpass filtering makes the signals look like they have been filtered with notch-filters at half the frequency of wheel circumference. As indicated by the red lines in figure 3.9, there are notches instead of peaks at frequencies of 2.84m (0.3525 1/m) and 1.42m (0.705 1/m). Furthermore, the spectra in the vicinity of 0.705 1/m show the passband ripple typical for lower-order filters. The shape of the PSD of  $Q_{1.2}$  suggests that frequencies in the farther neighborhood of the notch are also attenuated by the filter. Filtering seems to have been performed during data acquisition since the noise level in the bottom of the notch equals that of the high frequency part of the PSD. These observations are in accordance with the information from the OEBB. Vertical wheel rail contact forces are measured by strain-gauges applied to the wheel discs. The signal coming from those strain-gauges has a trapezoidal shape for constant  $Q$ -force because of the geometric placement on the wheel disc. A dedicated computer converts this signal into the proper constant value. However, due to necessary low-pass filtering (the edges of the trapezoidal signal show damped oscillations) all multiples of half the wheel frequency are strongly attenuated. This effect is inherent to the measurement procedure and can only be

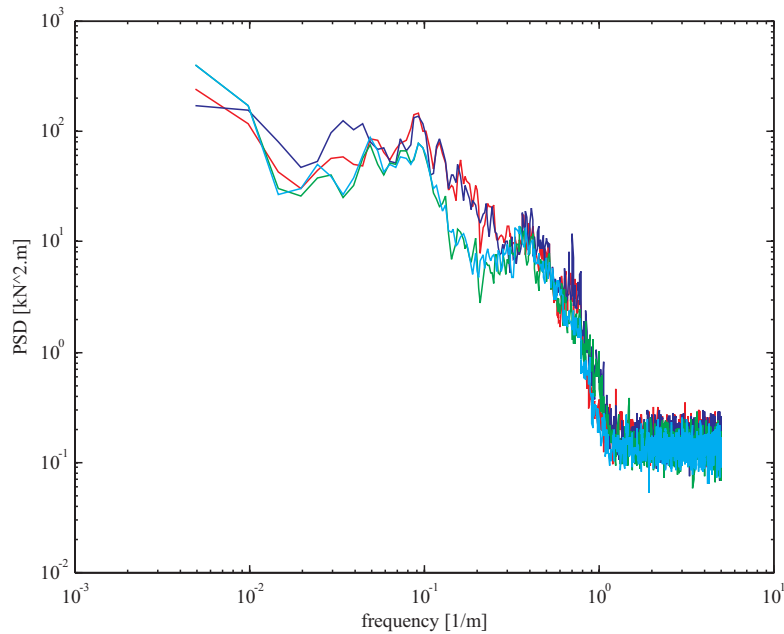


Abbildung 3.6: *Spectra of lateral wheel forces for test run m0008r, Angern-Drösing, km 41 to km 57.3.*

overcome by a change to a different measuring concept.

Spectra for test run m0008r are depicted in figure 3.10. Pronounced peaks in the low-frequency range are still present, although the maximum is less well defined. The maxima for signals of axle 1 respectively axle 2 seem to be at slightly different frequencies. However, the approximate frequency is 32.4m (0.0308 1/m), while an additional peak at 10m (0.0995 1/m) is present for all signals. Otherwise the spectra exhibit the same characteristics as those of test run m0006r including the effects of the notch-filters and the offset of  $Q_{2.1}$ .

Spectra of vertical wheel forces for test run m0010r are depicted in figure 3.11. Again, the same overall picture persists, although the low-frequency maximum is still harder to determine. Its approximate frequency is around 34.1m (0.0293 1/m). The peak at 10m (0.0995 1/m) exists for all signals as it did in the other test runs. The offset of signal  $Q_{2.1}$  is also present. It should be noticed that the effect of the notch-filter is nearly hidden by the low-pass filtering. Since the notch filter has a fixed frequency in the spatial domain and low-pass filtering is done in the time domain, the cut-off frequency of the low-pass filter shifts to smaller values in the spatial domain with increasing speed. Although not depicted here there is a dependence of vertical wheel forces upon the direction of travel. While the loads at the last axle of the car are clearly higher than the loads at the axle before, there is no significant difference between the vertical forces on the leading bogie.

### 3.7 Twist Between Bogie and Car Body

Statistical values were calculated for strictly straight section of track: Angern-Drösing, samples 25000:75000. Unfortunately, the values for test run m0006r listed in table 3.7 cannot be compared to data from the other two test runs because the quantization is 4 times more coarse.

The spectra of the various twist signals are depicted in figure 3.12. The broad resonance peak at a wavelength of about 27m (0.037 1/m) consists actually of two frequency peaks, which are revealed by additional spectra with higher resolution. The wavelengths of these two peaks are 23.5m (0.0425



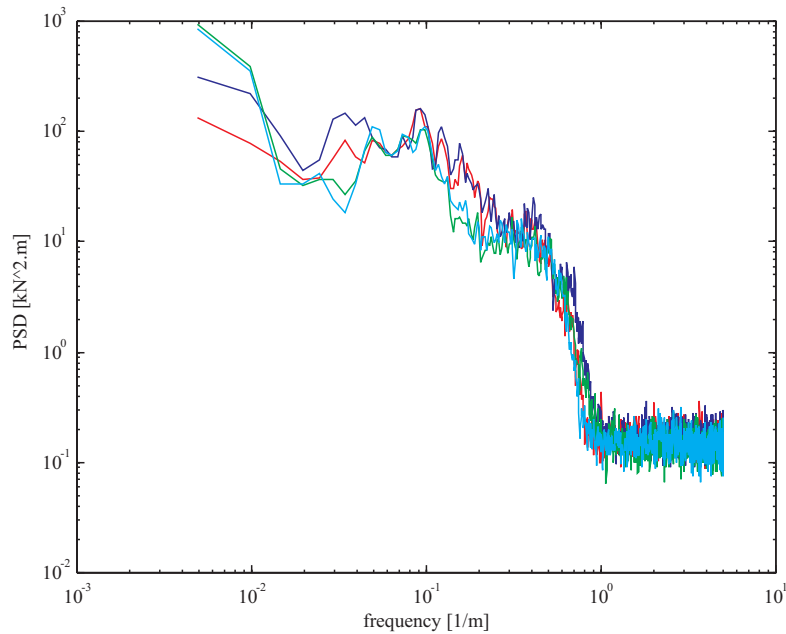


Abbildung 3.7: Spectra of lateral wheel forces for test run m0010r, Angern-Drösing, km 41 to km 57.3.

Test Run	Quantity	$\Psi_I^*$	Unit
m0006	mean	1.06	mrاد
	variance	0.762	mrاد <sup>2</sup>
m0008	mean	0.837	mrاد
	variance	0.453	mrاد <sup>2</sup>
m0010	mean	1.15	mrاد
	variance	0.611	mrاد <sup>2</sup>

Tabelle 3.7: Statistical values for twist between bogie and car body

1/m) and 31.1m (0.0322 1/m) respectively. These are typical wavelengths for the lateral movement of a wheelset on straight track [14]. Since the two wheelsets of a bogie as the two bogies of a car will never be identical, two closely neighboring frequencies in the above mentioned ranged may be found. An additional small peak where all spectra exhibit the same amplitude is present at 10m (0.1005 1/m).

There is a good agreement between all test runs except for the above mentioned difference in quantization, which makes the PSD of test run m0006r differ slightly from the other two. Only in the PSD for test run m0010r a small high-frequency peak at 0.34m (2.9358 1/m) or 90.1 Hz exists.

The spectra for the records on track Drösing-Angern show a slightly different characteristic. The main peaks seem to be approximately constant in time with frequencies of 0.0204 1/m or 0.79 Hz for m0507r, 0.0263 1/m or 0.80 Hz for m0508r, and 0.0321 1/m or 0.72 Hz for m0509r. However, only for test run m0509r this peak was really distinct, the other two PSDs had a rather level but jagged section in this region of frequency.

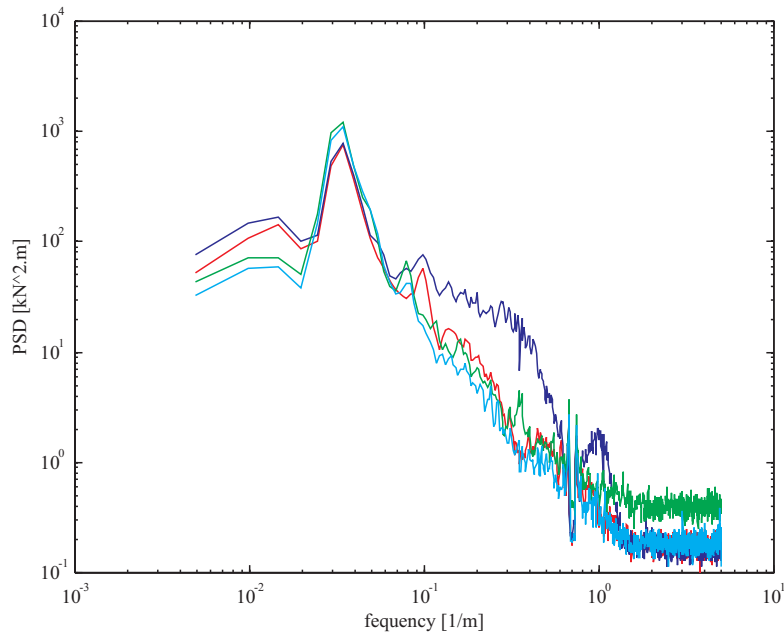


Abbildung 3.8: Spectra of vertical wheel forces for test run m0006r, Angern-Drösing, km 43.5 to km 48.5.

Test Run	Quantity	$\ddot{y}_I^*$	$\ddot{y}_M^*$	$\ddot{z}_I^*$	$\ddot{z}_M^*$	Unit
m0006	mean	-0.0043	0.0089	0.0196	-0.0114	$\text{m/s}^2$
	variance	0.0090	0.0052	0.0042	0.0031	$\text{m}^2/\text{s}^4$
m0008	mean	-6.25e-5	0.0115	0.0210	-0.0086	$\text{m/s}^2$
	variance	0.0186	0.0105	0.0224	0.0129	$\text{m}^2/\text{s}^4$
m0010	mean	-1.3e-4	0.0115	0.0213	-0.0083	$\text{m/s}^2$
	variance	0.0212	0.0110	0.0220	0.0226	$\text{m}^2/\text{s}^4$

Tabelle 3.8: Statistical values for car body accelerations

### 3.8 Car Body Accelerations

Car body accelerations were measured right above the vertical axis of the bogie and in the middle of the car. At each point the accelerations in vertical and in lateral direction were recorded. The statistical data are listed in table 3.8.

Spectra of car body accelerations show a variety of eigenmodes, consisting primarily of the secondary suspension but also of the motion of the bogie and elastic bending modes of the car body. Since some of these modes are linear resonance phenomena in good approximation (suspension, elastic modes) and others are of distinct nonlinear nature (bogie motion), the amplitudes and the characteristic frequencies of all these phenomena form a complex picture. The frequency of the bogie's sine run is typically fixed in the spatial domain, while the frequencies of linear oscillations are fixed in the time domain.

Spectra in figure 3.13 were computed from the car body accelerations in lateral direction right above the vertical axis of the bogie. The main peak represents the rigid body eigenmode of the car in lateral direction. The frequencies in the time domain are 0.0146 1/m or 0.57 Hz for test run m0507r, 0.0271 1/m or 0.61 Hz for m0508r, and 0.0185 1/m or 0.56 Hz for m0509r. These values were taken from the most left peak just before a step drop.

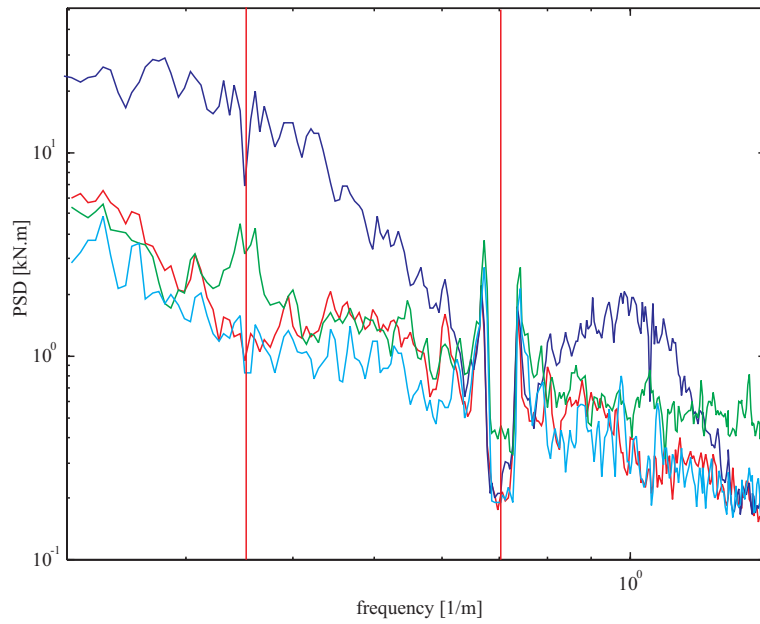


Abbildung 3.9: Spectra of vertical forces for test run m0006r, Angern-Drösing: Zoom on wheel frequency and double wheel frequency

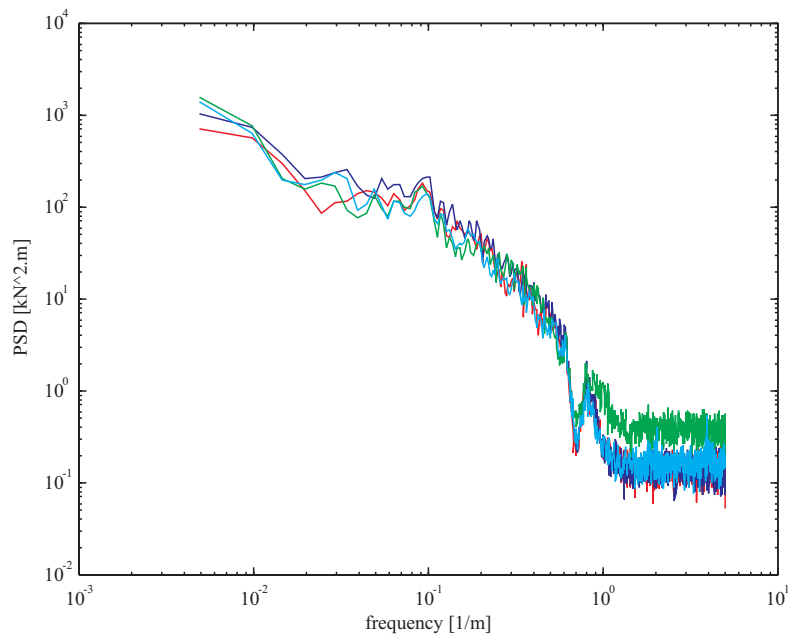


Abbildung 3.10: Spectra of vertical forces for test run m0008r, Angern-Drösing, km 41 to km 57.3.

The spectra for test runs on track Angern-Drösing differ from the those of track 2. They show main peaks at 30.3m (0.0330 1/m) for m0006r, 34.1m (0.0293 1/m) for m0008r, and 37.7m (0.0265 1/m) for m0010r. These frequencies could also be due to the lateral movement of the wheelsets. The reason for the differences could be the effect of a tight coupling to the neighboring car, which might exhibit a slightly different eigenfrequency. It is not obvious where the changes in the frequencies

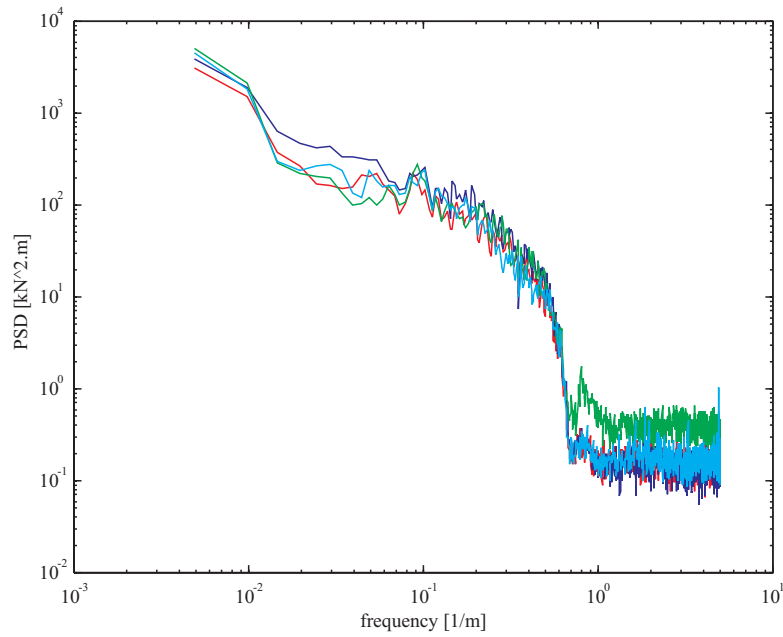


Abbildung 3.11: Spectra of vertical forces for test run m0010r, Angern-Drösing, km 41 to km 57.3.

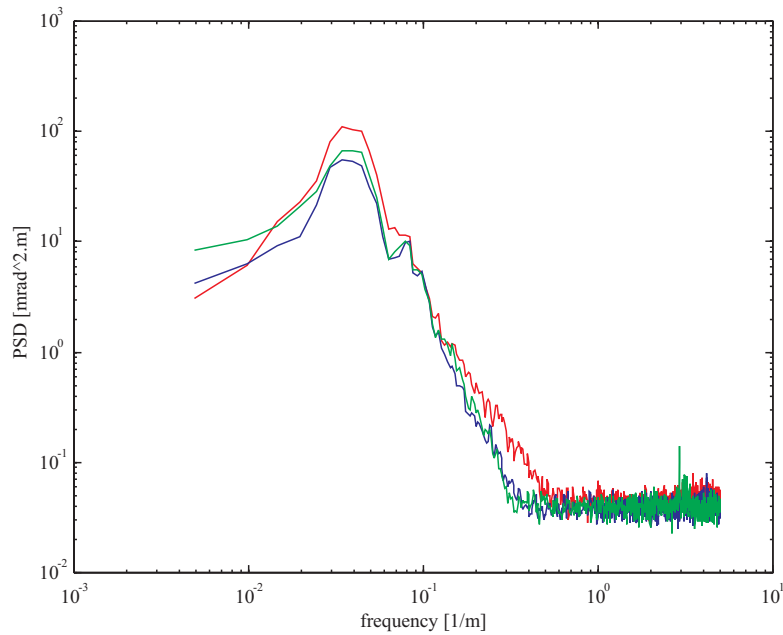


Abbildung 3.12: Spectra of twist between bogie and car body. All test runs on Angern-Drösing, km 43.5 to km 48.5.

come from, although the longitudinal loads applied to the train might be part of an explanation. Other marked peaks arise at 0.3169 1/m or 12.31 Hz for m0507r, 0.5322 1/m or 11.94 Hz for m00508r, and 0.4114 1/m or 12.56 Hz for m0509r. These frequencies seem to be associated with the rigid body eigenmode of the bogie frame.

The other distinct frequencies are fixed in the spatial domain although not all of them are

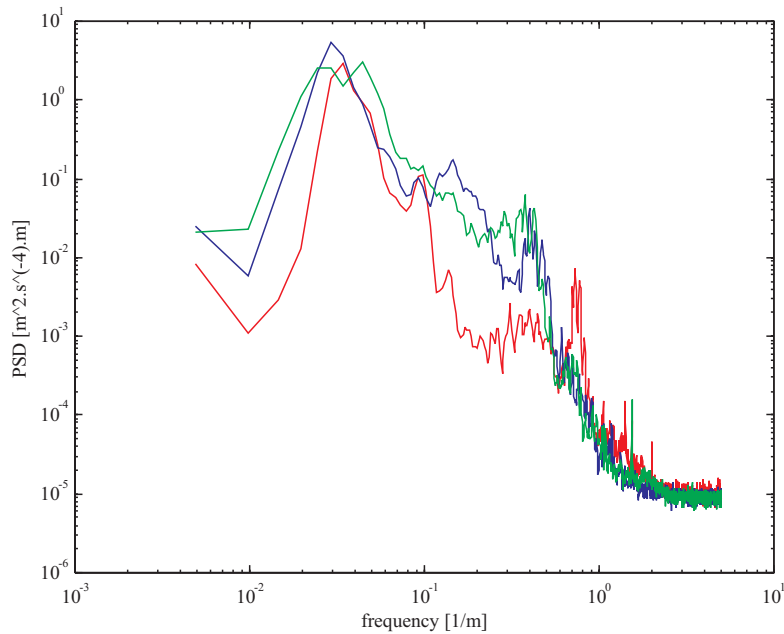


Abbildung 3.13: Spectra of lateral car body accelerations above bogie. Test run Angern-Drösing, km 41 to km 57.3.

Test Run	Frequency [Hz]			
m0507	0.55	1.55	8.86	14.4
m0508	0.59	1.46	8.94	15.2
m0509	0.54	1.49	8.78	15.5

Tabelle 3.9: Time domain frequencies in the spectra of test runs on track 2 (Drösing-Angern)

present in each signal. A marked peak in the spectrum for test run m0006r at 10m (0.1 1/m) is hardly perceptible in the spectra of the two other runs. However, a sharp peak at 0.65m (1.537 1/m) is also present in the spectrum of signal m0010r. Other sharp peaks in the high frequency range of the spectrum of m0006r are: 0.95m (1.055 1/m), 0.71m (1.408 1/m), and 0.50m (2.012 1/m).

Spectra in figure 3.14 were computed from the car body accelerations in lateral direction in the middle of the car body. The highest peaks again represent the rigid body eigenmode of the car in lateral direction. The frequencies in the spatial domain are 0.0322 1/m for test run m0006r, 0.0298 1/m for m0008r, and 0.0265 for m0010r, almost identical to the values from above the bogie. Differing from the spectra in figure 3.13, there is also a good agreement on the fixed spatial frequency of 10m (0.1 1/m). Other fixed spatial frequencies arising in all test runs come to lie at 4.16m (0.24 1/m), 3.22m (0.31 1/m).

The distinct peak in the PSD of test run m0006r at 1.53 1/m corresponds to 25.7 Hz. If this peak arises because of an structural oscillation, there should be respective peaks in the PSDs of the other two test runs. According to the speed of the other two test runs, there should be peaks at frequencies of 1.04 1/m for test run m0008r and 0.838 1/m for m0010r. These peaks can actually be found, proving a structural oscillation of the car body at 25.7 Hz.

A multitude of fixed frequencies in the time domain can be found in the spectra of the test runs on track 2 (Drösing-Angern). The values of the frequencies can be found in table 3.9.

Vertical accelerations of the car body above the vertical bogie axis have the spectra depicted

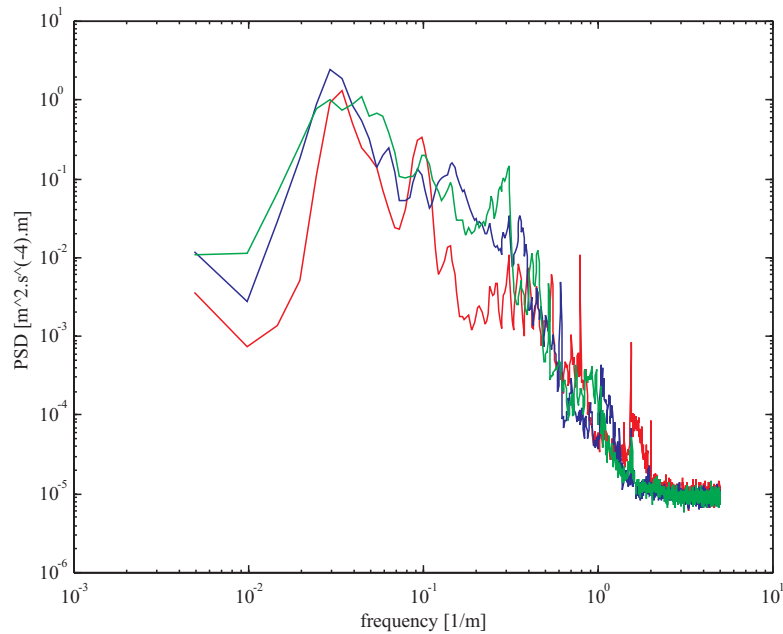


Abbildung 3.14: Spectra of lateral accelerations for middle of car body. Test run Angern-Drösing, km 41 to km 57.3.

in figure 3.15. The maxima of the respective spectra are found to be at 0.0234 1/m or 0.91 Hz for m0507r, 0.0371 1/m or 0.83 for m0508r, and 0.0271 or 0.83 Hz for m0509r. However, for test runs on track 1 the corresponding frequencies are 0.0502 1/m or 0.84 Hz for m0006r, 0.0493 1/m or 1.22 Hz for m0008r, and 0.0406 1/m or 1.25 Hz for m0010r. Since the last two test runs were conducted with pushing engine, it is likely that the longitudinal pressure forces between the cars alter the frequency of this eigenmode.

Additional peaks with approximately constant frequency in the time domain are found at frequencies of 0.3705 1/m or 14.4 Hz for m0507r, 0.680 1/m or 15.3 Hz for m0508r, and 0.5068 1/m or 15.5 Hz for m0509r. The peaks found in the recordings of the test runs on track 1 are associated to the frequencies of 13.3 Hz, 15.1 Hz, and 16.0 Hz respectively.

Peaks present in all spectra are located at 25.3m (0.0396 1/m), at 2.85m (0.3513 1/m), being caused by the wheel revolutions, at 1.42m (0.7031 1/m), 0.95m (1.0527 1/m), 0.65m (1.5346 1/m), and 0.6m (1.6672 1/m). In the spectrum of test run m0006r the peaks at 0.95m and 0.65m are not perceptible. In all other recordings the peak at 0.65m shows a remarkable amplitude which is dependent on speed: It increases strongly with the speed of the measuring train. Spectra of vertical car body accelerations in the middle of the car body are depicted in figure 3.16. The lowest frequencies containing most of the energy are located at 0.0245 1/m or 0.95 Hz for m0507r, 0.0383 1/m or 0.86 Hz for m0508r, and 0.0304 1/m or 0.93 Hz for m0509r. The three sharp peaks which were present in figure 3.15 at 14.4 Hz, 15.3 Hz, and 15.5 Hz show up also very clearly. Additional marked peaks arise at 10.0 Hz for m0507r, 9.9 Hz for m0508r, and 10.7 Hz for m0509r. This frequency obviously does not depend on speed or on the longitudinal loads, making it likely to be an eigenmode of the car body structure.

The peaks at 0.95m (1.053 1/m) and 0.65m (1.534 1/m) are also present, although in the spectra of figure 3.16 test run m0008r shows the smallest amplitudes at these frequencies while the other test runs produce quite marked peaks. In the spectra of test runs on track 2 there are again fixed peaks at 10.2m (0.0984 1/m), 7.3m (0.1376 1/m), 2.85m (0.3505 1/m), and 1.46m (0.6864 1/m).

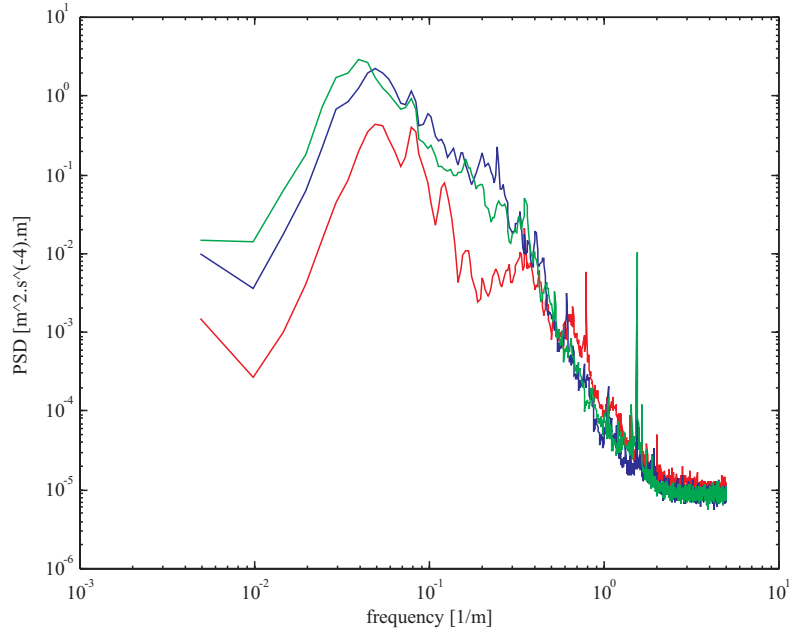


Abbildung 3.15: Spectra of vertical car body accelerations above bogie. Test run Drösing-Angern, km 57.3 to 41.

### 3.9 Accelerations of Mounting Frame (Measuring Coach)

Since recordings of the mounting frame accelerations from test run m0006r contain merely low-level noise, only the signals of the other two test runs provide useful information. Moreover, the lateral and vertical accelerations are identical except for amplitude, so that only one spectrum for each test run contains all available frequency information.

The narrow-band peaks of the two spectra in figure 3.17 come to lie at frequencies of approximately 0.4137 1/m or 10.2 Hz for m0008r, 0.3501 1/m or 10.7 Hz for m0010r, 0.4242 1/m or 9.52 Hz for m0508r, and 0.3429 1/m or 10.5 Hz for m0509r respectively. There is a multitude of peaks in both spectra at identical frequencies: Most marked are the peaks at 2.89m (0.3466 1/m) again caused by the wheel revolution, and its whole numbered multiple frequencies which can be found up to order 14. Other distinct peaks in the spectra exist at 1.05m (0.9481 1/m), 0.96m (1.0385 1/m), 0.72m (1.3818 1/m), and 0.65m (1.538 1/m). However, the most distinct peaks are those at wheel frequency and its multiples (2.89m to 0.207m).

There are many more sharp peaks in the high-frequency remainder of the spectrum, but since they are very closely placed it would be difficult to assign them to the counterpart of the other test run.

The signals of vertical acceleration of the mounting frame are identical to the signals for lateral acceleration except for an additional factor  $\alpha$

$$\ddot{z}^+(k) = \alpha \ddot{y}^+(k), \quad (3.3)$$

where  $\alpha = 1.7$  for test runs on track 1 and  $\alpha = 1.8$  for test runs on track 2. Therefore, the spectra are identical to those of figure 3.17, but their amplitudes are bigger by about 4.6dB. It should be noted that no phase shift is present in relation 3.3.

Accelerations of the mounting frame for test runs m0006r and m0507r were obviously not recorded. Instead, only noise is present in the signals for lateral and vertical accelerations. The noise is white within the frequency band of interest with a distinct peak at 0.389m (2.5723 1/m, or

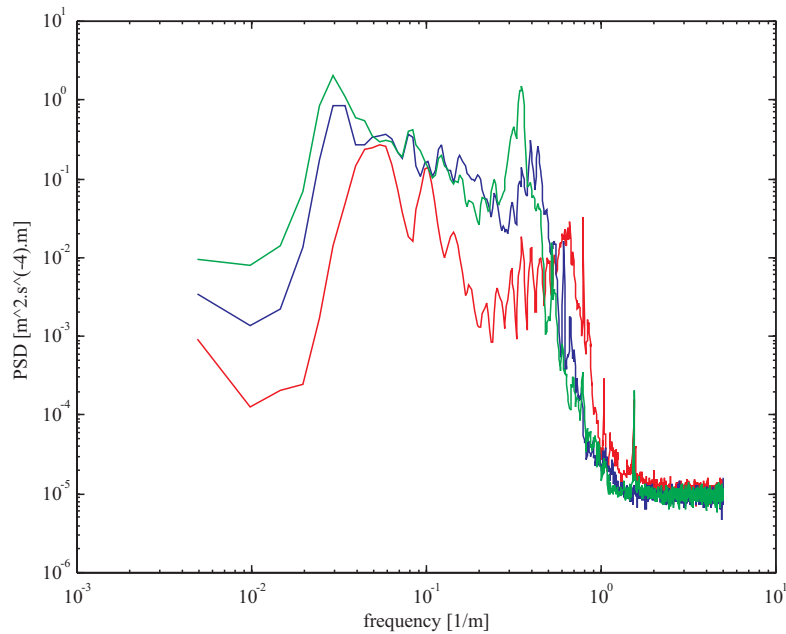


Abbildung 3.16: Spectra of vertical car body acceleration in middle of car. Test run Drösing-Angern, km 57.3 to 41.

100 Hz). It is most likely caused by the frequency of a source voltage. However, its peak amplitude is much smaller than the signal levels and it will certainly not affect the measurements.

It is important to notice that the erratic behavior of the gauge recordings described in section 2.10 coincides with larger peak values in the acceleration signals of the mounting frame. This could either be reason for the wrong gauge readings or a symptom of the worn rail profile. Without additional information on this specific track section no final answer is possible.

## 3.10 Evaluation of Vehicle Data

### 3.10.1 Distance

The distance readings seem to exhibit different types of errors. First, there is a constant difference in sampling length, showing up as a linear trend in the shift between different test runs. This problem can be overcome by a constant resampling of one of the signals. Second, there exist some nonlinear but continuous changes in the shift between test runs. These local shifts could be removed by an adaptive resampling of one of the signals. However, since the shift between signals is a relative quantity, additional knowledge is necessary to decide which of the signals is to be resampled or how the shift should be divided between the signals.

### 3.10.2 Speed

Speed recordings show no particular errors. Since the internal clock of the measurement system can be regarded as exact when compared to errors in distance, the values of speed will be only as accurate as the distance measurements. A comparison between speed readings of track measuring coach and vehicle measuring coach showed a difference of 0.86%, which is most likely caused by insufficient knowledge of the wheel circumference. However, because of the conical running surface the circumference of the wheel depends upon the lateral displacement relative to the rail, therefore



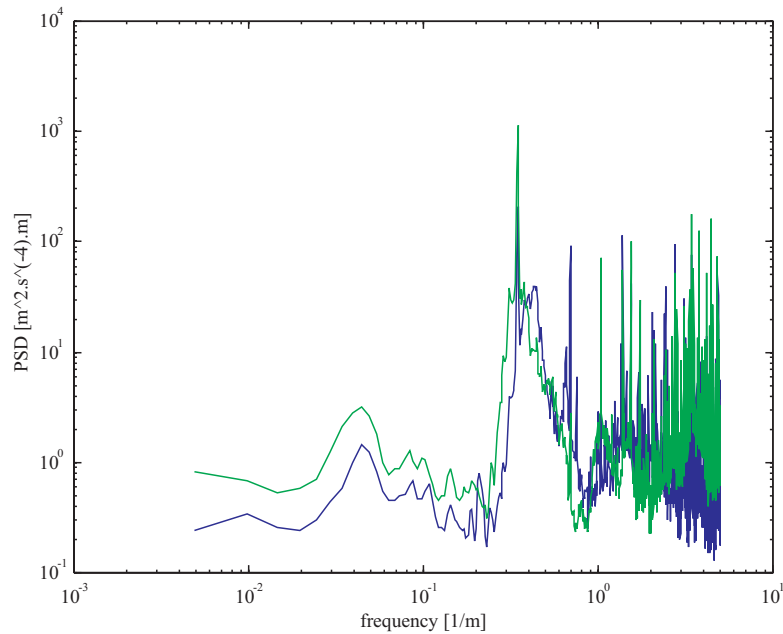


Abbildung 3.17: Spectra of lateral accelerations of mounting frame. Test run Drösing-Angern, km 57.3 to 41.

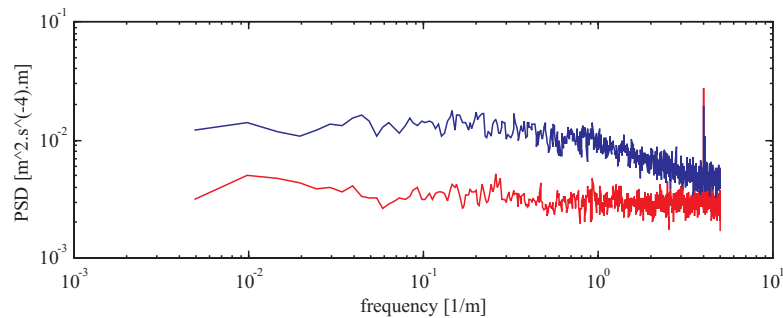


Abbildung 3.18: Spectra of acceleration of mounting frame for test run m0006r. Angern-Drösing, km 57.3 to 41.

inherently limiting the achievable accuracy.

### 3.10.3 Lateral Forces ( $Y$ )

Lateral forces acting upon the wheels provide guidance along the track. Since the alignment of the individual rails will cause nonlinear but proportional lateral forces, the spectra of track alignment and lateral forces are indeed similar. The main difference comes from the fact that the wheelsets together with the bogies and the car body show some distinct dynamics which do not have a counterpart in the rail alignment. There are peaks at approximately 31m for all test runs, which could be most likely caused by the sine-run of the bogie along the track. Other sharp peaks arise at the wheel frequency and its whole numbered multiples. There are some other marked peaks at fixed frequencies in spatial domain, maybe corresponding to waves from the manufacturing process, sleeper spacing or rail length. All signals are low-pass filtered.

Data from table 3.5 indicates that the variance of force signals increases with speed, while the absolute values for the mean show strong differences due to offset errors. In addition to these

offset errors between test runs there are approximately linear trends within the force records which lead to inconsistent means. Because of these errors it becomes quite difficult to retrieve correct absolute values for  $Y$ -forces. Data for curved track additionally shows jumps in the mean values at nonuniform intervals because of on-line corrections (see section 3.1). However, correct absolute values of lateral forces are vital to compute the criterion for safety against derailment (Prud'homme criterion).

The strong differences in the behavior of the individual lateral wheel forces depending on direction of travel and curve suggest that these cases should be investigated independently. It seems reasonable to perform a dedicated identification for each of these setups.

### 3.10.4 Vertical Forces ( $Q$ )

Records of vertical wheel forces do not show the problems appearing in data of lateral forces. Data listed in table 3.6 indicate that the variance of  $Q$ -forces strongly increases with speed, while the mean values remain practically constant. It is interesting that the diagonal facing wheels show approximately the same mean values although the values for the individual diagonal differ considerably. This phenomenon could either be caused by an offset in calibration or a mechanical asymmetry in the bogie or in the suspension of the wheelsets.

Two characteristics of the spectra are apparently artificial: The spectra of signal  $Q_{2,1}$  reveal that the level of this signal has been adjusted after recording of data. Secondly, the fixed frequencies in the spatial domain at the wavelengths of the wheel circumference (2.84m) and especially at its half (1.42m) have been strongly attenuated by the inherent characteristics of the measurement setup. Furthermore, due to the pass-band ripple of these filters, signal components close to these frequencies are also attenuated. All signals are low-pass filtered.

The spectra show peaks at 32m and 34m respectively, lying very close to the values found for  $Y$ -forces. For the test runs on track 2, Drösing-Angern, peaks at 22.9m respectively 25.6m are more pronounced. An additional but not very distinct peak is present at 10m.

Since there is a significant difference in vertical wheel forces with the direction of travel during cornering, the two cases should be investigated individually.

### 3.10.5 Twist

The twist signal has fixed frequencies in the spatial domain at approximately 23.5m and 31.1m. These frequencies obviously are in agreement with those found in the  $Q$ -forces. The small 10m peak is also present. However, the spectra of twist also show less distinct peaks which mark a frequency in the time domain at about 0.8Hz. This frequency could be associated with an eigenmode of the car body.

### 3.10.6 Car Body Accelerations

Statistical values from table show that there are no considerable offsets present in data. The variances for the individual test runs indicate that at first there is an increase with speed, but then the variance stays about constant with a further rise in speed. This could be due to the decoupling effect of a soft secondary suspension, which will effectively eliminate high frequency disturbances from the track.

The spectra of lateral car body accelerations show an abundance of distinct frequencies, both in the spatial and in time domain. The lowest frequency is 0.56Hz, being most likely the first eigenmode of the car body. Other frequencies are 1.5Hz, 8.9Hz, 15Hz and 25.7Hz. These frequencies represent eigenmodes of the rigid body system of the bogie as well as elastic modes of the car body structure.

Fixed spatial frequencies are found at about 34m, 25.3m, 10m, 0.95m, 0.65m, and 0.6m. Not all of these frequencies can be found in every PSD, but they are included in this listing since they have appeared in the spectra of various test runs on different tracks. Wheel frequencies can be found in the acceleration signals of nearly all test runs.

The situation for vertical car body accelerations is very similar, only the values are different. Fixed frequencies in the time domain arise at 0.86Hz, 10.2Hz, and 15.1Hz. Only the frequency at 15.1Hz is in good agreement with the frequencies from lateral accelerations, all other frequencies seem to be caused by orthogonal oscillations. Fixed spatial frequencies can again be found at 10m, 0.95m, and 0.65m.

### **3.10.7 Accelerations of Mounting Frame**

Although lateral and vertical accelerations of the mounting frame were recorded independently they show exactly the same spectra and also the same time history except for the amplitudes. Since there is no phase shift between the two signals this would suggest a diagonal oscillation of the frame. However, this seems to be only reasonable if the suspension or the load of the frame are asymmetrical, or the excitation by the bogie frame already exhibits such a pronounced asymmetry.

A frequency of approximately 10.2Hz shows up in all acceleration signals of the mounting frame. The amplitude peaks at the frequency of the wheel circumference (2.89m) and its multiples up to order 14 are very sharp and high. Other fixed frequencies come to lie at 1.05m, 0.96m, 0.72m, and 0.65m.

## Kapitel 4

# Data Synchronization

Data in the present investigation were recorded with a dedicated measuring train incorporating the test object, the dynamics measuring car, and the superstructure testing car (train configuration depicted in figure 2.1). In this configuration a common time base could be used for data recording and the known spatial distances between sensor locations could be utilized to refer all data to a common reference point on the train. However, routine testing of cars as well as of the superstructure is always performed by individual test teams so the vast majority of data for vehicles and superstructure are recorded completely independently. Hence, the importance of proper synchronization between the vehicle data and the track (superstructure) data is evident. For statistical comparisons between track data and vehicle reactions an approximate synchronization as provided by curvature readings and observations of the train position is sufficient. For the purpose of an identification, however, there is a much smaller acceptable error margin. It is quite apparent that a synchronization error of five samples will be fatal for an identification scheme which takes only the past four samples into consideration.

The main problem of a synchronization of track and vehicle signals lies within the fact that no absolute reference is available for any signal. Both data sets are sampled in the spatial domain with the assumption of known constant sampling intervals. Due to wrong nominal sampling intervals, curve negotiation, wheel profile, and even varying gauge<sup>1</sup> the sampling intervals will vary, the absolute position of the car cannot be established exactly, and the absolute position error due to wrong nominal sampling intervals will even grow with distance. The observations made by personnel from the moving train are far too inaccurate to provide useful synchronization marks. Nevertheless, if there is a sufficiently close correlation between input (track) and output (vehicle reactions) one can hope to find a sufficiently accurate relative synchronization between these data sets. This means that each sample in one signal corresponds to a distinct sample in the other signal but there is no certainty that the intervals between these corresponding samples are constant. Therefore, we do not know the absolute position and can not provide an absolute synchronization (i.e. corresponding samples in both data sets *and* known position of each sampling instant).

The chapter is structured into several sections. In the first one the problem of sampling rate conversions is addressed since it poses a methodological prerequisite for every synchronization procedure unless the sampling rates are exactly identical. The second section gives a short comparison of linear and nonlinear correlations which can be used for input-output synchronization. In the third section the algorithm of the shift function estimate is derived. The problem of absolute shift is discussed and properties of the shift estimate are given. To improve the accuracy of the resampling algorithm with correlation methods a model based approach is also discussed. Numeric simulations confirm the correctness of the results and give practical limits for the applicability. An investigation of the effects of absolute shift on the accuracy of the relative shift estimate concludes the chapter.

---

<sup>1</sup>Since the wheel tread is conical and the wheel set shows a sine run along straight track the mean rolling radius of the wheel and therefore the sampling interval will depend upon these parameters.

## 4.1 Sampling Rate Conversion

Only for input-output data with exactly identical sampling rates correlation procedures can be directly applied. This is the normal case when both data sources are recorded with the same sampling scheme. If input and output are sampled independently, two informations are necessary to establish the exact connection between the data sets:

1. The knowledge of one absolute time (or position) mark in both data sets
2. The knowledge of the exact constant sampling interval for each data set

If the sampling intervals are not identical there is a need to resample at least one data set in order to establish an unique correspondence between the samples of the two data sets. A more complicated situation arises if the second information listed above is replaced by a list of absolute time (or position) for each sampling instant where the sampling interval varies. This is the case when sampling is done in the spatial domain with constant sampling intervals  $\Delta x$  at varying speed and we want to transform the signals into the time domain. Then, the varying sampling interval in the time domain is given by  $\Delta t(k) = \frac{\Delta x}{v(k)}$  which requires the knowledge of speed  $v(k)$  at each sampling instant. This information is equivalent to the knowledge of the absolute time of each instant but has the shortcoming of accumulating small bias errors in the speed reading. In both cases the signals in the time domain have to be resampled utilizing some additional information. Therefore, the remainder of this section is divided into resampling for constant speed and for varying speed, respectively.

### 4.1.1 Constant Speed

If the speed of the train is constant the simple algebraic relation

$$f_t = f_x \cdot v = \frac{v}{\lambda_x}, \quad v = \text{const.} \quad (4.1)$$

states that any frequency in the time domain  $f_t$  is equal to the respective frequency recorded in the spatial domain  $f_x$  and scaled by the constant speed of the train  $v$ . The inverse of the spatial frequency  $f_x$  is the wavelength  $\lambda_x$ . Relation 4.1 can also be written for the constant sampling interval  $\Delta x = \frac{1}{f_{\Delta x}}$  being the inverse spatial sampling frequency  $f_{\Delta x}$ . The resulting expression is hence

$$\Delta x = \Delta t \cdot v, \quad v = \text{const.} \quad (4.2)$$

where  $\Delta t$  is the constant sampling time.

The track data (input) is sampled at a nominal spatial sampling interval of  $\Delta x_t$  while the vehicle reactions are sampled at a different but also constant interval of  $\Delta x_v$ . In order to find the corresponding samples in each data set a sampling rate conversion to a common sampling interval  $\Delta x_c$  must be carried out. This can either be achieved by decimation or interpolation by a natural number of one or the other data set. For the sake of numerical efficiency it is of interest to find the minimum order of resampling filters to achieve a common sampling interval. The minimum-order realization can be found by analyzing the factor  $\eta$  between the two sampling rates

$$\Delta x_t = \eta \Delta x_v \quad (4.3)$$

where  $\eta > 1$  for  $\Delta x_t > \Delta x_v$ . There are three distinct cases which have to be distinguished.

1.  $\eta$  is an integer

If  $\eta$  is an integer it can be decomposed by prime factorization

$$\eta = \prod_1^{j=n} p_j \quad (4.4)$$

into its  $n$  prime factors  $p_j$ . Hence, a non-unique partitioning of the prime factors

$$\eta = \prod_1^{j=n} p_j = \prod_1^{i=n-k} p_i \cdot \prod_k^{j=n} p_j = P_1 \cdot P_2 \quad (4.5)$$

into the product of the first  $k - 1$  and the remaining  $n - k + 1$  factors is possible leading to the product of two integer numbers  $P_1$  and  $P_2$ , each of them being a factor of  $\eta$ . Inserting 4.5 into relation 4.3 and rearranging gives two possible solutions for the common sampling interval  $\Delta x_c$

$$\begin{aligned} \Delta x_{c1} &= \frac{1}{P_1} \Delta x_t = P_2 \Delta x_v \\ \Delta x_{c2} &= \frac{1}{P_2} \Delta x_t = P_1 \Delta x_v \end{aligned} \quad (4.6)$$

where track data is decimated by a factor of  $P_1$  and vehicle data is interpolated by  $P_2$  or vice versa. As mentioned above these solutions are not unique since the partitioning of  $\eta$  in 4.5 was not unique in itself. However, the criterion of a minimal order requires that both  $P_1$  and  $P_2$  are minimized at the same time with the constraint of equation 4.5. This apparently leads to a criterion for the partitioning of the form

$$\left| \frac{P_1(k)}{P_2(k)} - 1 \right| \stackrel{!}{=} \min_k \quad (4.7)$$

It should be noted that no assumptions were made on the order of prime factors in 4.5. Therefore, the criterion 4.7 requires to test a large number of possible combinations in order to find the global minimum. But since  $\eta$  will usually be a small number ( $1 \leq \eta \leq 15$ ) the combination leading to minimal realizations of resampling filters can be found at first glance.

For reasons beyond the numerical problems of resampling it may prove useful to choose other resampling factors. If, for instance, both input and output data have a much higher Nyquist frequency than the bandwidth of the signals it will be more efficient to decimate both signals to a lower common sampling frequency.

## 2. $\eta$ is a rational number

In the case of  $\eta$  being rational the prime factorization of 4.5 can be applied to both numerator and denominator leading to

$$\eta = \frac{\prod_1^{j=n} p_j}{\prod_1^{l=m} p_l} = \frac{\prod_1^{i=n-k} p_i \cdot \prod_k^{j=n} p_j}{\prod_1^{o=m-r} p_o \cdot \prod_r^{l=n} p_l} = \frac{P_1 \cdot P_2}{P_3 \cdot P_4} \quad (4.8)$$

which can be used to give a variety of solutions for a common sampling interval  $\Delta x_c$ :

$$\begin{aligned} \Delta x_{c1} &= P_3 \cdot P_4 \Delta x_t = P_1 \cdot P_2 \Delta x_v \\ \Delta x_{c2} &= \frac{P_3}{P_1} \Delta x_t = \frac{P_2}{P_4} \Delta x_v \\ \Delta x_{c3} &= \frac{P_4}{P_2} \Delta x_t = \frac{P_1}{P_3} \Delta x_v \\ \Delta x_{c4} &= \frac{P_4}{P_1} \Delta x_t = \frac{P_2}{P_3} \Delta x_v \\ \Delta x_{c5} &= \frac{P_3}{P_2} \Delta x_t = \frac{P_1}{P_4} \Delta x_v. \end{aligned} \quad (4.9)$$

The solution of  $\Delta x_{c1}$  will be out of question here since it means a decimation of both data sets by factors which are definitely not minimal. All other solutions of 4.9 involve resampling by a rational number which is done by first interpolating with the numerator factor and then decimating with the denominator factor. Properties of this procedure can be found in [41]. The partitioning for a minimal realization of these filters and the selection of the optimal solution from 4.9 will give much more possible combinations as in the previous case. Still, a complete set of factors can be computed and the optimal solution can be found by a search among these factors.

For the same reasons as already mentioned in case 1 the solution of  $\Delta x_{c1}$  may actually be of practical use in the case of small  $P_i$ . In general, any solution yielding a non-minimal realization might give an optimal solution for a special purpose. When the data sets are synchronized for the purpose of an identification it will depend upon the bandwidth of the signals of the system which parameter choice is optimal. In the case of a rational resampling factor  $\eta$  there will be rarely a chance to determine the optimal parameter set for resampling when all these objectives are taken into account.

### 3. $\eta$ is an arbitrary number

Since interpolation and decimation by up- and downsampling can only be performed in integer steps an exact solution would only be possible by using infinitely large resampling factors. The alternate approach by use of Lagrange or spline interpolation might give optimal results but at a high computational cost. A reasonable compromise in many practical applications is the approximation of  $\eta$  by a rational number with suitable numerator and denominator integers. However, with increasing time (or distance) the error between the desired and the actual sampling position will accumulate and eventually exceed every bound. To overcome this problem an additional approximation is used: After the interpolation (upsampling) of the signal the downsampling is achieved by taking only those samples which lie closest in time (or distance) to the desired sampling instant. This will lead to a non-uniformly resampled signal and will introduce a certain amount of distortion.

Following [41] the inverse of the resampling factor  $\eta$  can be expressed as

$$\frac{1}{\eta} = \frac{d}{U} + \varepsilon \quad (4.10)$$

where  $d$  and  $U$  are positive integers and the approximation error  $\varepsilon$  is limited by

$$0 < \varepsilon < \frac{1}{U}. \quad (4.11)$$

Using this inequality together with 4.10 gives the bounds for the ideal conversion rate

$$\frac{d}{U} < \frac{1}{\eta} < \frac{d+1}{U} \quad (4.12)$$

which represent the upper and lower conversion rates possible by rational approximation.  $U$  corresponds to the interpolation (upsampling) rate and will influence the accuracy of the resampled signal as already indicated by 4.11.

Assuming that the signal has a flat low-pass spectrum with bandwidth  $\omega$ , the distortion introduced by sampling time (position) approximation is computed in the frequency domain. The resulting signal-to-distortion ratio  $R_{SD}$  is found to be

$$R_{SD} = \frac{P_s}{P_e} \geq \frac{12U^2}{\omega^2} \quad (4.13)$$

where  $P_s$  denotes the total power contained in the original signal and  $P_e$  stands for the total error power. From 4.13 it can be seen that the  $R_{SD}$  is proportional to the square of the interpolation

factor  $U$ . Regarding system identification, it is important to note that the sampling position error  $\delta\varepsilon_x$  is bounded by

$$|\delta\varepsilon_x| \leq \frac{0.5}{U} \Delta x \quad (4.14)$$

which is inversely proportional to the interpolation factor.

### 4.1.2 Varying Speed

Varying speed of the measuring cars together with uniform sampling in the spatial domain will result in non-uniformly sampled time signals. The speed of the train  $v(k)$  can be calculated by

$$v(k) = \frac{\Delta x}{\Delta t(k)} = \frac{\Delta x}{t(k) - t(k-1)} \quad (4.15)$$

where  $t(k)$  is the absolute time stamp of each sample and  $\Delta t(k)$  is the time interval between the last and the current sample. Therefore, the time stamp of each sample can be computed recursively by a simple equation

$$t(k) = t(k-1) + \Delta t(k) = t(k-1) + \frac{\Delta x}{v(k)}. \quad (4.16)$$

For constant speed equation 4.16 will be equivalent to 4.2. For varying speed the sampling intervals in the time domain  $\Delta t(k) = \frac{\Delta x}{v(k)}$  will vary indirectly proportional to the local speed. This will cause a nonuniform sampling in the time domain. Therefore, spline or Lagrange interpolation becomes necessary to reconstruct the signal in the time domain in an optimal way. This situation is apparently very similar to resampling with an arbitrary factor. In the former case the ideal sampling instants were uniformly spaced and in the current problem they are spaced depending on the local speed. Nevertheless, in both cases the exact sampling instant of the resampled signal is known and approximated by the closest sampling point of an oversampled signal. The distance  $x(l)$  of the uniformly sampled signal in the time domain with a constant sampling interval of  $\Delta t$  can be written as

$$x(l) = \sum_{m=1}^l v(m) \Delta t, \quad \Delta t = \text{const.} \quad (4.17)$$

which is the counterpart to equation 4.2 for constant speed. Following the reasoning of case 3. in the previous section the sampling instants of the original signal at

$$x(k) = \sum_{m=1}^k \Delta x = k \Delta x, \quad \Delta x = \text{const.} \quad (4.18)$$

are interpolated by a factor of  $U$  giving a signal with the sampling instants at  $x(u)$

$$x(u) = \sum_{m=1}^u \frac{\Delta x}{U} = u \frac{\Delta x}{U}, \quad \Delta x, U = \text{const.} \quad (4.19)$$

From the signal with the sampling instants  $x(u)$  only those are taken which lie closest to the desired sampling instants  $x(l)$ . This guarantees an approximation of the ideal sampling instants  $x(l)$  with an accuracy of at least

$$|\delta\varepsilon_t(l)| \leq \frac{0.5}{U} \frac{\Delta x}{v(l)} \quad (4.20)$$

in the time domain. Note that the accuracy in the time domain is indirectly proportional to the oversampling factor  $U$  but also to the speed  $v(l)$  which makes the upper error bound not any longer constant (compare equation 4.14 for the error bound in the spatial domain).



## 4.2 Data Correlations

Correlation procedures can be mainly found in the world of parallel processing in computer technology. Another area where synchronization is a known keyword is data transmission. Especially in the latter field there exist a multitude of papers which concentrate on correlation methods to synchronize incoming data sequences with a given time base [17]. However, these approaches always assume that some distinct known carrier frequency is present in the incoming signal. Unfortunately there exists no equivalent in the problem at hand.

The crucial part of the synchronization is the determination of a relative local shift. By means of a moving window sections of the input and output signals inside the window are used for the computation of the local shift estimate. This is necessary since the only source of information for correct synchronization are the signals themselves. No additional information on the location of the individual samples is available.

The intuitive way to compare the relative position of two signals with respect to each other is to look for similar features in both signals and evaluate the average shift (delay) between these corresponding features. A quantitative way to do this is the use of cross-correlation functions (CCF), which, when the input is white noise or of sufficiently broad bandwidth, will also give an estimate of the systems impulse response. For the purpose of shift estimation this additional information will not be utilized since the knowledge of the position of a distinct feature of the CCF (a global extreme or a distinct peak) will suffice. The first subsection shortly describes the theoretical background for linear cross-correlations while in the second subsection the advantages and shortcomings of nonlinear correlations are discussed briefly.

### 4.2.1 Linear Correlations

From the physical properties of the vehicle-rail interaction it is quite apparent that correlations between track characteristics and vehicle response are strongest in the vertical direction. While a pure level irregularity should only cause a vertical acceleration, any alignment error will effect the lateral as well as the vertical movement of the vehicle. Moreover, the relation between alignment irregularities and lateral forces is known to be of pronounced nonlinear nature, while the vertical interaction may be modelled by a linearized Hertzian spring. For this reason, the level signals of the track (left and right level signals) and the vertical wheel forces of axle one are used as signals for a linear correlation analysis.

Data for correlation analysis were taken from test run 0006-ad7 (Angern-Drösing), where a straight portion of track selected (samples. 10418:30305 in 0006-ad7 and 25145:74920 in m0006r). Since the nominal sampling interval in track data is 0.25m whereas in vehicle data it is 0.1m, a decimation of both data sets to 0.5m was performed in order to have same nominal sampling rates in both data sets. The straight portion of track was then identified by means of the curvature signal and the bogie twist  $\Psi_I$ , respectively. The straight portion in both resampled data sets was found to lie between samples 5258:15147.

If the input signal  $u(k)$  (profile) and the output signal  $y(k)$  are of finite length  $N$ , the Wiener-Hopf relation

$$R_{yu}(\tau) = \sum_{k=0}^{\infty} g(k)R_{uu}(\tau - k) \quad (4.21)$$

for a linear system with weighting function (impulse response)  $g(k)$  can be rewritten as

$$\hat{R}_{yu}(\tau) = \sum_{k=0}^N \hat{g}(k)\hat{R}_{uu}(\tau - k), \quad (4.22)$$

where only estimates of the covariance functions  $R_{yu}$ ,  $R_{uu}$  and the weighting function  $g(k)$  are present. Furthermore, if the input  $u(k)$  is white noise, the estimate of the auto-covariance function

$\hat{R}_{uu}(\tau)$  becomes the Kronecker  $\delta$ -function weighted with the variance of the input  $\hat{R}_{uu}(0)$  plus a constant offset and the summation is replaced by a single multiplication:

$$\hat{R}_{yu}(\tau) = \hat{g}(k)\hat{R}_{uu}(0) \quad (4.23)$$

This makes the calculation of the weighting function estimate especially easy, since it is just a scaled version of the cross-covariance function estimate  $\hat{R}_{yu}(\tau)$ :

$$\hat{g}(k) = \frac{\hat{R}_{yu}(\tau)}{\hat{R}_{uu}(0)} \quad (4.24)$$

However, if the input is not white noise the relation 4.24 can not be utilized unless an additional prewhitening filter is employed. This filter is designed to use white noise as input and to produce an output which has the same spectral density as the original input  $u(k)$  (usually by modeling the input as an AR-process). Now the assumption of a white input signal holds again and the weighting function of the linear system  $\hat{g}(k)$  can be estimated if both input  $u(k)$  and output  $y(k)$  signals are filtered with the inverse prewhitening filter. In the last step the weighting function estimate  $\hat{g}(k)$  is calculated by again using equation 4.24.

It should be noted that the assumption of linear dependence between  $u(k)$  and  $y(k)$  as well as the performance of the prewhitening filter pose limitations to the practical applicability. On the other hand, if the power spectral density of the input is band-limited but has a sufficiently broad bandwidth, a biased but robust estimate  $\hat{g}(k)$  might be directly computed from equation 4.24 without prewhitening.

For the purpose of synchronizing two time-series an optimal estimate of the weighting function  $g(k)$  is not necessary. Rather, one is interested in a robust procedure for estimating the shift (time-delay) between these signals. The cross-correlation (cross-covariance) function estimate  $\hat{R}_{yu}(\tau)$  over a finite sequence can be used for such a procedure as long as the extrema of  $\hat{R}_{yu}(\tau)$  are well defined and consistent (i.e. a linear time invariant correlation exists and the input is at least piecewise stationary).

## 4.2.2 Nonlinear Correlations

The cross-correlation function is a versatile tool only if the input-output relation is linear in nature or the effects of nonlinearities are small compared to the linear interaction. In the special case of shift estimation there are certain applications where nonlinear correlations prove to be superior. If the relation between input  $u(k)$  and output  $y(k)$  is described by the second-order Volterra model

$$y(k) = \sum_i h(i)u(k-i) + \sum_{i,j} q(i,j)u(k-i)u(k-j) \quad (4.25)$$

the ordinary cross-correlation

$$R_{uy}(i) = E\{u(k)y(k+i)\} \quad (4.26)$$

will only give a biased estimate of the linear kernel  $h(i)$ . In order to get an unbiased estimate of the linear as well as of the quadratic kernel  $q(i,j)$  additional higher-order cross-cumulants have to be used

$$R_{yu_2}(i,j) = E\{y(k)u(k+i)u(k+j)\} \quad (4.27)$$

$$R_{u_3}(i,j,k) = E\{y(k)u(k+i)u(k+j)u(k+l)\}. \quad (4.28)$$

It should be noted that the higher-order cross-cumulants 4.27 and 4.28 are multidimensional ( $n = 2$ , respectively  $n = 3$ ) sequences, and that the listing given above is not complete.

An alternative way would be to build nonlinear combinations of the signals prior to computing only second-order cross-cumulants 4.26. The main problem with nonlinear combinations is that an abundance of possible nonlinearities exists and without a priori knowledge it will be a difficult and lengthy task to find an optimal structure. Nevertheless, higher-order cumulants can be projected into a single index higher-order correlation function

$$R_{y^n u^m}(i) = E\{y^n(k)u^m(k+i)\} \quad (4.29)$$

to find interactions between linear, quadratic, cubic, or even higher-order terms. Again, it becomes a matter of time and endurance up to which order an investigation is carried out. However, rarely will one expect to see a pure fourth-order interaction without the presence of lower-order terms.

Considering the problems of dimensionality and number of signal combinations it is advisable to test all physically meaningful linear combinations of signals as inputs to an ordinary cross-correlation function. Only if this approach gives inconclusive results or fails completely the nonlinear higher-order cumulants should be employed. An exception to this rule is the estimation of time delays in the presence of correlated gaussian noise, but the applications with such a type of signals are few and easily identified.

### 4.3 Calculation of Shift Function Estimate

Using the linear correlations from section 4.2.1 the relative shift between two signals is to be estimated. In this section a local shift estimate is defined which can be used to form an estimate for a shift function.

#### 4.3.1 Basic Principle

When defining the shift between two reasonable similar<sup>2</sup> functions  $f_1$  and  $f_2$  the cross-correlation function

$$R_{xy}(\tau) = E\{f_1(k)f_2(k-\tau)\} = \lim_{N \rightarrow \infty} \frac{1}{N} \sum_{k=0}^{N-1} f_1(k)f_2(k-\tau) \quad (4.30)$$

of the respective functions is a suitable tool. The shift  $s_{12}$  between the functions is then defined as the index of the global maximum

$$s_{12} = \arg \left[ \max_{\tau} |E\{f_1(k)f_2(k-\tau)\}| \right]. \quad (4.31)$$

Obviously, the definition of the expectation operator in equation 4.30 demands infinitely long functions. If this requirement is not met, one can only calculate an estimate of the cross-correlation function. The accuracy of this estimate seems to correlate with the length of the data sequences used. However, this is only true if the shift between the two functions is constant over the entire length. If the shift varies with increasing sampling indices, the formula given in 4.31 will only yield an average value. Again, this average will be more accurate with increasing data length.

If the interest is focussed on a local shift between functions an unsolvable dilemma arises: The more localized the shift will be, the more inaccurate (or even erratic) it will become. This is just the same phenomenon as with the time-frequency duality. As a matter of fact, this duality directly applies to the problem, if the Wiener-Khinchine relation 4.36 is used, which calculates the cross-correlation from the complex cross-spectrum.

---

<sup>2</sup>A quantitative measure for similarity would be the value of the global maximum of the cross-correlation function (correlation coefficient). However, the signal to noise ratio, the bandwidth of the signal as well as of the noise, and existence of at least a partial linear relation between the signals all influence the distinctiveness of the main peak.

In practice, a signal length is chosen which gives sufficiently accurate results for shift, and this shift value is the assigned to the middle of the section used for calculation (moving window). Actually, this value is the estimate of the average shift present in this specific section. In order to get an estimate of a continuous shift function (the shift between two functions calculated for each sample) overlapping segments of the signals (windows) are defined and the shift is repeatedly calculated for each segment.

It should be noted that poor correlations between signals will almost certainly lead to erratic results for the shift between them. Since the correlation might not be constant for the entire sequence, some sections might exist where no meaningful shift can be evaluated. Instead, equation 4.31 will find the index of some maximum value which only coincidentally is the global maximum. This can only be avoided by choosing a larger window or by reducing the range of  $\tau$  to the vicinity of the last meaningful maximum.

### 4.3.2 Calculation of Shift

The most simple and direct approach is to use the cross-correlation estimate inside each window to estimate the shift at the middle of the section under investigation. The calculation of the average shift  $s_{12}$  from 4.31 would therefore be altered to

$$s_{12}(k + \frac{W}{2}) = \arg \left[ \max_{\tau} |E \{f_1(j) f_2(j - \tau)\}| \right], \quad j \in [k, k + W] \quad (4.32)$$

where  $k$  is the index of the samples and  $W$  is the length of the moving window (assumed to be even). Apparently the estimate of the shift function  $s_{12}(k)$  becomes more localized with decreasing window length  $W$ . However, the estimate of the cross-correlation function will become less reliable for short data sequences. A hard limit to the length of the moving window in any case is the actual shift between the two sequences. If the window is chosen smaller than this limit, the resulting shift function will be wrong and most likely erratic.

To calculate the shift between two functions within a window of finite length the Wiener-Khintchine relations with a windowed cross-spectrum can also be used. The window is calculated from the cross-coherence function in order to weight the spectral estimate optimally. This windowed estimate is then transformed into time (spacial) domain giving not only a more accurate result, but inherently smoothing the shift function and avoiding to introduce periodicities with window length.

The Wiener-Khintchine relations form a connection between cross-spectrum  $S_{xy}(f)$  and cross-correlation  $R_{xy}(\tau)$  (continuous-time)

$$S_{xy}(f) = \lim_{T \rightarrow \infty} \frac{1}{T} \bar{X}(f) Y(f) \quad (4.33)$$

$$R_{xy}(\tau) = \lim_{T \rightarrow \infty} \frac{1}{T} \int_0^T x(t) y(t + \tau) dt \quad (4.34)$$

using the Fourier transform. They read as follows [5], [4]:

$$S_{xy}(f) = \int_{-\infty}^{\infty} R_{xy}(\tau) e^{-j2\pi f\tau} d\tau \quad (4.35)$$

$$R_{xy}(\tau) = \int_{-\infty}^{\infty} S_{xy}(f) e^{j2\pi f\tau} d\tau \quad (4.36)$$

The advantage of transforming the problem into frequency domain lies within equation 4.33: The original convolution is substituted by a simple multiplication. If the transformation to and from frequency domain can be efficiently implemented, the calculation of the cross-correlation can be

strongly simplified. Even more important in the case of a comparatively small window is the fact that the cross-coherence function  $\gamma_{xy}^2(f)$  can be readily computed in the frequency domain [5]:

$$\gamma_{xy}^2(f) = \frac{|S_{xy}(f)|^2}{S_{xx}(f)S_{yy}(f)} \quad 0 \leq \gamma_{xy}^2(f) \leq 1 \quad (4.37)$$

The cross-coherence function  $\gamma_{xy}^2(f)$  can be interpreted as a measure for linear dependence at particular frequencies. This is the analogon to the correlation function, which does just the same in the time domain. Thus, it appears to be an important information for smoothing the cross-spectrum in order to reduce the effect of poorly estimated values. However, smoothing the spectrum is equivalent to multiplying a weighting function into the respective correlation function. Whereas this is desirable for the calculation of spectra, it must not be done in order to avoid a biased estimate for the correlation function [4]. In the special case where only the shift between two signals (equation 4.31) is to be estimated, such a biased estimate of the correlation function can in fact be better, since it allows for stronger influence of more coherent frequencies. The real valued weighting function (or window)  $w(f)$  is calculated according to

$$w(f) = \frac{\gamma_{xy}^2(f)}{(1 - \gamma_{xy}^2(f))|S_{xy}(f)|}. \quad (4.38)$$

The shift between two signals inside a predefined window is computed as follows:

1. Compute the Fourier transform for the current section of each signal.
2. Compute the cross- and auto-spectra according to equation 4.33.
3. Compute the cross-coherence function according to equation 4.37.
4. Calculate a windowed cross-spectrum by multiplying the window 4.38 into the original cross-spectrum.
5. Compute the inverse Fourier transform of the windowed cross-spectrum according to equation 4.36, yielding the estimate of the cross-correlation.
6. Find the index of the global absolute maximum of this estimate (equation. 4.31).

This algorithm can then be applied repeatedly to each of the overlapping sections of the two signals, leading to an estimate of the local shift with the restrictions already mentioned above.

Instead of the maximum-likelihood estimate described above any cross-correlation estimate can be used to compute the shift. Especially for short windows the direct implementation of the finite expectation operator

$$\hat{R}_{xy}(\tau) = E \{f_1(k) f_2(k - \tau)\} = \frac{1}{N} \sum_{k=0}^{N-1} f_1(k) f_2(k - \tau) \quad (4.39)$$

can be advantageous since it requires less computational effort than a detour via the complex frequency domain.

Another important issue for the practical application is robustness of the algorithm. There are two important issues which have to be considered:

- The cross-correlation (or ML) estimate computed from the data inside the first window does not necessarily show the same characteristics as the theoretical CCF. Due to the small amount of data and additional noise the peak which forms the real global absolute maximum might be smaller than a neighboring peak.

- The same problem exists for every other windowed estimate along the data set.

Although the above stated problems seem to be identical they fall apart in the way a solution has to be achieved. The second problem can be solved by iteratively storing the old value of the argument  $s_{12}$  at which the maximum occurs and to search only in the vicinity of this argument in the following step. This procedure is equivalent to a smaller adaptive window inside the moving window which always follows the maximum peak. The necessary assumption behind this remedy is that no sudden jumps bigger than half the small adaptive window size will occur in the shift function. When this assumption holds, the algorithm should be able to track the argument of the absolute maximum even if the property of the absolute extreme is replaced by a local extreme. Nevertheless, the algorithm is bound to fail if by chance the first extreme is some insignificant feature of the estimate. In this case it is quite likely that the initial peak will suddenly give way to a strictly monotonous estimate inside the adaptive window which does not identify an extreme. Therefore, it is necessary to ensure that the first extreme which will be consequently tracked is a distinct and marked feature in the estimate.

To find the peak which fulfills these conditions the following initial search can be used: In the beginning a section of data starting at  $k = 1$  and going up to  $k = L$  is used for computation of the estimate, where  $L \gg W$  is a number much bigger than the length of the moving window  $W$ . Since the amount of data has strongly increased the estimate should be more reliable, i.e. the features of the estimate should more closely resemble the average estimate of the moving window. Of course there will be an optimal data length  $W < \infty$  in many cases, due to the fact that for a monotonous shift function an estimate over too long an interval will eventually average out to zero. Assuming the initial interval  $W$  was chosen reasonably the same approach as described above with an adaptive window is utilized to track the most distinctive maximum. The only difference is that the beginning of the moving window is now kept constant at  $k = 1$  and the end point keeps approaching the point  $k = W$ . The window is therefore starting with a size of  $L$  samples and keeps contracting by moving only its end point until it has exactly  $W$  samples. Then the algorithm as described above starts and the window with a fixed length of  $W$  samples moves along the data set.

Another problem is the effect of the window size at start and end of the data. Because the estimate of the shift function corresponds to the middle of the window, no estimates for a length of half the window size exist at beginning and end of data under investigation. A purely cosmetical remedy is to extend available data over the end points by simply repeating it. This leads to a gradual transition of the endings of the shift function when it is computed by cross-correlation, but still gives an abrupt change for the ML-estimate.

## 4.4 Absolute Reference

The inherent problem of even a perfect relative synchronization is that the absolute position of the sampling instants is unknown. Theoretically, it could be possible that both input and output signals are resampled synchronously but with strongly varying sampling intervals. This is equivalent to a frequency modulation of both signals where sampling intervals bigger than the nominal interval mean a shift to higher frequencies while smaller than nominal intervals cause a shift to lower frequencies. For the purpose of a system identification this is certainly undesirable. No matter whether the data comes from a linear time invariant (LTI) or a linear time variant (LTV) system the system parameters of a discrete model will change with the actual sampling interval. Although Tsang and Billing have proposed a method to identify a continuous time model from non-uniformly sampled data [49] their approach is limited to linear continuous time systems. In order to avoid an unacceptable bias in the model parameters it is desirable to compute an estimate of the local absolute shift.

The drawback of removal of a relative shift lies in the fact that simultaneous and equally strong

shifts in both input and output functions are not detected. Although the shift function would be constant in this case, both signals would exhibit the same frequency distortions. This case is not unlikely at all, since both the superstructure testing car and the test object exhibit generic dynamics and run along the same track. Such frequency distortions would of course severely deteriorate any identification approach. Although an iterative algorithm (identification - simulation of output - shift between simulated and actual output - resampling of actual output according to shift) could eventually average out the distortions, it is most likely that for distortions which do not average out to zero a strong bias will remain.

It is therefore desirable to have some information on the frequency distortions (absolute shift) of each signal. In order to compute an estimate the following algorithm is employed: Under the assumption of piecewise stationary input/output signals an AR-model of the local time series is being estimated inside a moving window. The spectral magnitude of this estimate will exhibit more or less distinct peaks for the data under investigation. The most distinct peaks can be designated and consequently their frequency is tracked along all estimates inside the moving window. Therefore, for each peak an estimate of an absolute shift function is computed. The average of these shift functions is regarded as an estimate of the absolute shift of the signal. It should be noted, that the AR-model will not only reflect changes in sampling frequency due to wheel slippage but also changes in the signal characteristics which are existent in reality. That is, if the assumption of stationarity is not holding, the results will be severely biased. This shortcoming of the approach is especially important, since the wheel slippage and the change of track (and therefore of the response) characteristics is likely to occur at the same sections, primarily curve transitions.

This algorithm can be applied to both input and output signals. For the estimates of absolute and relative shift to be consistent, the first derivative of the relative shift must be proportional to the difference between the absolute shifts. This can be derived as follows: The undistorted input  $u(k\Delta x)$  and output  $y(k\Delta x)$  signals are distorted by a varying dimensionless shift (or phase) function  $\sigma_i(k) \in \Re$

$$u_d(k) = u(k[\Delta x + \sigma_u(k)\Delta x]) = u(k[1 + \sigma_u(k)]\Delta x) \quad (4.40)$$

$$y_d(k) = y(k[\Delta x + \sigma_y(k)\Delta x]) = y(k[1 + \sigma_y(k)]\Delta x), \quad (4.41)$$

where  $u_d(k)$  and  $y_d(k)$  denote the distorted (frequency modulated) signals. It is important to observe that the absolute shift functions  $\sigma_i(k)$  actually cause a frequency shift rather than a time shift. This fact can be illustrated by substitution in equations 4.40 and 4.41

$$f_d(k) = f(k[1 + \sigma(k)]\Delta x) = f(k\Delta x_d(k)), \quad (4.42)$$

where the new sampling interval is denoted by  $\Delta x_d(k)$ . In the case of a constant absolute shift function  $\sigma(k) = \sigma \neq 0$ , the original function  $f(k)$  is uniformly sampled at a new sampling interval of length  $\Delta x_d = (1 + \sigma)\Delta x \neq \Delta x$ . The sampling frequency  $\omega_{sd}$  of the distorted signal  $f_d(k)$  will now be  $\omega_{sd} = \omega_s \frac{1}{1 + \sigma}$ , compared to the original sampling frequency  $\omega_s$  of  $f(k)$ . If the shift  $\sigma$  is unknown and therefore a constant original sampling interval  $\Delta x$  is being assumed, the dimensionless frequencies  $\omega_{d0}$  of the distorted signal become  $\omega_{d0} = \frac{\omega}{\omega_{sd}}$  instead of their correct value of  $\omega_0 = \frac{\omega}{\omega_s}$ . Clearly,  $\omega_{d0} = \omega_0 \frac{\omega_s}{\omega_{sd}} = \omega_0 \frac{1 + \sigma}{1}$ , where for  $\sigma > 0$  the distorted frequency  $\omega_{d0}$  is higher than the actual  $\omega_0$ .

Assuming that  $u(k)$  is a piecewise stationary signal and the output  $y(k)$  is generated by a linear time invariant (LTI) system  $G(z)$ , where in the discrete frequency domain

$$Y(z) = G(z)U(z) \quad (4.43)$$

holds, the output  $y(k)$  is also a piecewise stationary signal, as long as  $G(z)$  does not have integral behavior. The latter condition is satisfied for all signal pairs under consideration, moreover, most

of them show differential behavior. Another assumption is that of zero mean for the shift functions  $\sigma_i(k)$ :

$$\bar{\sigma}_i = \frac{1}{N} \sum_{k=1}^N \sigma_i(k) = 0 \quad (4.44)$$

The AR estimates of input and output signals inside a moving window will yield polynomials  $A_i(q^{-1}, k)$  which in turn have distinctive root locations. If the corresponding wavelengths  $\lambda_{ij}(k)$  (inverse frequencies) of these roots are represented by multiples  $\eta_{ij}(k)$  of sampling instants  $\Delta x$  a unique mapping is established. The order  $n$  of the AR model has to be chosen carefully to avoid erratic results for overmodelling or an insensitive algorithm for too small models. The functions of the wavelengths of each root depending on the position  $k$  of the moving window (argument at the middle of the current window) can be denoted as

$$\lambda_{uj}(k) = \eta_{uj}(k) \Delta x, \quad \eta_{uj} \in \Re \quad (4.45)$$

$$\lambda_{yj}(k) = \eta_{yj}(k) \Delta x, \quad \eta_{yj} \in \Re. \quad (4.46)$$

The mean values computed over all multiples  $\eta_{ij}(k)$  at each sampling instant  $k$

$$\bar{\eta}_i(k) = \frac{1}{n} \sum_{j=1}^n \eta_{ij}(k) \quad (4.47)$$

serve as the basis for an estimate of the shift functions  $\sigma_i(k)$ . Because of the assumption 4.44 only the mean value has to be removed from 4.47 in order to get an estimate without offset

$$\hat{\sigma}_i(k) = \bar{\eta}_i(k) - \frac{1}{N} \sum_{k=1}^N \bar{\eta}_i(k). \quad (4.48)$$

The assumption of zero mean for the shift function 4.44 is not true if the nominal sampling interval differs from the actual one. In this case a constant absolute shift function is present for that signal, which will lead to a linear relative shift between signals. However, there is no way to determine this constant bias without a priori knowledge, so it is omitted altogether in the algorithm.

No assumptions on the length of the moving window and the bandwidth of the shift functions  $\sigma_i(k)$  have been made here. Nevertheless, it is clear that the moving window incorporates a low-pass characteristic and the approach described above will not be able to capture high-frequency modulations. The presence of uncorrelated noise will not change the results given here because of the linear nature of all parts of the algorithm. The window size and ultimately the performance of the entire algorithm, however, will strongly depend on the signal to noise ratio. Another important feature is the fact that the estimate  $\hat{\sigma}_i(k)$  is an average over the local shift function  $\sigma_i(l)$  (the argument  $l$  running only inside the moving window).

## 4.5 Properties of Relative Shift Estimate

In this section the results given above are extended to establish the properties of the shift function estimate computed by cross-correlation inside a moving window. The following notations are introduced: The estimate  $\hat{s}_{uy}^0(k)$  which calculates the cross-correlation function between input  $u(k)$  and output  $y(k)$  inside a moving window and gives the argument at which the absolute maximum occurs is denoted by

$$\hat{s}_{uy}^0(k) = \arg \left[ \max_{\tau} |E \{u(l) y(l - \tau)\}| \right] = \arg \left[ \max_{\tau} |R_{uy}(\tau)| \right]. \quad (4.49)$$



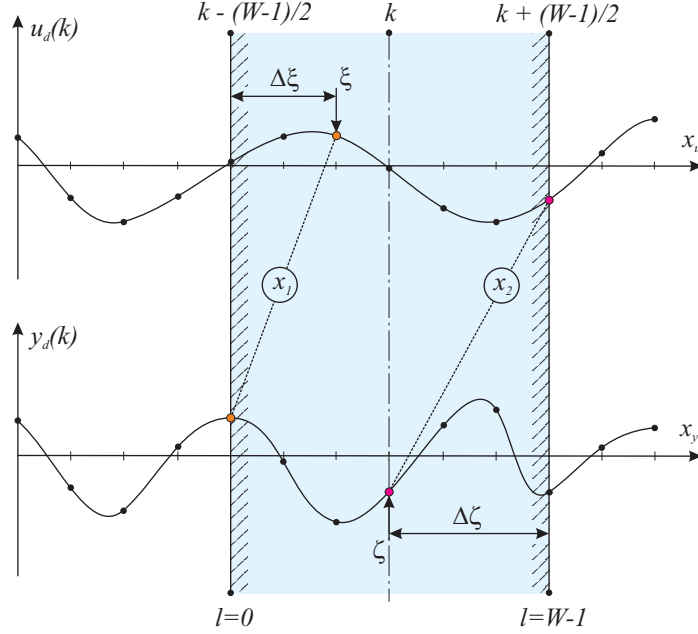


Abbildung 4.1: *Moving window for correlation analysis: Distorted abscissae. Input signal  $u_d$  and output signal  $y_d$  are plotted over normalized  $x$ -axis. Each axis is normalized by the respective sampling interval.*

The argument  $l$  counts the samples inside the moving window, whereas the argument  $k$  denotes the absolute position of samples. The local counter  $l$  is defined by

$$l = k - \frac{W-1}{2} + j, \quad j = 0, 1, 2, 3, \dots, W-1 \quad (4.50)$$

where  $W$  is the window size in samples. The estimate of the relative shift  $\hat{s}_{uy}^0(k)$  corresponds to the argument  $k$  at the middle of the moving window. In figure 4.1 both input and output signals are depicted with normalized sampling intervals. Note that the abscissas (denoting the individual distances) have different units so that each sampling instant in one signal is assigned to a distinct counterpart in the other signal. The correct assignment is indicated by the absolute coordinates  $x_1$  and  $x_2$ , respectively. In figure 4.2 an absolute abscissa is used for both signals. Now it becomes apparent that the samples which are assigned to each other actually come to lie at different positions. In general, only an approximate assignment between closest samples will be possible as indicated by triangular and circular markers for absolute coordinates  $x_1$  and  $x_2$ . Because of the assumption of stationarity the mean value of the  $\hat{s}_{uy}^0(k)$  is some constant value  $S_{uy}$

$$E \{ \hat{s}_{uy}^0(k) \} = E \left\{ \arg \left[ \max_{\tau} |R_{uy}(\tau)| \right] \right\} = S_{uy}, \quad (4.51)$$

which stands for a constant shift between the two signals (like introduced by a dead time due to filtering). If absolute shift functions  $\sigma_i(k)$  are present in both signals, the estimate of the relative shift will be altered to

$$\hat{s}_{uy}(k) = \arg \left[ \max_{\tau} \left| E \{ u(l[1 + \sigma_u(l) + S_u(l=0)] \Delta x) y(l[1 + \sigma_y(l) + S_y(l=0)] \Delta x - \tau) \} \right| \right], \quad (4.52)$$

where the total absolute shift at the first sample of the window is  $S_i$  calculated according to 4.65 by

$$S_i(k) = \sum_{j=1}^k \sigma_i(j) \quad (4.53)$$

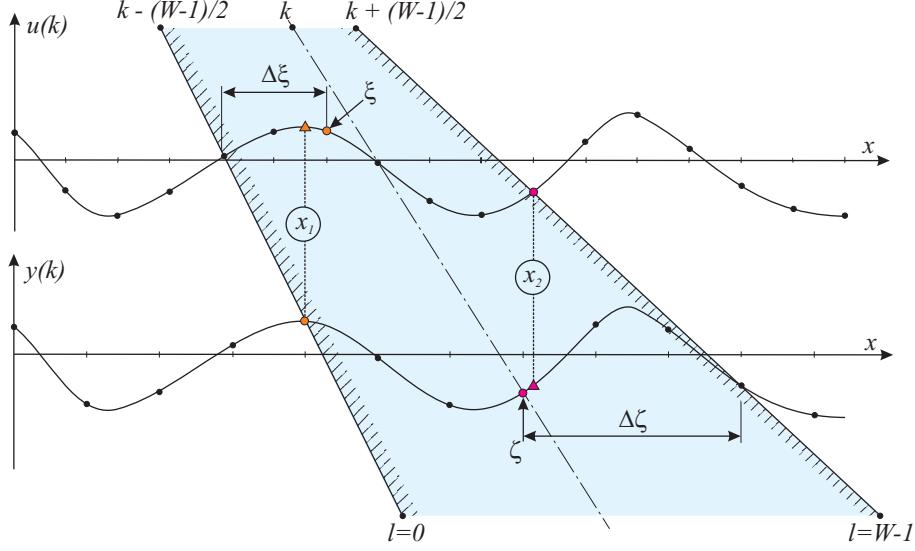


Abbildung 4.2: *Moving window for correlation analysis: Absolute abscissae. Input signal  $u_d$  and output signal  $y_d$  are plotted with their actual sampling intervals.*

Because the estimate of the absolute shift  $\hat{\sigma}_i(k)$  is an average over the window length and the expectation operator also averages over the window length, the absolute shift functions  $\sigma_i(l)$  inside the moving window may be replaced by their respective estimates at the window position:

$$\hat{s}_{uy}(k) = \arg \left[ \max_{\tau} |E \{ u(l [1 + \hat{\sigma}_u(k) + S_u(l=0)] \Delta x) y(l [1 + \hat{\sigma}_y(k) + S_y(l=0)] \Delta x - \tau) \}| \right] \quad (4.54)$$

Note that the  $\hat{\sigma}_i(k)$  in 4.54 no longer depend on the local argument  $l$  but rather can be regarded as constants inside the expectation operation. Therefore, a constant has been added to the sampling intervals of both signals inside the window as already shown in 4.42. The mean value of the  $\hat{s}_{uy}(k)$  is still the same constant value  $S_{uy}$  because of the assumption of zero mean for the shift functions  $\sigma_i(k)$  (see equation 4.44)

$$E \{ \hat{s}_{uy}(k) \} = E \left\{ \arg \left[ \max_{\tau} |R_{uy}(\tau)| \right] \right\} = S_{uy}, \quad (4.55)$$

which characterizes a constant shift between the two signals.

If we assume without loss of generality that the output lags behind the input, as depicted in figure 4.1, ( $0 < S_u(l=0) < S_y(l=0)$ ) and that  $0 < \hat{\sigma}_u(k) < \hat{\sigma}_y(k)$ , the arguments of the overlapping sections of the signals inside the window can be found by the following considerations. The absolute position  $x_1$  of the first sample of the window at  $k - \frac{W-1}{2}$  will be described by the output function since it lags behind the input:

$$x_1 = \Delta x \sum_{j=1}^{k - \frac{W-1}{2}} [1 + \sigma_y(j)] \quad (4.56)$$

The same absolute position  $x_1$  can also be described by the input function

$$x_1 = \Delta x \sum_{j=1}^{\xi} [1 + \sigma_u(j)], \quad (4.57)$$

thus leading to a nonlinear equation for the argument  $\xi \in \mathbb{N}^+$ , which corresponds to the absolute

position  $x_1$ :

$$\sum_{j=1}^{k-\frac{W-1}{2}} [1 + \sigma_y(j)] = \sum_{j=1}^{\xi} [1 + \sigma_u(j)] \quad (4.58)$$

which can be rewritten as

$$\sum_{j=1}^{k-\frac{W-1}{2}} [1 + \sigma_y(j)] = \frac{\xi(\xi+1)}{2} + \sum_{j=1}^{\xi} \sigma_u(j). \quad (4.59)$$

Since  $|\sigma_i(k)| \ll 1$  (wheel slippage between sampling instants is assumed to be much smaller than sampling intervals), the right hand side of equation 4.59 will be a strictly monotonous function in  $\xi$ . This guarantees a unique solution which, however, will have to be approximate since the  $\sigma_i(k)$  can assume continuous values, while  $\xi$  is quantized by definition. Thus, the sample  $k - \frac{W-1}{2}$  of the output function and the sample  $\xi$  of the input function correspond approximately to the same absolute position  $x_1$ . The same reasoning for the last sample of the window gives the equation

$$\sum_{j=1}^{k+\frac{W-1}{2}} [1 + \sigma_u(j)] = \frac{\zeta(\zeta+1)}{2} + \sum_{j=1}^{\zeta} \sigma_y(j), \quad (4.60)$$

where  $k + \frac{W-1}{2}$  is the sample of the input function which corresponds to the sample  $\zeta$  of the output function.

The nonlinear equations 4.59 and 4.60 can be linearized if the shift function inside the window is assumed to be constant (see equation 4.54). This step is problematic since the constant shift  $\hat{\sigma}_i(k)$  is computed over the entire window length and will in general differ from the average shift on the section it is applied to here. However, if the window size is small compared to the bandwidth of the shift function  $\sigma_i(k)$  the errors will be small. The linearized version of equation 4.59 is

$$\sum_{j=1}^{k-\frac{W-1}{2}} [1 + \sigma_y(j)] = \sum_{j=1}^{k-\frac{W-1}{2}} [1 + \sigma_u(j)] + \sum_{j=1}^{\Delta\xi} \underbrace{[1 + \hat{\sigma}_u(k)]}_{\text{constant}} = \sum_{j=1}^{k-\frac{W-1}{2}} [1 + \sigma_u(j)] + \Delta\xi [1 + \hat{\sigma}_u(k)], \quad (4.61)$$

which can be rearranged to give the approximate solution

$$\Delta\xi = \frac{1}{[1 + \hat{\sigma}_u(k)]} \left\{ \sum_{j=1}^{k-\frac{W-1}{2}} [1 + \sigma_y(j)] - \sum_{j=1}^{k-\frac{W-1}{2}} [1 + \sigma_u(j)] \right\}. \quad (4.62)$$

The difference in the braces is the shift between input and output functions right after  $k - \frac{W-1}{2}$  samples. It should equal the term  $\Delta\xi [1 + \hat{\sigma}_u(k)]$  in equation 4.61, which in turn defines the unknown parameter  $\Delta\xi$ . The linearized result for equation 4.60 follows immediately:

$$\begin{aligned} \sum_{j=1}^{k+\frac{W-1}{2}} [1 + \sigma_u(j)] &= \sum_{j=1}^{k+\frac{W-1}{2}} [1 + \sigma_y(j)] - \sum_{j=1}^{\Delta\zeta} \underbrace{[1 + \hat{\sigma}_y(k)]}_{\text{constant}} = \sum_{j=1}^{k+\frac{W-1}{2}} [1 + \sigma_y(j)] - \Delta\zeta [1 + \hat{\sigma}_y(k)] \\ \Delta\zeta &= \frac{1}{[1 + \hat{\sigma}_y(k)]} \left\{ \sum_{j=1}^{k+\frac{W-1}{2}} [1 + \sigma_y(j)] - \sum_{j=1}^{k+\frac{W-1}{2}} [1 + \sigma_u(j)] \right\} \end{aligned} \quad (4.63)$$

The shift at the beginning of the overlapping signal sections has therefore been determined to be  $\Delta\xi$  samples, while at the end of this section it is  $\Delta\zeta$  samples. Since these results were achieved

under the assumption that the shift functions  $\hat{\sigma}_i(k)$  are constant inside the window, the absolute shift between the two signals is linear, and the average shift as detected by the estimate  $\hat{s}_{uy}(k)$  from equation 4.54 is approximately the arithmetic mean of the two extremes from the borders of the overlapping section:

$$\hat{s}_{uy}(k) \cong \frac{\Delta\xi + \Delta\zeta}{2} \quad (4.64)$$

The resulting frequency shift causes a compression of the signals in time domain for positive  $\hat{\sigma}_i(k)$  and an expansion for negative  $\hat{\sigma}_i(k)$ . The extent of this distortion for each signal in the time domain depends upon two parameters: First, the absolute shift  $\sigma_i(k)$  of the individual signal determines the local contribution, but equally important is the cumulative effect of the shift in the time domain, i.e. the present relative shift between signals at a given sample depends on how the signals were absolutely shifted all the way to the sample under consideration. Obviously, the sum of the difference of all local distortions of each signal together with the constant  $S_{uy}$  (equation 4.51) gives the relative shift at a given sample:

$$s_{uy}(k) = \sum_{j=1}^k [\sigma_y(j)\Delta x - \sigma_u(j)\Delta x] + S_{uy} = \Delta x \sum_{j=1}^k [\sigma_y(j) - \sigma_u(j)] + S_{uy} \quad (4.65)$$

Equation 4.65 states the relationship between actual absolute and relative shift functions. Since the estimates of the absolute shift function have zero mean by definition (see equation 4.48), the ideal relation 4.65 will not hold if estimates of the absolute shifts are inserted. Nevertheless, the error introduced by inserting estimates instead of actual functions will be a purely linear function in  $k$ . This can be seen by splitting the actual absolute shift functions in their constant means  $\bar{\sigma}_i$  and the respective variation  $\sigma_i^0(k)$ :

$$\sigma_i(k) = \bar{\sigma}_i + \sigma_i^0(k) \quad (4.66)$$

Inserting 4.66 in 4.65 yields

$$s_{uy}(k) = \Delta x \sum_{j=1}^k [\sigma_y^0(j) - \sigma_u^0(j) + \bar{\sigma}_y - \bar{\sigma}_u] + S_{uy} = \Delta x \sum_{j=1}^k [\sigma_y^0(j) - \sigma_u^0(j)] + \Delta x [\bar{\sigma}_y - \bar{\sigma}_u] k + S_{uy}. \quad (4.67)$$

Inserting the estimates of the absolute shift functions obtained by 4.48, where due to the zero-mean property

$$\hat{\sigma}_i(k) = \hat{\sigma}_i^0(k) \quad (4.68)$$

holds, will yield a similar expression

$$\tilde{s}_{uy}(k) = \Delta x \sum_{j=1}^k [\hat{\sigma}_y^0(j) - \hat{\sigma}_u^0(j)] + S_{uy} \quad (4.69)$$

which otherwise lacks the linear term. Apparently, if we have unbiased and consistent estimates  $\hat{\sigma}_i(k)$  we can at best get a biased estimate 4.69, with the error being a purely linear function

$$e_s(k) = s_{uy}(k) - \tilde{s}_{uy}(k) = \Delta x [\bar{\sigma}_y - \bar{\sigma}_u] k. \quad (4.70)$$

Nevertheless, this condition can be used as a validation of the absolute shift functions. On the other hand, if the relative shift is constant or zero (meaning that the absolute shift functions are parallel or identical) both input and output signals should be resampled according to their absolute shift.

## 4.6 Model Based Synchronization

The only assumption necessary for the method outlined in section 4.3 was the existence of a linear (or at least partly linear) correlation between input and output signals. The estimate of the relative shift involves a search for the global extreme of the CCF estimate. Obviously, the maximum allowable relative shift to be detected can get as big as the value of  $\tau_{\max}$  (the maximum shift of the CCF estimate) which can be easily adjusted. The trade-off for this fairly simple and robust approach is a very limited resolution of the relative shift function with respect to the spatial axis. The size of the moving window can typically not be reduced to less than 500m (1024 samples at  $\Delta x = 0.5m$ ) which in turn does not allow for a more localized estimate of the shift. Smaller windows with fewer samples may allow for sufficiently distinct CCF estimates but not for all sections of the track.

From a system identification point of view the CCF-estimate without a prewhitening filter is a biased nonparametric estimate of a linear model. Since we have a finite input/output sequence with quite a small number of samples inside each window the accuracy of the CCF-estimate will deteriorate quickly with shrinking window size. The same is true for a parametric linear estimate. If, however, a parametric linear model is identified using all data points available, a consistent estimate can be expected if the shift between input  $y(k)$  and output  $u(k)$  is constant in average, i.e. a linear trend as imposed by slightly differing sampling intervals must be removed prior to identification. A possible choice of a linear model would be the output-error (OE) model

$$y(k) = \frac{B(q^{-1})}{F(q^{-1})}u(k-d) + e(k) \quad (4.71)$$

where  $B(q^{-1})$  and  $F(q^{-1})$  are the numerator respectively denominator polynomials and  $q^{-1}$  is the unit shift operator. An existing dead time  $t_d$  between input and output is approximated by multiples of the sampling interval

$$t_d \approx d \Delta T. \quad (4.72)$$

The noise  $e(k)$  is assumed to be statistically independent white noise with

$$\begin{aligned} E\{e(k)\} &= 0 \\ E\{e(k)e(k+\tau)\} &= \sigma_e^2 \delta_0(\tau). \end{aligned} \quad (4.73)$$

The OE model can be interpreted as a special case of the ARMAX model

$$y(k) = \frac{B(q^{-1})}{A(q^{-1})}u(k-d) + \frac{C(q^{-1})}{A(q^{-1})}e(k) \quad (4.74)$$

where

$$A(q^{-1}) = C(q^{-1}) = F(q^{-1}). \quad (4.75)$$

The linear model of choice should then be able to capture the system dynamics "in average". To explain this assumption we will consider the influence of different sampling rates on the identified model 4.71.

We assume that uniformly sampled data of a sampling interval  $\Delta x$  are available for input  $y(k)$  and output  $u(k)$  of a deterministic LTI system which has a continuous transfer function  $G(s)$  of the form

$$Y(s) = G(s)U(s)e^{-st_d} = \frac{M(s)}{N(s)}U(s)e^{-st_d}. \quad (4.76)$$

No measurement or system noise shall be present in the sampled data. The poles  $n_i(s)$  and zeros  $m_i(s)$  (the roots of denominator and numerator polynomials) of system 4.76 are of the form

$$s = -\zeta\omega_n + j\omega_d = -\zeta\omega_n + j\omega_n\sqrt{1-\zeta^2} \quad (4.77)$$

and assumed to be known exactly. Using the sampled input/output data any unbiased identification algorithm will yield a discrete transfer function  $G(z)$

$$Y(z) = G(z)U(z) z^{-d} = \frac{M(z)}{N(z)}U(z) z^{-d} \quad (4.78)$$

where the dead time (right shift)  $d$  is derived according to equation 4.72 which is assumed to be exact in this case. The poles  $n_i(z)$  and zeros  $m_i(z)$  of the discrete model 4.78 are related to their continuous counterparts according to the z-transform by

$$z = e^{s\Delta x} = e^{-\zeta\omega_n\Delta x + j\omega_d\Delta x}, \quad (4.79)$$

where  $\omega_n$  can be substituted to give

$$z(\Delta x) = \exp\left[-\frac{\zeta\omega_d}{\sqrt{1-\zeta^2}}\Delta x + j\omega_d\Delta x\right] = \exp\left[\Delta x\left(-\frac{\zeta\omega_d}{\sqrt{1-\zeta^2}} + j\omega_d\right)\right]. \quad (4.80)$$

Equation 4.80 states that the locations of the poles and zeros of the discrete model show a direct dependence on the sampling interval  $\Delta x$ . Moreover, the mapping defined in equation 4.80 represents a diffeomorphism with respect to the variable  $\Delta x$ . This means that a continuous variation of the sampling interval will cause an also continuous variation in the location of the discrete poles and zeros. The coefficients of the real valued polynomials  $N(z)$  and  $M(z)$  will reflect these variations accordingly, i.e. also continuously. Therefore, an identification algorithm like the LS-method, which estimates the polynomial coefficients by minimizing a prediction error criterion, will yield an averaged result over these variations.

An identified LTI model derived from data with varying sampling intervals

$$\hat{y}(k) = \frac{\hat{B}(q^{-1})}{\hat{F}(q^{-1})}u(k-d) \quad (4.81)$$

can be used to give a simulated output  $\hat{y}(k)$  from the measured input  $u(k)$ , which, by definition, will not show a varying shift relative to the input<sup>3</sup>. This implies that the simulated output  $\hat{y}(k)$  will exhibit exactly the same nonlinear shift relative to the measured output  $y(k)$  inside a moving window as the measured input does:

$$\hat{s}_{uy}(k) = \arg\left[\max_{\tau} |E\{u(l)y(l-\tau)\}|\right] \quad (4.82)$$

To estimate this relative shift 4.82 we can now use the simulated and measured output signals for the linear correlation analysis:

$$\hat{s}_{\hat{y}y}(k) = \arg\left[\max_{\tau} |E\{\hat{y}(l)y(l-\tau)\}|\right] = \hat{s}_{uy}(k) \quad (4.83)$$

Ideally, the cross correlation function estimates for  $\hat{y}(k)$  and

$$R_{\hat{y}y}(\tau) = E\{\hat{y}(l)y(l-\tau)\} \quad (4.84)$$

will be identical to the auto correlation function estimate of the simulated output

$$R_{\hat{y}\hat{y}}(\tau) = E\{\hat{y}(l)\hat{y}(l-\tau)\} \quad (4.85)$$

---

<sup>3</sup>A constant shift like a dead time between input and output was already taken care of by shifting the arguments of the input (see equation 4.71). Therefore, for each shift estimate inside the moving window  $\hat{s}_{u\hat{y}}(k) = \arg\left[\max_{\tau} |E\{u(l)\hat{y}(l-\tau)\}|\right] = c$  where  $c = const.$  holds.

since the measured output would equal the simulated output plus uncorrelated white noise

$$y(k) = \hat{y}(k) + e(k) \quad (4.86)$$

it follows that

$$\begin{aligned} R_{\hat{y}y}(\tau) &= E\{\hat{y}(l)y(l-\tau)\} = E\{\hat{y}(l)[\hat{y}(l-\tau) + e(l-\tau)]\} = \\ &= E\{\hat{y}(l)\hat{y}(l-\tau) + \hat{y}(l)e(l-\tau)\} = E\{\hat{y}(l)\hat{y}(l-\tau)\} + 0 = R_{\hat{y}\hat{y}}(\tau). \end{aligned} \quad (4.87)$$

For sufficiently broad-bandwidth input the CCF-estimate between  $\hat{y}(k)$  and  $y(k)$  will have a very distinct and dominant extreme at  $\tau = 0$ . In this application, the peak will be of a much more slender shape and therefore more easy to detect. Therefore, a smaller length of the moving window becomes possible. Furthermore, the shift function  $\hat{s}_{\hat{y}y}(k)$  4.83 will vary around a fixed value which can be easily adjusted to be zero. This ensures maximum confidence in the shift estimate<sup>4</sup> and indicates the quality of the relative shift (compression or expansion) already by sign.

Once a linear trend in the relative shift between input  $u(k)$  and output  $y(k)$  is removed this model based shift estimation can be applied iteratively to ensure optimal performance. This could become necessary since we assumed that the LTI model 4.81 is accurate at least on average. However, if the model is biased the predicted output  $\hat{y}(k)$  will not any longer satisfy equation 4.86 and therefore the identity 4.86 will not hold. Nevertheless, as long as the error between predicted output  $\hat{y}(k)$  and actual output  $y(k)$  does not become too large, the generic shape of the cross correlation estimate will not change. And as long as a sufficiently consistent and distinct global extreme of the CCF-estimate can be detected a consistent shift estimate is possible. This shift estimate can be used to either resample the actual input  $u(k)$  or output  $y(k)$ , respectively. Since the variation in shift has been reduced in that step the next identification will yield a more accurate model and output prediction. Eventually, the reduction of the variance of the shift function will come to a halt and the input/output synchronization can be regarded as complete.

There are two shortcomings to this approach: Firstly, the maximum allowable values of the shift between input and output for a consistent linear identification are not known. Secondly, the removal of a linear trend in the shift function is necessary prior to applying the identification. Therefore, a shift function estimate has to be computed by some alternate procedure in the first place. Fortunately, the removal of the linear trend does not require a highly resolved shift function. Even a rough estimate given by the CCF estimate of input/output signals is sufficient. Although the analytical solution to the first problem is not known, the nonlinear variations in the shift function after removal of a linear trend seem to pose no problems for the identification in this special application.

## 4.7 Simulation Results

### 4.7.1 Relative Shift

Data for simulation were prepared in the following way: The signal consisting of differences of level signals sampled at an interval of  $= 0.5m$  was taken as input  $u(k)$ . It is assumed in the following that this geometric track signal is free of any distortions and jitter except for additional white noise. The corresponding output signal  $y(k)$  is the difference of  $Q$ -forces at axle 1. It is computed as the output of the Box-Jenkins model

$$y(k) = \frac{A(q^{-1})}{F(q^{-1})}u(k) + \frac{C(q^{-1})}{D(q^{-1})}e(k) = G_s(q^{-1})u(k) + G_n(q^{-1})e(k), \quad (4.88)$$

---

<sup>4</sup>Since the cross correlation estimates are computed with finite data sequences there are more data points available for the estimates closer to zero shift ( $\tau = 0$ ). The extremes are  $\tau = 0$  where all data pairs are used, and  $\tau = \tau_{\max}$  at half the sample size where only a single data pair remains.

Transfer Function	Zeros	Poles	Gain
System $G_s(z)$	$-0.79 \pm j 0.66$	$-0.14 \pm j 0.98$	0.0587
	$-0.16 \pm j 1.08$	$0.21 \pm j 0.83$	
	$0.39 \pm j 0.85$	$0.97 \pm j 0.10$	
	1.01	$0.53 \pm j 0.53$	
	0.96		
Noise $G_n(z)$	$-0.96 \pm j 0.15$	$-0.06 \pm j 0.78$	36.5
	$-0.79 \pm j 0.66$	0.93	

Tabelle 4.1: Poles, zeros, and gain for 8th-order Box-Jenkins model from filtered data (3rd-order noise model).

with  $u(k)$  and the gaussian random noise  $e(k)$  as input. The system transfer function  $G_s(z)$  and the noise filter  $G_n(z)$  were determined by identification from measured and synchronized data. The respective zeros, poles, and gains are listed in table 4.1. In addition to the noisy output a noise free simulation was also performed. An additional constant shift of 10 samples (dead time) was introduced between  $u(k)$  and  $y(k)$ . The relative shift function  $s(k)$  was constructed by low-pass filtering gaussian noise and subtracting the mean value.

The abscissa of all signals is equal to the distance giving the absolute position of each instant by

$$x(k) = k \Delta x. \quad (4.89)$$

By normalizing the distance values of each sampling instant with the sampling interval we get sampling instants at each integer number:

$$x_0(k) = \frac{k \Delta x}{\Delta x} = k \quad (4.90)$$

Since the relative shift function  $s(k)$  is already scaled in samples, the samples of the shifted input  $\tilde{u}(k)$  come to lie at

$$\tilde{x}_0(k) = k + s(k) \quad (4.91)$$

along the dimensionless abscissa which corresponds to the absolute distance of

$$\tilde{x}(k) = [k + s(k)] \Delta x. \quad (4.92)$$

Due to the zero mean property of  $s(k)$  the overall average shift will not be altered. The resampling of the original input  $u(k)$  at the new sampling locations  $\tilde{x}_0(k)$  is done by cubic spline interpolation (see appendix D for details). The actual shift function  $s(k)$  (black), and the estimates of the relative shift  $\hat{s}(k)$  (red for noise free output and blue for noisy output) can be seen in figure 4.3. Both estimates are in good agreement with the actual shift although the window used for the computation of the cross-correlation function was only 150 samples long. By applying the resampling method outlined earlier the shift can be partially removed from the distorted input signal  $\tilde{u}(k)$  leading to an estimated restored input  $\hat{u}(k)$ . An identification with an OE model of order 6/6 is performed with both signal pairs  $u(k)/y(k)$  and  $\hat{u}(k)/y(k)$ , respectively. The best fit for the model identified with original signals is 2.44 while for the model with the restored input it is 2.58. The square-root of the sum squared error between the two simulated outputs is 0.93 while the quadratic mean of the actual output (without noise) is 9.1. These numbers indicate that a relative error of approximately 10% will occur with the present model structure. However, this error can be decreased by applying a low-pass filter to the shift estimates and using a more complex model.



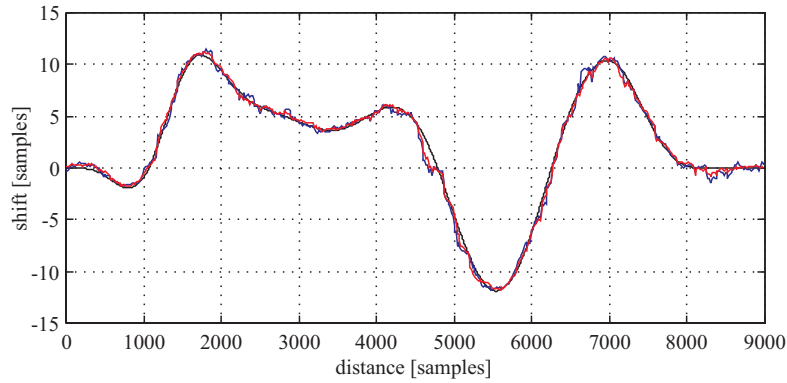


Abbildung 4.3: *Relative shift functions from simulated data. Actual shift (black), shift estimate with ideal output (red), and shift estimate with noisy output (blue).*

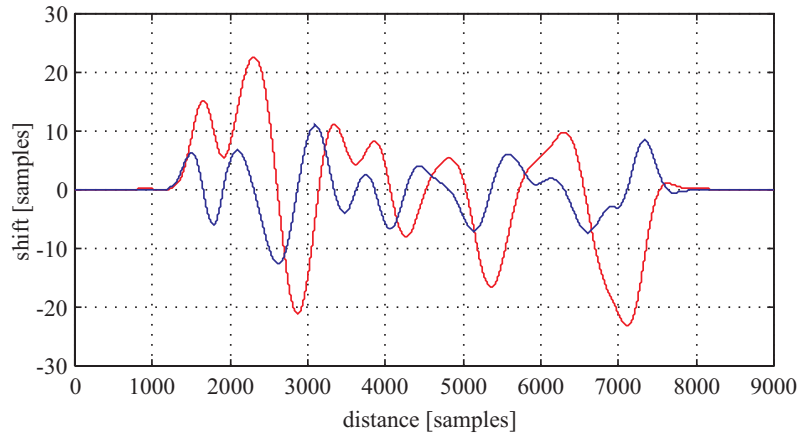


Abbildung 4.4: *Absolute shift function (red) and difference of absolute shift (blue)*

## 4.7.2 Absolute Shift

An investigation of the absolute shift estimate according to section 4.4 reveals that the poles of the AR model do not change their natural frequencies in a similar way. Rather, some poles stay largely unaffected by an absolute shift while others react strong but also erratically. This behavior is partly explained by the presence of strong signal attenuations outside the pass-band which are also modelled by some poles. To demonstrate these effects the simulated output from a 6th-order Box-Jenkins model for difference of  $Q$ -forces with band limited cant (difference of level signals) as input is used as a test signal. The estimates of the natural frequencies of an 5th-order AR-model are depicted in figure 4.7. Since a moving window with a length of 512 samples has been used there are strong transitional effects at the first and last 256 points of the estimate. The y-axis denotes the relative difference in sampling intervals which is equivalent to a frequency shift. For the original undistorted data the sampling intervals have been constant throughout the entire signal and the estimates therefore show a certain bandwidth around 0. By introducing a known shift to the original function the actual sensitivity of this approach may be evaluated. The shift function is designed as an increase in sample size from samples 3001 to 5000 followed by a corresponding decrease between samples 5001 to 7000. The remainder of the signal stays unaffected. Three shifted signals with different amounts of shift applied are generated. The actual sampling intervals after the shift has been applied by cubic spline interpolation are plotted in figure 4.8. The nominal sampling size is  $\Delta x = 0.5m$  while the shifted sections show an increase or decrease of  $\Delta x_s = \pm 0.05m$ ,  $\pm 0.1m$ , and

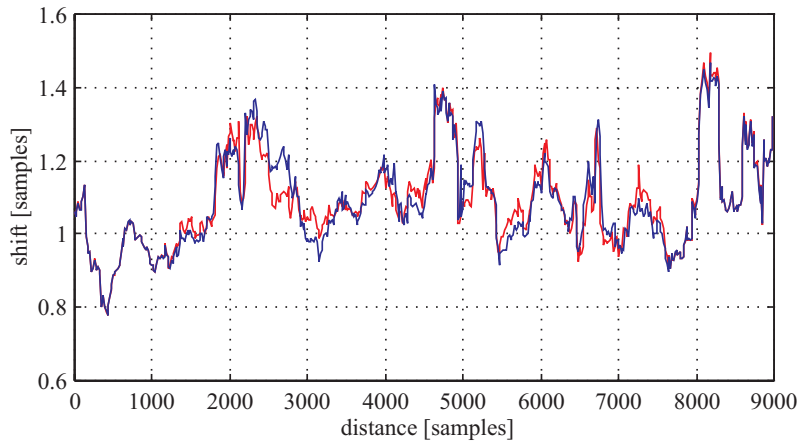


Abbildung 4.5: *Estimates of the absolute shift functions. Computed from original cant signal (red) and from shifted cant signal (blue).*

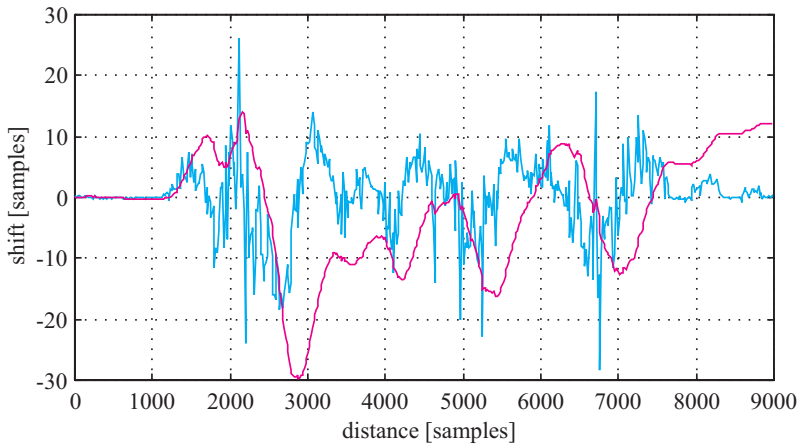


Abbildung 4.6: *Difference of absolute shifts (cyan) and cumulative sum of differences (magenta).*

$\pm 0.2m$ , respectively. The estimates of the natural frequencies of the AR-model inside a moving window clearly show some severe shortcomings of the method. As can be seen in figure 4.9 where a shift of  $\Delta x_s = \pm 0.05m$  has been applied frequencies associated to some poles do not change at all while the change of others is not significant. This result indicates that a 10% change in sampling interval size will not be detectable in general. Moreover, the effects of positive and negative changes in the size of the sampling interval are symmetrical. Rather, an increase in sampling interval size produces a much more pronounced change in the natural frequencies of the AR-model than a decrease does. This effect is very obvious from figure 4.10 where the estimates of the frequencies for a signal with a change in sampling interval size of  $\Delta x_s = \pm 0.2m$  are depicted. In the range from samples 3001 to 5000 (transitional effects seem to broaden this section) a strong increase in sampling interval size is at least partially correctly detected. However, the corresponding decrease between samples 5001 to 7000 is far too small for the actual change in sampling interval size. It is therefore apparent that this method may be used to detect strong changes in sampling interval size although its sensitivity especially to a decrease in sampling interval size is strongly limited.

For the sake of completeness another method for the estimation of absolute shift is included in this section. It makes use of the fact that the dynamic vehicle reactions are sampled with constant spatial sampling intervals although the original signal is low-pass filtered in the time domain. As

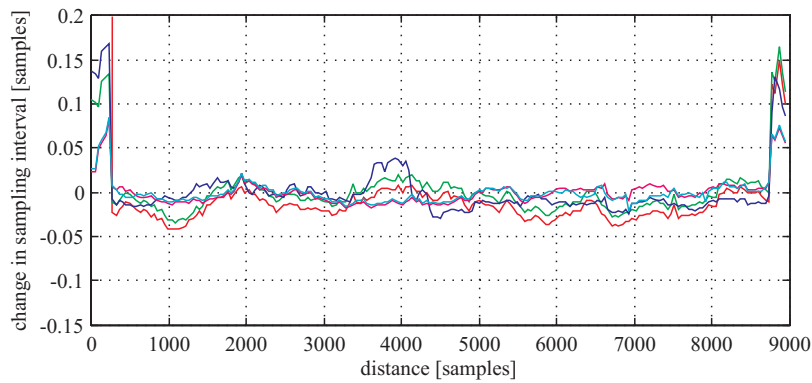


Abbildung 4.7: *Natural frequencies of AR-model (5th-order). Simulated difference of Q-forces.*

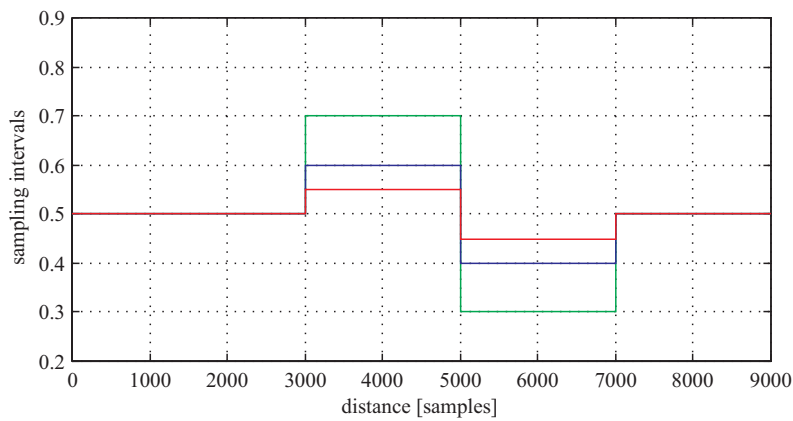


Abbildung 4.8: *Sampling interval size for shifted signals.*

already shown in chapter 1 this procedure leads to a cut-off frequency in the spatial domain which is depending on the speed of the measuring object. However, this variation may not only be caused by changes in actual speed but may also be the result of wheel slippage. Therefore, speed recordings and the spatial cut-off frequency of vehicle reactions should exhibit the same course throughout all recordings. There is no way to determine from those criteria if the original cause was an

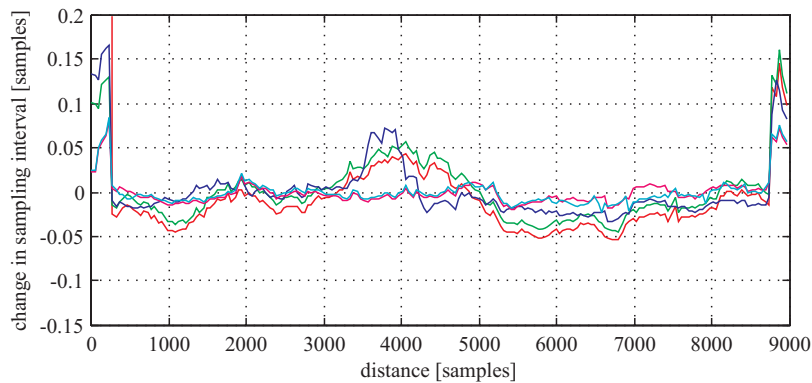


Abbildung 4.9: *Natural frequencies of the AR-model (5th-order). Simulated difference of Q-forces with shift applied ( $\Delta x_s = 0.05m$ ).*

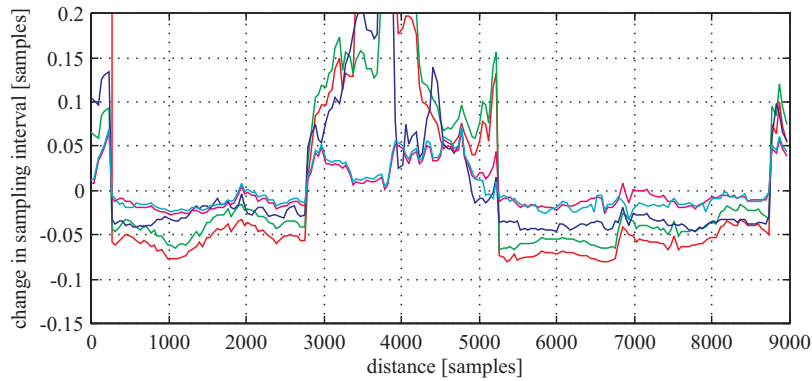


Abbildung 4.10: *Natural frequencies of AR-model (5th-order). Simulated difference of Q-forces with shift applied ( $\Delta x_s = \pm 0.2m$ ).*

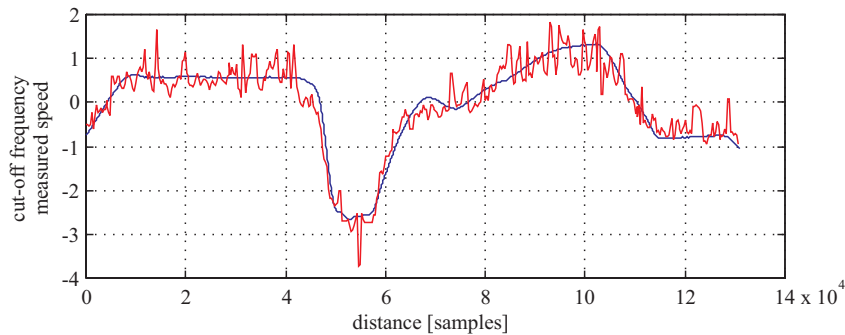


Abbildung 4.11: *Estimate of filter cut-off frequency (red) versus measured speed (blue). Both signals normalized to  $\sigma = 1$ .*

actual variation in speed or wheel slippage. Even a high correlation between speed variations and curvature does not necessarily indicate the presence of slippage. As known from experience [14] and confirmed by both theoretical investigations [18] and numerical simulations [12] the additional resistance during curve negotiation will most likely affect the speed of the train. This may even be true if a speed control is in use since the control schemes are usually fairly simple and some dynamic effects remain.

To demonstrate the effects mentioned above a test run where both variations in speed and curves were present was selected. Track: Böckstein - Schwarzach St. Veit, track 1, km33 to km20. The vehicle reaction used for this investigation is the difference of Y-forces on axle 1. By use of a spectrogram inside a moving window, consecutive interpolation, low-pass filtering and logarithmic transformation an estimate of the intersection between the high frequency noise and the filter shape is obtained. Since the high frequency noise is constant in amplitude and the filter shape does not depend on the amplitude of the signal a consistent estimate is possible. Figure 4.11 shows the measured speed of the train in blue, while the estimated cut-off frequency is plotted in red. Both signals have been normalized in order to show the good agreement between them. The high correlation between train speed and the estimate of the cut-off frequency confirms the theoretical demands. Correlations between train speed and curvature, and cut-off frequency and curvature, respectively, have shown no significant relationship between those signals. Therefore, neither speed recordings nor cut-off frequency estimates can be used to estimate the absolute shift of vehicle response signals.

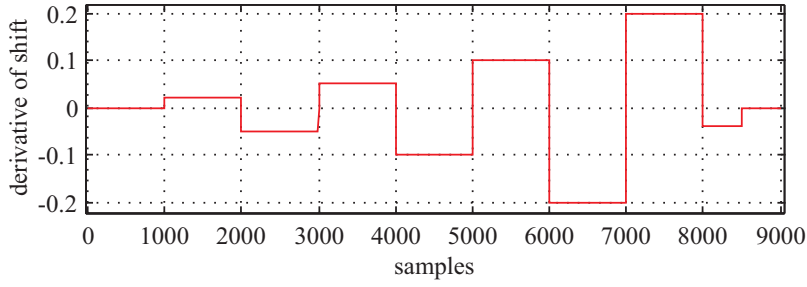


Abbildung 4.12: Derivative of shift function  $s(k)$ .

## 4.8 Effect of Absolute Shift on the Relative Shift Estimate

A piecewise linear shift function  $s(k)$  is applied to both input  $u(k)$  and output  $y(k)$  of the original data yielding shifted functions  $\tilde{u}(k)$  and  $\tilde{y}(k)$ . Additionally, original input-output data are shifted for 10 samples so that the overall constant shift becomes 20 samples. The same shift function  $s(k)$  is also applied to these data. Since the shift function  $s(k)$  is piecewise linear its discrete derivative  $\frac{s(k)-s(k-1)}{\Delta k}$  is a piecewise constant function. Because the shift function  $s(k)$  was already scaled in samples its derivative actually becomes  $s(k) - s(k-1)$ . The derivative of the shift function is depicted in figure 4.12. An important information of this derivative lies in the fact that it directly shows the increase and decrease in sampling interval length. A value of -0.2 tells us that the sampling interval of the shifted signal will in fact be

$$\Delta\tilde{x}(k) = \Delta x(k) [1 - 0.2] = 0.8 \Delta x(k), \quad k \in ]6000, 7000] \quad (4.93)$$

which means that the original sampling interval  $\Delta x(k)$  is 25% larger than the distorted one  $\Delta\tilde{x}(k)$ .

The computation of the relative shift function by cross-correlation estimates inside a moving window should give an approximately constant function for the original signals. It should be around 10 samples for the original data set and around 20 for the data set with additional constant shift. The CCF-estimate should also stay the same for the data sets with the shift function  $s(k)$  applied since both input and output are affected in the same way. However, the change in sampling intervals will also affect the CCF-estimate: If the sampling interval is bigger than the nominal one the CCF-estimate will shrink along the  $\tau$ -axis, if the sampling interval shrinks the CCF-estimate will become inflated along the  $\tau$ -axis. A global maximum of the CCF-estimate from the data sets without varying shift at  $\tau_{\max}$

$$\tau_{\max} = \arg \max_{\tau} [R_{uy}(\tau)] \quad (4.94)$$

will move to another location  $\tilde{\tau}_{\max}$

$$\tilde{\tau}_{\max} = \arg \max_{\tilde{\tau}} [R_{\tilde{u}\tilde{y}}(\tilde{\tau})] \quad (4.95)$$

for the shifted input  $\tilde{u}(k)$  and output  $\tilde{y}(k)$ . Under the assumption that the system and therefore its CCF-estimate stays unchanged the ratio  $\alpha$  of the arguments of the maxima of the CCFs

$$\alpha = \frac{\tau_{\max}}{\tilde{\tau}_{\max}} \quad (4.96)$$

must equal the ratio  $\beta$  of the sampling intervals

$$\beta = \frac{\Delta x}{\Delta\tilde{x}} = \frac{\tau_{\max}}{\tilde{\tau}_{\max}} = \alpha. \quad (4.97)$$

Therefore, it is possible to estimate an absolute shift function by computing the relative shift function and first evaluating the local sampling interval

$$\Delta\tilde{x}(k) = \Delta x \frac{\tilde{\tau}_{\max}(k)}{\tau_{\max}} \quad (4.98)$$

and finally summing up these intervals to get the absolute position of the shifted signals

$$\tilde{x}(k) = \sum_{j=1}^k \Delta\tilde{x}(j). \quad (4.99)$$

Although the value of  $\tau_{\max}$  may not be known a priori it can be replaced by the mean value

$$\bar{\tau}_{\max} = \frac{1}{N} \sum_{k=1}^N \tilde{\tau}_{\max}(k). \quad (4.100)$$

This is equivalent to an unknown nominal sampling interval, nevertheless, the deviations from the chosen reference  $\bar{\tau}_{\max}$  can be estimated. If the absolute shift function  $s(k)$  has zero mean the function  $\tilde{\tau}_{\max}(k)$  will also be of zero mean and the estimate 4.100 will be unbiased.

Furthermore, equation 4.98 allows for a simple estimate of the accuracy of  $\Delta\tilde{x}(k)$ . We assume that the true value of  $\tau_{\max}$  denoted by  $\tilde{\tau}_{\max}^0$  and the estimate 4.95 fulfill

$$\tilde{\tau}_{\max}^0 = \tilde{\tau}_{\max} + \Delta\tau, \quad \Delta\tau \in [-a, a] \quad (4.101)$$

with  $\pm a$  being some constant (e.g. the 95% confidence interval). Then apparently

$$\Delta\tilde{x}(k) = \Delta x \frac{\tilde{\tau}_{\max}(k)}{\tau_{\max}} = \Delta x \frac{\tilde{\tau}_{\max}^0(k) - \Delta\tau}{\tau_{\max}} = \Delta x \left[ \frac{\tilde{\tau}_{\max}^0(k)}{\tau_{\max}} - \frac{\Delta\tau}{\tau_{\max}} \right] = \Delta x \left[ \frac{\tilde{\tau}_{\max}^0(k)}{\tau_{\max}} - \varepsilon_{\tau} \right] \quad (4.102)$$

holds, where the possible error  $\varepsilon_{\tau}$  is bounded by

$$|\varepsilon_{\tau}| \leq \frac{a}{\tau_{\max}}. \quad (4.103)$$

In the inequality 4.103 the constant  $a$  is given by the data characteristics but the value of  $\tau_{\max}$  can be increased deliberately to any reasonable value by adding a constant shift  $S$  to the input/output data set ( $\tilde{y}(k) \rightarrow \tilde{y}(k - S)$ ). Let us finally note that such a constant shift does not affect the accuracy of the CCF-estimate 4.95. If the signals  $\tilde{u}(k)$  and  $\tilde{y}(k)$  give an estimate of

$$\tilde{\tau}_{\max} = \arg \max_{\tilde{\tau}} [E \{ \tilde{u}(k) \tilde{y}(k - \tilde{\tau}) \}] = \arg \max_{\tilde{\tau}} [R_{\tilde{u}\tilde{y}}(\tilde{\tau})] \quad (4.104)$$

the estimate with an additional constant shift  $S$  will simply be

$$\tilde{\tau}_{\max}^s = \arg \max_{\tilde{\tau}} [E \{ \tilde{u}(k) \tilde{y}(k - \tilde{\tau} - S) \}] = \arg \max_{\tilde{\tau}} [R_{\tilde{u}\tilde{y}}(\tilde{\tau} + S)] = \tilde{\tau}_{\max} + S. \quad (4.105)$$

Since the signal lengths available for computing the CCF-estimate are finite, the accuracy of the estimate will actually decrease with increasing  $\tau$ . In practical implementations a trade-off between window length and optimal  $\tau_{\max}$  will exist.

The results of the numerical evaluation for the data sets described above are depicted in figure 4.13. The relative shift functions of the data sets without  $s(k)$  applied (magenta and cyan) are identical except for the offset of 10 samples. The relative shift functions for these data sets, however, show the expected deviation from the original versions. Moreover, the deviations for the data set with a constant shift of 20 samples are twice as large as for the data set with a constant shift of 10 samples. The dash-dotted lines indicate the bandwidth of  $\pm 1$  sample around the nominal shift. If

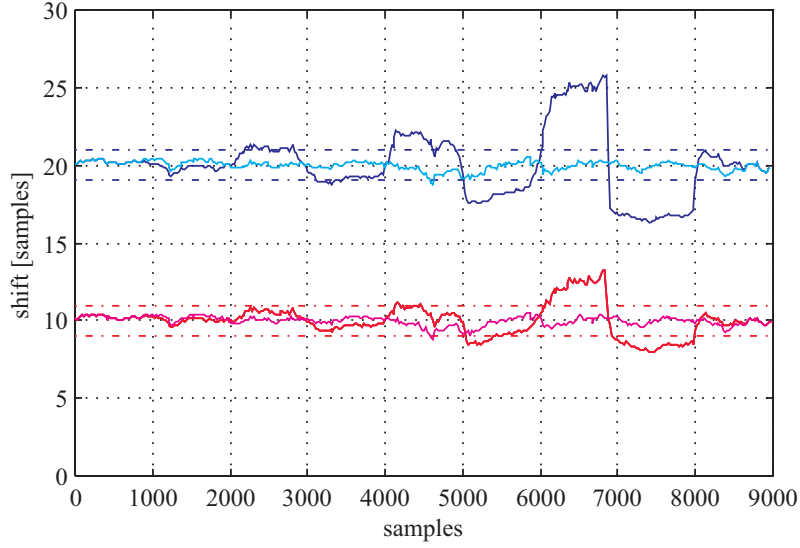


Abbildung 4.13: *Relative shift functions.* Original data set with a constant shift of 10 samples (magenta), same data with shift function  $s(k)$  applied (red), original data set with a constant shift of 20 samples (cyan), same data with shift function  $s(k)$  applied (blue).

we consider this somewhat arbitrary boundaries as indicators of an absolute shift inside our data, it is obvious that the larger constant shift allows for earlier detection. The quantitative results also confirm equation 5.3. From samples 6000 to 7000 the increase of the functions shift is 25% just as predicted.

The most important consequence from equation 4.98 is the fact that the argument  ${}_{\sigma}\tilde{\tau}_{\max}(k)$  due to an absolute shift is proportional to the reference argument  $\tau_{\max}$  or  $\bar{\tau}_{\max}$ , respectively. This can also be clearly seen in figure 4.13. However, the argument  ${}_s\tilde{\tau}_{\max}(k)$  due to a relative shift can always be written as

$${}_s\tilde{\tau}_{\max}(k) = S + {}_s\tau_{\max}^0(k) \quad (4.106)$$

where

$$S = E \{ {}_s\tilde{\tau}_{\max}(k) \} , \quad E \{ {}_s\tau_{\max}^0(k) \} = 0. \quad (4.107)$$

Any additional constant shift will therefore only alter the constant  $S$  but it will not affect the zero-mean relative shift  ${}_s\tau_{\max}^0(k)$ . Under the assumption that both relative and absolute shifts are present in the data set, the argument  $\tilde{\tau}_{\max}(k)$  of the CCF-estimate can be written as

$$\tilde{\tau}_{\max}(k) = {}_{\sigma}\tilde{\tau}_{\max}(k) + {}_s\tilde{\tau}_{\max}^0(k) \quad (4.108)$$

where again

$$S = E \{ \tilde{\tau}_{\max}(k) \} = E \{ {}_{\sigma}\tilde{\tau}_{\max}(k) \} , \quad E \{ {}_s\tau_{\max}^0(k) \} = 0. \quad (4.109)$$

In equation 4.108  ${}_{\sigma}\tilde{\tau}_{\max}(k)$  is the absolute shift and  ${}_s\tilde{\tau}_{\max}^0(k)$  stands for the zero-mean relative shift. The zero-mean property of the relative shift can be assumed without loss of generality since any constant shift as denoted by  $S$  in equation 4.106 can be assumed to be included in the argument of the absolute shift  ${}_{\sigma}\tilde{\tau}_{\max}(k)$ . From equation 4.108 alone only the constant shift  $S$  may be evaluated by use of the first equation of 4.109. The remaining shift (i.e. the deviations from the constant shift) can not be divided into the two different types of shift. However, by deliberately adding an additional constant shift  $\Delta S$  the following changes will occur: According to equations 4.106 and 4.107 the relative zero-mean shift  ${}_s\tilde{\tau}_{\max}^0(k)$  will be unaffected by definition so that the zero-mean relative shift after adding  $\Delta S$  will be the same as before:

$$\frac{\Delta S}{{}_s}\tilde{\tau}_{\max}^0(k) = {}_s\tilde{\tau}_{\max}^0(k) \quad (4.110)$$

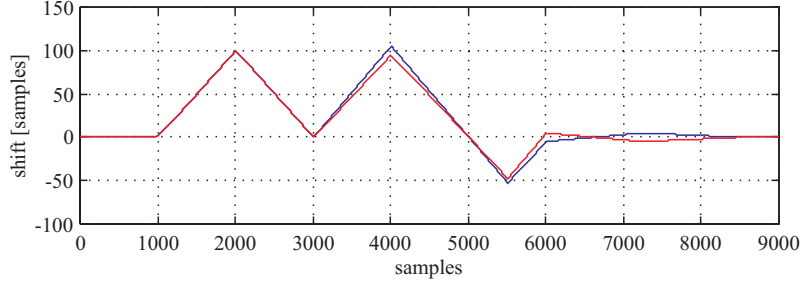


Abbildung 4.14: Absolute shift functions of output  $y(k)$  (red) and input  $u(k)$  (blue).

However, equation 4.97 rewritten for a varying absolute shift argument

$$\beta(k) = \frac{\Delta x}{\Delta \tilde{x}(k)} = \frac{\tau_{\max}}{\sigma \tilde{\tau}_{\max}(k)} = \frac{S}{\sigma \tilde{\tau}_{\max}(k)} \quad (4.111)$$

can be rearranged to

$$\sigma \tilde{\tau}_{\max}(k) = S \frac{\Delta \tilde{x}(k)}{\Delta x}. \quad (4.112)$$

Since  $\tau_{\max}$  in equations 4.111 and 4.112 has been chosen as  $S = E\{\sigma \tilde{\tau}_{\max}(k)\}$  according to equation 4.100, the absolute shift estimate after addition of the constant shift  $\Delta S$  will be altered to

$$\frac{\Delta S}{\sigma} \tilde{\tau}_{\max}(k) = (S + \Delta S) \frac{\Delta \tilde{x}(k)}{\Delta x} = (S + \Delta S) \frac{\sigma \tilde{\tau}_{\max}(k)}{S} = \sigma \tilde{\tau}_{\max}(k) \left(1 + \frac{\Delta S}{S}\right) \quad (4.113)$$

since

$$E\left\{\frac{\Delta S}{\sigma} \tilde{\tau}_{\max}(k)\right\} = \tau_{\max} + \Delta S \quad (4.114)$$

holds. Therefore, the new argument  $\frac{\Delta S}{\sigma} \tilde{\tau}_{\max}(k)$  of the CCF-estimate can be written as

$$\frac{\Delta S}{\sigma} \tilde{\tau}_{\max}(k) = \frac{\Delta S}{\sigma} \tilde{\tau}_{\max}(k) + \frac{\Delta S}{s} \tilde{\tau}_{\max}^0(k) = {}_s \tilde{\tau}_{\max}^0(k) + \sigma \tilde{\tau}_{\max}(k) \left(1 + \frac{\Delta S}{S}\right). \quad (4.115)$$

Calculating the difference between the two shift functions 4.96 and 4.48 yields

$$\frac{\Delta S}{\sigma} \tilde{\tau}_{\max}(k) - \tilde{\tau}_{\max}(k) = \sigma \tilde{\tau}_{\max}(k) \frac{\Delta S}{S}. \quad (4.116)$$

Equation 4.116 shows that only a scaled version of the absolute shift function estimate remains. The relative shift has been removed completely and the scaling factor  $\frac{\Delta S}{S}$  can be chosen deliberately, allowing for a better detection of absolute shifts by choosing a larger additional shift  $\Delta S$ .

The method outlined above is not applicable to measured data sets with unknown absolute reference. By adding an additional constant shift  $\Delta S$  the overall constant shift will be increased without affecting the relative shift component  ${}_s \tilde{\tau}_{\max}^0(k)$  (with zero-mean). In other words, if a pair of input/output signals has varying constant shift, the algorithm will always detect the same relative shift after introduction of  $\Delta S$ .

To demonstrate the effects of mixed shifts we perform a simulation of the exact case where the additional constant shift  $\Delta S$  is added to the undistorted ideal signals *before* the relative and absolute shift functions are applied. The results should be in direct agreement with the theoretical considerations above. By comparing the results to the known shifts a quantitative estimate of the accuracy should be possible.

Input and output data for this simulation are the same as described earlier in this section. This implies that a constant shift of 10 samples is present in the original data while an additional constant shift of  $\Delta S = 10$  is applied to the signals according to the previous section (cant/qsim



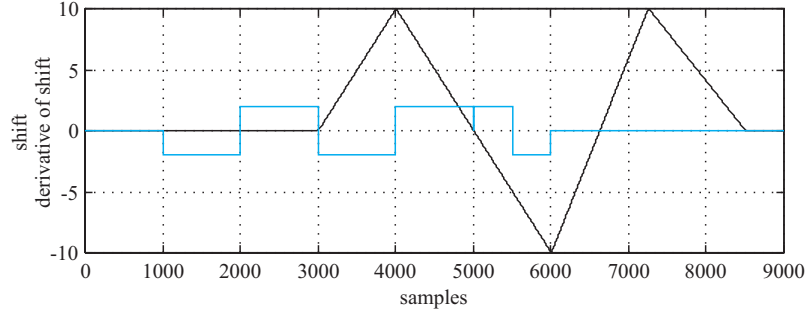


Abbildung 4.15: *Relative shift (black) and numerical derivative of absolute shift (cyan).*

- 10 samples, uk/yk - 20 samples). Since the value of the constant shift is known a priori the value of  $\tau_{\max} = 10$  can be assigned. Therefore, the relative shift function  ${}_s\tilde{\tau}_{\max}^0(k)$  will not be zero-mean but the more favorable feature of vanishing relative shift at the beginning and end of the signals can be assured. The individual absolute shift functions applied to these signals are depicted in figure 4.14 (shift\_u2, shift\_y2). The shift function for the output  $y(k)$  is plotted red while the shift for the input  $u(k)$  is depicted in blue. It is of great importance to note that the relative shift  ${}_s\tilde{\tau}_{\max}^0(k)$  between input and output is the *difference* of the respective shift functions, while the absolute shift  ${}_s\tilde{\tau}_{\max}^0(k)$  is the *mean* value of the individual shift functions. Furthermore, the algorithm will compute the relative shift directly, while it will detect only the derivative of the absolute shift. These two functions as computed from the known individual shifts are depicted in figure 4.15. The relative shift is plotted black while the numerical derivative is depicted in cyan. To correct for numerical as well as systematical offsets the derivative has to be scaled. Since the shift estimates are evaluated at 450 points along the 9000 samples the step size is 20 samples. Therefore 20 is multiplied to the amplitude of the derivative. Additionally, since the constant shift  $S = 10$  this has also be multiplied to the derivative giving a total scaling factor of 200 in this case. The only partially different shift functions are applied to the undistorted signals by cubic spline interpolation. Because there are two undistorted signal pairs with different constant shifts two shifted signal pairs will result:

$$S = 10 : \quad u_{10}(k)/y_{10}(k) \xrightarrow{\text{shift}} \tilde{u}_{10}(k)/\tilde{y}_{10}(k) \quad (4.117)$$

$$S = 10, \Delta S = 10 : \quad u_{20}(k)/y_{20}(k) \xrightarrow{\text{shift}} \tilde{u}_{20}(k)/\tilde{y}_{20}(k) \quad (4.118)$$

The resulting shift estimates  $\hat{\tau}_{\max_j}(k)$  from the algorithm incorporating CCF-estimates inside a moving window

$$\tilde{u}_{10}(k)/\tilde{y}_{10}(k) \implies \hat{\tau}_{\max_{10}}(k) \quad (4.119)$$

$$\tilde{u}_{20}(k)/\tilde{y}_{20}(k) \implies \hat{\tau}_{\max_{20}}(k) \quad (4.120)$$

are plotted for both data sets. Figure 4.16 shows the estimate  $\hat{\tau}_{\max_{10}}(k)$  in red while the estimate  $\hat{\tau}_{\max_{20}}(k)$  is plotted blue. The base values of  $S = 10$  and  $S + \Delta S = 20$  are clearly visible in both estimates. Making use of 4.116 the difference

$$\Delta\tau_{\max}(k) = 2\hat{\tau}_{\max_{10}}(k) - \hat{\tau}_{\max_{20}}(k) = \hat{\tau}_{\max_{10}}(k) - {}_\sigma\hat{\tau}_{\max}(k) \frac{\Delta S}{S} = {}_s\hat{\tau}_{\max}^0(k) \quad (4.121)$$

obviously is identical to the estimate for the relative shift and is plotted in black. The estimate for the derivative of the absolute shift function is plotted in cyan and can be computed according to 4.116 as

$$\delta\tau_{\max}(k) = \hat{\tau}_{\max_{10}}(k) - \hat{\tau}_{\max_{20}}(k) = {}_\sigma\hat{\tau}_{\max}(k) \frac{\Delta S}{S} \quad (4.122)$$

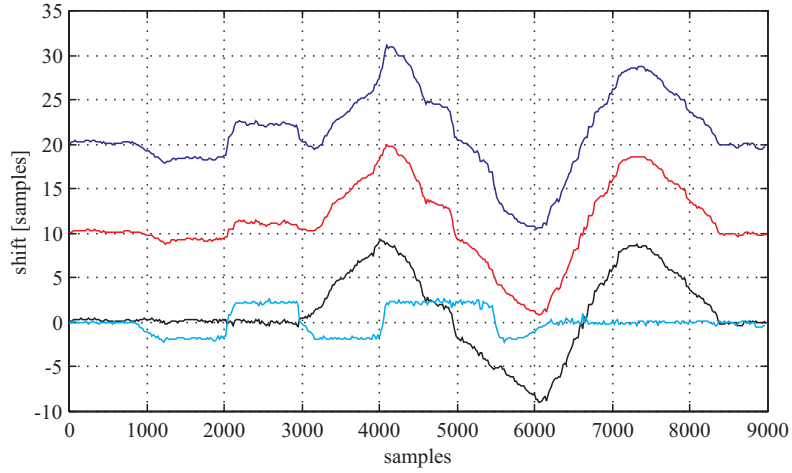


Abbildung 4.16: Shift estimates  $\hat{\tau}_{\max_{10}}(k)$  (red),  $\hat{\tau}_{\max_{20}}(k)$  (blue), relative shift  ${}_s\tilde{\tau}_{\max}^0(k)$  (black), and derivative of absolute shift  $\sigma\tilde{\tau}_{\max}(k)$  (cyan).

which yields an estimate with the constant shift  $S$ . Otherwise, the absolute shift estimate can of course be computed as the total shift subtracted by the relative shift

$$\sigma\hat{\tau}_{\max}(k) = \hat{\tau}_{\max_{10}}(k) - [2\hat{\tau}_{\max_{10}}(k) - \hat{\tau}_{\max_{20}}(k)] = \quad (4.123)$$

$$= -\hat{\tau}_{\max_{10}}(k) - \hat{\tau}_{\max_{20}}(k) = \quad (4.124)$$

$$= \hat{\tau}_{\max_{10}}(k) - {}_s\hat{\tau}_{\max}^0(k). \quad (4.125)$$

Apparently there is a very good agreement with the theoretical prediction depicted in figure 4.15.

## Kapitel 5

# Synchronization of Measured Data Sets

The methods and algorithms derived in the previous chapter are applied to real measurement data in this chapter. It is structured as follows: After a few remarks on coarse adjustment of data sets the best linear combination of signals is sought for. A satisfactory combination of input-output signals is found and the two methods for synchronization outlined before are tested with this combination of signals. Firstly, data from straight track are used to limit the complexity of the synchronization process. Finally, data from curved track are also used for synchronization, the differences to straight track are discussed and conclude the chapter.

The shift between input and output of a system can be defined in two ways. Either the dynamics of the system are ignored and only a dead time is accepted as shift or the shift is defined as some time-delay between input and output which incorporates dead-time as well as time-delays due to system dynamics. In the latter case a crucial part of the definition lies within the computation of the time delay. In the rail-vehicle interaction a dead time (and therefore shift following the first definition) is not expected. Even if there should be some amount of slackness in the vehicle structure the delay introduced by it will be negligible compared to the sampling intervals. On the other hand the railway vehicle is known to exhibit distinct eigenmodes [12, 18] with partially slow and slightly damped poles. Therefore, the input-output shift will be defined as the shift of the global extreme or a distinct peak of the cross-correlation function. This measure will be intuitively correct since it is equivalent to the time delay between an impulse as input and the corresponding maximum in the output.

### 5.1 Coarse Adjustment

The best suited signals for coarse synchronization are the curvature record in track data and the relative twist between bogie and car body in vehicle data. Each transition before and after a curve as well as switches can be used for a rough estimate of a synchronization point. The accuracy of this method is usually poor since the relative twist is not only a record of track properties but also reflects the dynamics of the bogie. Therefore, the twist records typically show marked oscillations along the transition curves, making it very hard to detect the beginning or end of the transition. Furthermore, the quantization of the curvature signal is very coarse ( $\delta_c = \frac{10}{9}mm$ ) leading to a signal which can not resolve small deviations along straight track.

The approximate accuracy using a 1000 point CCF at a sampling interval of  $\Delta x = 0.5m$  therefore is  $\pm 10m$  at best which is far too inaccurate for synchronization but provides a good means for initial data adjustment.

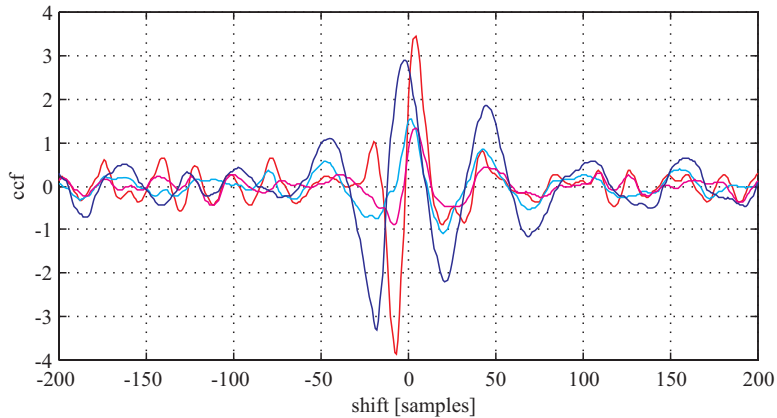


Abbildung 5.1: *Cross-correlation estimates for level /  $Q$ -force interaction on axle 1: left rail /  $Q_{1.1}$  (magenta), right rail /  $Q_{1.2}$  (cyan), profile /  $\sum Q_1$  (red),  $\text{diff}(\text{level}) / \text{diff}(Q_1)$  (blue).*

## 5.2 Comparison of Signal Pairs

The cross-correlation analysis and the identification used for synchronization are both linear procedures utilizing a linear relationship between input and output signal. The performance of these procedure will therefore critically depend on the characteristic of the actual relationship between these signals. Since all input-output relations in the track-car system are of a more or less nonlinear nature, the goal is to find the input-output pair which comes closest to a purely linear dependence. This property should of course be preserved regardless of speed, track quality, and nominal track geometry (curves).

From physical reasoning it is apparent that track characteristics become less influential and eigenmodes are more important the farther away vehicle reactions are measured from the track-vehicle contact point. Therefore, the wheel-rail contact forces measured at the axles of the test object seem to be the most promising vehicle responses for the problems at hand. This consideration is backed up by the spectra of the different vehicle reactions. Car body accelerations show a much more pronounced influence of the eigenmodes than wheel-forces do.

### 5.2.1 Cross Correlation Estimates

The task is to determine which combination of track signals (input) paired with another combination of wheel-force signals (output) gives the best performance in the terms stated above. The nominal track of the section used for investigation contains straight track, transition curves to and from stationary curves, and stationary curves themselves at approximately the same number of samples for each type of track. The cross-correlation function estimates of various signal pairs from this section are computed and the respective features of these estimates are compared.

The most promising interaction should be the one in z-direction, since this is the most pronounced SISO-connection between track and vehicle with the least nonlinear characteristic [12, 14, 18]. The CCF-estimates depicted in figure 5.1 were computed for level /  $Q$ -force of left rail (magenta), and right rail (cyan), and for profile / sum of  $Q$ -forces (red) as well as for difference of level / difference of  $Q$ -forces (blue). Clearly, the correlations for single sides of the track (magenta, cyan) are much weaker than those for combined signals (red, blue). Although the CCF of the sum of signals (red) shows higher amplitudes, the CCF for difference of signals exhibits a most pronounced oscillation with the least influence of noise. The reason why combined signals of left and right track achieve better correlation than those of individual sides alone is most likely the coupling between left and right  $Q$ -forces. Since the Hertzian spring constant is much larger than

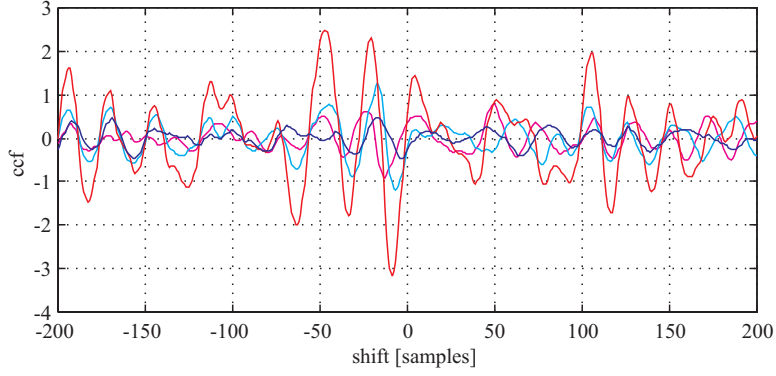


Abbildung 5.2: *Cross-correlation estimates for alignment / Q-force interaction on axle 1: left rail /  $Y_{1.1}$  (magenta), right rail /  $Y_{1.2}$  (cyan), alignment /  $\sum Y_1$  (red),  $\text{diff}(\text{alignment}) / \text{diff}(Y_1)$  (blue).*

the primary suspension in z-direction ( $1.5 \cdot 10^9 \frac{N}{m}$  versus  $0.7 \cdot 10^6 \frac{N}{m}$ ) [14], the axles can be regarded as decoupled relative to the bogie. Due to the moment of inertia of the wheelset, a Q-force impulse on one side will cause a proportional but smaller force pulse on the other side.

An alternative but equivalent signal to the difference of level signals would be a high-pass filtered version of the cant signal. The original cant signal contains the nominal track features, which introduce low frequencies at a high amplitude. The resulting cross-correlation estimate with the difference of Q-forces is therefore useless. After high-pass filtering with a 5th-order Butterworth filter at a cut-off frequency of  $f_c = 0.03f_\nu = 0.015f_s = 0.03 \frac{1}{m}$  basically the same signal as the difference of level signals remains, which produces a nearly identical estimate as the one already derived (blue function estimate in figure 5.1) except for a stronger noncausal oscillation.

The estimates for lateral interaction are expected to exhibit much weaker correlations, since the lateral wheel-rail forces are known to depend strongly nonlinear from alignment errors [12, 18, 29]. This is confirmed by the CCF-estimates depicted in figure 5.2. The color coding is the same as in figure 5.1, revealing a much less organized picture than for vertical interaction. The mean alignment / mean Y-forces signal pair (red) produces the most distinct absolute maximum at about the same shift  $\tau$  as the estimate of its counterpart for vertical interaction. However, it lacks the marked difference between maximum amplitudes and the remainder of the correlation. The reason for this poor correlation is probably the much closer values of lateral wheel stiffness (which is strongly but nonlinearly dependent on lateral displacement) and primary suspension in y-direction ( $4.8 \cdot 10^6 \frac{N}{m}$ ). This causes the lateral wheel forces to be coupled between axles, meaning that a force impulse in  $Y_{1.1}$  will cause a proportional but smaller pulse in  $Y_{2.2}$ . Thus, a combination of these signals should exhibit a better correlation with alignment signals. Because of the wheel base of the bogie the signals have to be combined with a proper shift. For test run 6117 axle 1 leads axle 2 with a wheel base of  $2.5m$  equivalent to 5 samples of  $\Delta x = 0.5m$ . This means that the combined track  $a_i(k)$  and Y-force signals  $Y_i(k)$  should be constructed as

$$\begin{aligned} a_1(k) &= a_l(k) \mp a_r(k - 5) \\ Y_1(k) &= Y_{1.1}(k) \pm Y_{2.2}(k) \end{aligned} \quad (5.1)$$

or as

$$\begin{aligned} a_2(k) &= -a_r(k) \pm a_l(k - 5) \\ Y_2(k) &= Y_{1.2}(k) \pm Y_{2.1}(k). \end{aligned} \quad (5.2)$$

The diagonally coupled signal pairs 5.1 and 5.2 can be combined again to form a closed expression

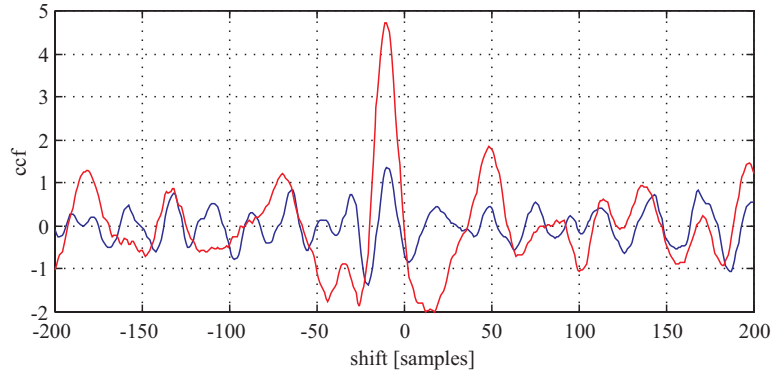


Abbildung 5.3: *Cross-correlation estimates for alignment / Y-force interaction on bogie 1:  $\sum \text{alignment} / \sum Y$  (red),  $\text{diff}(\text{alignment}) / \sum M_Y$  (blue).*

incorporating all 4 signals:

$$\begin{aligned} a_c(k) &= a_1(k) - a_2(k) = a_l(k) \mp a_r(k-5) + a_r(k) \mp a_l(k-5) \\ Y_c(k) &= Y_1(k) - Y_2(k) = Y_{1.1}(k) \pm Y_{2.2}(k) - Y_{1.2}(k) \mp Y_{2.1}(k) \end{aligned} \quad (5.3)$$

$Y_c$  from 5.3 with the upper signs is identical to the sum of moments in z-direction divided by the half wheel base while the version with the lower signs is identical to the sum of forces in y-direction. The CCF-estimates computed according to the combined signals 5.3 are depicted in figure 5.3. The blue estimate is the result of the version with the upper sign (sum of moments) while the red one was achieved by the combination with the lower sign (sum of forces). Obviously the sum of forces leads to an estimate which is not only superior to the other combined signals but also to all estimates from single axles or individual track sides as depicted in figure 5.2. This clearly points out the coupled influence of several geometry inputs on vehicle reactions. Although in this case it is possible to combine these inputs to a single signal this might not be feasible in general. It should be noted that the signals producing the best result for the lateral direction can be rewritten as

$$\begin{aligned} a_c(k) &= 2[\bar{a}(k) + \bar{a}(k-5)] = 2 \left[ \frac{a_l(k) + a_r(k)}{2} + \frac{a_l(k-5) + a_r(k-5)}{2} \right] \\ Y_c(k) &= \sum Y_i^+(k) = Y_{1.1}(k) - Y_{1.2}(k) + Y_{2.1}(k) - Y_{2.2}(k), \end{aligned} \quad (5.4)$$

where  $a_c(k)$  is the sum of the mean alignments at first and second axle (multiplied by 2) while  $Y_c(k)$  is the algebraic sum of lateral wheel rail forces.

### 5.2.2 Shift Function Estimates

The results from the comparison of CCF-estimates should somehow be reflected in the computation of the shift functions. A more distinct absolute maximum in the CCF-estimate should enable the use of a smaller window (fewer points for CCF-estimate) or a more robust estimate with respect to isolated and erratic track irregularities. First the interactions in the vertical direction are compared by computing the respective shift functions with the CCF-estimate. As can be seen in figure 5.4 the detrended estimates for sum (blue) and difference (red) of  $Q$ -forces and level signals respectively show good agreement along the entire track section. Only at the beginning of the shift function a transient with less coherence is present for the length of the moving window. The shift function computed with the difference signals is slightly smoother than that of the sum signals. This also means that a smaller window size is possible without erratic results. Although the CCF-estimate with the high-pass filtered cant is almost identical to that of the difference of level signals, the shift

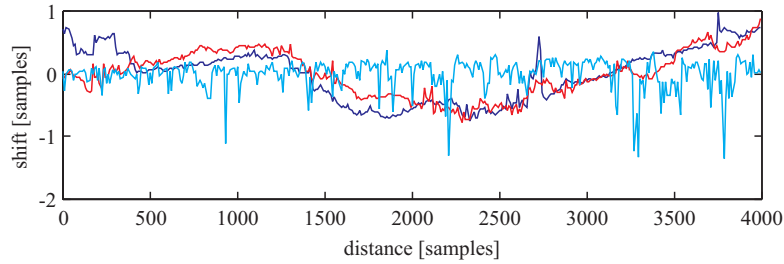


Abbildung 5.4: *Shift functions for curved track - vertical interactions. Difference of Q-forces / diff of level (red), difference of Q-forces / high-pass filtered cant (cyan), sum of Q-forces (blue).*

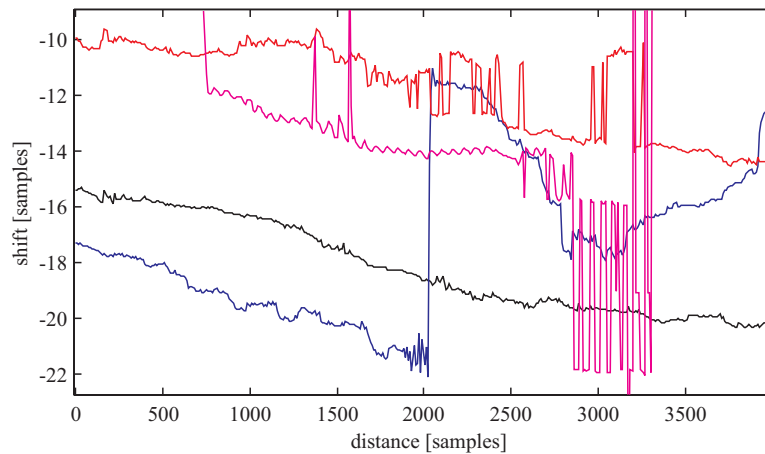


Abbildung 5.5: *Shift functions for curved track - lateral interactions. Sum of moments (blue), sum of Y-forces (red), sum of Y-forces / ML-estimate (magenta), diff of Q-forces (black).*

function computed with the cant signal is erratic and does not show any resemblance of the shape of the two other estimates. The cant signal is therefore not suitable for the computation of a shift function estimate.

The results for interactions in the y-direction are definitely poorer than those for z-direction. This can be concluded from looking at figure 5.5 where several shift functions from lateral interaction are plotted against the shift function for difference of  $Q$ -forces (black). The estimates from lateral interaction are all calculated by CCF-estimates with a moving window length of 1524 samples except for one (in magenta) which was computed using the ML-estimate. The estimate for sums of  $Y$ -forces (red) seems to have the overall best performance although it exhibits erratic changes which cover up the actual behavior. The window length of the adaptive window cannot be chosen smaller than used for this computation because the extremum would be lost altogether. The result for sums of moments is even worse since it exhibits a huge jump to a completely different extremum. Again, a suitable combination of parameters for a smooth estimate could not be found in this case. The result for the ML-estimate is also unsatisfying. It is obviously more sensitive to the influence of beginning and ending data sequences, but it also exhibits strong oscillations around an offset mean value. Nevertheless, there is a section between the samples of approximately  $k = 750$  to  $k = 2000$  where at least the linear trend is similar in all shift functions. From figure 5.5 it is quite apparent that only the signals of sums of  $Y$ -forces may prove to be useful as a validation of shift functions from other signal pairs.

The shift functions depicted in figure 5.6 show the results of the cross-correlation estimate (red) and the ML-estimate (black). Both shift functions were computed with a moving window of 500

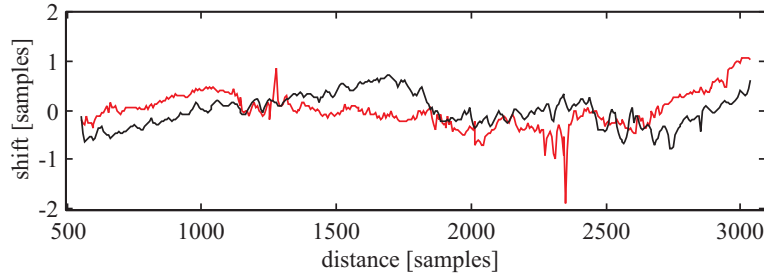


Abbildung 5.6: *Shift functions for curved track. CCF-estimate (red), ML-estimate (black).*

samples length and 600 points along the total 4000 samples of the data sets. The window size clearly affects the ML-estimates beginning and end, therefore these sections were cut off and only the part where the moving window was fully inside the available data was plotted. Shift functions were detrended before plotting to remove offsets and linear trends. The difference between the functions stays within 0.5 samples for almost all points. The main trend of the nonlinear shift is reflected by the results of both methods, however, the ML-estimate produces a much smoother estimate at the given window length. For the purpose of resampling the signals both methods provide sufficient accuracy, although the method best suited for a special case has to be checked on each application.

## 5.3 Synchronization of Data Sets

### 5.3.1 Straight Track

The correlation analysis outlined in section 4.3.2 was employed to estimate the shift between two signals from input (track geometry) and output (vehicle response) data sets. Rather than averaging over the entire data sequence the moving window approach described earlier is utilized. The more localized cross-correlation estimate inside the window makes it possible to deal with linear and nonlinear (including discontinuous) shift functions.

The shift function was calculated using a moving window of length  $W = 2048$ , moved along 200 evenly spaced points of the 8000 signal samples (corresponding to a step size of 40 samples between each CCF-estimate). Each CCF-estimate was directly calculated by repeated multiplication and summation. Data were taken from test run m0006r, Angern-Drösing. Instead of using the optimal signal pair (cant/difference of  $Q$ -forces) the combination profile/sum of  $Q$ -forces is used to demonstrate the robustness of the algorithm.

In figure 5.7 the shift function before and after resampling is depicted. Real values for shift are calculated by three point interpolation over the global maximum. The upper plot shows that the shift function can be approximated by a linear function (indicated by a dash-dotted line). This means that the main effect of the shift between the two data sets is caused by a small drift in sampling locations. The reason for this is most likely the unknown exact sampling interval in both data sets. The nominal values of the sampling intervals are  $\Delta x_t = 0.25m$  for track data and  $\Delta x_v = 0.1m$  for vehicle data, suggesting a common sampling rate of  $\Delta x^d = 0.5m$ . This requires a simple decimation by a factor of 2 and 5, respectively. However, if the actual sampling interval of the track data is not  $0.25m$  but rather  $\Delta x_t = \alpha 0.25m$ , with  $\alpha$  very close but not equal to 1, the resulting sampling interval after decimation would be  $\Delta x_t^d = \alpha 0.5m$ . With the same reasoning the actual sampling interval after decimation for vehicle data would be  $\Delta x_v^d = \beta 0.5m$ , with  $\beta$  also very close but not equal to 1. In general,  $\alpha \neq \beta$  will hold and therefore the decimated sampling intervals  $\Delta x_t^d$  and  $\Delta x_v^d$  will slightly differ from each other. If we further assume that  $\alpha, \beta = const.$ , a linear change in shift will result. This is the physical justification for a linear approximation of



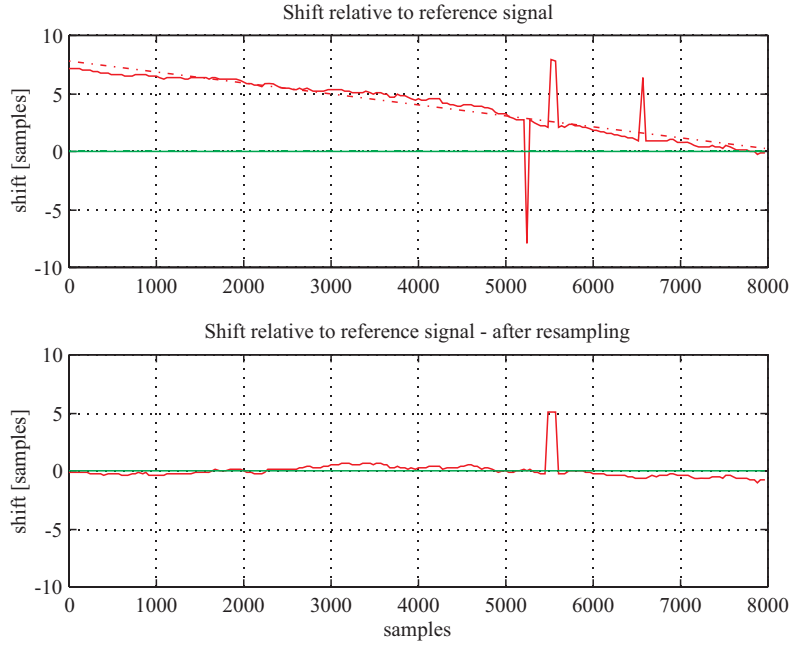


Abbildung 5.7: *Shift between profile (input/red) and averaged vertical wheel forces from axle 1 (output/green). Test run m0006r, Angern-Drösing.*

the numerically evaluated shift function. The total average change in shift  $\Delta S$  between the two signals is simply the value of the linear regression line at  $k = 1$  minus the value at  $k = 8000$ . Therefore,

$$\Delta S = 8000 \left( \Delta x_t^d - \Delta x_v^d \right) = 4000 (\alpha - \beta) = -7.52m. \quad (5.5)$$

Solving for  $\alpha - \beta$  we finally get a value of

$$\alpha - \beta = \frac{-7.52}{4000} = 0.00188m. \quad (5.6)$$

This means that the sampling intervals  $\Delta x_t^d$  and  $\Delta x_v^d$  show a difference of nearly  $2mm$  at a nominal value of  $\Delta x^d = 0.5m$ . It should be noted that no information is available to calculate absolute deviations  $\alpha$  and  $\beta$ , because there is no reference to absolute synchronization points. Nevertheless, the relative shift between the two data sets can be removed, even if we do not know the exact interval of the common sampling.

A straightforward although crude method to approximately synchronize the two signals is to simply round the local shift to the nearest integer and assign the properly shifted sample to the corresponding sample of the other signal. This method obviously results in simply omitting one sample every time the rounded shift function decreases by one. By looking at the shift between original input and its resampled version this effect becomes apparent. Although not visible in figure 5.7 due to the smoothing effect of the broad window ( $W = 2048$ ), a direct comparison between the original and the corrected signal with  $W = 64$  clearly shows the stepwise approximation of the linear shift function (figure 5.8). In spite of the three point interpolation the steps with plateaus at integer numbers are clearly visible. This approximation (besides nonlinearities) leads to the deviations found in the lower plot of figure 5.7. The erratic jumps around samples 5500 and 6500 are due to poor correlations because of weak excitation (the track quality is very high at these sections).

The lower plot of figure 5.7 indicates that the smoothed shift between the input and output signals does not exceed half a sample as it should be expected from the synchronization procedure.

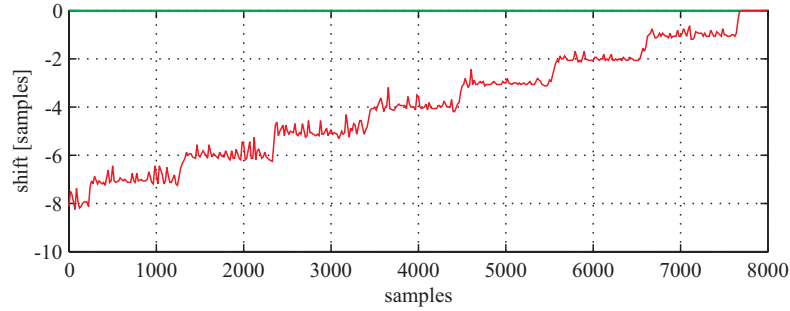


Abbildung 5.8: *Shift between original and resampled input. Linear shift removed, no oversampling. Test run ad7-0006.*

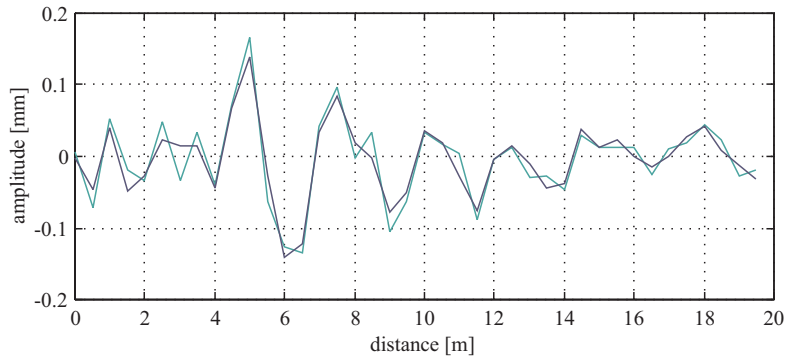


Abbildung 5.9: *Impulse responses for two correlation estimates. Green - order of prewhitening filter  $n=8$ , blue -  $n=16$ .*

If the model to be identified covers only the low frequency behavior this shift may be regarded as jitter. With this assumption the data sequences may be considered synchronized but an unknown constant shift still remains. If we can assure that this constant shift appears like a dead time, this dead time could be estimated with the model parameters. If, on the other hand, the shift makes the model to be identified noncausal, that model would not be of any physical meaning. Fortunately, by means of curvature and bogie twist signals we can already assure a causal model. By utilizing correlation analysis we can even get a more accurate and quick estimate of the shift (dead time) between the input and output signals.

### Linear Model Estimation

Figure 5.9 shows the estimated impulse response of the linear nonparametric model identified by correlation analysis. Two estimates are shown, the green one for a prewhitening FIR-filter of order 8 and the blue one for a filter of order 16. The prewhitening FIR-filter is used to model the input data as an AR-process of the respective order and to then filter both input and output data with it. The shift between data sequences (dead time) appears to be 9 samples (notice that the sampling interval is 0.5m). To verify this result a twofold approach is used: Firstly, linear parametric models with different structures and orders are identified in order to gain insight into the linear relation between input and output. Secondly, linear spectral estimates are used to validate the frequency response of the parametric models.

The performance indices of an output error (OE) model (red)

$$y(k) = \frac{B(q)}{F(q)}u(k - n_k) + e(k) \quad (5.7)$$

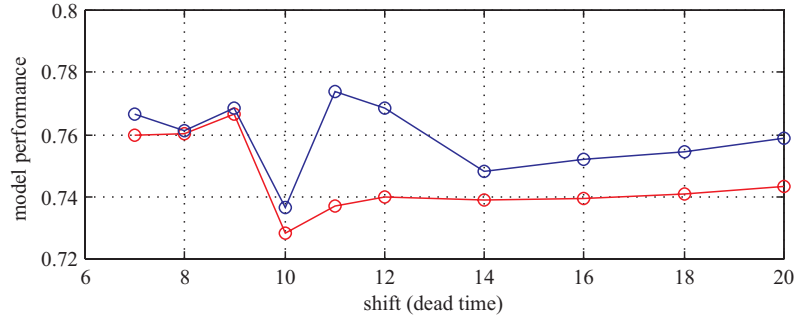


Abbildung 5.10: Performance indices over shift (dead time) for two 4th-order models. Output error (OE) model (red) and ARMAX model (blue).

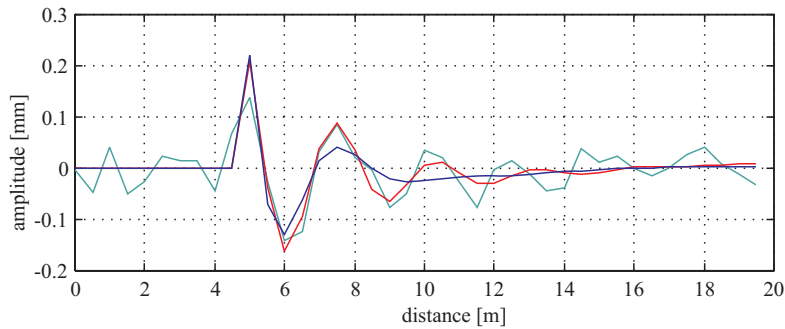


Abbildung 5.11: Impulse responses for OE (red) and ARMAX model (blue) versus correlation estimate with 16th-order prewhitening filter.

with  $B(q)$  and  $F(q)$  being polynomials of the unit-shift operator  $q$ ,  $n_k$  being the input-output delay, and an ARMAX model (blue)

$$y(k) = \frac{B(q)}{A(q)}u(k - n_k) + \frac{C(q)}{A(q)}e(k) \quad (5.8)$$

are depicted in figure 5.10. The output error model 5.7 had 4 poles and 3 zeros, the ARMAX-model 5.8 had 4 poles and 3 zeros in each transfer function. In both models  $n_k$  was varied from 7 to 20 and the coefficients of the polynomials were estimated by a prediction error/maximum likelihood method, by minimizing the error term  $e(k)$ . It is apparent from the minimum at an input-output shift of 10 that the shift detected by the correlation estimate is correct.

The impulse responses for the models with  $n_k = 10$  are depicted in figure 5.11. Especially the impulse response of the OE model (red) is in good agreement with the correlation estimate (green). The simulated output of these linear models still shows a lack in modelling the high frequency components of the measured output (see figure 5.12). Both models seem to capture the low to middle frequency behavior of the system to some extent, but the performance is certainly not satisfying. If the model order is not sufficient, the correlation functions of the model residuals  $\varepsilon(k) = y(k) - \hat{y}(k)$  ( $y(k)$  being the measured and  $\hat{y}(k)$  being the simulated output) should show some distinct deviations from their ideal shape. Model fits: oe4410-0.72804, amx44410-0.7366, amx66610-0.73284.

These deviations can indeed be found in figure 5.13. The autocorrelation function of the model residuals  $\varepsilon(k)$  should resemble that of white noise, i.e. at  $\tau = 0$  its value should be equal to the noise variance, and at all other values of  $\tau$  it should be zero or at least inside the 99% confidence intervals (indicated by dashed lines). The autocorrelation function (ACF) for the 4th-order OE model (red)

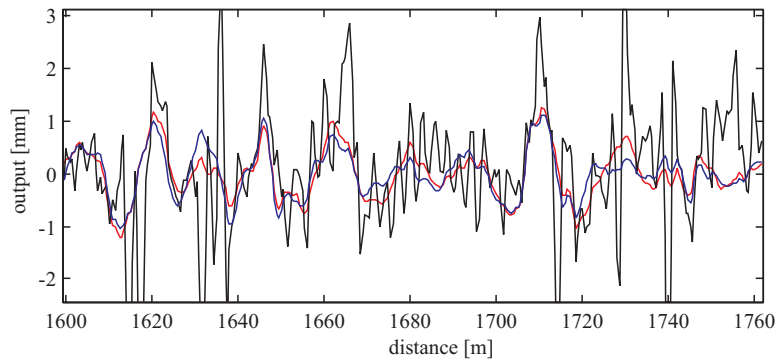


Abbildung 5.12: *Measured versus simulated model output. Measured output (black), OE model (red), and ARMAX model (blue).*

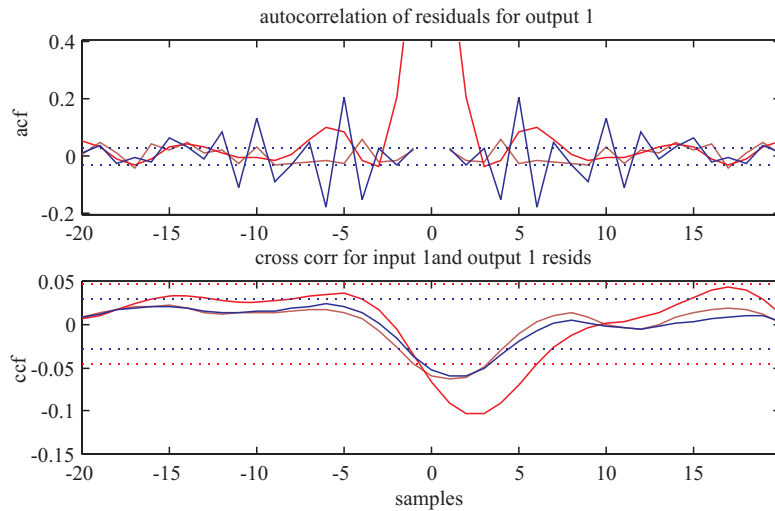


Abbildung 5.13: *Correlation functions of model residuals for 4th-order OE (red) and ARMAX model (blue), and 6th-order ARMAX model (brown).*

clearly shows that the model residuals still contain some information, while the ACF of the 4th-order ARMAX model (blue) is acceptable only on the average, showing multiple exceedances. A 6th-order ARMAX model (brown) is finally capable of modelling an appropriate noise filter, resulting in a nearly perfect ACF estimate. It should be noticed that a 6th-order OE model does not at all improve the residuals. However, the cross-correlation function (CCF) between input and model residuals, which should ideally be zero, deviates very significantly for all models. This may be a hint to a partially nonlinear dependency between input and output.

The frequency response of the different models together with a nonparametric spectral estimate is depicted in figure 5.14. The OE models of orders 4 (red) and 6 (cyan) are nearly indistinguishable, while the ARMAX models of order 4 (blue) and 6 (brown) show some differences in the magnitude. Nevertheless, the 6th-order ARMAX model resembles the OE frequency responses closer.

The smoothed Fourier transform estimate of the transfer function (orange) supports the main frequency characteristics of the parametric models. The strong high-frequency variance is due to the high frequency resolution. There is a deviation between the spectral and the parametric estimates only in the range between 0.9 and 1.3 rad/m. This might be due to the fact that the additional parameters of the 6th-order models are employed to model high frequency noise components above 4.5 rad/m. To overcome this problem input-output data are band-pass filtered, decimated to a

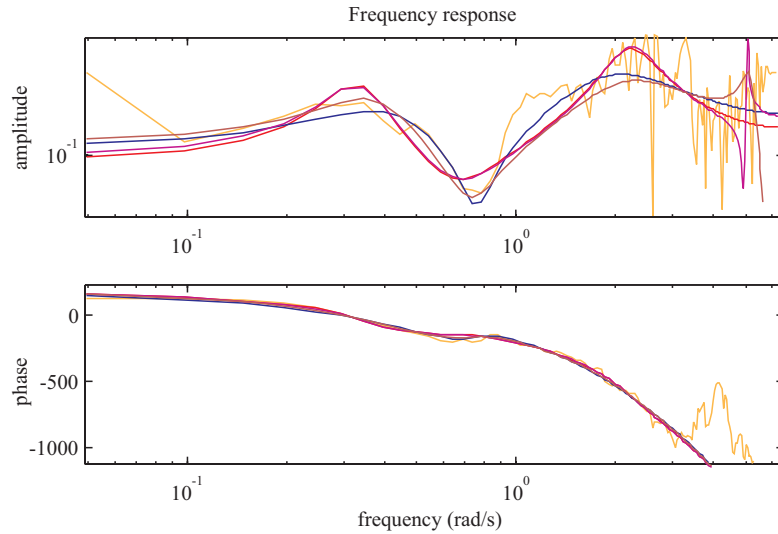


Abbildung 5.14: *Bode plot for different models. OE (red, cyan), ARMAX (blue, brown), and smoothed Fourier transform (orange).*

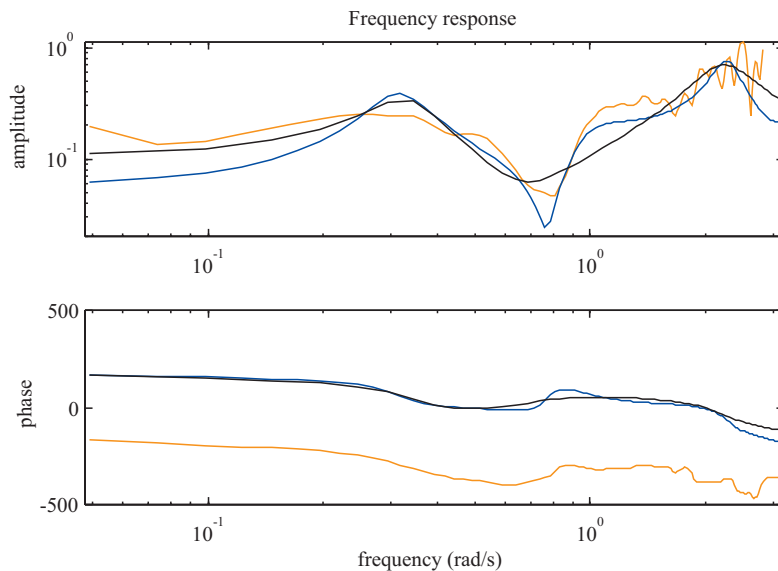


Abbildung 5.15: *Bode plot for different models. OE 6th-order  $\Delta x = 1m$  (blue), OE 6th-order  $\Delta x = 0.5m$  (black), and smoothed Fourier transform (orange).*

sampling interval of 1m, and the shift (dead-time) of 9 samples is removed. The procedure of band-pass filtering to produce more robust estimates is also used in other areas, e.g. speech recognition [25]. The resulting bode-plot can be seen in figure 5.15. The blue frequency plots correspond to the system identified with filtered data (OE 6th-order) and are in much better agreement with the spectral estimate (orange) than the OE system of same order but identified with the original data (black). The results in the frequency domain are supported by slightly smaller errors of the systems output predictions.

The transfer function  $G_{OE6}(s)$  of the 6th-order OE model identified with filtered data in continuous form is

	Location	Frequency [ $\frac{rad}{m}$ ]	Damping
<b>Poles</b>	$p_{1,2} = -0.1965 \pm j2.2762$	2.28	0.0860
	$p_{3,4} = -0.1942 \pm j0.9308$	0.951	0.204
	$p_{5,6} = -0.0570 \pm j0.3103$	0.315	0.181
<b>Zeros</b>	$z_{1,2} = -2.0917 \pm j1.5831$	2.62	0.797
	$z_{3,4} = -0.0276 \pm j0.7816$	0.782	0.0353
	$z_5 = -0.4093$	0.409	1
	$z_6 = +0.1870$	0.187	1
<b>Gain</b>	$k = 0.0855$		

Tabelle 5.1: Poles, zeros, and gain for 6th-order OE model from filtered data

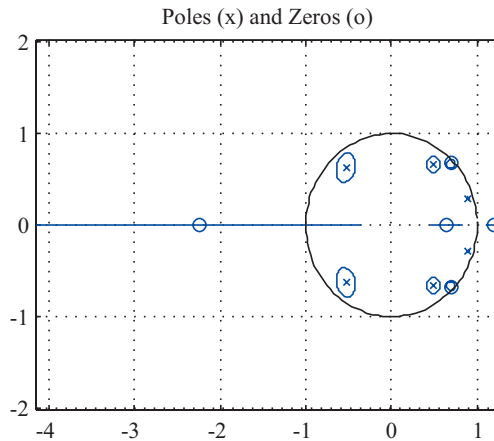


Abbildung 5.16: Poles and zeros for the 6th-order OE model from filtered data.

$$G_{OE6}(s) = \frac{0.085478s^6 + 0.38132s^5 + 0.73427s^4 + 0.37024s^3 + 0.36508s^2 + 0.060765s - 0.027539}{s^6 + 0.89513s^5 + 6.465s^4 + 3.1748s^3 + 5.6156s^2 + 0.77467s + 0.46974}, \quad (5.9)$$

which has poles, zeros, and a gain as listed in table 5.1. From the positive zero  $z_6 = +0.1870$  it is clear that the identified model is non minimum-phase. However, the step response does not show any significant influence of this positive zero. To check for pole-zero cancellation the poles and zeros of the original discrete-time system ( $\Delta x = 1m$ ) are plotted with their individual 99% confidence ranges. The resulting portrait is depicted in figure 5.16. From the non-overlapping confidence ranges it is obvious that pole-zero cancellation is very unlikely.

There is still the possibility that a noncausal model will give a better performance than the causal ones. Since all the computations are done off-line this would also be a way to reconstruct the output properly. However, there is no physical support for such a model.

To check whether the identified OE model of 6th-order is also consistent with respect to shift, between the simulated and the measured output correlation analysis is carried out again. The local cross-correlation (inside a moving window) is computed and the shift at which the global maximum occurs is plotted versus the center of the moving window just as outlined in section 4.2.1. The shift between the measured output (band-pass filtered and decimated to  $\Delta x = 1m$ ) and the simulated output from the linear model was evaluated. Input to the linear model was the measured input, which was also band-pass filtered and decimated to  $\Delta x = 1m$  matching the measured output signal. The resulting estimate of the shift function is depicted in figure 5.17. Most important is the fact that the relative shift between the two signals stays well within  $\pm 1$  sample, which is in agreement

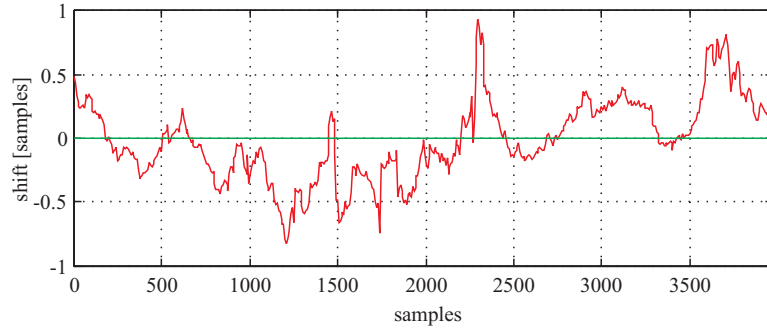


Abbildung 5.17: *Estimate of shift function between measured and simulated output for 6th-order OE model. Model oe660c, all measured signals were band-pass filtered and decimated to  $\Delta x = 1m$ .*

with the original input-output shift after resampling (see figure 5.7). Nevertheless, there are still strong deviations within that range, making it likely that an identified model will not be able to show correct dynamics in the high frequency range. But since the linear model is apparently able to correctly reproduce the middle to low frequency behavior, a low-pass filtered version of the shift function depicted in figure 5.17 could be used to resample the measured signals in order to get a better estimate. This process could then be repeated iteratively until a certain allowable shift is not exceeded. The main drawback of the situation without an absolute reference is that it can not be determined from the data itself which signal (input or output) is to be resampled according to the shift function. It may be one or the other, but probably both of them will contribute to the relative shift, since they both are sampled by the same principle. Still, if the relative shift is divided equally between both input and output signals (since we do not know of any other evidence) we will be able to reduce an existing shift to the half in the worst case.

### 5.3.2 Curved Track

In curved track additional reasons for wheel slippage arise which may aggravate the problem of synchronization: The nonstationary motion through transitions before and after curves with constant radii, and the negotiation of curves with constant radii. Due to the rigid axles and different rail lengths for the inner and outer side of the track, torsional stresses occur in the axle and are known to lead to high frequency oscillations which in turn let one or the other wheel slip on the rail in longitudinal direction. An indication of this process is given by the special form of the speed signal of the superstructure measuring coach. To check whether a connection between nonlinear shifts and curvature exist some test are performed in the following subsection.

#### Connection Between Shift and Curvature

As already explained in chapter 2 the speed signal exhibits distinct frequencies at multiples of the wheel circumference. Additionally, there is random noise superposed to the deterministic signal. If the variance of the speed signal is computed inside a moving window, an estimate of the local variance of the speed signal will result. In order to prevent deterministic low-frequency components from influencing the variance estimate, the speed signal has to be high-pass filtered. Data for curved track are taken from test run m1012-6117, Klagenfurt-Villach, km 127.03 - km 143.41.

From the spectra of speed signals the cut-off frequency of the high-pass filter was chosen to be  $0.1865 \text{ 1/m}$ . Since the Nyquist frequency is  $2\frac{1}{m}$  for track data, this corresponds to a dimensionless factor of  $\omega_n = \frac{0.1865}{2} = 0.09325$  used for design of a 5th-order high-pass Butterworth filter. The filtered speed signal is then used as input to a function which estimates the local variance by a moving window. The detrended output (normalized variance) is the red curve in figure 5.18 and the

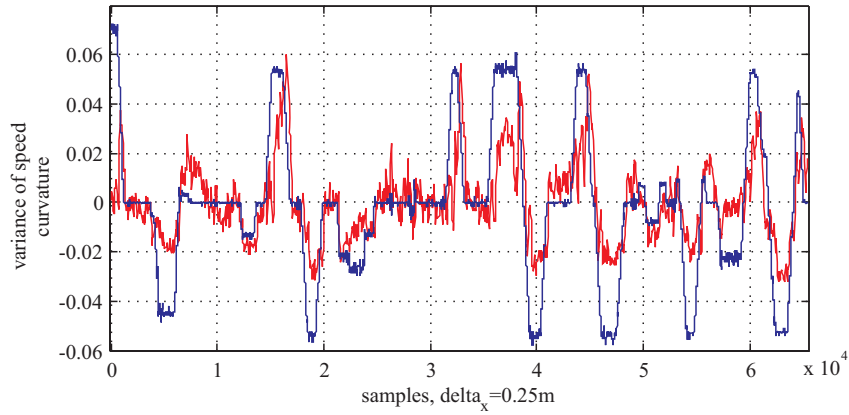


Abbildung 5.18: *Variance of speed signal (red) and curvature\*0.001 (blue).*

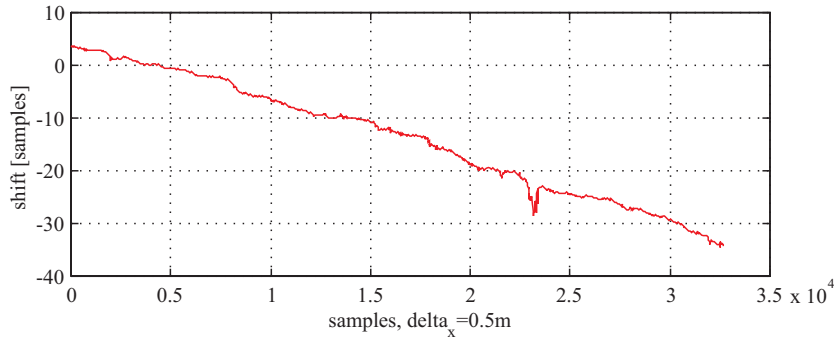


Abbildung 5.19: *Estimate of relative shift function for curved track. Computed with cant and difference of  $Q$ -forces.*

rescaled curvature (blue) clearly shows a strong correlation. For straight track a certain constant variance exists (which is normalized to zero in the plot), while for positive curvature an increase in variance and for negative curvature a decrease occurs. There are two possible explanations which actually both may contribute to this phenomenon: Firstly, it could simply be some asymmetry in the bogie setup, however, it may also be caused by the fact that the decoder for the wheel angle is located on one side of the axle. This setup could be more sensitive to slippage of the wheel on the side of the decoder than to slippage of the opposite wheel, therefore leading to the phenomena of varying variance.

In order to synchronize the data sets more efficiently both track and vehicle data are decimated to a common sampling interval of 0.5m. The signals used for synchronization are the band-pass filtered cant signal  $c(k) = l_l(k) - l_r(k)$  computed as the difference between left and right level signals  $l_l(k)$  and  $l_r(k)$ , respectively, and the difference of vertical forces acting upon axle 1:  $\Delta Q_1(k) = Q_{11}(k) - Q_{12}(k)$ . By use of a CCF-estimate both data sets were synchronized in average. The following local shift estimate reveals that the shift function depicted in figure 5.19 is basically linearly dependent on the distance but does not show an obvious correlation with curvature. However, figure 5.20 shows that a weak correlation exists. The blue graph is the rescaled curvature signal of the track while the black line is the first derivative of the above shift function estimate. Especially at the beginning and end of curve transitions the variance shows increases, although there are other sections without the corresponding curvature showing larger amplitudes.

For the purpose of comparison the same procedure is executed for band-pass filtered signals. This becomes necessary in the case of a linear identification of a SISO-model. Since the level and



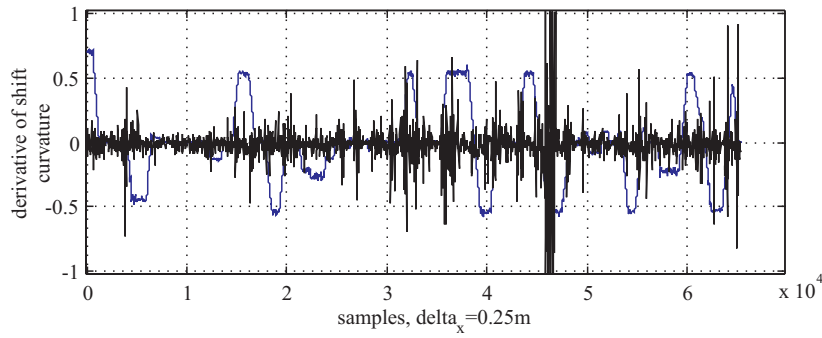


Abbildung 5.20: *Derivative of shift (black) and scaled curvature (\*0.01, blue).*

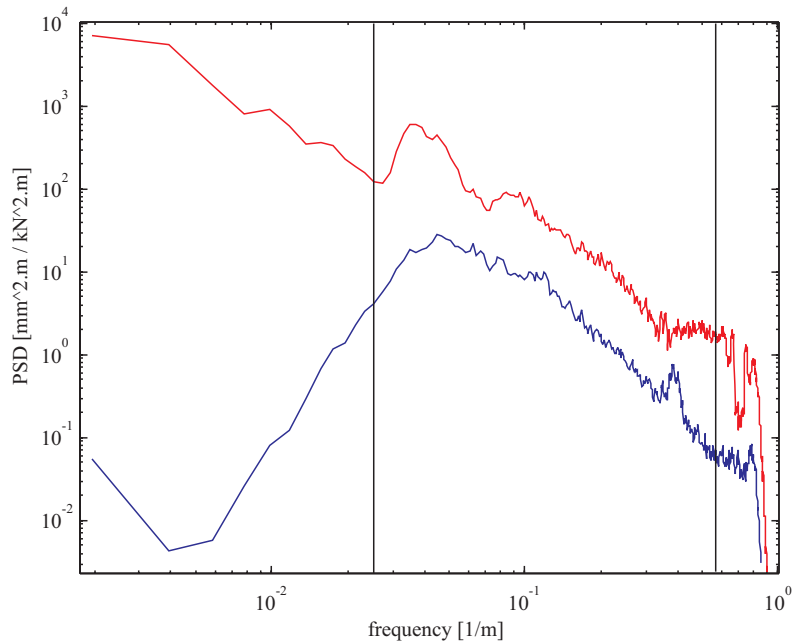


Abbildung 5.21: *Spectral estimates for cant (diff. of level signals, blue) and diff. of Q-forces at axle 1.*

therefore the cant signal  $c(k)$  are band-pass filtered, the output should be filtered in the same way to ensure that only the frequency range with good coherence is used for identification. Figure 5.21 shows spectral estimates of the input and output signals with cut-off frequencies indicated by black lines which arise quite naturally: The low cut-off frequency is chosen below the resonance peak of the force signal (red), while the high frequency counterpart is located right before the influence of the notch-filter. The spectra of figure 5.21 were calculated from decimated signals at  $\Delta x = 0.5m$ . The lower and upper cut-off frequencies of the filter are  $f_l = 0.0251 \frac{1}{m}$  and  $f_u = 0.5628 \frac{1}{m}$ , respectively. Because the Nyquist frequency is  $1 \frac{1}{m}$  the normalized cut-off frequencies stay unchanged:  $\omega_{nl} = \frac{0.0251}{1} = f_l$  and  $\omega_{nu} = f_u$ . If the so filtered signals are used as inputs for computation of a shift function the result is nearly indiscernible from the shift function obtained earlier. Figure 5.22 is virtually the same as figure 5.19, which indicates that only the frequencies inside the pass-band are necessary for an accurate shift estimate.

When the linear shift is removed by resampling of the input signal, the remaining shift between input and output signals still varies in a nonlinear manner (see figure 5.23). It should be noted that the remaining shift is much bigger than for the data of straight track (compare figure 5.17). The

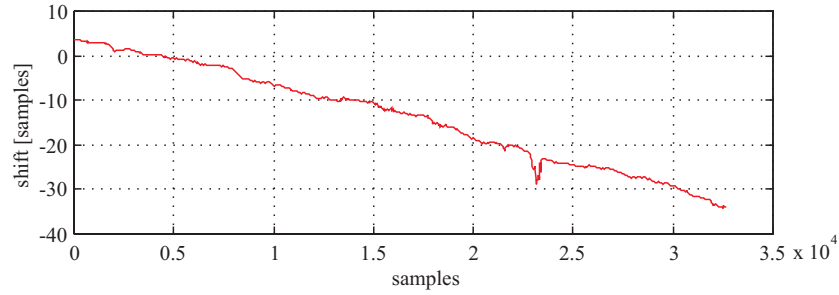


Abbildung 5.22: *Estimate of relative shift function for curved track. Computed with band-pass filtered cant and band-pass filtered difference of  $Q$ -forces.*

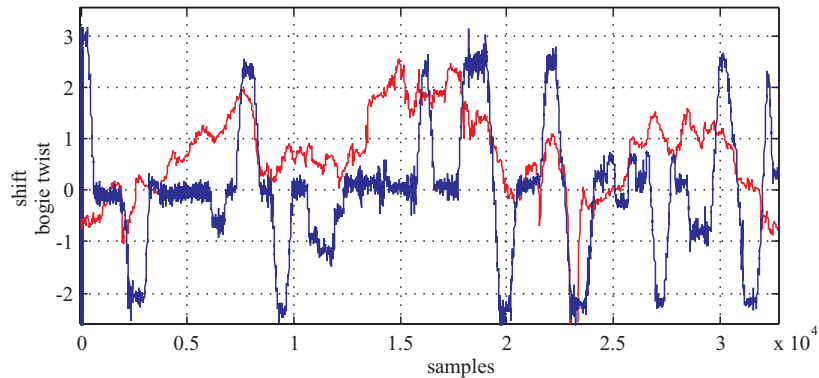


Abbildung 5.23: *Shift estimate from curved track with band-pass filtered signals after resampling (red) versus bogie twist  $\Psi$  (blue).*

blue function is the rescaled relative twist between bogie and car body  $\Psi_I$  plotted for orientation. Part of this effect might be the larger sample size of data for curved track. Since the shift covers a span between -1 and 2.5 samples a nonlinear resampling scheme seems appropriate. However, for subsections of the signals the current resampling might provide sufficient synchronization. The shift function after the nonlinear resampling algorithm has been applied in fact shows a much smaller deviation. As can be seen from figure 5.24, the shift stays well within a band of  $\pm 0.4$  samples except for some outliers. Again, some discontinuities in the shift function seem to be correlated with curvature, although the underlying pattern is difficult to detect.

### Linear Model Evaluation

A comparison of identification results for data sets with linear and nonlinear resampling illustrates the difference in performance. Four data sets have been used: `curv_l`, `val_l`, `curv_nl`, and `val_nl` contain data from linear resampling and nonlinear resampling, respectively. Each data set used for identification has a corresponding validation data set (samples 14001:18000). Data for identification were taken from samples (4011:13010) for input (difference of level signals), and from samples (4001:13000) for output (difference of  $Q$ -forces on axle 1). All signals have been band-pass filtered as described above.

Just like in the case of the linear identification with data from straight track, the constant dead time (shift) between input and output was assessed by correlation estimates with different orders of prewhitening filters. A plot of the impulse response with a correlation estimate and two different output-error models can be seen in figure 5.25. Comparing it to figure 5.11 it seems as if the gain would have been reversed. However, this effect could also be caused by the non-minimum

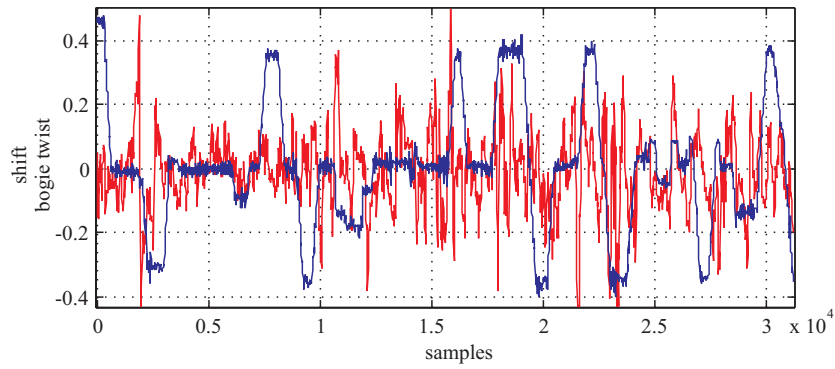


Abbildung 5.24: *Shift function for nonlinearly resampled band-pass filtered signals (red) versus bogie twist  $\Psi$  (blue).*

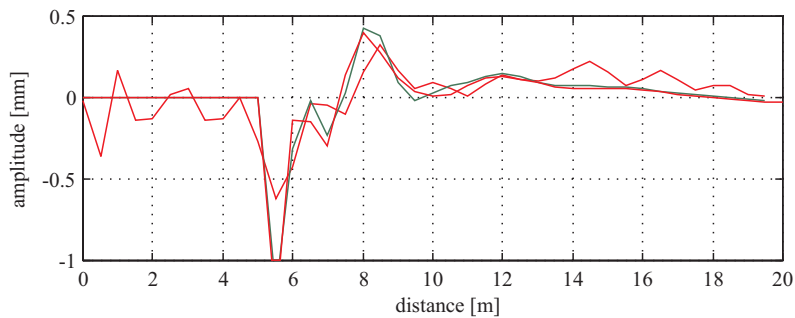


Abbildung 5.25: *Impulse response for linearly resampled data from curved track. 6th-order correlation model (orange), 6th-order OE model with dead-time of 11 samples (red), and 6th-order OE model with dead-time of 10 samples (green).*

phase structure of the models whose responses are depicted in figure 5.11. Two models of identical structure (except for the varying time delay) were identified for both data sets. They consisted of a 6th-order output-error model and an 6th-order ARMAX model. Both had 5 zeros in the system transfer function, the ARMAX system uses 4 zeros in the noise transfer function.

The results of the model validation with data not used for identification are depicted in figures 5.26 (linear resampling) and 5.27 (nonlinear resampling). From the two plots it is already obvious that the nonlinear resampling results in a data set which allows for better model fit. Moreover, regardless of the training data used, the nonlinearly resampled validation data always gives better performance. The performance measured as the mean square fit is listed for each model with both data sets in table 5.2. From the data in this table it is apparent that the nonlinearly resampled validation data yields better results than the other data set. However, this is true for all models regardless of their training data. As a matter of fact, the absolutely best performance is delivered by the output-error model trained on the linear resampled data set. The reason for this unexpected result might be that the ability of generalization of the model is enhanced by slightly distorted learning data. This speculation is supported by results from noisy learning data in neural networks [24].

Although the model performance in predicting the output is fairly good considering the nonlinear nature of the underlying system, the model residuals reveal that the unexplained dynamics are far from being a white process. As can be seen in figure 5.28 the autocorrelation functions (ACF) of the model residuals is especially bad for the output-error models, while those the ARMAX models are at least in average equivalent to the ACF of white noise. The cross correlations between input

Trainings Data	Model	Validation Data	
		Linear Resampling	Nonlinear Resampling
Linear Resampling	oe6610	3.10	2.77
	amx66511	3.36	3.12
Nonlinear Resampling	oe669	3.38	2.81
	amx66510	3.62	3.22

Tabelle 5.2: Mean square fits for different models

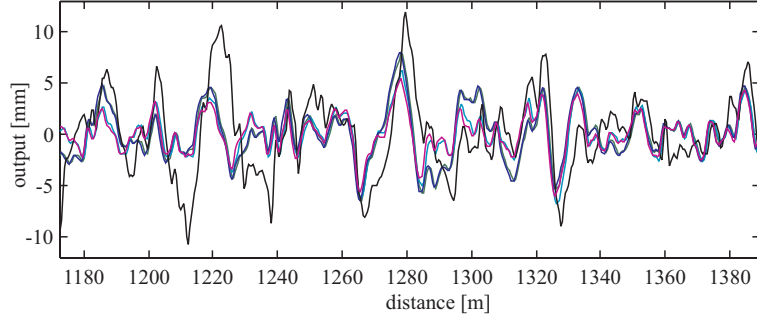


Abbildung 5.26: Simulated outputs and measured output with linear resampling.

and residuals show unexplained dynamics for all models. There is also a big difference to data from straight track in the bode plot. One effect is the differing speed, which affects the bode diagram since the data under investigation are sampled in the spatial domain whereas the system dynamics have constant frequencies in the time domain. If this would be the only difference, it would lead to a shift of the whole bode plot to the left or right without altering the appearance of the functions. It is equivalent to a rescaling of the frequency axis. The nominal speed of data for straight track is 60 km/h while for data from curved track it is 80 km/h. The eigenfrequency of some slightly damped pair of poles in the vehicle dynamics shall be denoted by  $f_e$  [ $\frac{1}{s}$ ]. Then the frequency in the spatial domain is  $f_s = f_e \cdot \frac{3.6}{60}$  [ $\frac{1}{m}$ ] for straight track and  $f_c = f_e \cdot \frac{3.6}{80}$  [ $\frac{1}{m}$ ] for curved track. Obviously, the frequency in the spatial domain gets proportionally smaller with higher speeds. This means that the bode plots of figure 5.14 should simply be shifted to the left by a factor of  $\sigma = \frac{f_c}{f_e} = \frac{60}{80} = 0.75$  if no other differences exist. However, figure 5.29 clearly shows a different picture from the bode plots of the straight track data. First of all, there is the band-pass nature of input/output data, leading to strongly attenuated high- and low-frequency tails. Moreover, the distinct notch is situated at a totally different frequency which cannot be explained by the frequency shift due to higher speed because it now lies at a higher frequency instead of a lower one. The same is true for the

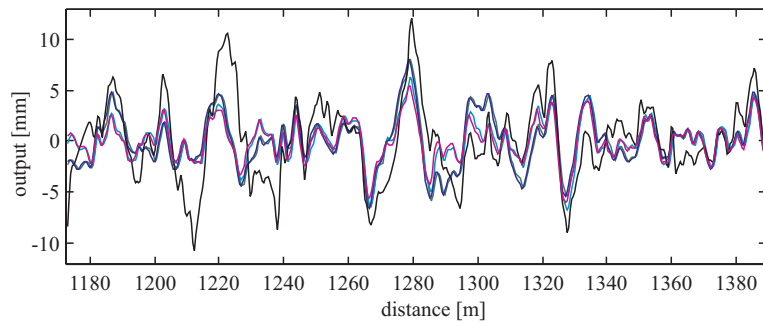


Abbildung 5.27: Simulated outputs and measured output with nonlinear resampling.

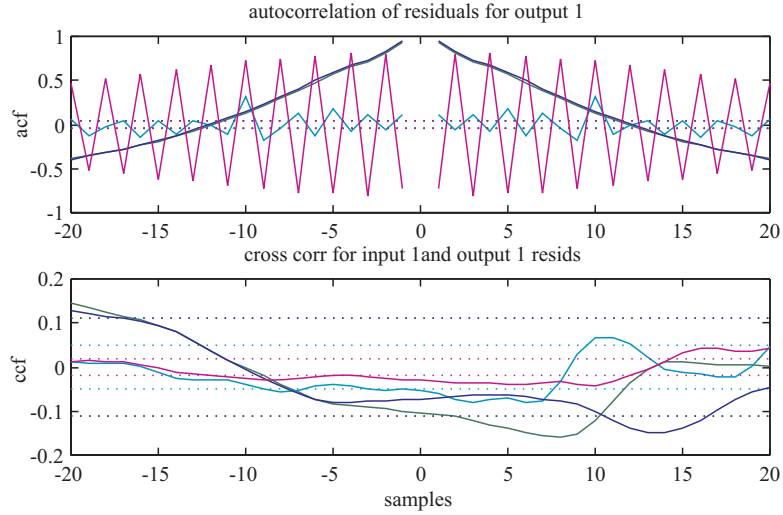


Abbildung 5.28: *Model residuals for output-error and ARMAX models. Validation data from non-linearly resampled signals.*

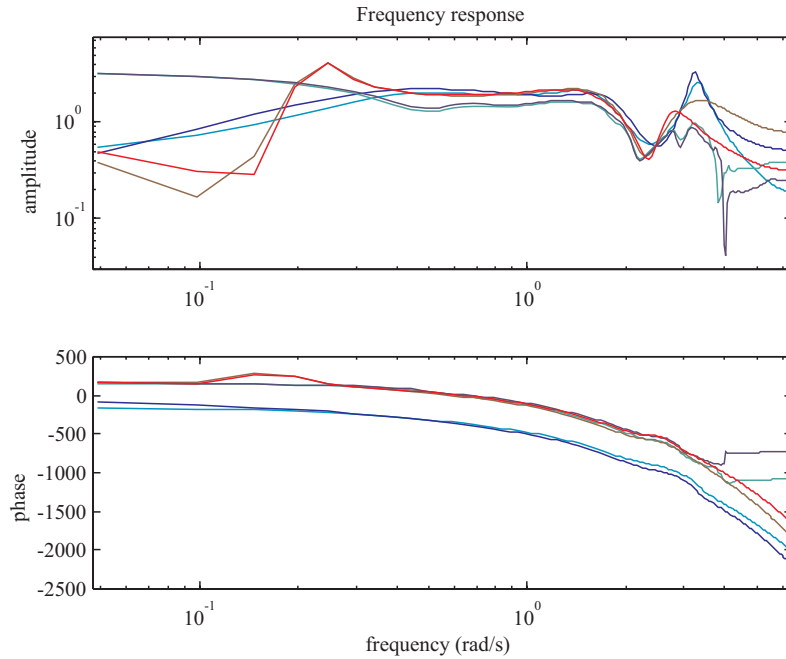


Abbildung 5.29: *Bode plots for spectral estimates, OE, and ARMAX models.*

high-frequency peak which has also moved up. Only the low-frequency peak could correspond to the same poles, since it moved to a lower frequency at approximately the predicted factor  $\sigma$ .

The transfer function  $G_{OE6}(s)$  of the model OE6610 in the continuous time domain without dead-time is

$$G_{OE6}(s) = \frac{0.8004s^5 - 8.9421s^4 + 0.72382s^3 - 49.0419s^2 - 0.6916s - 0.67121}{s^6 + 2.4961s^5 + 15.1276s^4 + 15.7481s^3 + 32.6531s^2 + 2.601s + 1.5311} \quad (5.10)$$

with poles, zeros, and gain as listed in table 5.3. A check of the 99% confidence intervals shows that pole-zero cancellation is very unlikely. Again, this system is non-minimum phase as caused by the right-hand plane zero  $z_5$  at 11.55. The location of poles and zeros is analog but far from

	Location	Frequency [ $\frac{rad}{m}$ ]	Damping
<b>Poles</b>	$p_{1,2} = -0.7213 \pm j3.1686$	3.25	0.222
	$p_{3,4} = -0.4966 \pm j1.6406$	1.71	0.290
	$p_{5,6} = -0.0302 \pm j0.2201$	0.222	0.136
<b>Zeros</b>	$z_{1,2} = -0.1835 \pm j2.2930$	2.30	0.0798
	$z_{3,4} = -0.0072 \pm j0.1169$	0.117	0.0613
	$z_5 = +11.5535$	11.6	1
<b>Gain</b>	$k = 0.8004$		

Table 5.3: Poles, zeros, and gain for 6th-order OE model from filtered data

identical to those of the model for straight track as listed in table 5.1. There is no good agreement between the frequencies of complex poles in the respective models. This has to be expected from the already differing shapes of the bode plots.

Another validation of the better data set can be made by use of coherence functions. The coherence functions were estimated from decimated data sets in order to extend the low-frequency range. Coherence functions were calculated by Welch's periodogram method with a window of 512 samples and a 1024 point FFT. The resulting coherence functions between linearly resampled cant (red) and difference of  $Q$ -forces as well as for nonlinearly resampled cant (blue) and the same output are depicted in figure 5.30. The coherence is generally poor ( $<0.85$ ), especially at the closely spaced wavelengths of  $34.2m$  and  $31.7m$  which lie right inside the distinct notch, as can be seen by a window and FFT of 1024 points. These frequencies are exactly the same as the resonance peaks found in the spectra of the  $Q$ -forces. Since these peaks are very pronounced in the output without having a corresponding amplitude in the input at the same frequency the coherence is very poor ( $\approx 0.1$ ). A possible explanation is an eigenmode of the car body, which should exhibit a constant frequency in the time domain and therefore a frequency in the spatial domain varying with speed. However, regardless of the speed the resonance peaks of the  $Q$ -force spectra always come to lie at the same spatial frequency. A possible cause for this behavior could be a nonlinear limit cycle with a fixed spatial frequency just like the sine run of the bogie. The two closely spaced wavelengths from above would then correspond to the wavelengths of the sine runs of the two bogies of the car, which are of identical construction but may differ slightly in their respective parameters (springs, dampers, friction).

Nevertheless, the coherence functions of figure 5.30 show that an improvement was achieved by the nonlinear resampling over a broad bandwidth. Only at the lower cut-off frequency of the band-pass filter the linearly resampled data is clearly better. This part of the spectra does not contribute to the dynamics of the model. This is illustrated by the frequency of the dominant pair of poles  $p_{5,6}$  at  $0.035\frac{1}{m}$  which is indicated by the vertical red line in figure 5.30. Only the pair of zeros  $z_{3,4}$  are lying at a lower frequency. A simple comparison of the average value of coherence  $\bar{c}_i$  between the wavelengths of  $114m$  and  $2.88m$  gives results of

$$\bar{c}_{lin} = 0.461 \quad (5.11)$$

$$\bar{c}_{nonlin} = 0.486, \quad (5.12)$$

which shows more than a 5% improvement. It should be noted that the averaging of discrete points of the coherence estimate effectively implements an exponential weighting along the frequency axis since the FFT points are more closely spaced at higher frequencies.

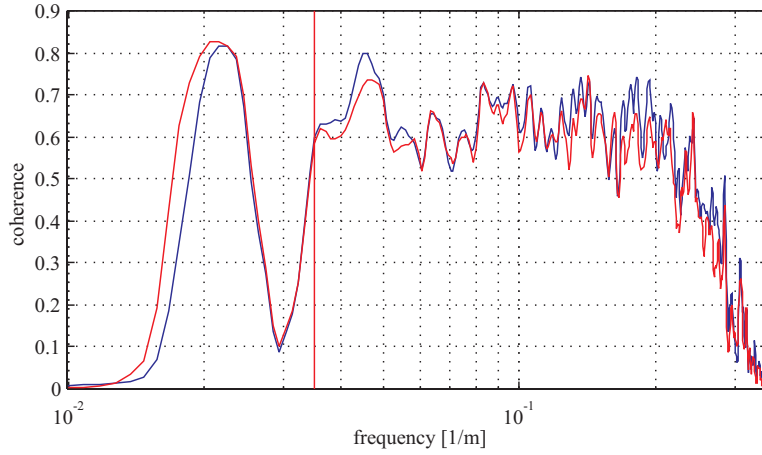


Abbildung 5.30: *Coherence functions for linearly (red) and nonlinearly (blue) resampled cant and difference of  $Q$ -forces.*

## 5.4 Comparison of Synchronization Methods

When the model based synchronization algorithms were outlined in section 4.6 the answer to the question which signal would be resampled in each iteration was left open. It could be either the measured input  $u(k)$  or the measured output  $u(k)$ . To evaluate which version of the model based synchronization algorithm is more efficient the following tests were performed. Data for this comparison were taken from curved track, test run m1012-6117, Klagenfurt-Villach, km 127.03 - km 143.41. Data used for synchronization are band-pass filtered difference of level  $c_f(k)$  (cant) as input and difference of  $Q$ -forces  $\Delta Q_f(k)$  on axle 1 as output.

At first, the linear shift estimated by cross-correlation functions is removed from the cant signal  $c_f(k)$  yielding the signal  $c_l(k)$ . With the new cant signal  $c_l(k)$  the average shift between cant and difference of  $Q$ -forces is zero although a nonlinear shift still remains. The cant signal with this nonlinear shift also removed is named  $c_{nl}(k)$ . This signal is actually computed by estimating the relative shift between  $c_f(k)$  and  $\Delta Q_f(k)$  and correcting the local shift after interpolation by a factor of 3. Therefore, by definition the relative shift between  $c_l(k)$  and  $c_{nl}(k)$  should be identical to the relative shift between  $c_l(k)$  and  $\Delta Q_f(k)$ . In both cases only the nonlinear component of the shift with zero mean should be present.

The model based synchronization is applied to signal pairs  $c_l(k)$  and  $\Delta Q_f(k)$  only. As explained in section 4.6 the average shift has to be removed before the algorithm can be applied since use of the signals  $c_f(k)$  and  $\Delta Q_f(k)$  does not lead to a converging algorithm. The corrected input using this approach is named  $u_c(k)$  while the corrected output is named  $y_c(k)$ . Parameters used for the synchronization are an OE model of order [6 6 1], a moving window of 512 samples length ( $256m$ ), and cross-correlations used for shift estimation.

If the results from the different algorithms and corrections are consistent the shift estimate between the original input to the algorithms and the corrected signal should be the same for all versions (i.e. the nonlinear zero mean shift component). Furthermore, identifications using the different input-output pairs should give equal performance. The relative shifts between the original and the corrected signals are depicted in figure 5.31. Model based shifts (blue, green) are practically identical since the same criterion and resampling algorithm is used in both cases. However, note that the corrected signal for model based algorithms is either the input  $c_l(k)$  or the output  $\Delta Q_f(k)$ . There is a very good agreement between the model based shifts and the correlation based shift (red) from the start to sample 4200 but there are some major deviations above that position. The difference ranges up to 1 sample which is quite influential for an identification. From figure 5.31

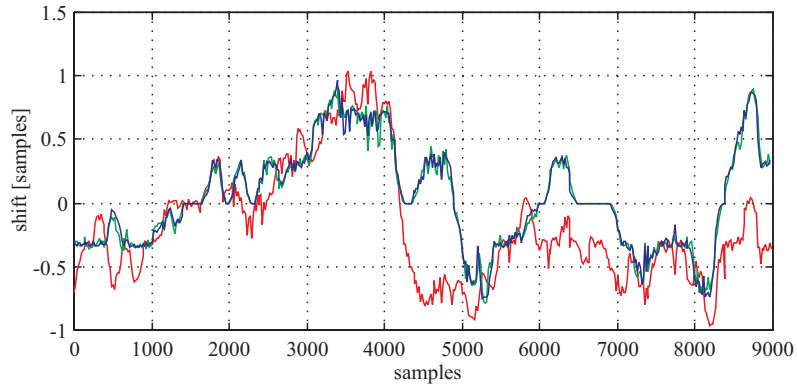


Abbildung 5.31: *Shift between original and corrected signals.  $c_f(k)$  versus  $c_l(k)$  (red),  $c_l(k)$  versus  $u_c(k)$  (blue),  $\Delta Q_f(k)$  versus  $y_c(k)$  (green, negative shift plotted).*

Data Set	Signals	Training Data	Validation Data
$S_{corr}$	$c_{nl}(k)/\Delta Q_f(k)$	1:6000	6001:9000
$S_{yc}$	$c_l(k)/y_c(k)$		
$S_{uc}$	$u_c(k)/\Delta Q_f(k)$		

Tabelle 5.4: *Data structure for comparison of synchronization methods*

alone it can not be decided which algorithm is more accurate in these sections.

To compare the performance of the different algorithms the results from linear identification procedures are investigated. Data were divided in three input-output pairs each with separate training and validation sequences. The data structure is listed in table 5.4, sample ranges correspond to the variables stored in the file 'kv6\_02.mat'. Three different LTI models were identified for each data set: A smoothed Fourier transform as a nonparametric model, an ARMAX model of orders [6 6 3 1], and an OE model of orders [6 6 1]. for identification. The mean square fit between the simulated and the measured output was evaluated for each parametric model with every validation data set giving a total of 18 performance numbers. The results are listed in table 5.5. In each cell the first number corresponds to the OE model and the second number refers to the ARMAX model. The italic numbers in the cells immediately neighboring the data set's names constitute the mean values of fits from rows, columns, and the diagonal, respectively. These results can be interpreted in different ways: First, by comparing the results columnwise it becomes apparent that the two models perform differently regarding the training data set. While the OE model shows a rather robust performance with respect to different training data the ARMAX model performs clearly worse with the  $S_{yc}$  training data set. As a matter of fact, this is also the training data set which achieves best performance for the OE model. The overall performance of the OE model is better for all training data sets. The comparison of mean values for validation data does not show

		Training Data			
		$S_{corr}$	$S_{yc}$	$S_{uc}$	
		<i>2.71/2.95</i>	<i>2.79/2.91</i>	<i>2.72/3.21</i>	<i>2.74/2.80</i>
Validation Data	$S_{corr}$	<i>2.77/2.99</i>	<i>2.73/2.87</i>	<i>2.79/3.24</i>	<i>2.80/2.86</i>
	$S_{yc}$	<i>2.73/2.96</i>	<i>2.81/2.93</i>	<i>2.68/3.19</i>	<i>2.70/2.77</i>
	$S_{uc}$	<i>2.75/2.97</i>	<i>2.83/2.94</i>	<i>2.70/3.20</i>	<i>2.71/2.78</i>

Tabelle 5.5: *Best fits for OE and ARMAX models: All combinations of training and validation data*



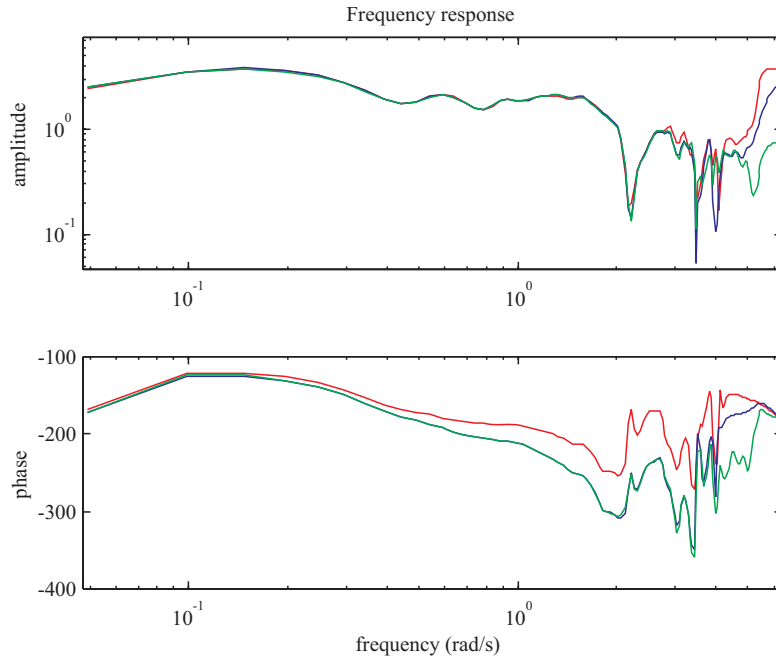


Abbildung 5.32: *Spectral Estimation. Smoothed Fourier transform models for the data sets  $S_{corr}$  (red),  $S_{yc}$  (green), and  $S_{uc}$  (blue).*

a distinctive variation. Overall performance of the OE model is again superior and both models show best performance with a validation data set of  $S_{yc}$ . Mean values of the diagonal indicate that the OE model will give best results when validated with the same type of data set as the training data. As already mentioned, the ARMAX model achieves best results with training data  $S_{uc}$  and either  $S_{yc}$  or  $S_{uc}$  as validation data. The overall best performance is given by the OE model using  $S_{yc}$  for both training and validation.

It seems that the OE model is preferable to the ARMAX model since it shows a more robust and superior performance. Furthermore, the model based synchronization methods give better results than the pure correlation method. However, these favorable results are certainly caused by the fact that the OE model was already incorporated in the model based synchronization procedure. The data sets  $S_{yc}$  and  $S_{uc}$  are therefore tailored for a good performance with this model. Still, the OE model outperforms the ARMAX model with the  $S_{corr}$  data set. This is a more reliable indicator that the OE model is in fact better for the current objective.

Another type of model is used to verify that the differences between the data sets actually influence the identification results. The bode plots depicted in figure 5.32 were derived from smoothed Fourier transform models from the training data. No validation data is used for comparison. From the shapes of the different models two major differences become apparent: First, only for frequencies above  $0.55 \frac{1}{m}$  ( $3.48 \frac{rad}{m}$ ) the differences in magnitude become important, and second, the phase clearly shows a difference between the model for the  $S_{corr}$  data set (red) and the model based data sets  $S_{yc}$  (green) and  $S_{uc}$  (blue). The frequency of  $0.55 \frac{1}{m}$  does not accidentally match the cut-off frequency of the band-pass filter for the data sets ( $f_c = 0.563 \frac{1}{m}$ ). Strongly varying models above the higher cut-off frequency of the band-pass filter are not surprising at all since the coherence between input and output will be very small. The difference in phase mentioned above looks like a gradually additional drop for  $-90^\circ$ , a phenomenon which is probably caused by the model based algorithms who could easily introduce such a delay. To verify this, bode plots of all OE models, the ARMAX model from  $S_{corr}$  data set, and the spectral estimate from  $S_{yc}$  are compared in picture 5.33. The phase plot reveals that the OE models from data sets with model based synchronization

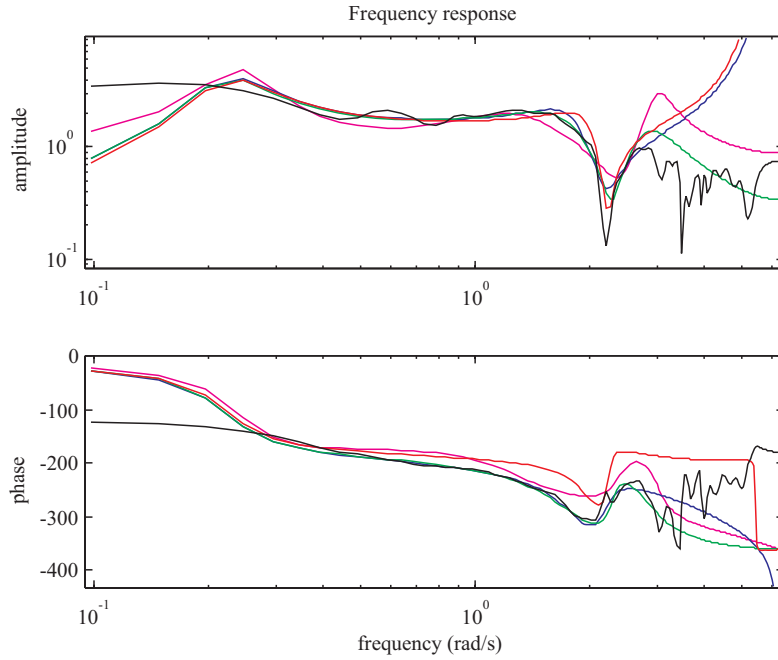


Abbildung 5.33: Bode plots for different models. Smoothed Fourier transform from  $S_{yc}$  (black), OE models from  $S_{corr}$  (red),  $S_{yc}$  (green), and  $S_{uc}$  (blue), and the ARMAX model from  $S_{corr}$  (magenta).

actually (blue, green) actually fit the phase of the spectral estimation from  $S_{yc}$  (black) over a broad range. Deviations occur only outside the bandwidth of the band-pass filter initially applied to all data sets. However, the OE model from the  $S_{corr}$  data set shows a smaller drop of phase in the region around  $1.69 \frac{rad}{m}$  although the fit in the high-frequency region is definitely bad. These findings seem to confirm two characteristics of the model based algorithms in the present application: They show a capability of synchronizing up to much higher frequencies than pure correlation algorithms (especially with higher-order model structures), and they imprint the frequency characteristics of their model on the data set. Nevertheless, this imprint need not be a disadvantage since the model dynamics are optimized to fit the data, and the final objective is to find a model with the best fit, no matter how the data were synchronized. This synchronization process could be seen as a part of the model - it may not produce absolutely true data but it will optimize the ability of the model to predict outputs. Figure 5.33 also shows that the ARMAX model from data set  $S_{corr}$  is not able to properly model the zeros and the resonance peak around  $2.5 \frac{rad}{m}$ . This model structure is apparently inferior to the OE models in this application.

## 5.5 Absolute Shift in Measured Data

Although simulations in section 4.4 did not yield encouraging results the algorithm derived there is also tested on real measurement data. Data for the calculations were taken from the portion of track described in the previous section. Decimation and band-pass filtering were also conducted according to that section.

First, the influence of band-pass filtering on the data is evaluated. Original data were decimated to a sampling interval of  $\Delta x = 0.5m$  for all signals. The AR model used for calculation was of order 7, the length of the moving window was 628 points, and the AR model was evaluated at 400 evenly spaced points along the signal (corresponding to an overlap of the windows of 87%). The comparison of the estimates of the absolute shift  $\hat{\sigma}_i(k)$  (see equation 4.48) for the input function  $c(k) = l_i(k) - l_r(k)$  (cant of the track) in original and band-pass filtered form is shown in figure

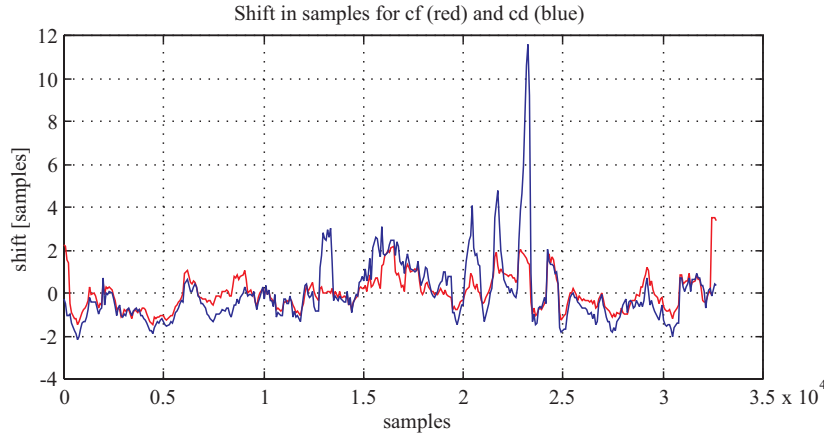


Abbildung 5.34: *Shift functions for original (blue) and band-pass filtered cant signal (red).*



Abbildung 5.35: *Shift functions for original (blue) and band-pass filtered force differences (red).*

5.34. For the purpose of easier comparison the values of the absolute shift functions are expressed in samples (i.e., the functions plotted are actually  $\Delta x \hat{\sigma}_i(k)$ ). They are in good agreement, although the shift estimate of the original function shows much higher peaks at some sections. The good correlation between the two versions can be explained by the inherent band-pass nature of the level signals which is transferred to the cant signal. The differences between the two versions of the output signal  $\Delta Q_1(k) = Q_{11}(k) - Q_{12}(k)$  (difference of vertical wheel forces) proof to be much more distinctive. Since the wheel force signals are low-pass filtered, the procedure of band-pass filtering strongly affects the spectral shape. Hence, the AR-estimates are clearly different as can be seen in figure 5.35. The shift estimate of the original signal (blue) obviously shows some erratic spikes over a nearly constant course. On the other hand, the estimate of the band-pass filtered signal (red) strongly resembles the shapes of the estimates for the input (depicted in figure 5.34). This allows for the conclusion that band-pass filtered signals are better suited for calculation of shift function estimates in practice. Following the reasoning of the previous section, the cumulative sum of the difference between absolute shifts  $\sigma_i(k)$  plus a constant should equal the relative shift  $s_{uy}(k)$  (equation 4.65). If we compute this cumulative sum for the band-pass filtered signals the estimate depicted in figure 5.36 arises. In this figure the scaled estimate from absolute shift functions is plotted in red, and the relative shift function (blue) with the linear trend removed is added for comparison. It is obvious that the relative shift estimates do not agree well. There is just one feature common to both estimates which is the negative peak at approximately sample 23000. The poor correlation between the two estimates should be evaluated in the light of absolute shift values:

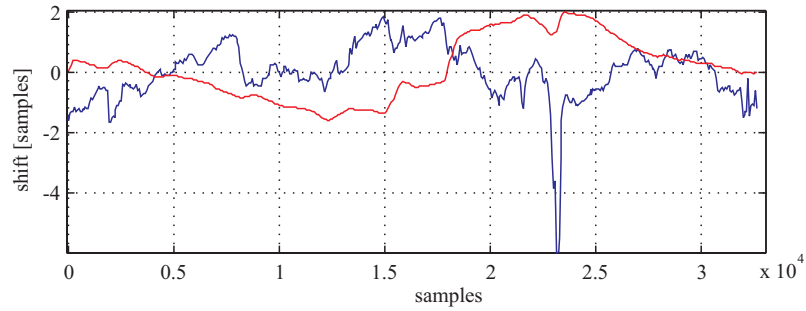


Abbildung 5.36: *Comparison of shift functions. Cumulative sum of the difference of absolute shifts (red) and relative shift (blue), respectively. Input cant  $c(k)$ , output difference of  $Q_1$ -forces  $\Delta Q_1(k)$ .*

Except for the peak mentioned above the relative shift estimate stays well within the  $\pm 2$  sample range. This is quite a small value for a detection by use of absolute shift functions, and the data from this application might not show the predicted correlation. Nevertheless, figure 5.36 clearly shows that the absolute shift estimates are not reliable for detection of shifts smaller than at least 2 samples.

## Kapitel 6

# Identification of Vehicle Dynamics

The identification of railway vehicle dynamics is especially difficult due to the nonlinear character of the rail-wheel interaction [29]. Although the dynamic model for other rail guided vehicles is also nonlinear (e.g. electromagnetic levitation system in Transrapid [30, 31]) the classic railway superstructure has to be modelled as a dynamic structure [51], thus complicating a detailed modeling procedure considerably. Nevertheless, several suitable black-box approaches exist, one of them being ANNs. ANNs can be utilized to model dynamic systems [23, 38] using different types of network structures. Either classic feedforward structures [35], Hammerstein model structures [1], or Radial Basis Function networks [13] have been shown to produce excellent results.

Due to serious systematic errors in the measurement data the identification part of the current work has to be limited in nature. In this chapter procedures to estimate the optimal model order a priori and after identification are presented. Then, some basic procedures of identification are demonstrated for wheel-rail forces. The whole chapter rather shows the limitations of the current data sets and therefore, it does not give an exhaustive investigation.

### 6.1 Model Order Tests

Finding the optimal model orders is very important for every identification. A model of low order will converge (learn) fast and usually show robustness with respect to parameter changes. On the other hand, a certain minimal order will be necessary to ascertain a performance criterion. In general, the model order is increased from a small number until the performance criterion is met. In neural networks a different approach is also feasible, where the number of parameters is decreased after the training - this procedure is called pruning [43].

#### 6.1.1 Model Order Estimation Using Lipschitz Coefficients

The theoretical background and the corresponding reference is given in appendix B. Data investigated in this section were taken from a test run on the section Klagenfurt-Villach. The input to the algorithm are the difference of level signals as system input and the difference of  $Q$ -forces as system output. Both signals were band-pass filtered. Figure 6.1 shows the plot of the Lipschitz coefficients with increasing model order. System input was the difference of level signals, output was the difference of  $Q$ -forces at axle 1. The plot shows the typical function for system with low signal to noise ratio. As shown in appendix B, in the presence of noise the values of the coefficients show a monotonous decrease without a significant minimum or even a saturated range. The number of samples used for this first computation was 2000. To ascertain that the number of samples is not a limitation to the achievable accuracy the procedure was repeated with signal lengths of 4000 samples the resulting plot is shown in figure 6.2. Although the absolute values of

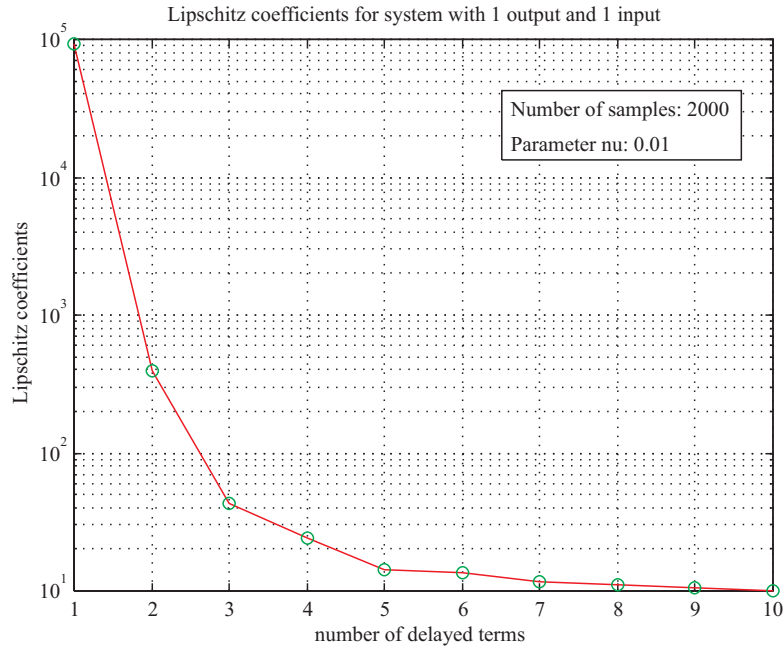


Abbildung 6.1: *Estimates of Lipschitz coefficients for different orders. Inputs are difference of level signals and difference of  $Q$ -forces on axle 1. Signal length 2000 samples.*

the individual Lipschitz coefficients have decreased by a small amount the relative magnitude is practically unaltered. A distinct system order can not be determined by this algorithm.

Nevertheless, because of the small decrease above order  $n = 7$  a dynamic model of this order will probably show a performance that is not far from that of a very high-order model. This is also a justification for use of a 6th-order model for the model-based synchronization algorithm. It should also be noted that only a SISO model structure was investigated here. It is still possible that a missing input causes the poor performance of the algorithm. Another explanation could be the fact that the  $Q$ -force signals show some variations which could not be explained by curve negotiations. If the influence of an unknown disturbance is captured in the output signal but not in the inputs the Lipschitz coefficients will certainly not show the desired characteristics.

### 6.1.2 Model Order Estimation Using Higher Order Correlations

The residuals of the parametric model used for the model-based synchronization algorithm are investigated by linear and nonlinear correlation analysis. The OE model used in chapter 4 was of order  $[6 \ 6 \ 1]$ , meaning that 6 zeros and 6 poles were used together with an input delay of 1 sample. No explicit noise model associated with an OE model so the model residuals are expected to show some correlations with themselves, the model inputs, and the model outputs. Input to the model was the signal of difference of level signals, the output should predict the difference of  $Q$ -forces at axle 1.

The linear correlation functions for this model are shown in figure 6.3 (top). The autocorrelation function (ACF) of the model residuals shows a shape very close to that of low-frequency noise, which exhibits an exponential decay. In any case, the residuals are still strongly self-correlated which is equivalent to the statement that they contain some information which has not been utilized yet. The cross-correlation function (CCF) between input and residuals depicted at the bottom of figure 6.3 also shows some significant correlation. The CCF does not stay within the dash-dotted green lines which indicate the 95% confidence-limits. This indicates that information contained in the

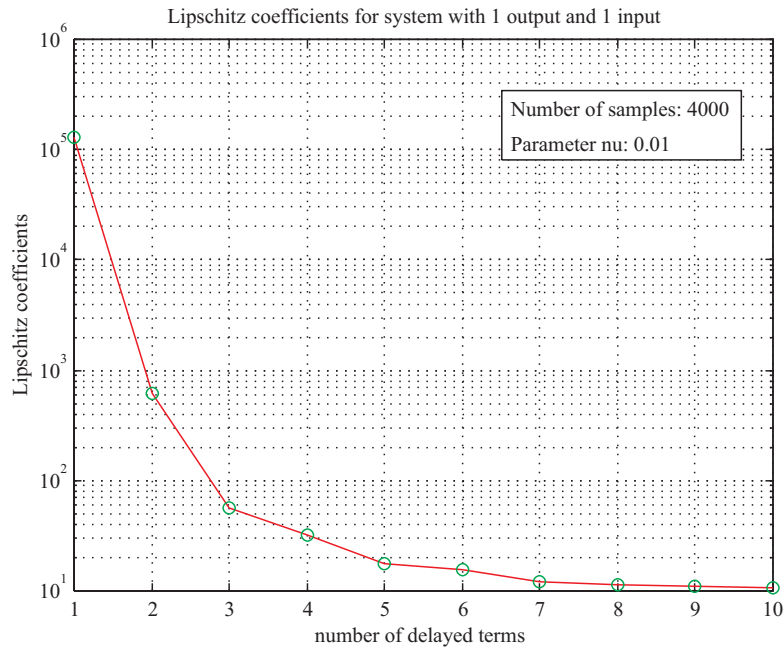


Abbildung 6.2: Estimates of Lipschitz coefficients for different orders. Inputs are difference of level signals and difference of  $Q$ -forces on axle 1. Signal length 4000 samples.

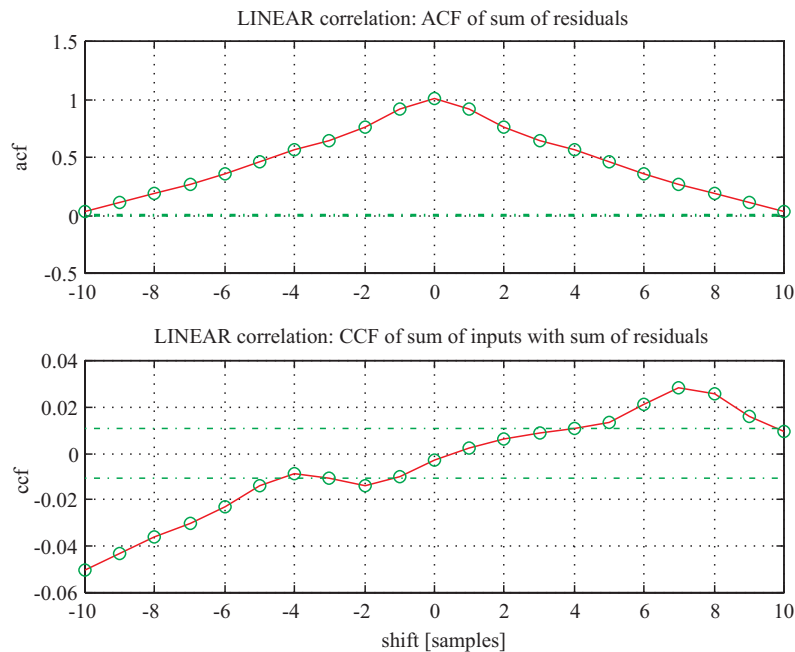


Abbildung 6.3: Linear correlations for Output-Error model with order [6 6 1].

inputs is still present in the residual signal. However, the CCF stays within the confidence limits in the vicinity of the origin. Again, this is equivalent to low-frequency errors in the model output.

Nonlinear correlation functions for the model were computed according to appendix B. The ACF is now replaced by a CCF between the squared residuals and the product of output and residuals (see figure 6.4, top). Although the peak has become a little sharper it still shows the

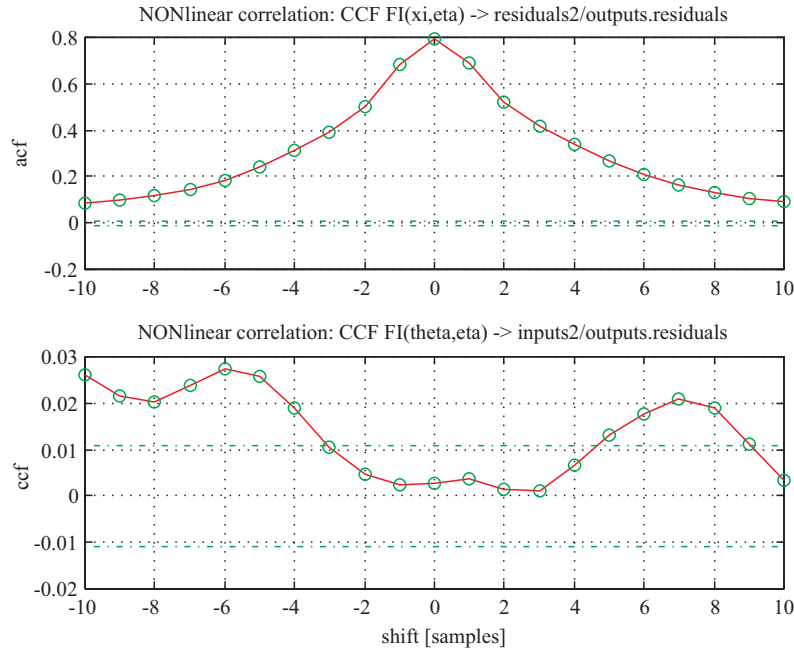


Abbildung 6.4: *Nonlinear correlations for Output-Error model [6 6 1].*

distinct shape of low-frequency noise. The CCF between the squared inputs and the product of output and residuals (bottom) also exceeds the confidence limits outside of -3 and +4 samples.

Apparently, the 6th-order OE model is sufficient in modeling the high-frequency content of the  $Q$ -force signals while it can not predict the low-frequency part of the output satisfactorily. This is in agreement with the fact that the input/output signals for model identification have been band-pass filtered, therefore inherently limiting the applicability of the model.

## 6.2 Identification of Wheel Forces

### 6.2.1 Identification of Low-Frequency Dynamics

Since the signals under consideration have been band-pass filtered, no information on the static gain and the low-frequency dynamics is available up to this point. Frequencies above the upper cut-off frequency of the band-pass filter are apparently of no interest, since they surpass the cut-off frequencies of the original measuring filters. Therefore, only the low-pass filtered components of the signals are subjected to further investigations. Data are low-pass filtered by a 5th-order Butterworth filter with a cut-off frequency of  $0.0251\omega_\nu$ . The difference of  $Q$ -forces of axle 1 is the output signal again while the cant signal is used as input. All signals used for identification are low-pass filtered as described above.

According to [14] the total vertical wheel force  $Q_\Sigma$  can be divided into four components:

$$Q_\Sigma = Q_{stat} + Q_{cent} + Q_{wind} + Q_{dyn} \quad (6.1)$$

in which  $Q_{stat}$  denotes the static wheel load on straight horizontal track,  $Q_{cent}$  is the component due to centripetal forces,  $Q_{wind}$  is caused by cross winds, and  $Q_{dyn}$  covers all dynamic phenomena (sprung mass, unsprung mass, corrugations wheel flats, welds). Neglecting the wind forces, the quasi-static equilibrium during curve negotiation depends on the geometry of the car, its total mass and speed, and the track geometry. The balance of moments around the symmetry point of



both wheel-rail contacts yields

$$(Q_l - Q_r) \frac{g_0}{2} = hm [g \sin(\alpha) + a_{cent} \cos(\alpha)] \quad (6.2)$$

where  $Q_l - Q_r$  is the difference of Q-forces on one axle,  $g_0$  is the nominal gauge,  $h$  is the height above rails of the center of gravity of the car,  $m$  is the proportional mass of the car,  $g$  is the gravitational acceleration,  $a_{cent}$  is the centripetal acceleration, and  $\alpha$  is the inclination of the track. Since  $\alpha \ll 1$  (according to [14]  $\tan(\alpha) < \frac{180}{1435} = 0.12544$ , which means that  $\alpha < \arctan(0.12544) = 0.12479$ ) equation 6.2 can be simplified to

$$(Q_l - Q_r) \frac{g_0}{2} = hm [g\alpha + a_{cent}]. \quad (6.3)$$

Substituting  $\alpha \cong \frac{c}{g_0}$ , where  $c$  denotes the cant, and  $a_{cent} = \frac{v^2}{R}$ , where  $v$  is the speed of the train and  $R$  is the radius of the curve equation 6.3 is transformed to

$$(Q_l - Q_r) \frac{g_0}{2} = hm \left[ \frac{gc}{g_0} + \frac{v^2}{R} \right]. \quad (6.4)$$

Assuming constant speed  $v$  expression 6.4 can be rewritten in terms of constant factors  $C_i$  and distance dependent variables:

$$\Delta Q(x) = Q_l(x) - Q_r(x) = \frac{2hm}{g_0} \left[ \frac{gc(x)}{g_0} + \frac{v^2}{R(x)} \right] = C_1 c(x) + C_2 \frac{1}{R(x)} \quad (6.5)$$

Equation 6.5 suggests that at least the cant signal  $c(x)$  and the curvature signal  $\frac{1}{R(x)}$  are necessary to correctly estimate the static gain of  $\Delta Q(x)$ . Furthermore, these static gains of  $\Delta Q(x)$  are linear constants  $C_{1,2}$ . However, when a model with this structure is identified and used for prediction the results are very poor. This is apparent from figure 6.5 where the measured output is plotted black while the predictions from the linear static model are red. The blue line is the output from a second-order MISO OE-model which has both cant  $c(x)$  and curvature  $\frac{1}{R(x)}$  for inputs. (A first-order MISO OE-model performs only slightly worse while higher-order models including such with a noise model do not improve performance significantly). The prediction of that model is much more accurate especially for the higher frequencies although at the larger part of the signal a considerable bias remains. It should be noted that the actual difference of Q-forces  $\Delta Q(x)$  is nearly proportional to the derivative of the cant  $\frac{dc(x)}{dx}$ . Despite this resemblance a SISO identification with only the derivative of cant as input yields still less satisfactory results than the MISO model mentioned above.

A slight improvement over the purely linear model is made by an second-order MISO OE-model which has cant  $c(x)$  and curvature  $\frac{1}{R(x)}$  for inputs to the dynamic model plus  $c^2(x)$  added with a static gain.

As can be seen from figure 6.6 the simulated output shows considerably smaller errors especially at large negative amplitudes (e.g. 11500m to 12000m). This indicates that a nonlinear model is indeed better suited to accurately describe the system dynamics. The result of a non-optimal identification with a Radial Basis-Function network is depicted in figure 6.7. A network with 60 basis-functions was trained by iteratively adapting the centers of the basis functions to the distribution of the real data. All network parameters were initialized as gaussian random variables.

3 runs with learning rate of centers: 0.1, 0.001, 0.000001. The resulting matrices from the previous run were used as initial values for the following run. Normalized signals (max. amplitude  $\pm 1$ ) with a spread of 1.2.

The resulting simulated output shows a similiary good fit to the actual measured output as in the example above. In most regions it is superior to the mixed linear/quadratic approach (especially at

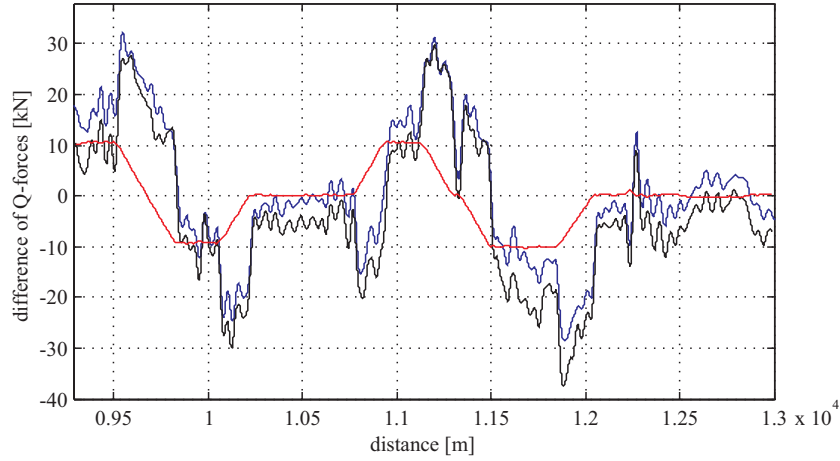


Abbildung 6.5: Measured output (black) and simulated outputs from static linear gains (red), second-order MISO OE-model (blue).

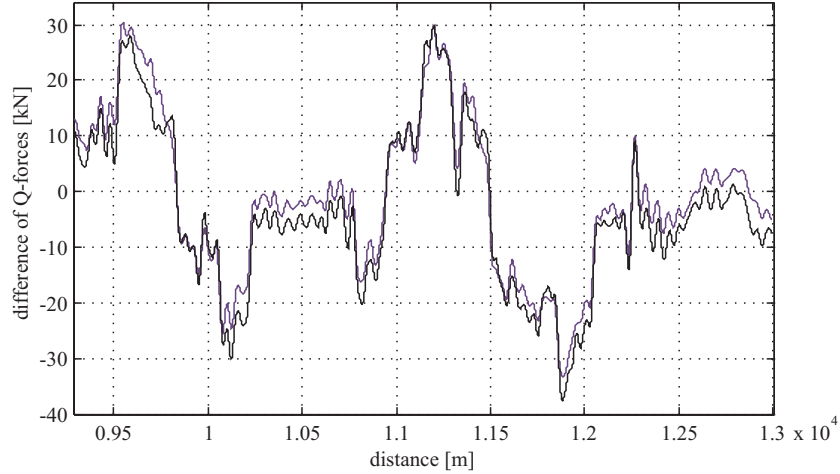


Abbildung 6.6: Measured output (black) and simulated outputs from second-order MISO OE-model (blue) with static gain of  $c^2(x)$

large negative amplitudes) while in some spots it shows a slightly worse fit. Note that the abscissa is greatly shortened compared to the other examples because of data decimation by a factor of 10. This procedure is favorable for an RBF-network identification since it removes redundancy from the data and hence the convergence of the learning algorithm can be expected to be better. It should be emphasized that all data are simulated outputs only, without validation data!

The identification of the sum of Q-forces  $Q_{\Sigma}(x)$  for one axle poses a much more pronounced nonlinear problem. This is due to the indifference of  $Q_{\Sigma}(x)$  with respect to the direction of curves. In effect this is like an absolute value operator acting upon both the cant  $c(x)$  and curvature  $\frac{1}{R(x)}$  signals. Considering the equilibrium of forces in the vertical direction of the car during curve negotiation we find that

$$Q_{\Sigma} = Q_l + Q_r = m [g \cos(\alpha) + a_{cent} \sin(\alpha)] \quad (6.6)$$

holds where the same notation as in equation 6.2 is used. Again, because of  $\alpha \ll 1$  equation 6.6

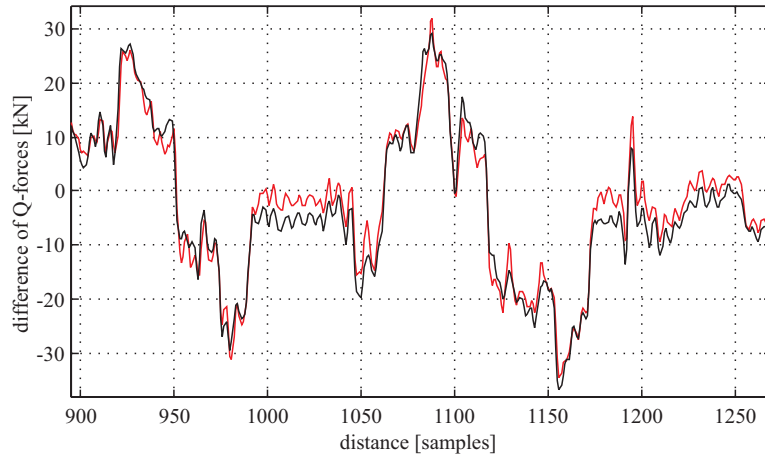


Abbildung 6.7: Measured output (black) and simulated output from RBF-model (red) with 60 basis functions and 6 inputs: 4 delayed cant signals and 2 delayed curvature signals.

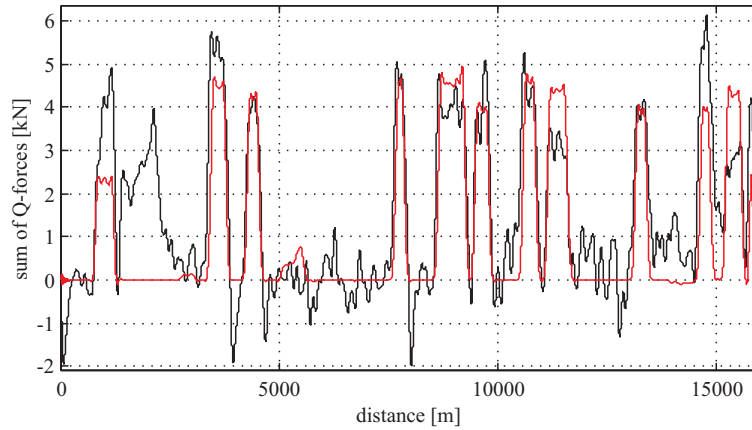


Abbildung 6.8: Sum of Q-forces for axle 1: Measured signal (black) and simulated output from second-order OE-model ([2 2 1]) (red).

can be approximated by

$$Q_{\Sigma} = Q_l + Q_r = mg + a_{cent}\alpha = mg + a_{cent}\frac{c}{g_0}, \quad (6.7)$$

which, under assumption of constant speed  $v$ , finally gives

$$Q_{\Sigma}(x) = Q_l(x) + Q_r(x) = mg + \frac{v^2}{R(x)} \frac{c(x)}{g_0} = C_1 + C_2 \frac{c(x)}{R(x)}. \quad (6.8)$$

Since the already simplified model of quasi-static curve negotiation yields a clearly nonlinear relation it can not be expected to be sufficiently modelled by a purely linear model. It should be noted that the fraction  $\frac{c(x)}{R(x)}$  always has a positive sign for all curves with correct superelevation regardless of direction. To achieve better results with a linear identification the input signal  $\frac{c(x)}{R(x)}$  is normalized by its maximum value and the output signal  $Q_{\Sigma}(x)$  is also rescaled and additionally an offset is subtracted in order to get approximate zero value for straight portions of track. Finally, both signals are lowpass filtered by a 5th-order Butterworth filter (`butter(5,0.051)`). The resulting output can

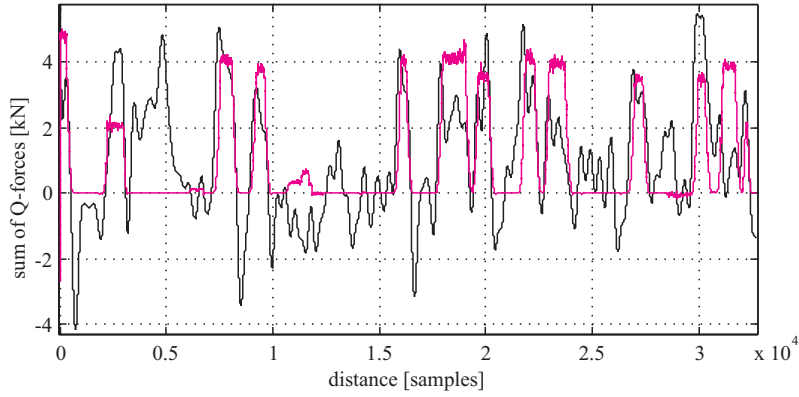


Abbildung 6.9: *Sum of all Q-forces at bogie 1 (black). Nonlinear combination of input signals  $\frac{c(x)}{R(x)}$  (magenta).*

be found plotted black in figure 6.8 while the red signal is the simulated output from a second-order OE-model. Obviously, the linear model is not able to explain some of the larger peaks and most of the smaller ones. More complex linear models do not achieve significantly better results. To check whether an identification with all Q-forces (i.e. the total contact force in vertical car direction for bogie 1) is more successful the Q-forces at bogie 1 are summed up to give  $Q_{tot}(x)$ . For easier comparison a constant value of 288 kN is removed from signal  $Q_{tot}(x)$ . The resulting signal is plotted black in figure 6.9. The nonlinear combination of input signals  $\frac{c(x)}{R(x)}$  is depicted in magenta. From the graphical comparison it is quite obvious that this input is not sufficient to explain the variations in the force signal  $Q_{tot}(x)$ . However, it remains doubtful that there is any combination of measured signals which is able to explain the force signal. The reasoning for this conjecture is simple: Between samples 3300 and 6000 the car runs along perfectly straight track as indicated by the zero-valued input  $\frac{c(x)}{R(x)}$ . Nevertheless, the output  $Q_{tot}(x)$  shows a peak value of nearly 5 kN in this range. Moreover, it stays above 2 kN for more than 750m. It is completely obscure where such a quasi-static load could come from if not from curve negotiation. On the other hand, the variation of  $Q_{tot}(x)$  is quite small compared to its absolute value. The standard deviation is  $\sigma = 4.94$  kN while its mean is  $\bar{Q}_{tot} = 288.98$  kN leading to a relative variation of only 1.71%. Maybe in tighter turns or at higher speeds the influence of the function  $\frac{c(x)}{R(x)}$  will increase.

## 6.2.2 Lateral Wheel Forces

In order to use a simple form of the signal combinations from section 5.2, these signals are formed by

$$\begin{aligned} a_c(k) &= a_l(k) + a_r(k) + a_l(k - 5) + a_r(k - 5) \\ Y_c(k) &= Y_{1.1}(k) - Y_{1.2}(k) + Y_{2.1}(k) - Y_{2.2}(k), \end{aligned} \quad (6.9)$$

where  $a_c(k)$  denotes the input as sum over alignment errors for bogie 1 and  $Y_c(k)$  denotes the output as sum over all lateral forces. Note that the lateral forces have alternating signs since the positive direction of different sides is opposite by definition. It is also important that the signals are aligned for axle 1, therefore, for the alignment at axle 2 a shift of 5 samples (2.5m) has to be introduced. This choice of signals has been proven to have a distinct cross-correlation function. However, a spectral analysis uncovers an inherent shortcoming of this combination. As can be seen in figure 6.10 the combination of alignment signals  $a_c(k)$  has zeros at  $\frac{2.5}{1}$ ,  $\frac{2.5}{3}$ , and  $\frac{2.5}{5}m$  which is also reflected by amplified magnitudes in that range for the combination of force signals  $Y_c(k)$ . The reason are the kinematics of the bogie: Track errors with those particular wavelengths will

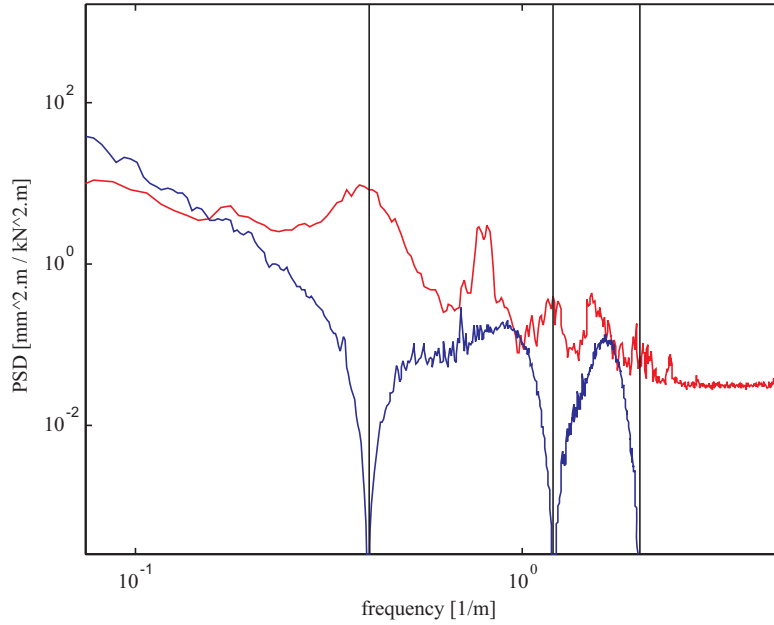


Abbildung 6.10: Spectral estimates for sum of alignments  $a_c(k)$  (blue) and sum of Y-forces  $Y_c(k)$  (red). Black ordinates at 2.5, 0.83, and 0.5m.

rotate the bogie around the z-axis without causing a lateral movement of its center. On the other hand lateral wheel forces will show a maximum not only at those frequencies but also for the even fractions of  $2.5m$  (corresponding to purely parallel movement of both wheelsets).

If only the low-frequency range is of interest, these transmission zeros are of no effect otherwise the identification will certainly be affected. Another problem results from the fact that the measured Y-forces are drifting and for this reason they are periodically set to zero mean at portions of straight track. To overcome that drift and its manual corrections the Y-force signals have to be specially detrended. An example for this systematic measurement error can be seen in figure 6.11. The green line corresponds to the actually recorded signal of  $Y_{1,1}$ . At sample 16878 (corresponds to sample 281 in the figure due to downsampling with a factor of 60) a bias correction for  $+7.58kN$  was made and again at sample 25356 (sample 423 in the figure) an offset of  $+2.5kN$  was applied. The red line shows the signal with the first correction removed while the blue line has both jumps removed. The detection and removal of the jumps was done manually here although many suitable off-line algorithms exist [3] which are able to automatically detect the artificial jumps. The remaining signal clearly shows a trend to negative values although it is difficult to decide if this trend is purely linear or if the offset proceeds in a stepwise fashion. Since this cannot be uniquely determined from measurement data alone it seems justified to follow both assumptions and compare the performance of a following identification. From a physical point of view a slightly more complicated progression seems reasonable since the offset is probably caused by increasing temperature of the wheel discs due to a surplus in friction during curve negotiation. Under the assumption of friction being proportional to the lateral forces there is a certain amount of approximately constant friction along every section of track. If we further assume linear heat transfer between wheel disc and surrounding atmosphere the balance of heat transfers becomes

$$\frac{dT}{dt} = K(T_a - T) + H_f + H_r. \quad (6.10)$$

In equation 6.10  $T$  is the temperature of the disc (assumed to be uniformly distributed),  $T_a$  is the atmospheric temperature,  $K$  is the heat transfer coefficient (assumed to be constant),  $H_f$  is the

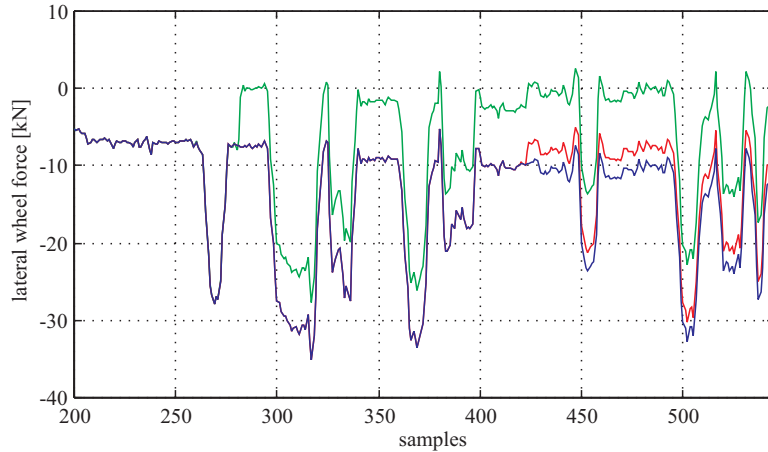


Abbildung 6.11: *Biased Y-force signal  $Y_{1,1}$ : Recorded signal (green), first correction removed (red), second correction removed (blue). Signals decimated by a factor of 60.*

amount of heat generated by friction, and  $H_r$  is the amount of heat due to radiation.  $H_r$  will most likely be very close to zero or positive since the heat loss due to radiation will be very small at the relatively low temperatures of the disc while it is possible to have a considerable amount of heating by sunlight. The solution to equation 6.10 is given by

$$T(t) = (1 - e^{-Kt}) \left[ T_a + \frac{H_f + H_r}{K} \right] + T_0 e^{-Kt} \quad (6.11)$$

where  $T_0$  is the initial disc temperature. The disc temperature is governed by equation 6.11 if all the right hand side inputs are assumed to be piecewise constant. This would mean that for a small  $K$  after every curve the disc temperature is higher than before and only gradually decreases. If the curves are closely spaced along the track an approximately stepwise increase in temperature can be expected.

Since data for straight track are sparse a model based correction is problematic. Instead, a linear regression can be computed for data from straight track. In order to achieve a correct regression the signal sections which correspond to straight track have to be identified. This is easily done by inspection of the signal from relative twist. Then, the corresponding sections of the Y-force signals are used as inputs for a linear regression. In the last step this linear regression is subtracted from the original signal thus yielding a Y-force signal which is at least in average detrended. The resulting signals for lateral force signal  $Y_{1,1}$  can be seen in figure 6.12. (Plotted with data from file 'ycorr.mat', using function 'linreg.m'.)

Although the linear regression provides a suitable method to compensate for a global linear shift it may not be optimal for individual short sections of the signal. Therefore, bias errors still exist in the corrected signals. In the case of axle 2 the maximum remaining offsets are in the range of  $\pm 1kN$  which is about 12% of the peak amplitudes. Compared to the original offsets of approximately 50% of peak amplitudes this is only a modest achievement. However, a more complex model which completely removes the offsets at signal sections corresponding to straight track would be problematic since we would have to interpolate over large sections with only a few fixed data points.

For identification purposes the corrected Y-force signals are divided into two separate frequency domains: A low-pass component and the high-frequency content are separated by 5th-order Butterworth filters with a cut-off frequency of  $0.0251\omega_v$ . Since the filters are symmetric relative to the cut-off frequency the sum of the filtered signals equals exactly the original signal. A linear static identification for the low-pass component of  $Y_{1,1}$  yields the results given in figure 6.13. The

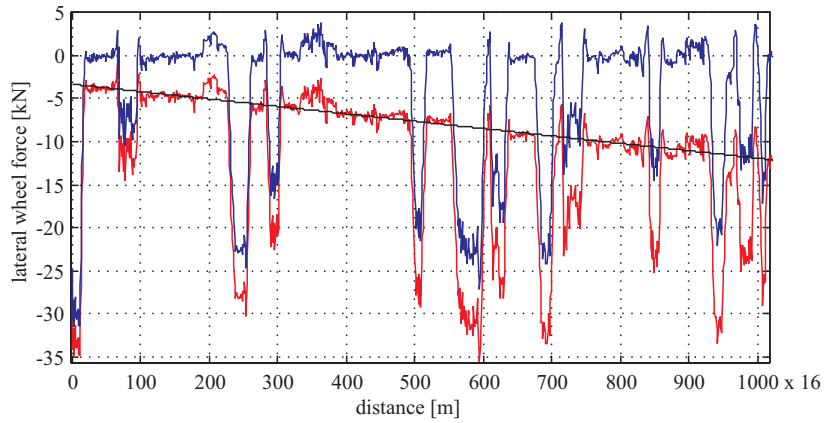


Abbildung 6.12: Lateral force signal  $Y_{1.1}$ : Signal with jumps removed (red), linear regression computed from signal sections corresponding to straight track (black), and corrected signal with linear trend removed (blue).

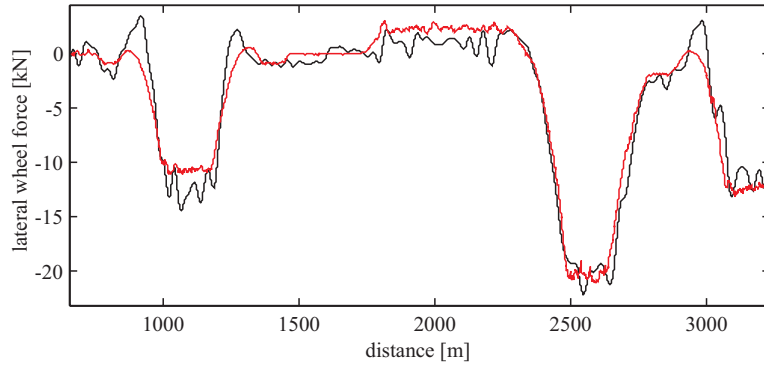


Abbildung 6.13: Validation data for linear identification of  $Y$ -forces: Static model with low-pass filtered  $Y_{1.1}$  as output and curvature  $\rho(x)$  and combined signal  $c(x)\rho(x)$  as inputs.

validation of the model

$$Y_{L1.1}(x) = -0.091\rho(x) - 0.0022c(x)\rho(x) \quad (6.12)$$

yields the plots depicted there. Although the validation data show satisfying accuracy the data used for identification are not always equally well predicted. Use of low- or higher-order dynamic transfer functions does not increase accuracy.

Another inherent problem of modeling the  $Y$ -forces arises from non-symmetrical curve negotiation. The lateral wheel-rail forces at the front bogie show a distinct pattern during curve negotiation. The sum of the lateral forces assure a proper guidance of the vehicle. The forces at the front axle of the leading bogie are much larger than those of the rear axle. Furthermore, the inside wheel of the rear axle is the only one which exhibits a positive lateral force during curve negotiation. This typical pattern was already mentioned in [37] and represents the stable stationary situation. However, due to asymmetries in the structure of the bogie and differences in the individual wheel-rail contact geometries other stable conditions may be possible. In that case the lateral wheel forces at the rear axle show different signs which stay constant regardless of the direction of the curve. On the other hand, the lateral wheel-rail force  $Y_{1.1}$  tends to positive values. These phenomena can be seen in figure 6.14 where  $Y_{1.1}$  is plotted red. In most curves  $Y_{1.1}$  is as negative as  $Y_{1.2}$  while in some other curves it assumes positive values. There are also some instances where  $Y_{1.1}$  starts to increase at the beginning of the curve, then decreases quickly to a negative (stationary)

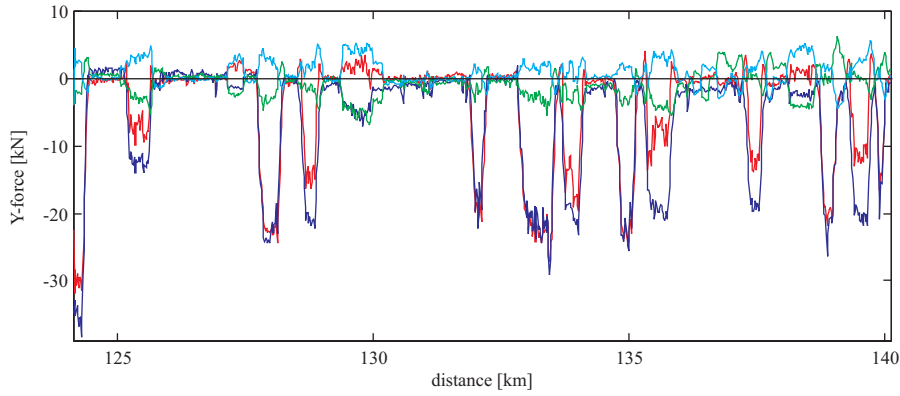


Abbildung 6.14: *Y-forces during curve negotiation. Test run Klagenfurt-Villach, km 124 to km 140.  $Y_{1.1}$  red,  $Y_{1.2}$  blue,  $Y_{2.1}$  green, and  $Y_{2.2}$  cyan.*

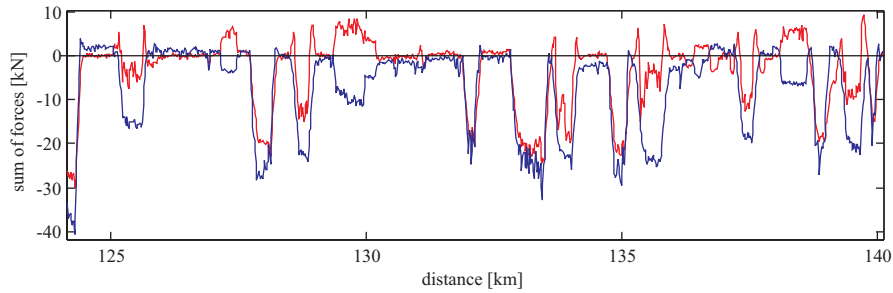


Abbildung 6.15: *Sum of diagonal Y-forces during curve negotiation. Test run Klagenfurt-Villach, km 124 to km 140.  $Y_{d1}$  red,  $Y_{d2}$  blue.*

value and finally jumps back again to a positive value. This behavior is very similar to a nonlinear stability transition where a former stable state suddenly becomes unstable (bifurcation). The investigation of such phenomena is complex and certainly beyond the scope of this work. In [48] an introduction with many examples is given. The different modes of curve negotiation are best depicted in the following way: The lateral wheel-rail contact forces are summed up diagonally,

$$\begin{aligned} Y_{d1} &= Y_{1.1} + Y_{2.2} \\ Y_{d2} &= Y_{1.2} + Y_{2.1}, \end{aligned} \tag{6.13}$$

where  $Y_{d1}$  is proportional to a negative moment in direction of the  $z$ -axis and  $Y_{d2}$  is proportional to a counteracting moment. In figure 6.15 both signals are plotted along curved track ( $Y_{d1}$  red,  $Y_{d2}$  blue). In some curves both signals have same amplitude, therefore compensating each others effect, while in other curves there is a considerable difference between the two signals. As mentioned above, there are three smaller curves where  $Y_{d1}$  becomes positive for the entire duration of curve negotiation.

Another asymmetry lies within the lateral forces on straight track. Depending on the stiction between bogie and car body the bogie remains in a slightly angled position relative to the car body. Therefore,  $Y_{1.2}$  either assumes a positive value (around km 126.5) or it becomes negative (around km 131).  $Y_{1.2}$  remains at zero mean for most straight portions.

The main point for the current work is that from geometric track data alone these phenomena cannot be predicted precisely because of the strong influence of vehicle specific parameters.



# Kapitel 7

## Conclusion

The aim of the present work was to study the feasibility of track quality assessment by prediction of vehicle dynamics with artificial neural networks. An important part of the of the present work was therefore to evaluate existing measurement data of both track geometry and vehicle response to learn about inherent characteristics (filtering, cut-off frequencies, and transfer functions), systematic and stochastic errors. Furthermore, by utilizing multiple measurements from the same track section and redundant information within each data record the accuracy and consistency of the measuring procedures could be assessed. Data properties which pose a strong limitation to a use for an identification are isolated and listed. Methods for proper synchronization of track and vehicle data have been developed and the performance of the individual algorithms have been thoroughly tested with simulated and measured data. The achievable synchronization accuracy of these algorithms is much higher than a use of synchronization marks or curvature readings. Furthermore, the synchronization algorithms make use of each sample in the data records as opposed to simple approaches which just take into account distinct features which are often far apart from each other. Due to the limitations posed by the data sets, only a few exemplary identification procedures were carried out. Nevertheless, the results clearly indicate that a prediction of a generic vehicle response could be possible although the effects of nonlinear stability phenomena can not be reliably predicted with acceptable costs.

### 7.1 Data Acquisition

Investigations of data were divided into two parts: The track geometry data as recorded by the superstructure measuring car and the dynamic vehicle responses as recorded by the dynamics measuring car. Measurement data exhibit several shortcomings:

#### **Distance**

Distance records suffer from the systematic problem of unknown wheel circumference. Due to wear, change in wheel temperature, and the conicity of the wheel tread the exact circumference and consequently the sampling interval length is not known. Since all those influences may change during and between test runs the absolute positions of the vehicle on the track are not known exactly. Absolute position marks which are recorded from the moving train by releasing a button when a distinct milestone is passed are not of any use for an accurate synchronization since they may be wrong up to 30m. Even if exact synchronization points would be known a linear resampling between those points would only be meaningful if the reference points are not too far apart. The results given in section 5.3.2 show that a difference of one sample may occur within one kilometer.

## Speed

Speed readings of the superstructure measuring car exhibit marked harmonic oscillations at multiples of the wheel circumference. Additionally, the variance of the speed signal shows a good correlation with curvature signals. Wheel faults which are more pronounced on one wheel are probably the cause for these phenomena. Although the agreement of speed readings of both measuring cars is good (the error is smaller than 1%) this is already one limitation for an identification in the time domain since all data records have to rely on the speed signals for the conversion into the time domain.

## Track Geometry

Data of track geometry show several differently grave errors. In level measurements the eigenmodes of the measuring car are visible, thus leading to the problem that no identification algorithm will be able to correctly model the vehicle response at those sensitive frequencies. This effect becomes especially pronounced with high train speeds ( $v \geq 120\text{km/h}$ ). Another harmonic disturbance is caused by wheel faults. Although this is clearly a problem of the measuring car the effects of the additional vibrations are falsely recorded as track characteristic. Here the same problem as before arises, i.e. an insensitive model at these frequencies will result from an identification with those data. The most severe limitation is posed by the inherent high-pass filtering of level data. Data records show a cut-off frequency in the 30 to 40m range which is of great importance for the excitation of car body oscillations in high-speed trains. Therefore, the track data records are limited in their applicability to the identification of low- to medium-speed trains.

In alignment signals no eigenmodes of the measuring coach were found but all the other problems effective for level are also present here. The amplitudes of the different test runs on the same section of track differ especially at the wheel frequencies. A measuring speed dependent result is therefore unavoidable. As shown in section 6.2.2 the measurement of alignment is also compromised by the coupling of the lateral wheel forces through the bogie structure.

The main problem with gauge signals is the spontaneous occurrence of large (up to 15mm) deviations without recognizable reason. It is most likely that these errors are caused by adverse conditions of the rail head (corrosion, lipped, or soiled rail surface at the reference point for gauge measurement). However, the confidence in the whole gauge signal is considerably impaired by such errors. The track data records may be checked for inconsistencies between gauge and difference of alignment signals but if a poor agreement is detected it is not possible to decide which signal really is wrong.

Records of curvature also show an influence of the eigenmodes of the measuring coach. Furthermore, longitudinal loads alter the variance of the curvature signal. This was confirmed by a simple model which could perform with an error of less than 2%. Aside from those errors, the curvature assumes maximum values of 90mm which leaves quite a coarse quantization for a stationary signal.

Cant signals basically show the same problems as level signals do. However, the eigenfrequencies which are fixed in the time domain did not fit the eigenmodes of the car body. The reasons for those oscillations have not become clear yet; the effects on an identification are weighty anyway. In some test runs a temporary offset in the signal levels of up to 4mm occurs.

## Wheel Forces

The measurement of lateral  $Y$ -forces proves to be most problematic. These signals show a pronounced drift to negative values. In test runs on curved track the local offset is sometimes removed in a stepwise fashion. For the reconstruction of the actual  $Y$ -force the exact point and amount of these steps has to be identified, the steps have to be reversed, and finally the drift has to be removed. It is more than likely that the actual force signal will not be constructed correctly. Another

inherent problem of railway cars also occurs: Although  $Y$ -forces should be symmetric with regard to curve negotiation they are clearly asymmetric in the current data because of a slightly offset bogie. This effect can also be seen in the relative twist signal (which does not return to zero on straight track). Additionally, the nonlinear stability problem of how the leading bogie actually runs through the curved track can be found in the data. Depending on the physical parameters either the outer or the inner wheel of the rear axle will be in two-point contact with the rail head. It is known [48] that only very complex nonlinear models are capable of reproducing such a dynamical behavior.

Spectra of  $Q$ -force signals show a distinct notch at wheel-frequency and half the wheel-frequency. This is caused by the special processing of the measuring signal. Nevertheless, it is a systematic interference with the actual frequency content of the measured signals. Another severe problem was pointed out in section 6.2.1. The sum of  $Q$ -forces on bogie 1 showed variations of 5kN while running along perfectly straight track. Although wind, coupling forces between cars and other influences exist the actual reason for those variations remains unknown.

Car body accelerations exhibit no apparent systematic errors; however, these signals have not been used in an identification yet which limits the extent of this statement.

## 7.2 Signal Synchronization

The eminent problem of properly synchronizing the data records of track data (input) and vehicle response (output) has been thoroughly investigated and two algorithms have been developed for a localized synchronization.

To estimate the local shift between two signals a correlation estimate inside a moving window is performed. To assure a continuous shift estimate the algorithm is initialized by the search for a distinct global extreme inside the CCF-estimate. Once this extreme has been found the CCF is computed repeatedly for each window position and the shift of the extreme is the estimate for the local shift between the two signals. The resulting shift function may be used to resample one of the two signals in order to remove the relative shift or achieve a constant relative shift between the signals (dead-time).

To reduce the size of the moving window a model based resampling algorithm was developed. In this approach a parametric linear model is identified from given input/output data and the predicted output from that model is used to compute a shift estimate with the actual output signal. Because of the strong correlation of the predicted and the actual output a much smaller window may be used.

Both algorithms are tested with simulated data as well as with actual measurement data. The model based resampling algorithm was shown to perform superior to the pure correlation approach. To find the optimal pair of input/output signal for the synchronization task several signal combinations were tested by correlation analysis. It should be noted here that linear resampling of data sets is more accurate if the parameters for the resampling procedure are computed from a continuous shift function rather than from two small sections at opposite ends of the data record. This is all the more true since a continuous shift function also allows for a check of the intermediate characteristics of the shift. And in the case of strong nonlinear shift components a continuous localized shift function is prerequisite for any resampling.

Effects of the presence of absolute shift functions were also investigated. An algorithm to detect frequency shifts in the signals under the assumption of stationarity of the original process was proposed. However, investigations with simulated as well as actual measurement data clearly demonstrated that an absolute shift can not be detected until it has become very marked (more than +20% or -40% of the sampling interval).

## 7.3 Identification

The results of the identification part are very limited due to the problems with measurement data. Nevertheless, using linear and nonlinear model order tests the approximate order for an optimal model could be established. The results from this section are in agreement with the structure of the models found in chapter 5.

Furthermore, in the same chapter a linear dynamic model structure was established which was incorporated into the model based identification algorithm. The model itself already gave a fairly good prediction of the difference of  $Q$ -forces in a band-pass region. This parametric model was also validated with nonparametric correlation and spectral models.

The superior performance of nonlinear over linear models were demonstrated in the case of low-pass filtered difference of  $Q$ -forces predicted from cant signals. The theoretical formula proved to produce very poor results while both linear and nonlinear models delivered a much better performance. The identification of the sum of  $Q$ -forces necessary for the prediction of individual  $Q$ -forces could not be finished successfully because of the problems already mentioned in section 7.1. A rough prediction of individual  $Q$ -forces would be possible at the present state although it would be much too inaccurate for the construction of safety criterion.

The identification of  $Y$ -forces ended even earlier since the problems with measurement data were so numerous. It did not seem reasonable to identify a proper high-frequency model when the vast part of the  $Y$ -force amplitudes is determined by low- to medium frequency signal components (curve negotiation).

## 7.4 Outlook

The logical direction to continue this work would be the improvement of measuring procedures to record appropriate data sets. However, it must not be overlooked that most of the data investigated here were not primarily recorded for identification purposes. Instead, the accuracy of most signals is sufficient for the purposes they were recorded for. For now, only the possibility of identifying biased models seems feasible. This may seem useless at first glance but a look back in history of track recording systems shows that a strong and ongoing development exists. It is therefore only a question of time when data records will meet all requirements of an identification procedure. If the proper algorithms already exist they will be certainly used to increase safety and decrease the costs for track maintenance. Furthermore, the development of such procedures will reveal the remaining shortcomings of present-day measuring concepts and can be of assistance in the search for better methods.

# Appendix A

## Transfer Functions in Geometry Measurement

### A.1 Versine Measurement

Versine measurement is a method where the end points of a chord of predefined length are moved along the track and the orthogonal distance from a distinct point on the chord (often chosen to be the middle of the chord) to the track is used as a measure for track irregularities. Unfortunately its transfer function suffers from severe shortcomings: Its magnitude is nonlinear with respect to frequency, moreover, it has an infinite number of zeros well inside the frequency range of interest. It is therefore not possible to reconstruct the original geometry in a unique way. Furthermore, the inverse transfer function, needed for compensation, exhibits large magnitude in the vicinity of the original zeros, thus leading to unacceptable signal to noise ratios.

Without loss of generality the transfer function of the symmetrical versine measurement can be derived from the geometrical properties displayed in figure A.1. Since the end points of the chord ( $A$  and  $B$ ) are always attached to the rail, the versine is effectively measured in a relative coordinate system moving along the track. In this coordinate system the angle  $\varphi \ll 1$  between chord and x-axis by definition. Therefore, the versine  $v$  may be substituted for the vertical distance  $h$  between the point of reference on the chord ( $R$ ) and the point of track with the same ordinate  $x$  ( $F$ ). From geometry the relation

$$v(x) \cong h(x) = f(x) - \frac{f(x + \frac{L}{2}) + f(x - \frac{L}{2})}{2} \quad (\text{A.1})$$

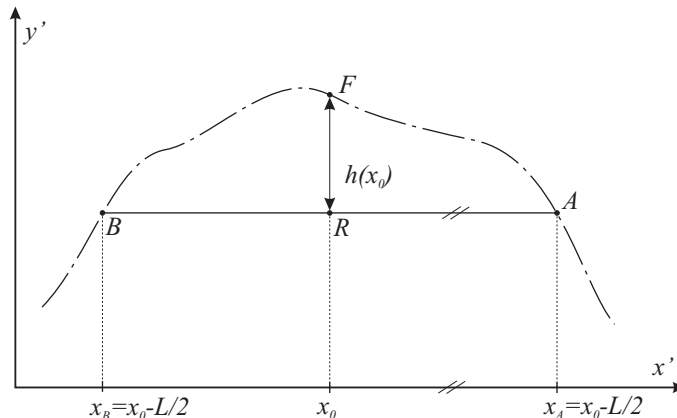


Abbildung A.1: *Symmetrical versine measurement in relative coordinates: chord length  $L$ .*

can be derived, with  $L$  being the length of the chord. The discrete version of equation A.1 can be readily written as

$$v(k) \cong h(k) = f(k) - \frac{f(k + \frac{M-1}{2}) + f(k - \frac{M-1}{2})}{2} \quad (\text{A.2})$$

with  $k$  denoting multiples of the sampling instance ( $x = k \Delta x$ ) and defining  $M$  by

$$L = (M - 1) \Delta x. \quad M = 2n + 1, \quad n \in \mathbb{N} \quad (\text{A.3})$$

A  $z$ -transform of equation A.2 would require to transform a term with a positive shift. However, since no real-time output is required the whole equation can be shifted to obtain only negative shifts

$$v(k - \frac{M-1}{2}) \cong f(k - \frac{M-1}{2}) - \frac{f(k) + f(k - M + 1)}{2}, \quad (\text{A.4})$$

and this can easily be transformed into

$$V(z) \cong F(z) \frac{-0.5z^{-M+1} + z^{-\frac{M-1}{2}} - 0.5}{z^{-\frac{M-1}{2}}}, \quad (\text{A.5})$$

yielding a transfer function of

$$G(z) = \frac{V(z)}{F(z)} \cong \frac{-0.5z^{-M+1} + z^{-\frac{M-1}{2}} - 0.5}{z^{-\frac{M-1}{2}}}. \quad (\text{A.6})$$

The modulus of this transfer function oscillates between maxima of 2 and minima of zero (see figure A.2 for  $L = 10m$ ). For the minima and maxima the following scheme holds:

$$|G(z)| = 0 \quad \Leftrightarrow \quad \omega = \frac{4k\pi}{L}, \quad k = 0, 1, 2, \dots, \frac{L}{4\Delta x} \quad (\text{A.7})$$

$$|G(z)| = 2 \quad \Leftrightarrow \quad \omega = \frac{2\pi(2k-1)}{L}, \quad k = 1, 2, \dots, \frac{L}{4\Delta x} \quad (\text{A.8})$$

It is quite obvious that the recovery of the original signal will be possible only inside a very limited frequency range. If an amplification of the measured signal of a factor 2 is acceptable, then the biggest continuous frequency range would come to lie between 6m and 30m wavelength (blue lines in figure A.2). A stronger amplification would considerably increase the frequency range, however, this increase would primarily be caused by an extended low frequency range, whereas the upper frequency bound does not change much (for an amplification of factor 10 the range would be 5.39m to 70.8m).

The assumptions made above are equivalent to assuming that the track characteristic under investigation  $f(x)$  has a band-pass spectrum. While this is not true for most real signals, it is a sufficient hypothesis for the purpose of track maintenance. The tamping machines are only able to compensate track irregularities within a band-pass range. Any information outside this frequency range cannot be utilized for corrections.

## A.2 Moving Average

The moving average (MA) over a predefined number of samples is used as a reference for geometry irregularities. It apparently has a low-pass characteristic, however, its transfer function is far from an ideal low-pass filter. This is due to the fact that wavelengths above the cut-off frequency (which is a little smaller than the window length) are not attenuated strong enough.

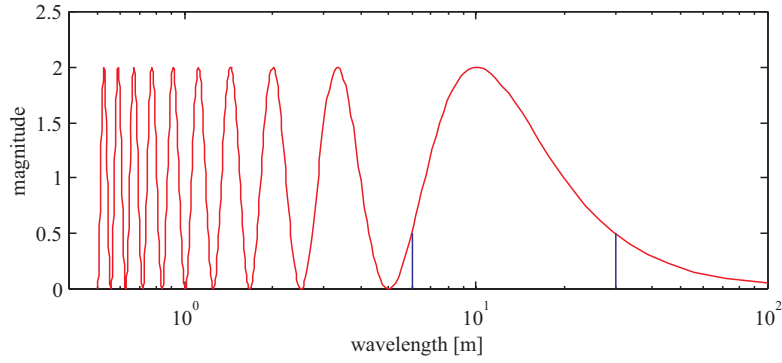


Abbildung A.2: Modulus of transfer function for symmetrical versine measurement: length of chord 10m, discretized at 0.25m

The MA  $m(k)$  of a discrete signal over a predefined number of samples  $N$  ( $N$  being odd) is defined by

$$m(k) = \frac{1}{N} \sum_{k-N+1}^k f(k), \quad (\text{A.9})$$

taking into account the past  $N$  samples. The  $z$ -transform of equation A.9 is therefore

$$M(z) = \frac{1}{N} F(z) \sum_0^{N-1} z^{-j}. \quad (\text{A.10})$$

If averaging is done off-line or at least with some delay, the MA may be assigned to the sample right in the middle of the moving window:

$$M(z) = \frac{1}{N} F(z) \left[ \sum_0^{N-1} z^{-j} \right] z^{\frac{N-1}{2}} \quad (\text{A.11})$$

Rewriting equation A.11, the transfer function of the MA with  $f(k)$  as input may be written as

$$G(z) = \frac{M(z)}{F(z)} = \frac{1}{N} \frac{\sum_0^{N-1} z^{-j}}{z^{\frac{1-N}{2}}}. \quad (\text{A.12})$$

An example for  $N = 121$ ,  $\Delta x = 0.25m$  (average over 30m) can be seen in figure A.3. The cut-off frequency (-3dB) comes to lie at 68.4m. However, at the first hump the attenuation of the filter is only -13.3dB at 21.2m. This is equivalent to a -20dB per decade decrease in magnitude, which in turn corresponds to first order low-pass filter. An advantage of the MA filter is the phase portrait, which shows a nearly constant zero shift well above the passband. But since the phase for this version of the filter drops off  $180^\circ$  at each minimum of the magnitude, the frequencies at the first hump will also show a strong phase shift.

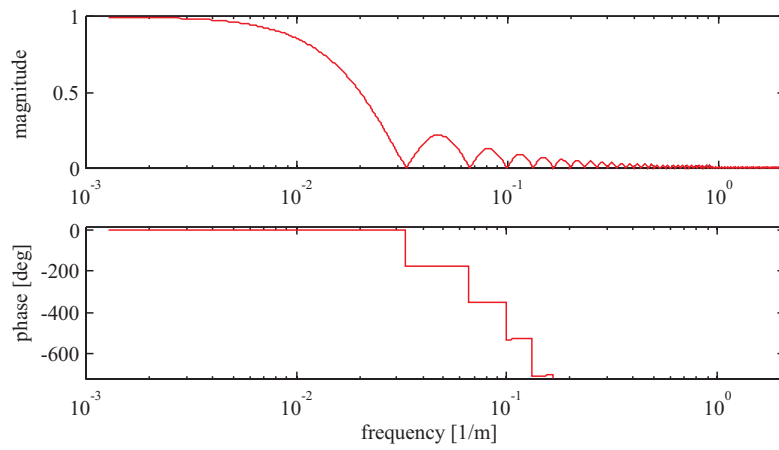


Abbildung A.3: *Transfer function of moving average. Top: magnitude, bottom: phase. Sampling interval of 0.25m, average over 121 points (30m). Both plots over spatial frequency (1/m).*



# Appendix B

## Nonlinear Model Validation

### B.1 Higher Order Correlations

In [7] the basic concept of using the auto-correlation function of the residual as criterion for sufficient model order is extended in two ways:

- Correlations are calculated from second order functions
- Additional cross-correlations are calculated from inputs, outputs, and residuals respectively.

The original method for SISO-systems is adapted for MIMO-systems in [8]. Because of the choice of test functions and their combination it becomes possible to detect missing model terms by the characteristics of the correlation functions.

The number of correlation functions necessary for the testing of MIMO-systems  $q^2 + qr + 2$  increases rapidly with the number of inputs  $r$  and outputs  $q$ , leading to large numbers of correlation plots for systems with higher input/output dimensions. Still, a large number of correlations does not limit the applicability of the method since only a few shifts have to be calculated for each correlation (typically  $\tau \in [-10, 10]$ ).

The main drawbacks of the method are:

- The method is susceptible to noise, although the correlations exhibit an inherently averaging effect.
- Model terms with small residuals do not show up significantly.
- Theoretically, only the absence of polynomial model terms up to second order can be clearly detected. However, the method produces useful results in the case of other nonlinearities although the correlation functions will be less decisive.
- Nonlinear cross-coupling effects between test functions complicate the interpretation of the results.

#### B.1.1 Basic Principle and Algorithm

Since the concept for SISO-systems introduced in [7] is included in the framework of MIMO-systems [8], the algorithm will be outlined for the MIMO case. The MIMO system is defined as

$$\mathbf{y}(k) = \mathbf{f}(\mathbf{y}(k-1), \dots, \mathbf{y}(k-n_y), \mathbf{u}(k-1), \dots, \mathbf{u}(k-n_u), \varepsilon(k-1), \dots, \varepsilon(k-n_\varepsilon)) + \varepsilon(k) \quad (\text{B.1})$$

with  $\mathbf{y}(k)$ ,  $\mathbf{u}(k)$ , and  $\varepsilon(k)$  denoting the output, input, and residual respectively and  $\mathbf{f}(\cdot)$  is a linear or nonlinear vector-valued function with

$$\mathbf{y}(k) = \begin{bmatrix} y_1(k) \\ \dots \\ y_q(k) \end{bmatrix} \quad \mathbf{u}(k) = \begin{bmatrix} u_1(k) \\ \dots \\ u_r(k) \end{bmatrix} \quad \varepsilon(k) = \begin{bmatrix} \varepsilon_1(k) \\ \dots \\ \varepsilon_q(k) \end{bmatrix}. \quad (\text{B.2})$$

The nonlinear global tests, which check for correlations among all the sub-model input, output and residual vectors, are defined as

$$\left. \begin{aligned} \Phi_{\xi\eta}(\tau) &= E[\xi(k)\eta(k+\tau)] \\ \Phi_{\vartheta\eta}(\tau) &= E[\vartheta(k)\eta(k+\tau)] \end{aligned} \right\} \quad (\text{B.3})$$

where  $\xi(k)$ ,  $\eta(k)$ , and  $\vartheta(k)$  are given by

$$\left. \begin{aligned} \xi(k) &= \varepsilon_1^2(k) + \dots + \varepsilon_q^2(k) \\ \eta(k) &= y_1(k)\varepsilon_1(k) + \dots + y_q(k)\varepsilon_q(k) \\ \vartheta(k) &= u_1^2(k) + \dots + u_r^2(k) \end{aligned} \right\} \quad (\text{B.4})$$

The expectation operator in B.3 is replaced by normalized correlation functions, computed over a finite record length

$$\Phi_{xy}(\tau) = \frac{\sum_{k=1}^N x^o(k)y^o(k+\tau)}{\sqrt{\sum_{k=1}^N (x^o(k))^2 \sum_{k=1}^N (y^o(k))^2}} \quad (\text{B.5})$$

where the superscript  $o$  stands for the standardized version

$$\begin{aligned} \xi^o(k) &= \frac{\varepsilon_1^{2o}(k)}{\sqrt{\frac{1}{N} \sum_{k=1}^N (\varepsilon_1^{2o}(k))^2}} + \dots + \frac{\varepsilon_q^{2o}(k)}{\sqrt{\frac{1}{N} \sum_{k=1}^N (\varepsilon_q^{2o}(k))^2}} \\ \eta^o(k) &= \frac{(y_1(k)\varepsilon_1(k))^o}{\sqrt{\frac{1}{N} \sum_{k=1}^N (\varepsilon_1^{2o}(k))^2}} + \dots + \frac{(y_q(k)\varepsilon_q(k))^o}{\sqrt{\frac{1}{N} \sum_{k=1}^N (\varepsilon_q^{2o}(k))^2}} \\ \vartheta^o(k) &= \frac{u_1^{2o}(k)}{\sqrt{\frac{1}{N} \sum_{k=1}^N (u_1^{2o}(k))^2}} + \dots + \frac{u_r^{2o}(k)}{\sqrt{\frac{1}{N} \sum_{k=1}^N (u_r^{2o}(k))^2}} \end{aligned} \quad (\text{B.6})$$

with

$$\begin{aligned} \varepsilon_i^{2o}(k) &= \varepsilon_i^2(k) - \overline{\varepsilon_i^2} & \overline{\varepsilon_i^2} &= \frac{1}{N} \sum_{k=1}^N \varepsilon_i^2(k) \\ (y_i(k)\varepsilon_i(k))^o &= y_i(k)\varepsilon_i(k) - \overline{y_i\varepsilon_i} & \overline{y_i\varepsilon_i} &= \frac{1}{N} \sum_{k=1}^N y_i(k)\varepsilon_i(k) \\ u_j^{2o}(k) &= u_j^2(k) - \overline{u_j^2} & \overline{u_j^2} &= \frac{1}{N} \sum_{k=1}^N u_j^2(k) \end{aligned} \quad (\text{B.7})$$

Ideally, if every subsystem in the MIMO model is valid the residual vector  $\varepsilon(k)$  will be an uncorrelated random noise vector and the normalized correlations (B.3 respectively B.5) will yield for  $N \rightarrow \infty$

$$\begin{aligned} \Phi_{\xi\eta}(\tau) &= \begin{cases} k, & \tau = 0 \\ 0, & \text{otherwise} \end{cases} \\ \Phi_{\vartheta\eta}(\tau) &= 0, \quad \forall \tau \end{aligned} \quad (\text{B.8})$$

where  $k > 0$  is some positive constant. If one of the tests B.8 fails, localized tests can be used to check for correlations between submodel residuals, outputs and inputs:

$$\Phi_{\varepsilon^2\eta}(\tau) = E[\varepsilon^2(k)\eta^T(k+\tau)] = \begin{bmatrix} \Phi_{\varepsilon_1^2\eta_1}(\tau) & \dots & \Phi_{\varepsilon_1^2\eta_q}(\tau) \\ \vdots & \ddots & \vdots \\ \Phi_{\varepsilon_q^2\eta_1}(\tau) & \dots & \Phi_{\varepsilon_q^2\eta_q}(\tau) \end{bmatrix} \quad (\text{B.9})$$

$$\Phi_{\mathbf{u}^2\eta}(\tau) = E[\mathbf{u}^2(k)\eta^T(k+\tau)] = \begin{bmatrix} \Phi_{u_1^2\eta_1}(\tau) & \dots & \Phi_{u_1^2\eta_q}(\tau) \\ \vdots & \ddots & \vdots \\ \Phi_{u_r^2\eta_1}(\tau) & \dots & \Phi_{u_r^2\eta_q}(\tau) \end{bmatrix} \quad (\text{B.10})$$

where

$$\begin{aligned}\varepsilon^2(k) &= [\varepsilon_1^2(k) \dots \varepsilon_q^2(k)]^T \\ \eta(k) &= [(y_1(k)\varepsilon_1(k)) \dots (y_q(k)\varepsilon_q(k))]^T \\ \mathbf{u}^2(k) &= [u_1^2(k) \dots u_r^2(k)]^T\end{aligned}\tag{B.11}$$

are squared residual, residual and output product, and squared input vectors respectively. In the case of local correlations ideally an analog result to B.8 holds.

The procedure of model validation is therefore split up into two parts: First the global tests B.3 are applied to check for uncorrelated residuals; stop if these tests are satisfied. Second the local tests B.9 and B.10 are applied to determine which of the submodels is incorrect.

To assure optimal sensitivity, linear correlations can also be used in the first (global) tests.

## B.1.2 Simulated Examples

### Nonlinear Deterministic SISO System

A simple nonlinear deterministic SISO system consisting of polynomial terms

$$y(k) = 0.9y(k-1) + 0.7y(k-2)u(k-2) + 0.2u(k-1)\tag{B.12}$$

is used for demonstration. If the nonlinear term  $0.7y(k-2)u(k-2)$  is deliberately omitted, the model output becomes

$$\hat{y}(k) = 0.9y(k-1) + 0.2u(k-1)\tag{B.13}$$

leading to a model residual of

$$\varepsilon(k) = y(k) - \hat{y}(k) = 0.7y(k-2)u(k-2)\tag{B.14}$$

Since the residual is a nonlinear combination of input and output signals respectively, linear correlation functions fail to detect the incomplete model. Figure B.1 shows the auto-correlation function of the residual  $\varepsilon(k)$  in the upper plot and the cross-correlation function of input  $u(k)$  and residual  $\varepsilon(k)$  in the lower plot. The dash-dotted green lines indicate 95% confidence intervals as criterion for outlying values of the correlation functions. Both plots indicate that no linear correlations are present, which indeed is true, since the residual  $\varepsilon(k)$  is a purely nonlinear combination of signals. The nonlinear correlations B.3 (which in the case of a SISO system are already the local tests B.9 and B.10 respectively) clearly indicate a missing model term by the values outside the confidence intervals (figure B.2). Furthermore, by looking at the time shift  $\tau$  where the extremes occur, the structure and time delay of the missing terms can be reconstructed. The lower plot of figure B.2 shows the nonlinear correlation function  $\Phi_{\partial\eta}(\tau)$ . Instead of remaining within the confidence interval, there is a marked exceedance at  $\tau = 2$ . This indicates that the residual contains a term of  $u(k-2)$  in a nonlinear combination with other terms. In the upper plot the nonlinear correlation function  $\Phi_{\xi\eta}(\tau)$  is depicted. Obviously, the shape differs most strongly from the ideal one given in B.8. Although there is no distinct peak at the correct delay, the absolute maximum of  $\Phi_{\xi\eta}(\tau)$  comes to lie upon the correct time delay for the output term in the residual,  $y(k-2)$ . Using both of these informations the missing of a model term  $y(k-2)u(k-2)$  can be concluded.

It should be noted that the model output must not be calculated with past model outputs. Rather, the past outputs of the real system are to be used to form the model output. If the model output was to be used for feedback, the residual would be highly auto-correlated, therefore leading to useless nonlinear correlation functions.

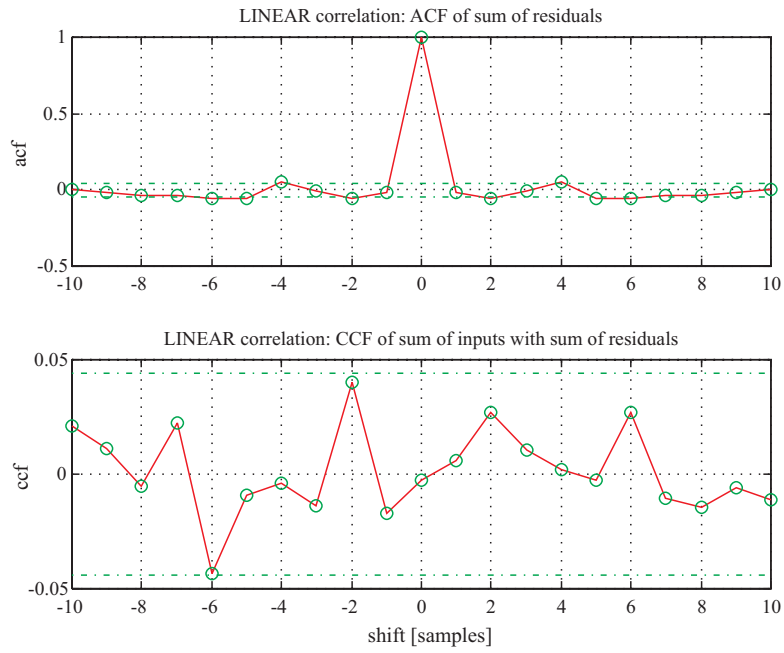


Abbildung B.1: *Model validity tests: Linear correlations*

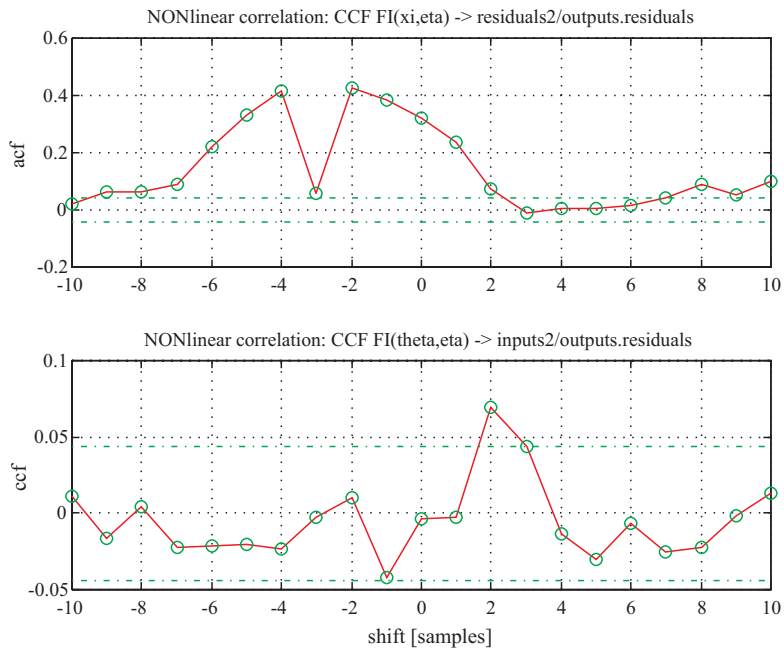


Abbildung B.2: *Model validity tests: Nonlinear correlations*

### Nonlinear SISO System

The nonlinear modified SISO model taken from [21] is used to demonstrate the ability and limits of the method to detect missing model terms in other than polynomial models. The deterministic

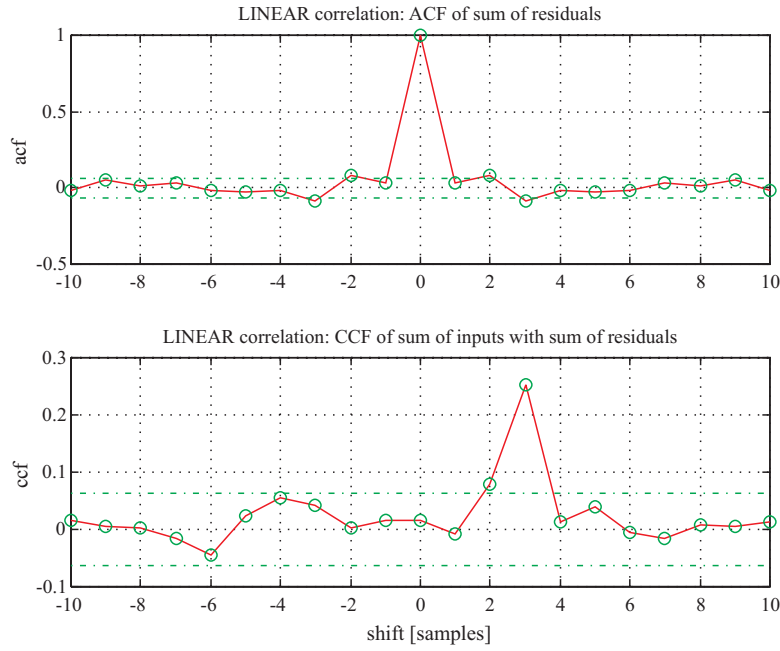


Abbildung B.3: *Model validity test: Linear correlations*

system equation is

$$y(k) = \frac{\alpha y(k-1)y(k-2)y(k-3)u(k-2)(y(k-3)-1) + u(k-1)}{1 + y(k-1)^2 + y(k-2)^2} \quad (\text{B.15})$$

where  $\alpha = 3$ . If the model is restricted to the simplified expression (for  $\alpha = 0$ )

$$\hat{y}(k) = \frac{u(k-1)}{1 + y(k-1)^2 + y(k-2)^2} \quad (\text{B.16})$$

the residual  $\varepsilon(k)$  will be a nonlinear combination of past inputs and outputs respectively. However, the algorithm should be capable of detecting  $y(k-3)$  and  $u(k-2)$  as missing model terms. If classical linear tests are used the correlation functions fail to indicate the correct terms (figure B.3). Although the linear cross-correlation function of the input  $u(k)$  and the residual  $\varepsilon(k)$  shows a small exceedance at  $\tau = 2$  it falsely indicates a stronger correlation at  $\tau = 3$ . The auto-correlation function shows small exceedances at  $\tau = 3$ , which will become insignificant for a smaller parameter  $\alpha$ . The nonlinear correlations are much more significant (see figure B.4) and therefore also yield correct results for a smaller  $\alpha$ . Still, the nonlinear cross-correlation function shows smaller exceedances at time shifts greater than the correct  $\tau = 2$ .

Obviously, the applicability of the method does strongly depend on the structure and the parameters of the nonlinear system. In practice, a clear result which enables the designer to reconstruct the optimal model will be seldom achieved. However, with some experience in the interpretation of nonlinear correlation functions the iterative process of model identification and validation can be considerably sped up.

## B.2 Continuity Property of Function Mapping

A completely different approach is made by [21]. The basic idea is to exploit the continuity property of the nonlinear functions which represent input-output models of continuous dynamic SISO

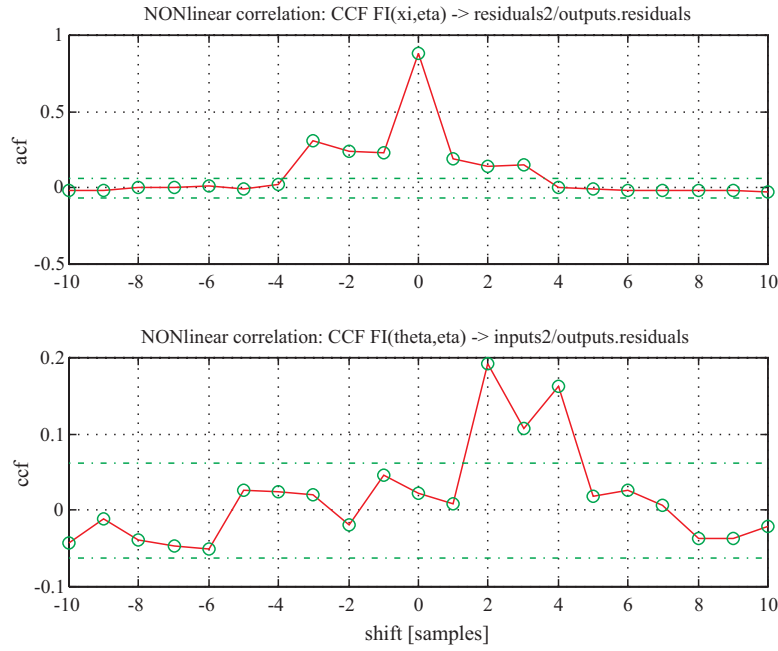


Abbildung B.4: *Model validity test: Nonlinear correlations*

systems. The approach does not depend on any nonlinear function approximation methods and solely depends on the system's input-output data measured in experiments. By evaluating an index with successive modification of model orders, the appropriate model order can be determined.

The big advantage of this approach lies in the a-priori nature of model order determination. However, the drawbacks are numerous:

- The algorithm is computational intensive, requiring  $\frac{n^2}{2} - n$  calculations for each model order, with  $n$  being the number of data samples.
- In order to find the optimal model realization, all permutations of model terms up to a maximum order should be investigated. Instead, only a subset of model terms is investigated in [21] for sake of simplicity. This leads to increasing problems with MISO systems.
- The algorithm is not sensitive to model terms with small residuals.
- If noise is present in the system, the decisive power of the algorithm decreases rapidly with decreasing signal to noise ratio. To compensate at least partly for noise, considerably larger sample numbers have to be used.

### B.2.1 Basic Principle and Algorithm

A general input-output formulation is given by

$$y = f(x) = f(x_1, x_2, \dots, x_n) \quad (\text{B.17})$$

which is a continuous and smooth multivariable function. The partial derivatives of the function  $f(x)$  with respect to its arguments are assumed to be bounded,

$$|f_i| = \left| \frac{\partial f}{\partial x_i} \right| \leq M, \quad i = 1, 2, \dots, n \quad (\text{B.18})$$

where  $M$  is a positive value.

The objective is to reconstruct the nonlinear function  $f(x)$  from the input-output data pairs  $(\mathbf{x}_i, y_i)$ . The Lipschitz quotient  $q_{ij}$  is then given by

$$q_{ij} = \frac{|y_i - y_j|}{|\mathbf{x}_i - \mathbf{x}_j|}, \quad (i \neq j) \quad (\text{B.19})$$

as the ratio of the difference between the two outputs to the distance of the corresponding input vectors. Because of the Lipschitz condition the quotient defined in B.19 must be bounded by some real value. By applying sensitivity analysis and using Schwartz's inequality the following inequality can be established:

$$q_{ij}^{(n)} = \frac{|\partial y|}{\sqrt{(\partial x_1)^2 + \dots + (\partial x_n)^2}} \leq M \frac{|\partial x_1 + \dots + \partial x_n|}{\sqrt{(\partial x_1)^2 + \dots + (\partial x_n)^2}} \leq \sqrt{n}M \quad (\text{B.20})$$

where the superscript  $n$  in  $q_{ij}^{(n)}$  represents the number of input variables in the input-output formulation B.17.

If one of the necessary input variables is not included in the reconstruction of the unknown function, the distance between two points in the input space becomes  $\sqrt{(\partial x_1)^2 + \dots + (\partial x_{n-1})^2}$ . However, the distance between the corresponding outputs remains to be  $|\partial y|$ . If  $x_n$  is independent of the other input variables  $x_1, x_2, \dots, x_{n-1}$ , Lipschitz quotient  $q_{ij}^{(n-1)}$  may be unbounded or extremely large. The more input variables are missing, the larger the quotients may be. In this case any nonlinear function approximation cannot yield optimal results.

When a redundant input variable is included, the distance of two input data points becomes  $\sqrt{(\partial x_1)^2 + \dots + (\partial x_{n+1})^2}$ . This value, if at all, will only be slightly smaller than the distance between the input vectors of the correct model order. If two or more redundant input variables are included, the Lipschitz quotients will still be close to  $q_{ij}^{(n)}$ . Therefore, one should be able to identify the optimal number of input variables from successively computed Lipschitz quotients for increasing model order.

The following index is used as an estimate for the upper bound of the  $q_{ij}^{(n)}$ :

$$q^{(n)} = \sqrt{n} \left[ \prod_{k=1}^p q^{(n)}(k) \right]^{\frac{1}{p}} \quad (\text{B.21})$$

where  $q^{(n)}(k)$  is the  $k$ -th largest Lipschitz quotient among all  $q_{ij}^{(n)}$  ( $i \neq j$ ,  $i, j = 1, 2, \dots, N$ ) with the  $n$  input variables  $(x_1, x_2, \dots, x_n)$ .  $N$  is the number of samples and  $p$  is a positive integer ( $p = (0.01 \sim 0.02)N$  is recommended). The estimate B.21 simply replaces the positive value of  $M$  in B.20 with the geometric mean of the  $k$  largest values for all Lipschitz quotients  $q_{ij}^{(n)}$ .

If the indices  $q^{(n)}$  are plotted versus the model order  $n$ , a characteristic curve should result, which enters a saturated minimum at the optimal model order.

## B.2.2 Simulated Examples

### Linear SISO System

A SISO system represented by the difference equation

$$y(k) = y(k-1) + a_2y(k-2) + a_3y(k-3) + u(k-1) + b_2u(k-2) + ce(k) \quad (\text{B.22})$$

was simulated for 400 data points with the input  $u(k)$  being an uncorrelated sequence with uniform distribution in the interval  $[-1; 1]$ . The noise  $e(k)$  was chosen to be an uncorrelated normally distributed sequence with zero mean and a variance of  $\sigma^2 = 0.1$ .

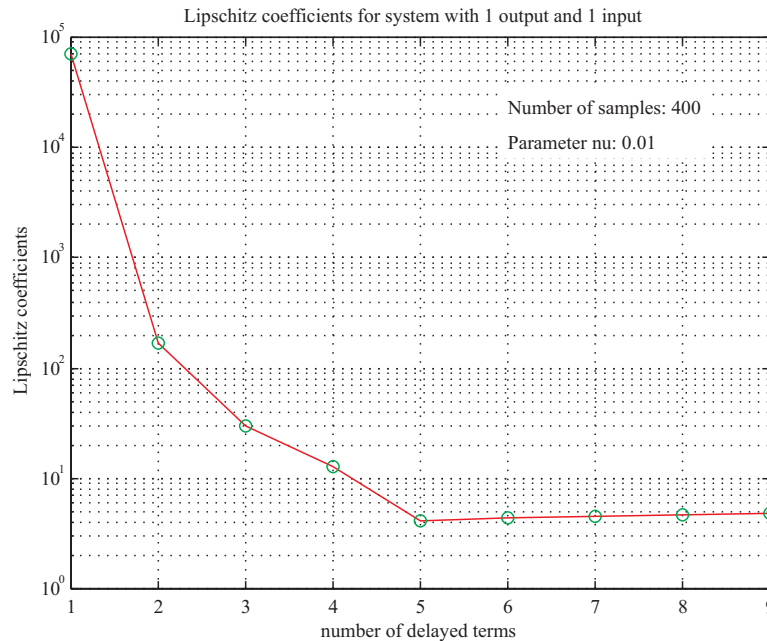


Abbildung B.5: *Lipschitz coefficients for linear SISO system without noise. Correct system order of  $n = 5$  detected.*

Data from the system with a parameter vector  $\theta = [a_2 \ a_3 \ b_2 \ e] = [-0.7 \ 0.5 \ 0.8 \ 0]$  produced the result shown in figure B.5. The number of delayed terms can be clearly read from the plot to be 5, since for numbers 6 and higher even an increase in the value of the coefficients is visible. If the coefficient  $b_2$  is much smaller, e.g.  $b_2 = 0.01$ , the corresponding coefficient at index 4 will not lie on the same slope as the neighboring points, but its magnitude will only be slightly smaller than that of the one with index 3. However, the overall system order is still apparent from the plot.

If the parameter vector is chosen to be  $\theta = [-0.09 \ 0.05 \ 0.8 \ 0]$  a different plot will result. Since neglecting the small parameters will only result in a 5% error, the algorithm does not detect the small contributions well enough. Because the coefficient for the term with index 4 is the last significant one, the algorithm indicates a system order of 4 (see figure B.6). With even smaller coefficients ( $\theta = [-0.09 \ 0.05 \ 0.09 \ 0]$ ) the plot will indicate an order of 3, at least detecting the one most important model term with a small coefficient. Obviously, the algorithm's sensitivity is proportional not to the values of the coefficients but to the residuals of the respective model terms. This should be expected by the theoretical background of the method.

In the case of  $e \neq 0$  the decisive power of the method is strongly reduced. Since there is no noise model employed, the effects of the noise are regarded as part of the system dynamics. Since the noise under consideration is uncorrelated, there will be no more saturation above the optimal index. Instead, a monotonical decrease over the whole range is to be expected. In the extreme case where uncorrelated noise signals are taken as input and output respectively, a plot like a rescaled and offset  $y = \frac{1}{x}$  function will result. The plots for data with noise are therefore more difficult to interpret. Figure B.7 shows the plot for the linear system B.22 with the parameter vector  $\theta = [-0.7 \ 0.5 \ 0.8 \ 2]$ . With smaller residuals for the model terms the influence of noise is even more disturbing. From the plot in figure B.8 neither the real nor the optimal model order can be detected. Instead, a much too high model order is proposed in order to compensate for the presence of the uncorrelated noise terms. Even triple the sample size does not alter the characteristic of the plot, although there is a slight increase for the coefficients before the optimal index and a decrease for those above. In general, a great increase in sample size will only yield small improvements,



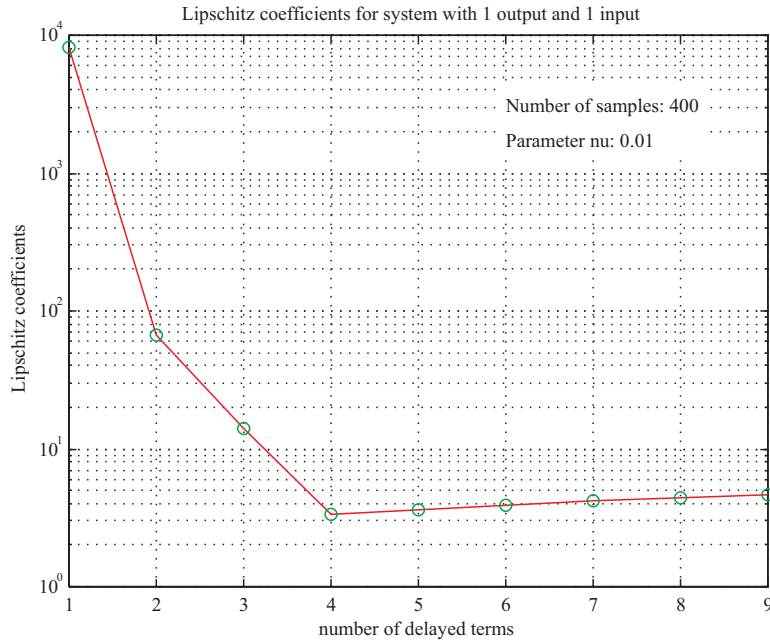


Abbildung B.6: Lipschitz coefficients for linear SISO system without noise. Wrong system order of  $n = 4$  detected (correct system order  $n = 5$ ).

although these improvements could be of crucial importance.

### Nonlinear SISO System

The nonlinear system under investigation is taken from [21] and modified. The third power for  $x_1$  has been exchanged to a square, since the original system obviously does not fulfill the criterion of being a smooth and continuous function. The systems output equation

$$y(k) = f[y(k-1) \quad y(k-2) \quad y(k-3) \quad u(k-1) \quad u(k-2)] = f(\mathbf{x}) \quad (\text{B.23})$$

with the nonlinear function  $f$  of the form

$$f(\mathbf{x}) = \frac{\alpha x_1 x_2 x_3 x_5 (x_3 - 1) + x_4 + e x_1}{1 + x_1^2 + x_2^2} \quad (\text{B.24})$$

is bounded, since the input is bounded and the denominator is always greater or equal 1. The original system had a denominator of  $1 + x_1^3 + x_2^2$ . This expression can become zero for certain  $x_1$  and  $x_2$ , therefore leading to an unbounded  $y(k)$ . The additional factor  $\alpha$  has been introduced and a nonlinear noise term  $e x_1$  has been added to the numerator. The noise sequence is the same as defined above. The plot in figure B.9 shows the Lipschitz coefficients for  $\alpha = 1$  and no noise. Although the sample size is more than twice the size of the linear example, the optimal system order is not as clearly indicated. This becomes even more obvious when the factor  $\alpha$  is set to the value  $\alpha = 0.33$ . This purely quantitative modification produces a strong qualitative change in the Lipschitz coefficients. Figure B.10 clearly demonstrates that even in the absence of noise a wrong indication of the optimal order is achieved. The additional presence of a nonlinear noise term has the same influence as noise in linear systems. The plot in figure B.11 shows a slight dip at the correct order, but without prior knowledge it would be difficult to detect ( $\alpha = 1$ ). With  $\alpha = 0.33$  and additional nonlinear noise term the plot is nearly the same (figure B.12). Obviously the shape of the curve is already determined by the noise term, with little influence left for the factor  $\alpha$ .

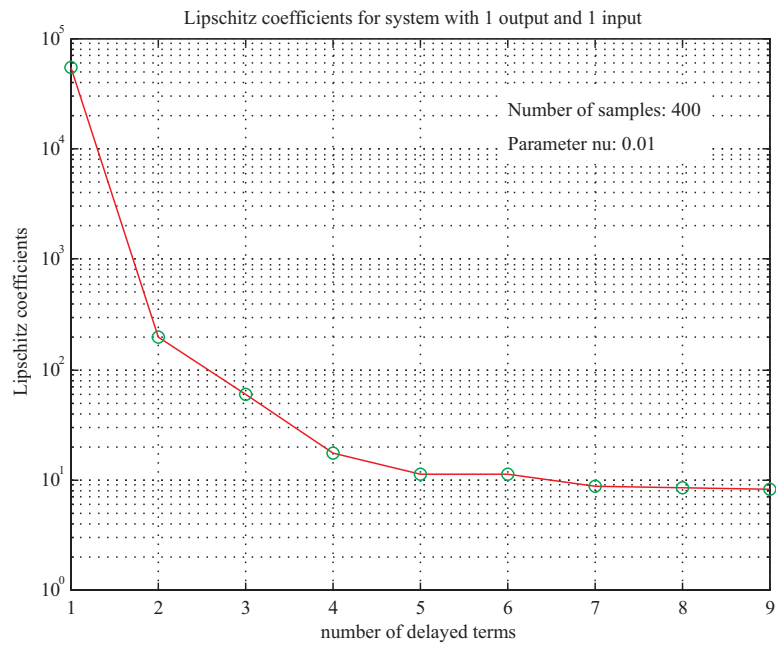


Abbildung B.7: *Lipschitz coefficients for linear SISO system with noise. Correct system order  $n = 5$  not detectable.*

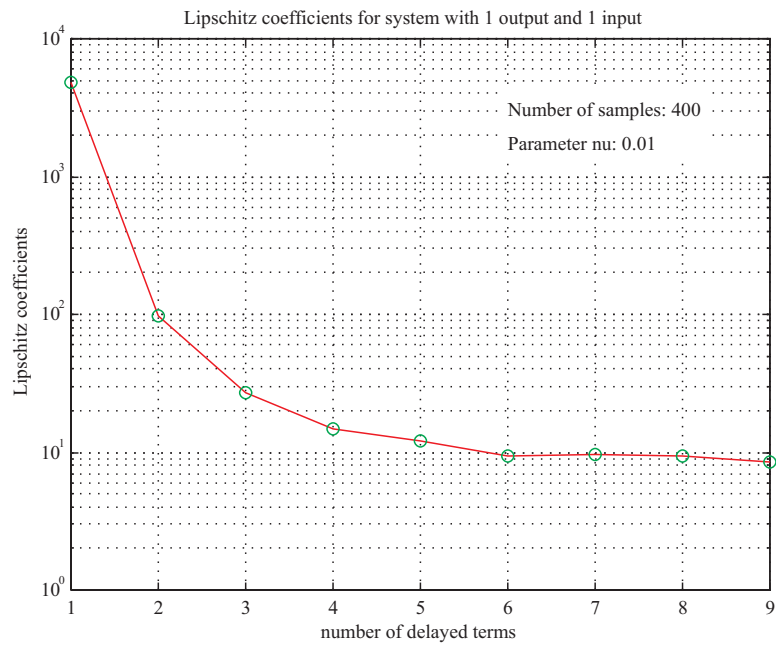


Abbildung B.8: *Lipschitz coefficients for linear SISO system with noise. Correct system order  $n = 5$  not detectable.*

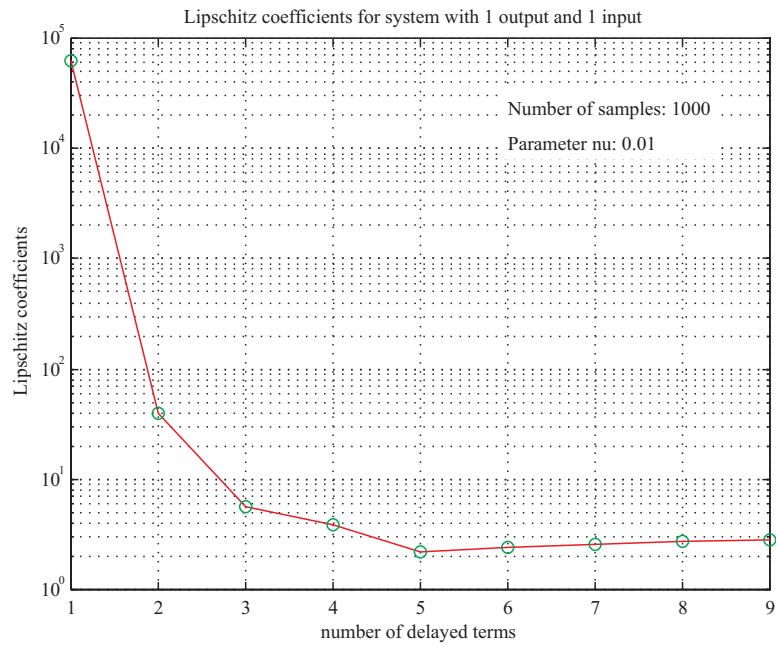


Abbildung B.9: Lipschitz coefficients for nonlinear SISO system without noise and  $\alpha = 1$ .

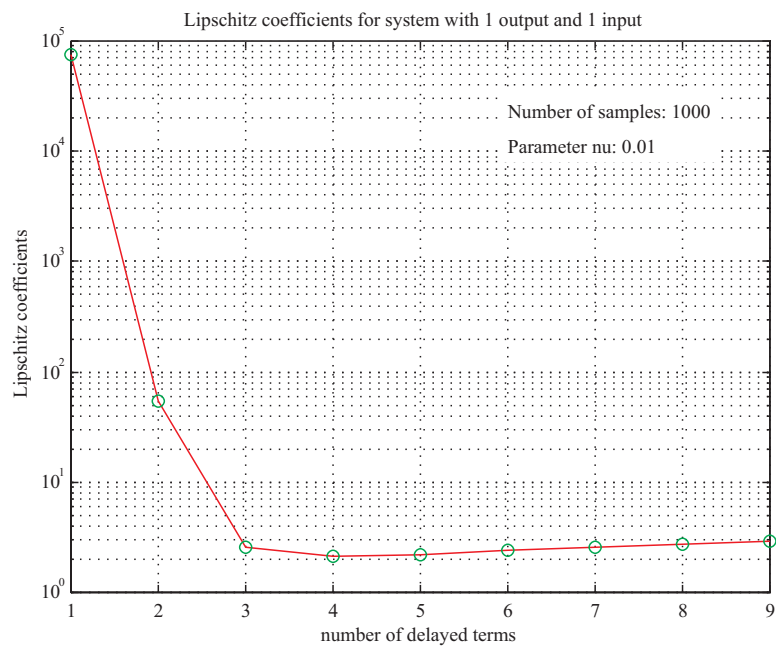


Abbildung B.10: Lipschitz coefficients for nonlinear SISO system without noise and  $\alpha = 0.33$ .

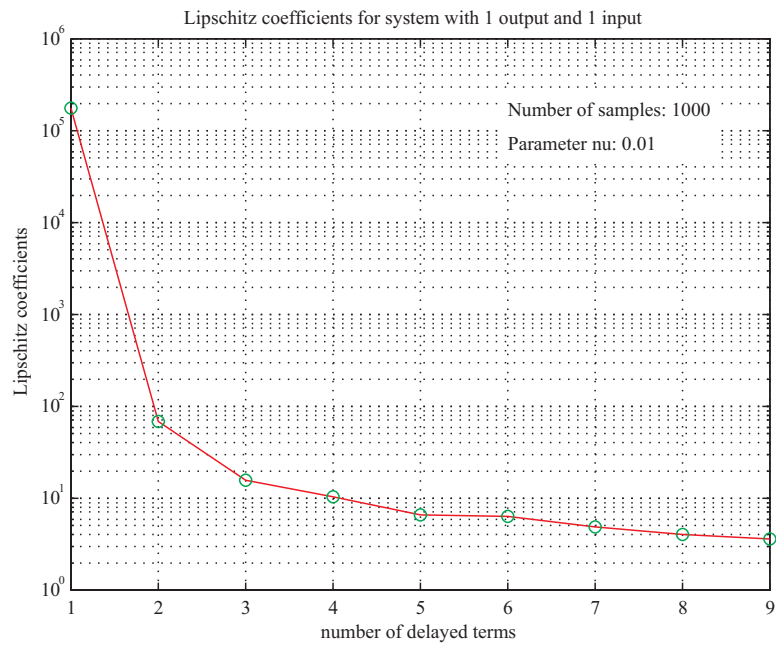


Abbildung B.11: *Lipschitz coefficients for nonlinear SISO system with nonlinear noise term and  $\alpha = 1$ .*

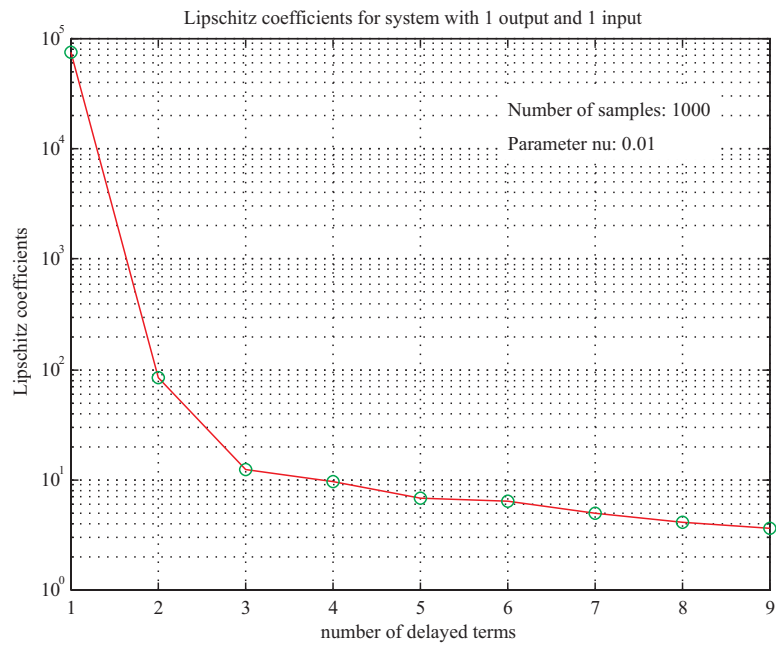


Abbildung B.12: *Lipschitz coefficients for nonlinear SISO system with nonlinear noise term and  $\alpha = 0.33$ .*

# Appendix C

## Calculation of Spectra

A spectrum is a representation of the distribution in frequency of power of a random process. Since all representations of signals with finite sample lengths do not allow for the limit operations necessary for the calculation of exact spectra, only estimates of their spectra can be computed. Obviously, the best way to get reliable estimates is to increase the length of the sampling sequence. If the number of samples is limited (and this happens to be the case in most applications) some uncertainties have to be accepted: Either the variance or the bias of the estimate will be high.

Spectral estimators may be classified as either parametric or nonparametric. The nonparametric spectral estimators require no assumption on the data other than wide-sense stationarity. On the other hand, parametric estimators are based on time-series or transfer function models, hence their application is more restrictive. The a priori model assumption is both an advantage (higher resolution) and an additional degree of freedom.

Extensive coverage of both types of spectral estimators is found in [32] and [41], where also a comparison of the performance of the classical nonparametric spectral estimates is given. Although analytical descriptions of track spectra are well known ([42], [16]) and state space filters using white noise input are a standard approach [29], their use in this application would be counterproductive, since the track spectra are investigated to reveal the presence of any additional influences. With a parametric estimator using a specific model these influences could be suppressed by design.

### C.1 Nonparametric Spectral Estimation

#### C.1.1 Periodogram

The periodogram spectral estimator for a signal  $x(k)$  with length  $N$  is defined as

$$\hat{S}_x(f) = \frac{1}{N} \left| \sum_{k=0}^{N-1} x(k) e^{-j2\pi f k} \right|^2 = \frac{1}{N} |X(f)|^2, \quad (\text{C.1})$$

where  $X(f)$  denotes the Fourier transform of  $x(k)$ . It can be interpreted as a bandpass filter bank, where the output of each filter at a particular frequency  $f_0$  is used to compute the magnitude squared. It is most important to notice that the periodogram is asymptotically unbiased, however, it is not a consistent spectral estimator (i.e. the variance of the estimate does not decrease with increasing  $N$ ). Furthermore, the restriction to finite sample lengths is equivalent to multiplying an infinite sequence with a rectangular window. It is well known that any window will produce an effect called leakage, where energy is distributed from the original frequency range into neighboring frequencies. As a trade-off for reduced leakage, the spectral estimate will be smoothed, thus reducing the frequency resolution and making the estimate biased. It should also be noted here that zero padding of the signal and evaluating the discrete Fourier transform (DFT) at  $L > N$  points

does not improve the frequency resolution. It simply interpolates the values of the spectrum at more frequencies.

The units of the power spectral density can be found according to Parseval's theorem

$$\frac{1}{L} \sum_{i=0}^{L-1} \hat{S}_x(f_i) = \frac{1}{N} \sum_{k=0}^{N-1} x^2(k) \quad (\text{C.2})$$

which states that the normalized sum over all frequencies in the power spectral density equals the average power (covariance) of the signal in the time domain. If the input signal is in  $mm$  as a function of way  $[m]$  then the units on  $\hat{S}_x(f)$  are  $mm^2.m$ . The RMS value at a certain frequency is the square root of either side of equation C.2. However, the RMS value is a time average and does not directly relate to a local signal amplitude.

### C.1.2 Bartlett Method

Bartlett's Method [2] reduces the variance of the spectral estimate at the cost of frequency resolution by averaging over nonoverlapping data segments. It can be structured in three steps: First the signal is subdivided into nonoverlapping sections. For each of these sections the periodogram according to C.1 is computed. In the last step the average over all periodograms is evaluated.

If the length of each subsection was  $M = \frac{N}{K}$  samples,  $N$  being the number of all samples, it can be shown ([32], [41]) that the frequency resolution as well as the variance of the spectral estimate have been reduced by a factor  $K$ . However, as mentioned above, the averaging operation not only yields a smoothed periodogram but also introduces a bias.

### C.1.3 Blackman-Tukey Method

Blackman and Tukey [9] used the discrete weighted version of the Wiener-Khintchine relations 4.35 to compute a spectral estimate

$$\hat{S}_x(f) = \sum_{k=-(M-1)}^{M-1} R_{xx}(k) w(k) e^{-j2\pi fk}, \quad (\text{C.3})$$

where the window  $w(k)$  is of length  $2M - 1$  and is zero for  $|k| \geq M$ . The effect of multiplying a window into the estimate of the auto-correlation function is a smoothing of the estimate  $\hat{S}_x(f)$ , therefore achieving a reduced variance at the cost of reduced frequency resolution and bias.

### C.1.4 Welch Method

Welch [50] modified Bartlett's method in two ways: He allowed for overlapping data segments and additionally applied a window to the data segments prior to computation of the periodograms. Therefore the periodograms to be averaged can be denoted by

$$\hat{S}_x^{(i)}(f) = \frac{1}{MU} \left| \sum_{k=0}^{M-1} x_i(k) w(k) e^{-j\omega k} \right|^2, \quad i = 0, 1, \dots, L-1 \quad (\text{C.4})$$

where  $U$  is a normalization factor depending on the choice of the window  $w(k)$  and the length of the segments  $M$ :

$$U = \frac{1}{M} \sum_{k=0}^{M-1} w^2(k) \quad (\text{C.5})$$

The average of the periodograms C.4 over all data segments is the Welch spectral estimate. Again, less variance is traded against bias and frequency resolution.

The authors of [4] claim that the 'linear' windowing performed in equation C.4 is unnecessary, since the leakage suppression and smoothing is already assured by averaging, and linear weighting does not conserve power. However, Welch's method is widely in use today because of easy adaptation of variance/bias trade-off and numerical efficiency without showing any of the shortages claimed by [4].

## C.2 Errors in Spectral Analysis Due to Sampling Jitter

The results given in [6] indicate that sampling jitter in periodically (or pseudorandomly) sampled signals represents a source of significant bias and random error. This is especially true for the high-frequency components of the signals under investigation. In the case of normally distributed jitter with a variance of  $\sigma^2$  the relative systematic estimation error  $\delta$ , which corrupts estimation of the Fourier coefficients, can be written as

$$\delta = (S - 1) 100\% \quad (\text{C.6})$$

$$S = \exp(-2\pi^2\alpha^2\beta^2) \quad (\text{C.7})$$

where  $\alpha = f/f_s$  and  $\beta = \sigma f_s$  ( $f_s$  denoting the mean sampling rate). With equation C.7 a quantitative statement on the error caused by jitter becomes possible if the variance of jitter  $\sigma^2$  is known. For  $\alpha = 0.5$  (highest frequency component) and  $\beta = 0.05$  ( $\sigma = 0.5/f_s$ ) a relative systematic error of  $\delta = 1\%$  will result. Because of the more than exponential increase of  $\delta$  with  $\sigma$ , sampling jitter should be kept as small as possible.

However, if we take into account that the sampling rate of the OEBS measuring coach is  $f_s = 4\frac{1}{m}$ , the variance of sampling jitter would have to be  $\sigma^2 = (0.5/4)^2 = 0.0156m$ , which is certainly a very high value. It therefore seems to be justified to regard the spectral estimations performed in this thesis as being unaffected by jitter.

Furthermore, the maximum mean error in the sampling interval is limited to  $\pm 0.2\%$  according to statements of the OEBS systems measurement group. Such an error would merely lead to slightly shifted spatial, time, and frequency scales, which in turn would give slightly offset values for the identification. However, the identification itself is not affected by a constant deviation from the nominal sampling interval and will yield consistent results.

# Appendix D

## Spline Interpolation

An extensive coverage of the field of spline interpolation can be found in [10], which covers theoretical background, problems of practical implementation, as well as programming examples. The Spline Toolbox of MATLAB<sup>R</sup> was also written by the author of this book. A lot of excellent textbooks covering the area of curve and surface fitting with splines exist (e.g. [11]).

### D.1 Interpolation Polynomials

Interpolation polynomials may be used to establish a continuous function through a finite number of discrete points. For the task of interpolation a function is sought for, which runs exactly through the known points and has a smooth course in between those points. The following theorem gives a statement on existence and uniqueness of this interpolation polynomial and an error bound:

Let  $y = f(x)$  denote a  $(n + 1)$  times continually differentiable function of  $x$  defined on the interval  $a \leq x \leq b$ . For a given set of function points  $(x_i, y_i)$  with  $0 \leq i \leq n$  and  $x_i \neq x_j$  for  $i \neq j$  there exists exactly one interpolation polynomial  $P_n(x)$  with a degree of  $n$  for which  $P_n(x_i) = y_i$  holds. Furthermore, for every  $x \in [a, b]$

$$f(x) - P_n(x) = \frac{f^{(n+1)}(u)}{(n+1)!} \prod_{k=0}^n (x - x_k) \quad (\text{D.1})$$

holds where  $u \in [a, b]$ .

Although the computation of an interpolation polynomial is straightforward and requires only the solution of a system of linear equations the concept has some severe shortcomings.

- The distribution of the values  $x_k$  strongly influences the interpolation error. In the case of uniformly spaced points  $x_k$  stronger oscillations of  $P_n(x)$  will occur near the margins of the interval  $[a, b]$ .
- If a known pole of the function  $f(x)$  lies between two points  $x_l$  and  $x_{l+1}$  a rational function should be chosen for interpolation in the vicinity of those points.
- To keep the error D.1 small, piecewise interpolation with lower order polynomials may be advisable ( $1 \leq n \leq 5$ ).

A special case of the last possibility mentioned above is cubic spline interpolation.

### D.2 Cubic Spline Interpolation

Instead of trying to interpolate  $(n + 1)$  points  $(x_i, y_i)$  by a single high order polynomial  $P_n(x)$  of degree  $n$  the cubic spline interpolant  $s(x)$  is defined by the following characteristics:



- $s(x)$  is a polynomial  $s_i(x)$  of degree 3 in each subinterval  $x_i \leq x \leq x_{i+1}$
- $s(x)$  is a continuous function:  $s(x_i) = s_{i-1}(x_i) = s_i(x_i) = y_i$
- Continual first derivative of  $s(x)$ :  $s'(x_i) = s'_{i-1}(x_i) = s'_i(x_i)$
- Continual first derivative of  $s(x)$ :  $s''(x_i) = s''_{i-1}(x_i) = s''_i(x_i)$

The third and fourth points in the above list mean that the spline interpolant is smooth and neighboring spline polynomials have identical curvature at their common margins. To construct the cubic spline interpolant for a given function  $y = f(x)$  the following statement is used:

For each subinterval  $x_i \leq x \leq x_{i+1}$

$$s_i(x) = a_i(x - x_i)^3 + b_i(x - x_i)^2 + c_i(x - x_i) + d_i \quad (\text{D.2})$$

$$s'_i(x) = 3a_i(x - x_i)^2 + 2b_i(x - x_i) + c_i \quad (\text{D.3})$$

$$s''_i(x) = 6a_i(x - x_i) + 2b_i \quad (\text{D.4})$$

holds. By defining the individual interval lengths as  $h_i = x_{i+1} - x_i$  we can rewrite the above expressions for both endpoints of the interval:

$$s_i(x_i) = d_i = y_i \quad (\text{D.5})$$

$$s_i(x_{i+1}) = a_i h_i^3 + b_i h_i^2 + c_i h_i + d_i = y_{i+1} \quad (\text{D.6})$$

$$s'_i(x_i) = c_i \quad (\text{D.7})$$

$$s'_i(x_{i+1}) = 3a_i h_i^2 + 2b_i h_i + c_i \quad (\text{D.8})$$

$$s''_i(x_i) = 2b_i = y''_i \quad (\text{D.9})$$

$$s''_i(x_{i+1}) = 6a_i h_i + 2b_i = y''_{i+1} \quad (\text{D.10})$$

The unknown coefficients  $a_i, b_i, c_i$ , and  $d_i$  are substituted by the function values  $y_i$  and their second derivatives  $y''_i$ , respectively.

$$a_i = \frac{1}{6h_i}(y''_{i+1} - y''_i) \quad (\text{D.11})$$

$$b_i = \frac{1}{2}y''_i \quad (\text{D.12})$$

$$c_i = \frac{1}{h_i}(y_{i+1} - y_i) - \frac{1}{6}h_i(y''_{i+1} + 2y''_i) \quad (\text{D.13})$$

$$d_i = y_i \quad (\text{D.14})$$

The first derivative of the spline interpolant according to equation D.8 can now be rewritten as

$$s'_i(x_{i+1}) = 3a_i h_i^2 + 2b_i h_i + c_i = \quad (\text{D.15})$$

$$= \frac{1}{h_i}(y_{i+1} - y_i) + \frac{1}{6}h_i(2y''_{i+1} + y''_i) \quad (\text{D.16})$$

In a last step the property of equal derivatives is utilized

$$s'_{i-1}(x_i) = s'_i(x_i) = c_i \quad (\text{D.17})$$

$$h_{i-1}y''_{i-1} + 2(h_{i-1} + h_i)y''_i + h_i y''_{i+1} = \frac{1}{h_i}(y_{i+1} - y_i) - \frac{1}{6}h_i(y''_{i+1} + 2y''_i) \quad (\text{D.18})$$

where equation D.18 holds for  $1 \leq i \leq n$ .

Therefore, the final task is to solve a linear tridiagonal system with  $(n - 1)$  equations for the  $(n + 1)$  unknowns  $y''_0, y''_1, \dots, y''_{n-1}, y''_n$ . The second derivatives at the end points of the main interval  $[a, b]$  are apparently still not determined. The choice of

$$y''_0 = y''_n = 0 \quad (\text{D.19})$$

determines the so called "natural" spline function, although any reasonable choice of these values is possible. In any case, the effects of the actual values of  $y''_0$  and  $y''_n$  will rapidly decrease over a few points  $x_i$ .

The name "spline" stems from the fact that the differential equation of deformation for an elastic beam without external force

$$\frac{d^2}{dx^2} \left( c(x) \frac{d^2 y}{dx^2} \right) = 0 \quad (\text{D.20})$$

and a constant bending stiffness of  $c(x) = 1$  has the solution

$$y(x) = a(x - 1)^2(2x + 1) + bx(x - 1)^2 + cx^2(3 - 2x) + dx^2(x - 1). \quad (\text{D.21})$$

The constants are determined by the boundary conditions

$$y(0) = a, \quad y'(0) = b, \quad y(1) = c, \quad y'(1) = d. \quad (\text{D.22})$$

This analogy leads to the interpretation of the spline interpolant as an elastic beam of constant bending stiffness and without external loads which is supported at the points  $(x_i, y_i)$ . The end conditions of natural spline defined by equation D.19 is therefore equivalent to no external torque at the end points of the beam.

### D.2.1 Simulation: Comparison of Resampling by Cubic Splines versus Low-Pass Filtering

To evaluate the performance of cubic spline interpolation the following procedure is used. First, a function  $y = f(t)$  is generated by numerical simulation of a double pendulum where  $y = \dot{\gamma}(t)$  and  $\gamma(t)$  is the angle of the second pendulum. The original signal  $y = f(t)$  is sampled at  $\Delta T = 0.01s$  while the signal used as input for both interpolation schemes contains only every 10th sample from  $y$  ( $\Delta T = 0.1s$ ). The original signal is then reconstructed approximately and the results are compared. The spline interpolant was computed according to the equations in the previous section. Discrete lowpass interpolation was performed by a symmetric filter which allows to pass the original data unfiltered. 8 samples were used at a time to perform interpolation. The differences between the two interpolation schemes are small and both of them perform very good except for sections where the original samples come to lie at subsequent turning points. As clearly visible in figure D.1 both reconstructed signals tend to produce too small peaks at such sections. The sum squared error for a signal of 20s duration is 4.396 for the spline interpolant and 4.131 for the discrete filter giving a relative difference of 6%. Although the discrete filter is superior for equidistant resampling the advantage of spline interpolants clearly lies within their ability to reconstruct signal values at arbitrary time points. Using discrete methods would either lead to large approximation errors or it would require large interpolation ratios which is both inefficient with respect to computation time and memory requirements.

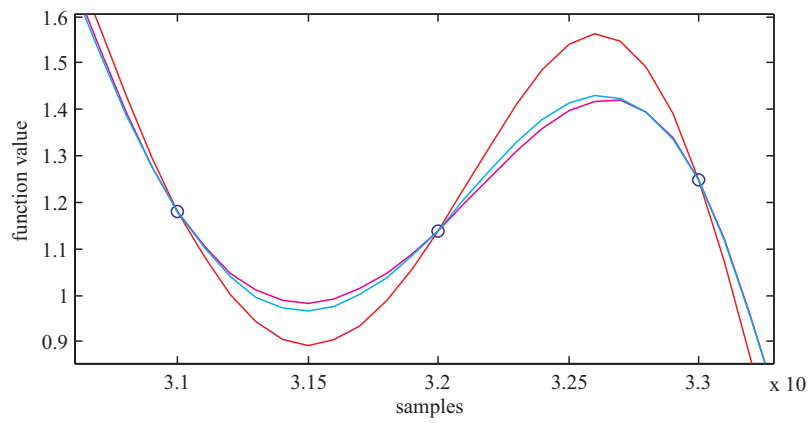


Abbildung D.1: *Comparison of interpolation techniques: Original signal (red), spline interpolant (magenta), and lowpass filtered discrete interpolation (cyan). Samples used for reconstruction denoted by blue circles.*

# Bibliography

- [1] H. Al-Duwaish, M. Nazmul Karim, and V. Chandrasekar. Hammerstein model identification by multilayer feedforward neural networks. *International Journal of Systems Science*, 28(1):49–54, 1997.
- [2] M. S. Bartlett. Smoothing periodograms from time series with continuous spectra. *Nature*, 161:686–687, may 1948.
- [3] Michèle Basseville. Detecting changes in signals and systems. *Automatica*, 24(3):309–326, 1988.
- [4] K. G. Beauchamp and C. K. Yuen. *Digital Methods for Signal Analysis*. George Allen & Unwin, 1979.
- [5] J. S. Bendat and A. G. Piersol. *Random Data: Analysis and Measurement Procedures*. Wiley-Interscience, 1971.
- [6] I. Bilinskis and A. Mikelsons. *Randomized Signal Processing*. Prentice Hall International Series in Acoustics, Speech and Signal Processing. Prentice Hall, 1992.
- [7] S. A. Billings and Q. M. Zhu. Nonlinear model validation using correlation tests. *International Journal of Control*, 60(6):1107–1120, 1994.
- [8] S. A. Billings and Q. M. Zhu. Model validation tests for multivariable nonlinear models including neural networks. *International Journal of Control*, 62(4):749–766, 1995.
- [9] R. B. Blackman and J. W. Tukey. *The Measurement of Power Spectra*. Dover, New York, 1958.
- [10] Carl De Boor. *A practical guide to splines*. Springer Verlag, New York, 1978.
- [11] P. Dierckx. *Curve and Surface Fitting with Splines*. Oxford University Press, New York, 1993.
- [12] Rao V. Dukkipati and Joseph R. Amyot. *Computer-Aided Simulation in Railway Dynamics*. Marcel Dekker, New York and Basel, 1988.
- [13] Sunil Elanayar and Yung C. Shin. Radial basis function neural network for approximation and estimation of nonlinear stochastic dynamic systems. *IEEE Transactions on Neural Networks*, 5(4):594–603, jul 1994.
- [14] Coenraad Esveld. *Modern railway track*. MRT-Productions, Duisburg, Germany, 1989.
- [15] F. Frederich. Kriterien für Fahrkomfort, Erfahrungen bei Schienenfahrzeugen. *VDI-Berichte*, (284):41–47, 1977.
- [16] F. Frederich. Die Gleislage - aus fahrzeugtechnischer Sicht. *ZEV-Glasers Annalen*, 108(12):355–362, dec 1984.

- [17] William A. Gardner. The role of spectral correlation in design and performance analysis of synchronizers. *IEEE Transactions on Communications*, COM-34(11):1089–1095, nov 1986.
- [18] Vijay K. Garg and Rao V. Dukkipati. *Dynamics of Railway Vehicle Systems*. Academic Press, 1984.
- [19] A. Ghazizadeh, A. Fahim, and M. El-Gindy. Neural networks representation of a vehicle model: 'Neuro-Vehicle (NV)'. *International Journal of Vehicle Design*, 17(1):55–75, 1996.
- [20] L. Gianone, J. Bokor, and K.M. Hangos. Grey box identification of vehicle dynamics. In *System Identification (SYSID'94): A postprint volume from the IFAC symposium*, volume 3, pages 1187–1192, Copenhagen, Denmark, jul 1994. Pergamon.
- [21] Xiangdong He and Haruhiko Asada. A new method for identifying orders of input-output models for nonlinear dynamic systems. In *Proc. American Control Conference*, pages 2520–2523, San Francisco, California, jun 1993. IEEE.
- [22] David Horwitz and Magdy El-Sibaie. Applying neural nets to railway engineering. *AI Expert*, pages 36–41, jan 1995.
- [23] Don R. Hush and Bill Horne. An overview of neural networks, part II: Dynamic networks. *Informatika y Automatica*, 25(2):17–32, 1992.
- [24] Kam-Chuen Jim, C. Lee Giles, and Bill G. Horne. An analysis of noise in recurrent neural networks: Convergence and generalization. *IEEE Transactions on Neural Networks*, 7(6):1424–1438, 1996.
- [25] Shoji Kajita, Kazuya Takeda, and Fumitada Itakura. Subband-crosscorrelation analysis for robust speech recognition. In H.T. Bunnell and W. Idsardi, editors, *Proceedings ICSLP 96. Fourth International Conference on Spoken Language Processing.*, volume 1, pages 422–425. IEEE New York, 1996.
- [26] Jerzy Kisilowski, editor. *Advanced Railway Vehicle System Dynamics*. Wydawnictwa Naukowo-Techniczne, Warszawa, Poland, 1991.
- [27] Monika Köhle. *Neuronale Netze*. Springer angewandte Informatik. Springer Verlag, Wien; New York, 1990. (in German).
- [28] Reinhard Korb. *Lineare und nichtlineare Black- und Grey-Box-Modellierung von Gasmotoren*. PhD dissertation, Vienna University of Technology, Institute for Machine and Process Automation, 1997. (in German).
- [29] W. Kortüm and P. Lugner. *Systemdynamik und Regelung von Fahrzeugen*. Springer-Verlag, 1994.
- [30] Martin Kozek. Modellbildung, Stabilitätsuntersuchung und Simulation eines MAGLEV-Tragsystems sowie Entwurf einer Sliding-Mode Regelung. Diplomarbeit, Vienna University of Technology, Institute for Machine and Process Automation, 1993. (in German).
- [31] Martin Kozek, Gregor Puchhammer, and Hanns P. Jrgl. A MISO sliding mode control for a high speed EMS MAGLEV-vehicle using disturbance estimation. In *Proceedings of the Third IEEE Conference on Control Applications*, pages 587–592, Glasgow, Scotland, August 1994. IEEE.
- [32] J. S. Lim and A. V. Oppenheim. *Advanced Topics in Signal Processing*. Prentice Hall Signal Processing Series. Prentice Hall, 1988.

- [33] James N.K. Liu and K.Y. Sin. Fuzzy neural networks for machine maintenance in mass transit railway system. *IEEE Transactions on Neural Networks*, 8(4):932–941, jul 1997.
- [34] Lennart Ljung. *System Identification: Theory for the User*. Information and System Sciences Series. Prentice-Hall, 1987.
- [35] Kumpati S. Narendra and Kannan Parthasarathy. Identification and control of dynamical systems using neural networks. *IEEE Transactions on Neural Networks*, 1(1):4–27, 1990.
- [36] International Union of Railways. UIC 518: Test and approval of railway vehicles from the points of view of dynamic behaviour, safety, track fatigue, and ride quality. Leaflet, Paris, France, 1995.
- [37] Per Erik Olson and Stig Johnsson. *Lateral Forces Between Wheels and Rails - An Experimental Investigation*, volume 3 of *Anthology of Railway Vehicle Dynamics 1973*, pages 253–261. ASME, 1960.
- [38] D.T. Pham and X. Liu. Dynamic system modelling using partially recurrent neural networks. *Journal of System Engineering*, 2:90–97, 1992.
- [39] Martin Pottmann. *Radial basis function networks for process identification and control*. PhD dissertation, Vienna University of Technology, Institute for Machine and Process Automation, 1993.
- [40] Gérard Presle. Der neue Oberbaumesswagen der Österreichischen Bundesbahnen. *Österreichische Zeitschrift für Verkehrswissenschaft*, 2(1):33–41, 1993. (in German).
- [41] J. G. Proakis, C. M. Rader, F. Ling, and C. L. Nikias. *Advanced Digital Signal Processing*. Macmillan Publishing Company, 1992.
- [42] A. Prud'homme. La voie. *Rev. Gen. Chemins de Fer*, 89(1):56–67, 1970.
- [43] Russell Reed. Pruning algorithms—a survey. *IEEE Transactions on Neural Networks*, 4(5):740–747, sept 1993.
- [44] Klaus Rießberger. Besonderheiten der Gleisunterhaltung für hohe Geschwindigkeiten. *Eisenbahntechnische Rundschau*, 9:573–579, 1988. (in German).
- [45] Wilson J. Rugh. *Nonlinear System Theory: The Volterra/Wiener Approach*. Johns Hopkins series in information sciences and systems. Johns Hopkins University Press, 1981.
- [46] Torsten Söderström and Petre Stoica. *System Identification*. Prentice-Hall, 4 edition, 1995.
- [47] Jenbacher Transportsysteme. Der neue Hochgeschwindigkeits-Oberbaumesswagen der Österreichischen Bundesbahnen. Brochure from manufacturer, 1992. (in German).
- [48] Hans Troger and Alois Steindl. *Nonlinear Stability and Bifurcation Theory: An Introduction for Engineers and Applied Scientists*. Springer Verlag, Wien, New York, 1991.
- [49] K. M. Tsang and S. A. Billings. Identification of systems from non-uniformly sampled data. *International Journal of Systems Science*, 26(10):1823–1837, 1995.
- [50] P. D. Welch. The use of fast fourier transform for the estimation of power spectra; a method based on time averaging over short modified periodograms. *IEEE Trans. Audio and Electroacoustics*, 15:70–73, jun 1967.

- [51] Wanming Zhai and Xiang Sun. A detailed model for investigating vertical interaction between railway vehicle and track. In Zhiyun Shen, editor, *The Dynamics of Vehicles on Roads and on Tracks*, volume 23, pages 603–615, Chengdu, China, aug 1993. Swets & Zeitlinger.

# List of Figures

1.1	<i>Black-box model. Top: Identification of model parameters with known input- and output-data. Bottom: Prediction of unknown output with known input. . . . .</i>	2
2.1	<i>Configuration of test train with two measuring cars and test object. . . . .</i>	5
2.2	<i>Cross section of railway track with wooden sleeper. Geometry in absolute coordinates. . . . .</i>	6
2.3	<i>Cross section of nominal (dotted lines) and actual (continuous lines) railway track with position of rails. Geometry measurements without absolute reference. . . . .</i>	7
2.4	<i>Shift function for left level signals. Test run Villach-Klagenfurt, km 145.5 to km 143.0. . . . .</i>	11
2.5	<i>Shift function for right alignment signals. Test run Villach-Klagenfurt, km 145.5 to km 143.0. . . . .</i>	12
2.6	<i>Spectra of speed signals. Test run Angern-Drösing (track 1), km 39.9 to km 38.4. . . . .</i>	13
2.7	<i>Spectra for left level. Test run Angern-Drösing (track1), km 50.5 to km 52.4. . . . .</i>	16
2.8	<i>Spectra for error signals of level. Test run Villach-Klagenfurt, km 145.5 to km 143.5. . . . .</i>	16
2.9	<i>Spectra for error signals of right level. Test run Villach-Klagenfurt, km 163 to km 127. . . . .</i>	17
2.10	<i>Spectra for left alignment (track 2). Test run Drösing-Angern, km 58.4 to 39.9. . . . .</i>	18
2.11	<i>Error spectra for left alignment (track 2). Test run Drösing-Angern, km 58.4 to 39.9. . . . .</i>	19
2.12	<i>Coherence function between left and right alignment signals. Test run Villach-Klagenfurt, km 163 to km 127. . . . .</i>	19
2.13	<i>PSD of mean alignment signal (blue) versus magnitude of transfer function of moving average (cyan): computed over 30m corresponding to 120 samples. Test run Angern-Drösing, km 39.9 to km 58.4, decimated to 1m sampling interval. . . . .</i>	20
2.14	<i>Spectra of curvature (track 2). Test run Drösing-Angern, km 58.4 to km 39.9. . . . .</i>	22
2.15	<i>Spectra of error signals for curvature (track 2). Test run Drösing-Angern, km 58.4 to km 39.9. . . . .</i>	23
2.16	<i>Transfer and coherence functions between mean alignment (output) and curvature (input): Estimated functions (red), theoretical functions (black). Test run Angern-Drösing, km 39.9 to km 58.4, decimated to 1m sampling interval. . . . .</i>	24
2.17	<i>Spectra of gauge measurements (track 1). Test run Angern-Drösing, km 39.9 to km 58.4. . . . .</i>	26
2.18	<i>Spectra of error signals for gauge (track 1). Test run Angern-Drösing, km 39.9 to km 58.4. . . . .</i>	26
2.19	<i>Gauge signals at a track section with large deviations (track 1). Test run Angern-Drösing, km 51.20 to km 51.26. . . . .</i>	27
2.20	<i>Spectra for error signals of gauge (track 2). Test run Drösing-Angern, km 58.4 to km 39.9. . . . .</i>	28
2.21	<i>Cant signals for track 2. Test run Drösing-Angern, km 43.4 to km 43.7. . . . .</i>	29
2.22	<i>Spectra for cant (track2). Test run Drösing-Angern, km 45.8 to 42.7. . . . .</i>	30
2.23	<i>Spectra of error signals for cant (track 2). Test run Drösing-Angern, km 45.8 to 42.7. . . . .</i>	30
2.24	<i>Spectra of cant versus difference of level (track 1). Test run Angern- Drösing, km 39.9 to km 58.4. . . . .</i>	32



2.25	<i>Spectra of error signals between cant and difference of level (track 2). Test run Drösing-Angern, km 58.4 to km 39.9.</i>	33
2.26	<i>Coherence function between cant and mean of level (blue) and between cant and difference in level (red). Test run Villach-Klagenfurt, km 163 to km 127.</i>	34
2.27	<i>Spectra of gauge versus difference of alignment (track 2). Test run Drösing-Angern, km 58.4 to km 39.9.</i>	35
2.28	<i>Spectra of error signals between difference of alignment and gauge (track 2). Test run Drösing-Angern, km 58.4 to km 39.9.</i>	36
2.29	<i>Coherence function between gauge and mean alignment (blue) and between gauge and difference of alignment (red). Test run Villach-Klagenfurt, km 163 to km 127.</i>	37
2.30	<i>Gauge and difference of alignment signals for curved track. Villach-Klagenfurt, test runs 1, 2, and 4, km 145.36 to km 145.4.</i>	38
3.1	<i>Rail forces for a single wheelset <math>i</math>, direction of travel into the paper plane.</i>	41
3.2	<i>Shift functions for <math>Y_1</math> forces. Test run Drösing-Angern, km 56.3 to km 44.2.</i>	44
3.3	<i>Sum of lateral wheel forces for test runs Angern-Drösing (track 1), km 41 to km 54.1.</i>	46
3.4	<i>Spectra of lateral wheel forces for test run m0006r, Angern-Drösing, km 43.5 to km 48.5.</i>	47
3.5	<i>Spectra of lateral wheel forces for test run m0507r, Drösing-Angern, km 52.2 to km 42.7.</i>	48
3.6	<i>Spectra of lateral wheel forces for test run m0008r, Angern-Drösing, km 41 to km 57.3.</i>	49
3.7	<i>Spectra of lateral wheel forces for test run m0010r, Angern-Drösing, km 41 to km 57.3.</i>	50
3.8	<i>Spectra of vertical wheel forces for test run m0006r, Angern-Drösing, km 43.5 to km 48.5.</i>	51
3.9	<i>Spectra of vertical forces for test run m0006r, Angern-Drösing: Zoom on wheel frequency and double wheel frequency</i>	52
3.10	<i>Spectra of vertical forces for test run m0008r, Angern-Drösing, km 41 to km 57.3.</i>	52
3.11	<i>Spectra of vertical forces for test run m0010r, Angern-Drösing, km 41 to km 57.3.</i>	53
3.12	<i>Spectra of twist between bogie and car body. All test runs on Angern-Drösing, km 43.5 to km 48.5.</i>	53
3.13	<i>Spectra of lateral car body accelerations above bogie. Test run Angern-Drösing, km 41 to km 57.3.</i>	54
3.14	<i>Spectra of lateral accelerations for middle of car body. Test run Angern-Drösing, km 41 to km 57.3.</i>	55
3.15	<i>Spectra of vertical car body accelerations above bogie. Test run Drösing-Angern, km 57.3 to 41.</i>	56
3.16	<i>Spectra of vertical car body acceleration in middle of car. Test run Drösing-Angern, km 57.3 to 41.</i>	57
3.17	<i>Spectra of lateral accelerations of mounting frame. Test run Drösing-Angern, km 57.3 to 41.</i>	58
3.18	<i>Spectra of acceleration of mounting frame for test run m0006r. Angern-Drösing, km 57.3 to 41.</i>	58
4.1	<i>Moving window for correlation analysis: Distorted abscissae. Input signal <math>u_d</math> and output signal <math>y_d</math> are plotted over normalized <math>x</math>-axis. Each axis is normalized by the respective sampling interval.</i>	74
4.2	<i>Moving window for correlation analysis: Absolute abscissae. Input signal <math>u_d</math> and output signal <math>y_d</math> are plotted with their actual sampling intervals.</i>	75
4.3	<i>Relative shift functions from simulated data. Actual shift (black), shift estimate with ideal output (red), and shift estimate with noisy output (blue).</i>	82
4.4	<i>Absolute shift function (red) and difference of absolute shift (blue)</i>	82

4.5	<i>Estimates of the absolute shift functions. Computed from original cant signal (red) and from shifted cant signal (blue).</i>	83
4.6	<i>Difference of absolute shifts (cyan) and cumulative sum of differences (magenta).</i>	83
4.7	<i>Natural frequencies of AR-model (5th-order). Simulated difference of Q-forces.</i>	84
4.8	<i>Sampling interval size for shifted signals.</i>	84
4.9	<i>Natural frequencies of the AR-model (5th-order). Simulated difference of Q-forces with shift applied (<math>\Delta x_s = 0.05m</math>).</i>	84
4.10	<i>Natural frequencies of AR-model (5th-order). Simulated difference of Q-forces with shift applied (<math>\Delta x_s = \pm 0.2m</math>).</i>	85
4.11	<i>Estimate of filter cut-off frequency (red) versus measured speed (blue). Both signals normalized to <math>\sigma = 1</math>.</i>	85
4.12	<i>Derivative of shift function <math>s(k)</math>.</i>	86
4.13	<i>Relative shift functions. Original data set with a constant shift of 10 samples (magenta), same data with shift function <math>s(k)</math> applied (red), original data set with a constant shift of 20 samples (cyan), same data with shift function <math>s(k)</math> applied (blue).</i>	88
4.14	<i>Absolute shift functions of output <math>y(k)</math> (red) and input <math>u(k)</math> (blue).</i>	89
4.15	<i>Relative shift (black) and numerical derivative of absolute shift (cyan).</i>	90
4.16	<i>Shift estimates <math>\hat{\tau}_{max_{10}}(k)</math> (red), <math>\hat{\tau}_{max_{20}}(k)</math> (blue), relative shift <math>s\tilde{\tau}_{max}^0(k)</math> (black), and derivative of absolute shift <math>\sigma\tilde{\tau}_{max}(k)</math> (cyan).</i>	91
5.1	<i>Cross-correlation estimates for level / Q-force interaction on axle 1: left rail / <math>Q_{1.1}</math> (magenta), right rail / <math>Q_{1.2}</math> (cyan), profile / <math>\sum Q_1</math> (red), <math>\text{diff}(\text{level}) / \text{diff}(Q_1)</math> (blue).</i>	93
5.2	<i>Cross-correlation estimates for alignment / Q-force interaction on axle 1: left rail / <math>Y_{1.1}</math> (magenta), right rail / <math>Y_{1.2}</math> (cyan), alignment / <math>\sum Y_1</math> (red), <math>\text{diff}(\text{alignment}) / \text{diff}(Y_1)</math> (blue).</i>	94
5.3	<i>Cross-correlation estimates for alignment / Y-force interaction on bogie 1: <math>\sum \text{alignment} / \sum Y</math> (red), <math>\text{diff}(\text{alignment}) / \sum M_Y</math> (blue).</i>	95
5.4	<i>Shift functions for curved track - vertical interactions. Difference of Q-forces / <math>\text{diff}</math> of level (red), difference of Q-forces / high-pass filtered cant (cyan), sum of Q-forces (blue).</i>	96
5.5	<i>Shift functions for curved track - lateral interactions. Sum of moments (blue), sum of Y-forces (red), sum of Y-forces / ML-estimate (magenta), <math>\text{diff}</math> of Q-forces (black).</i>	96
5.6	<i>Shift functions for curved track. CCF-estimate (red), ML-estimate (black).</i>	97
5.7	<i>Shift between profile (input/red) and averaged vertical wheel forces from axle 1 (output/green). Test run m0006r, Angern-Drösing.</i>	98
5.8	<i>Shift between original and resampled input. Linear shift removed, no oversampling. Test run ad7-0006.</i>	99
5.9	<i>Impulse responses for two correlation estimates. Green - order of prewhitening filter <math>n=8</math>, blue - <math>n=16</math>.</i>	99
5.10	<i>Performance indices over shift (dead time) for two 4th-order models. Output error (OE) model (red) and ARMAX model (blue).</i>	100
5.11	<i>Impulse responses for OE (red) and ARMAX model (blue) versus correlation estimate with 16th-order prewhitening filter.</i>	100
5.12	<i>Measured versus simulated model output. Measured output (black), OE model (red), and ARMAX model (blue).</i>	101
5.13	<i>Correlation functions of model residuals for 4th-order OE (red) and ARMAX model (blue), and 6th-order ARMAX model (brown).</i>	101
5.14	<i>Bode plot for different models. OE (red, cyan), ARMAX (blue, brown), and smoothed Fourier transform (orange).</i>	102

5.15	<i>Bode plot for different models. OE 6th-order <math>\Delta x = 1m</math> (blue), OE 6th-order <math>\Delta x = 0.5m</math> (black), and smoothed Fourier transform (orange).</i>	102
5.16	<i>Poles and zeros for the 6th-order OE model from filtered data.</i>	103
5.17	<i>Estimate of shift function between measured and simulated output for 6th-order OE model. Model oe660c, all measured signals were band-pass filtered and decimated to <math>\Delta x = 1m</math>.</i>	104
5.18	<i>Variance of speed signal (red) and curvature*0.001 (blue).</i>	105
5.19	<i>Estimate of relative shift function for curved track. Computed with cant and difference of Q-forces.</i>	105
5.20	<i>Derivative of shift (black) and scaled curvature (*0.01, blue).</i>	106
5.21	<i>Spectral estimates for cant (diff. of level signals, blue) and diff. of Q-forces at axle 1.</i>	106
5.22	<i>Estimate of relative shift function for curved track. Computed with band-pass filtered cant and band-pass filtered difference of Q-forces.</i>	107
5.23	<i>Shift estimate from curved track with band-pass filtered signals after resampling (red) versus bogie twist <math>\Psi</math> (blue).</i>	107
5.24	<i>Shift function for nonlinearly resampled band-pass filtered signals (red) versus bogie twist <math>\Psi</math> (blue).</i>	108
5.25	<i>Impulse response for linearly resampled data from curved track. 6th-order correlation model (orange), 6th-order OE model with dead-time of 11 samples (red), and 6th-order OE model with dead-time of 10 samples (green).</i>	108
5.26	<i>Simulated outputs and measured output with linear resampling.</i>	109
5.27	<i>Simulated outputs and measured output with nonlinear resampling.</i>	109
5.28	<i>Model residuals for output-error and ARMAX models. Validation data from nonlinearly resampled signals.</i>	110
5.29	<i>Bode plots for spectral estimates, OE, and ARMAX models.</i>	110
5.30	<i>Coherence functions for linearly (red) and nonlinearly (blue) resampled cant and difference of Q-forces.</i>	112
5.31	<i>Shift between original and corrected signals. <math>c_f(k)</math> versus <math>c_l(k)</math> (red), <math>c_l(k)</math> versus <math>u_c(k)</math> (blue), <math>\Delta Q_f(k)</math> versus <math>y_c(k)</math> (green, negative shift plotted).</i>	113
5.32	<i>Spectral Estimation. Smoothed Fourier transform models for the data sets <math>S_{corr}</math> (red), <math>S_{yc}</math> (green), and <math>S_{uc}</math> (blue).</i>	114
5.33	<i>Bode plots for different models. Smoothed Fourier transform from <math>S_{yc}</math> (black), OE models from <math>S_{corr}</math> (red), <math>S_{yc}</math> (green), and <math>S_{uc}</math> (blue), and the ARMAX model from <math>S_{corr}</math> (magenta).</i>	115
5.34	<i>Shift functions for original (blue) and band-pass filtered cant signal (red).</i>	116
5.35	<i>Shift functions for original (blue) and band-pass filtered force differences (red).</i>	116
5.36	<i>Comparison of shift functions. Cumulative sum of the difference of absolute shifts (red) and relative shift (blue), respectively. Input cant <math>c(k)</math>, output difference of <math>Q_1</math>-forces <math>\Delta Q_1(k)</math>.</i>	117
6.1	<i>Estimates of Lipschitz coefficients for different orders. Inputs are difference of level signals and difference of Q-forces on axle 1. Signal length 2000 samples.</i>	119
6.2	<i>Estimates of Lipschitz coefficients for different orders. Inputs are difference of level signals and difference of Q-forces on axle 1. Signal length 4000 samples.</i>	120
6.3	<i>Linear correlations for Output-Error model with order [6 6 1].</i>	120
6.4	<i>Nonlinear correlations for Output-Error model [6 6 1].</i>	121
6.5	<i>Measured output (black) and simulated outputs from static linear gains (red), second-order MISO OE-model (blue).</i>	123
6.6	<i>Measured output (black) and simulated outputs from second-order MISO OE-model (blue) with static gain of <math>c^2(x)</math></i>	123

6.7	Measured output (black) and simulated output from RBF-model (red) with 60 basis functions and 6 inputs: 4 delayed cant signals and 2 delayed curvature signals. . . .	124
6.8	Sum of Q-forces for axle 1: Measured signal (black) and simulated output from second-order OE-model ([2 2 1]) (red). . . . .	124
6.9	Sum of all Q-forces at bogie 1 (black). Nonlinear combination of input signals $\frac{c(x)}{R(x)}$ (magenta). . . . .	125
6.10	Spectral estimates for sum of alignments $a_c(k)$ (blue) and sum of Y-forces $Y_c(k)$ (red). Black ordinates at 2.5, 0.83, and 0.5m. . . . .	126
6.11	Biased Y-force signal $Y_{1.1}$ : Recorded signal (green), first correction removed (red), second correction removed (blue). Signals decimated by a factor of 60. . . . .	127
6.12	Lateral force signal $Y_{1.1}$ : Signal with jumps removed (red), linear rgression computed from signal sections corresponding to straight track (black), and corrected signal with linear trend removed (blue). . . . .	128
6.13	Validation data for linear identification of Y-forces: Static model with low-pass filtered $Y_{1.1}$ as output and curvature $\rho(x)$ and combined signal $c(x)\rho(x)$ as inputs. . . .	128
6.14	Y-forces during curve negotiation. Test run Klagenfurt-Villach, km 124 to km 140. $Y_{1.1}$ red, $Y_{1.2}$ blue, $Y_{2.1}$ green, and $Y_{2.2}$ cyan. . . . .	129
6.15	Sum of diagonal Y-forces during curve negotiation. Test run Klagenfurt-Villach, km 124 to km 140. $Y_{d1}$ red, $Y_{d2}$ blue. . . . .	129
A.1	Symmetrical versine measurement in relative coordinates: chord length $L$ . . . . .	134
A.2	Modulus of transfer function for symmetrical versine measurement: length of chord 10m, discretized at 0.25m . . . . .	136
A.3	Transfer function of moving average. Top: magnitude, bottom: phase. Sampling interval of 0.25m, average over 121 points (30m). Both plots over spatial frequency (1/m). . . . .	137
B.1	Model validity tests: Linear correlations . . . . .	141
B.2	Model validity tests: Nonlinear correlations . . . . .	141
B.3	Model validity test: Linear correlations . . . . .	142
B.4	Model validity test: Nonlinear correlations . . . . .	143
B.5	Lipschitz coefficients for linear SISO system without noise. Correct system order of $n = 5$ detected. . . . .	145
B.6	Lipschitz coefficients for linear SISO system without noise. Wrong system order of $n = 4$ detected (correct system order $n = 5$ ). . . . .	146
B.7	Lipschitz coefficients for linear SISO system with noise. Correct system order $n = 5$ not detectable. . . . .	147
B.8	Lipschitz coefficients for linear SISO system with noise. Correct system order $n = 5$ not detectable. . . . .	147
B.9	Lipschitz coefficients for nonlinear SISO system without noise and $\alpha = 1$ . . . . .	148
B.10	Lipschitz coefficients for nonlinear SISO system without noise and $\alpha = 0.33$ . . . . .	148
B.11	Lipschitz coefficients for nonlinear SISO system with nonlinear noise term and $\alpha = 1$ . . . . .	149
B.12	Lipschitz coefficients for nonlinear SISO system with nonlinear noise term and $\alpha = 0.33$ . . . . .	149
D.1	Comparison of interpolation techniques: Original signal (red), spline interpolant (magenta), and lowpass filtered discrete interpolation (cyan). Samples used for reconstruction denoted by blue circles. . . . .	156

# List of Tables

2.1	<i>Main characteristics of data sets</i>	9
2.2	<i>Color key for figures</i>	9
2.3	<i>Shift between test runs 506-da7, 507-da8, and 510-da11 respectively.</i>	10
2.4	<i>Test runs on track 1. Statistics for speed.</i>	12
2.5	<i>Test runs on track 1. Statistics for level.</i>	15
2.6	<i>Frequencies of maxima in error signals.</i>	15
2.7	<i>Test runs on track 1. Statistics for alignment.</i>	18
2.8	<i>Test runs on track 1. Statistics for curvature.</i>	21
2.9	<i>Shift between curvature signals. Reference signal: 0006-ad7</i>	24
2.10	<i>Test runs on track 1. Statistics for gauge.</i>	25
2.11	<i>Shift between gauge signals. Reference signal: 0006-ad7</i>	27
2.12	<i>Test runs on track 1 and 2. Statistics for cant.</i>	29
2.13	<i>Test runs on track 1. Shift between gauge and alignment signals.</i>	36
2.14	<i>Color coding for figure 2.30</i>	38
3.1	<i>Data channels for dynamic vehicle data</i>	43
3.2	<i>Color key for figures</i>	43
3.3	<i>Color key for figures</i>	43
3.4	<i>Vehicle data. Statistics for speed.</i>	45
3.5	<i>Statistical values for lateral wheel forces</i>	46
3.6	<i>Statistical values for vertical wheel forces</i>	48
3.7	<i>Statistical values for twist between bogie and car body</i>	50
3.8	<i>Statistical values for car body accelerations</i>	51
3.9	<i>Time domain frequencies in the spectra of test runs on track 2 (Drösing-Angern)</i>	54
4.1	<i>Poles, zeros, and gain for 8th-order Box-Jenkins model from filtered data (3rd-order noise model).</i>	81
5.1	<i>Poles, zeros, and gain for 6th-order OE model from filtered data</i>	103
5.2	<i>Mean square fits for different models</i>	109
5.3	<i>Poles, zeros, and gain for 6th-order OE model from filtered data</i>	111
5.4	<i>Data structure for comparison of synchronization methods</i>	113
5.5	<i>Best fits for OE and ARMAX models: All combinations of training and validation data</i>	113

# LEBENS LAUF

## Persönliche Daten:

Name Martin Kozek  
Geburtsdatum 13. Februar 1967  
Staatsbürgerschaft Österreich  
Familienstand verheiratet  
Adresse: Pfadenhauergasse 22/28  
1140 Wien

## Schul Ausbildung:

09/73 – 07/77 Grundschule in Salzburg;  
09/77 – 06/85 Bundesrealgymnasium in Salzburg, Matura mit ausgezeichnetem Erfolg;

## Studium:

09/85 – 11/93 Studium des Maschinenbaus an der Technischen Universität Wien  
Erste und zweite Diplomprüfung mit ausgezeichnetem Erfolg  
Diplomarbeit:  
*Modellbildung, Stabilitätsuntersuchung und Simulation eines  
MAGLEV-Tragsystems sowie Entwurf einer Sliding-Mode Regelung*  
(Institut für Maschinen- und Prozeßautomatisierung)  
11/93 – Doktoratsstudium der Technischen Wissenschaften  
07/97 – 07/98 Forschungsaufenthalt an der University of Utah, Salt Lake City, USA,  
gefördert durch ein Kurt-Gödel Auslandsstipendium

## Berufliche Tätigkeit:

07/86 AB Electronic, Salzburg  
Maschinenschlosser  
01/95 – Universitätsassistent, Institut für Maschinen- und Prozeßautomatisierung,  
Technische Universität Wien

## Grundwehrdienst:

04/94 – 12/94 Wehrdienst, Amt für Wehrtechnik, Abteilung Maschinenwesen